Doctoral Thesis

Highly Efficient Light Harvesting for High-Performance Polymer Solar Cells

Seo-Jin Ko

Department of Energy Engineering

Graduate School of UNIST

2015

Highly Efficient Light Harvesting for High-Performance Polymer Solar Cells

Seo-Jin Ko

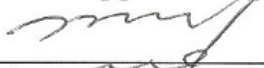Department of Energy Engineering

Graduate School of UNIST

Highly Efficient Light Harvesting for High-Performance Polymer Solar Cells

A thesis

submitted to the Graduate School of UNIST

in partial fulfillment of the

requirements for the degree of

Doctor of Philosophy

Seo-Jin Ko

07.20. 2015 of submission

Approved by

_____

Major Advisor

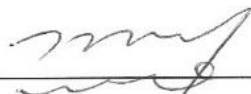Jin Young Kim

Highly Efficient Light Harvesting for High-Performance Polymer Solar Cells

Seo-Jin Ko

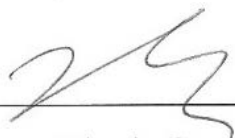This certifies that the thesis of Seo-Jin Ko is approved.

07. 20. 2015 of submission
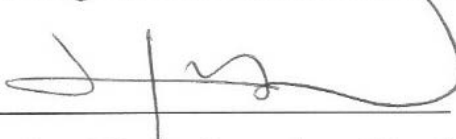
Thesis supervisor: Jin Young Kim

Changduk Yang: Thesis Committee Member #1

Tae-Hyuk Kwon: Thesis Committee Member #2

Myoung Hoon Song: Thesis Committee Member #3

Han Young Woo: Thesis Committee Member #4

Abstact

Polymer solar cells (PSCs) have gained a lot of attention due to their promising merits such as low cost, mechanical flexibility and solution processability for large area fabrication. Of various strategies, the surface plasmon resonance (SPR) effect using metal nanoparticles (MNPs), morphology control by processing additives, and ternary blend based bulkheterojunction (BHJ) are promising and efficient method to lead to maximizing the performance of PSCs. First, SPR effect from a localized electromagnetic surface wave at the metal and dielectric interface is effective way to enable active layer to absorb more incident light by field enhancement near MNPs. Second, morphology control by processing additives is one of the efficient methods to improve the PSCs accompanied with various morphology engineerings such as nanofibrilar structure, smooth surface, vertical phase separation etc.. Third, ternary blend sytem of PSCs is also promising engineering to achicve many advantages including compensated light absorption and tuning of built-in potential of BHJ.

Here, I report the SPR effect using PEDOT electrode incorporated with silver nanopartices (Ag NPs) for highly efficient ITO-free PSCs and polymer light-emitting diodes (PLEDs). Ag NPs can be easily synthesized and then dissolved in PEDOT:PSS electorode. This PEDOT:PSS electrode with Ag NPs electrode contributes to increments in light absorption/emission in the active layer, respectively, by enhanced electric field distribution. I also report morphology engineering of active layer using various conjugated polymers and processing additives with thick active layer to obtain more light absorption and higher efficieny with thick active layer. PSCs based on semi-crystalline, low band gap (LBG) polymers are fabricated with single-cell architecture using diphenyl ether (DPE) as a processing additive. By using DPE additive, the semi-crystalline polymer, PPDT2FBT, form a well-distributed nano-fibrillar networked morphology with $PC_{71}BM$ with balanced hole and electron mobilities. Notably, PPDT2FBT:$PC_{71}BM$ with DPE shows high efficiency event at ~ 1μm film thickness with well-formed isotropic morphology. DTDPPTT (P2) polymer also demonstrate bicontinuous interpenetrating donor:acceptor (D:A) network in both lateral and vertical direction of thick BHJ film with DPE additive. Finally, I present efficient ternary PSCs via the incorporation of both $PC_{61}BM$ and $PC_{71}BM$ mixture as mixed acceptors and the conjugated polymer, PTBT as a donor. This ternary blend system results in a remarkable improvement in the power conversion efficieny compared to binary mixtures of the components via enhanced light absorption by $PC_{71}BM$ and balanced chargetransport by $PC_{61}BM$. These virious and efficient methods using plasmonic MNPs, morphology engineering, and ternary blend may offer possibility for commercialization of PSCs.

Keywords: Polymer solar cells, surface plasmon resonance effect, metal nanoparticles, morphology control, processing additive, conjugated polymer, ternary solar cell.

Table of Contents

List of Figures

Figure 1.10. SEM cross-sectional images of MDMO-PPV:PCBM blend films on top of ITO from a) CB and b) toluene solution. The brighter objects in a) are polymer nanospheres, whereas the darker embedments are PCBM clusters. Schematic of film morphology of c) CB- and d) toluene-cast MDMO-PPV: PCBM blend active layers. In c), carriers form percolated pathways to reach their respective electrodes. In d), electrons and holes suffer from recombination due to undesirable phase separation.

Figure 1.11. AFM and TEM images of PCPCTBT/PC$_{71}$BM films without and with 1,8-octanedithiol and exposed PCPDTBT networks after removal of PC$_{71}$BM. AFM image of BHJ film a) without and b) with 1,8-octanedithiol. AFM image of exposed polymer networks c) without and d) with 1,8-octanedithiol. TEM image of exposed polymer networks e) without and f) with 1,8-octanedithiol.

Figure 1.12. Schematic representation of the cascade charge transfer in a ternary solar cell, where the P3HT:PCBM is employed as the host system and low bandgap material of C-/Si-PCPDTBT as the near IR sensitizer. The electronic energy levels of electrodes and semiconductors are presented in eV unit. Curved arrows indicate allowed charge transfer reactions in the ternary blend.

Figure 1.13. Photoinduced absorption spectra of annealed thin films (d ~ 100–150 nm) of P3HT:PCPDTBT:PCBM (0.8:0.2:1) (open squares), PCPDTBT:PCBM (1:1) (open circles), and P3HT:PCBM (1:1) (open triangles) which were all excited at 1.59 eV. P3HT:PCBM (1:1), excited at 2.33 eV (full line).

Figure 1.14. Schematic representation of the resonant energy transfer mechanism, as donor absorbs light (arrow 1) and transfers the energy to acceptor (arrow 2), which fl uoresces (arrow 3). The abbreviations of Abs. and PL represent the absorption and photoluminescence spectra of the donor and acceptor, respectively.

Figure 1.15. Schematic representation of the parallel-like charge transfer in a ternary solar cell, where polymer 1 and 2 are employed as the complementary absorbers blended in an acceptor. Curved arrows indicate charge transfer and linear arrows indicate charge transport in the ternary solar cell.

Figure 1.16 Structures and energy levels of P3HT, ICBA, and PC$_{61}$BM and V_{OC} for the ternary blend BHJ solar cells as a function of the amount of ICBA in the blend.

Figure 3.1. (a) Chemical structures, (b) noncovalent attractive interactions within the polymer chain, (c) UV-vis absorption spectra (dashed: in chloroform, solid: in the film), (d) TGA and DSC thermograms of PPDTBT, PPDTFBT and PPDT2FBT and (e) energy-band diagram.

Figure 3.2. Synthetic routes to the monomers and polymers. Reagents and reaction conditions: (i) 2-tributylstannylthiophene, Pd2(dba)3, tris(o-tolyl)phosphine, toluene; (ii) (CH3)3SnCl, LiN(Pr-i)2, THF; (iii) C16H33Br, KOH, 50% TBAB, toluene; (iv) Pd2(dba)3, tris(o-tolyl)phosphine chlorobenzene.

Figure 3.3. Torsional profiles for (a) thiophene-difluoro BT and (b) thiophene-dimethoxybenzene (yellow:sulfur, green: fluorine, red: oxygen). (c) The most stable conformation for PPDTBT, PPDTFBT and PPDT2FBT. (*) Methoxy substituents are replaced by ethyl groups in PPDT2FBT.

Figure 3.4. Calculated binding energies of HT-type cofacial dimeric structures for PPDTBT, PPDTFBT and PPDT2FBT. (*) Methoxy substituents are replaced by ethyl groups in PPDT2FBT. (red: oxygen, yellow:sulfur, green: fluorine)

Figure 3.5. Cyclic voltammogram of three polymers.

Figure 3.6. Calculated electronic structure of frontier orbitals.

Figure 3.7. *J-V* characteristics of (a) PPDTBT, (b) PPDTFBT and (c) PPDT2FBT based PSCs with different polymer:PC70BM blend ratios (solvent: o-dichlorobenzene).

Figure 3.8. (a) Current density versus voltage (J–V) characteristics (w/o TA: without thermal annealing, w/TA: with thermal annealing) and (b) temporal stability (at an annealing temperature of 130 °C) of polymer: $PC_{71}BM$ PSCs. All devices were prepared from o-dichlorobenzene solutions.

Figure 3.9. Tapping-mode AFM topography and phase images of polymer:$PC_{71}BM$ blend films (solvent: DCB) before and after thermal treatment at 130°C for 200 h. Before thermal treatment: PPDTBT (a_1 and a_2), PPDTFBT (b_1 and b_2), PPDT2FBT (c_1 and c_2), P3HT (d_1 and d_2). After thermal treatment: PPDTBT (e_1 and e_2), PPDTFBT (f_1 and f_2), PPDT2FBT (g_1 and g_2), P3HT (h_1 and h_2). The size of all images is 1.5 mm x 1.5 mm.

Figure 3.10. Photovoltaic characteristics of polymer:$PC_{71}BM$-based devices fabricated using a CB:DPE solvent mixture. (a) Current density versus voltage (*J–V*) characteristics and (b) external

Figure 3.20. *J-V* characteristics of (a)~(c) hole-only and (d)~(f) electron-only devices based on polymer:$PC_{71}BM$ blend films with various film thickness (solvent: CB:DPE = 98:2 vol%). Blue lines represent fits of the curves using the Mott-Gurney relationship.

Figure 3.21. Grazing incidence wide angle X-ray scattering (GIWAXS) images. GIWAXS images of pristine polymer films (upper two rows) (a) without and (b) with DPE, and polymer:$PC_{71}BM$ blend films (lower two rows) (c) without and (d) with DPE. Left, middle and right panels show the images for PPDTBT, PPDTFBT and PPDT2FBT, respectively.

Figure 3.22. In-plane (a and c) and out-of-plane (b and d) GIWAXS data for pristine polymers (a and b) and polymer:$PC_{71}BM$ (c and d) films with and without DPE.

Figure 4.1. Materials and schematic device architectures. (**a**) Molecular structures of PPDT2FBT and $PC_{71}BM$. (**b** and **c**) Conventional and inverted solar cell architectures, respectively. The top and side surface textures are constructed from re-colored AFM and cross-sectional TEM data, respectively. (**d** and **e**) Current density-voltage characteristics and incident photon conversion efficiency (IPCE), respectively, of optimized PPDT2FBT:$PC_{71}BM$ devices in conventional and inverted BHJ solar cells; the inset shows the dark currents for each device.

Figure 4.2. Optical constants. n and κ values used for (a) PPDT2FBT:$PC_{71}BM$, (b) P3HT:$PC_{61}BM$, (c) PCDTBT:$PC_{71}BM$, (d) PTB7:$PC_{71}BM$, (e) glass, (f) ITO, (g) PEDOT:PSS, (h) ZnO, (i) MoO_3, (j) Al and (k) Au. Blue traces represent n values while red traces represent κ values.

Figure 4.3. Observed J_{SC} compared to theoretical maximum photocurrent. (a and e) show data for PPDT2FBT; (b and f) show data for P3HT; (c and g) show data for PCDTBT; (d and h) show data for PTB7. (a to d) show data for conventional devices while (e to h) show data for inverted devices. Optically modeled currents appear as red and blue solid lines in conventional and inverted architectures, respectively, while observed J_{SC} values are plotted as blue-green circles.

Figure 4.4. Solar cell parameters vs. active layer thickness. (a) Ratio of observed J_{SC} (J_{OBS}) to optically modeled J_{SC} (J_{OPT}) (spectrally averaged IQE), (b) Fill factor, (c) power conversion efficiency observed for PPDT2FBT:$PC_{71}BM$ (blue), P3HT:$PC_{61}BM$ (red), PCDTBT:$PC_{71}BM$ (purple) and PTB7:$PC_{71}BM$ (green).

Figure 5.8. Comparison of measured J_{SC} from *J-V* characteristics and estimated J_{SC} from optical simulation of P2:PC$_{71}$BM PSCs with structure of ITO/PEDOT:PSS/active layer/Al as a function of active layer thickness.

Figure 5.9. AFM topography images of BHJ films with optimum (top row), thin (middle row), and thick (bottom row) thickness that were prepared from CF:DCB (a, d, g), CB (b, e, h), and CB:DPE (c, f, i). The scale bar is 1 μm.

Figure 5.10. Cross-sectional TEM images (a-c) and EDS S mapping (d-f) of optimum devices prepared from CF:DCB (a, d), CB (b, e), and CB:DPE (c, f), respectively. Scale bar is 100 nm.

Figure 5.11. EDS C (red dots, left column) and S mapping (green dots, right column) of optimum BHJ film prepared from (a, b) CF:DCB, (c, d) CB, and (e, f) CB:DPE, respectively. Scale bar of EDS mapping is 100 nm.

Figure 5.12. GIWAXS patterns of pristine polymer films prepared from CF:DCB (a), CB (b), and CB:DPE (c). d-f, GIWAXS patterns of P2:PC$_{71}$BM BHJ films prepared from CF:DCB (d), CB (e), and CB:DPE (f).

Figure 5.13. (a, c) In-plane and (b, d) out-of-plane linecuts of GIWAXS for pristine polymer (upper row) and blend films (lower row) prepared from different solvents. The Insets of Figure 5.13(b) and (d) indicate expanded out-of-plane linecuts for visualizing π-π face-on orientation.

Figure 5.14. Transfer (upper row) and output (lower row) characteristics of OFET based on (a, d) pristine polymer prepared from CB and (b, c, e-g) blend films prepared from different solvents. Bottom-gate/bottom-contact on a Si/SiO$_2$ substrate with a channel length of 160 μm and a channel width of 1000 μm are used for OFET characterization. n-decyltrichlorosilane (DTS) was used as the self-assembled monolayer on Si/SiO$_2$ substrate.

Figure 5.15. *J-V* characteristics of (a) hole- and (b) electron-only devices using P2:PC$_{71}$BM BHJ films prepared from different solvents. Blue lines indicate SCLC fits of curves based on Mott-Gurney relationship.

List of Tables

Table 6.2. 2D-GIXRD packing parameters along the in-plane and out-of-plane directions.

Table 6.3. Charge carrier mobility for ternary BHJ films with different blend ratios (PTBT:$PC_{61}BM$:$PC_{71}BM$) via SCLC measurements.

Table 6.4. Ambipolar device parameters of ternary blend BHJ FETs via different blend ratio (PTBT:$PC_{61}BM$:$PC_{71}BM$).

Chapter 1. Introduction

1.1 Backgound of Organic Solar Cells (OSCs)

The discovery of solar cells with photo voltaic effect were begun by Becquerel who found a photo current in 1839.[1] First, Adams and Smith made reported photoconductivity by use of selenium in 1873 and 1876, respectively. Pochettino and Volmer discovered anthracene as a first organic compound showed photoconductivity in 1906 and 1913, respectively.[2] In the 1950s and 1960s, the promising utilization of organic materials as photo-sensitizers for imaging system was recognized by many researchers. The increasing scientific interest and concentration for commercial potentials resulted in increased research into the photoconductivity and related field. In the 1960s, it was discovered that many dyes had semiconducting properties.

After the oil crisis in the 1970s, immense efforts were devoted to the development of photovoltaic cells and the industry tried to begin back to nature because manufacturing and costs grew, and the manufacturing facilities for producing the photovoltaic modules from silicon-based p-type and n-type junction solar cells were made in many countries. Afterward, low-cost solar cells were required for use generally, and also organic materials are utilized for the photovoltaic cell.

Tang *et al*. reported two organic materials, copper phthalocyanine (CuPc) and perylene tetracarboxylic derivatives in use of organic solar cells, which showed power conversion efficiency of 0.95% in 1986.[3]

One of the major breakthroughs in organic solar cell technology was the adoption of C60 fullerene and its derivatives (such as [6,6]-phenyl-C61-butyric acid methyl ester, PCBM) to replace the n-type molecules in organic solar cel devices. Owing to their strong electronegativity and high electron mobility, C60 derivatives have become standard n-type molecules in organic solar cells.

In the early 1990s, Heeger *et al*. and Yoshino *et al*. independently demonstrated electron charge transfer between a conjugated polymer and fullerene derivatives.[4, 5] They observed an extremely fast photoinduced electron transfer process of around 50–100 fs, which dominates over all other photophysical processes present. These discoveries provided a solid foundation for organic solar cell technology. In 1993, researchers made the first demonstrations of planar heterojunction solar cells.

The discovery of this result resulted in the development of organic solar cells *via* the polymer-fullerene composite. In addition, Yu *et al*. improved the power conversion efficiency of organic solar cells by introduction of bulk heterojunction structure.[6] Recently, power conversion efficiencies of organic solar cells have been achieved up to 10% by using new conjugated polymer, device architectures and various technics.

1.2 Physics of OSCs

1.2.1 Principle of OSCs

The solar cell is the device that generates electricity from the sunlight. Fisrt, an active layer absorbs photons in the device, and second electron-hole pair is generated as an exciton under illumination state. Third, the exciton diffuses to the donor–acceptor (DA) interface to be dissociated into free charge. Afterwards, electrons and holes are transfered to each electrode *via* their corresponding percolation pathway.[7] Four main steps are described as shown in **Figure 1.1**; i) absorption of photon (η_A), ii) diffusion of exciton (η_{ED}), iii) dissociation of exciton and charge transport of electron and hole (η_{CT}), vi) charge collection (η_{CC}). The efficiency is the result of each process.

These four processes determine the solar cell performance closely connected with external quantum efficiency (EQE) for the device. EQE is defined as a percentage of the number of charge carriers collected at the electrode under short-circuit condition to the number of photons incident on the device.[8] EQE can be expressed as the product of the above steps.

$$EQE = \eta_A \times \eta_{ED} \times \eta_{CT} \times \eta_{CC}$$
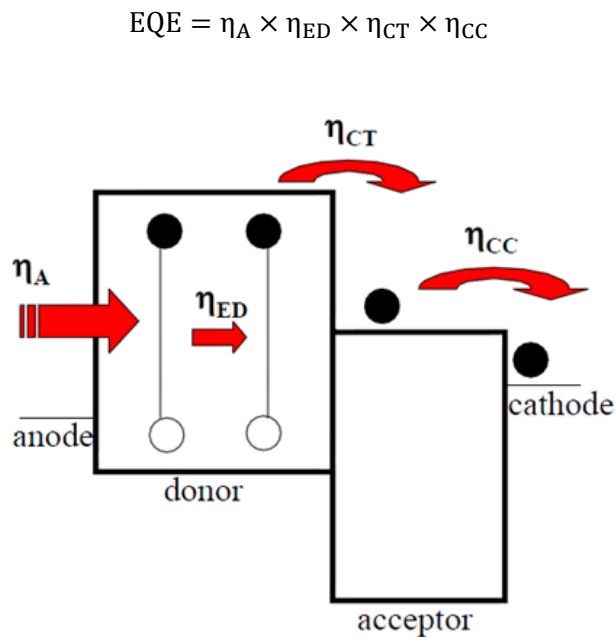
Figure 1.1. Main processes for generating the electricity under the illumination in the device.

Absorption of Photon (η_A)

The absorption of photon is determined from the absorption spectral band, optical absorption coefficient, and thickness of a photoactive layer, as well as internal reflection. Most of

semiconducting polymers (e.g., P3HT, MDMO-PPV, etc) have a bandgap larger than 2 eV, which limits light absorption range less than 650 nm. Therefore, only a small portion of sunlight can be absorbed in polymer solar cells. Usually, the thickness of an active layer is in the order of 100 nm to avoid exciton and charge tranport loss. To well balance sufficient light absorption and efficient charge transport, both a wide absorption spectral band and a high absorption coefficient become important for absorbing enough sunlight. The absorption coefficients of conjugated polymers were reported to be much higher than that of silicon so that a thin layer (e.g., 100 nm) of polymer is enough to absorb sufficient light.

Exciton diffusion (η_{ED})

The efficiency of exciton diffusion to a DA interface is related to its exciton diffusion length (L_D) and distance (L_i) between photoexciton location and DA interface which serves as a dissociation center.[9] The L_D is equal to $(D\tau)^{1/2}$, where D is diffusion coefficient and τ is exciton lifetime.[10] Excitons can diffuse to a DA interface with $L_i \leq L_D$, otherwise they may recombine with a reduced η_{ED}. Typically, exciton diffusion length is in the range of 4-20 nm for conjugated polymers.[11-13]

Exciton dissociation and charge transport (η_{CT})

The efficiency of exciton dissociation into free holes and electrons relies on DA LUMO energy offsets and internal electric field at a DA heterojunction.[8] From current understanding, the minimum energy required to dissociate an exciton in a conjugated polymer is what is needed to overcome the exciton binding energy.[14] This energy can be provided by the offset between the LUMO energy levels of the donor and the acceptor.

The η_{CT} is charge transport efficiency. The holes are transported in a conjugated polymer, while the electrons are transported in an inorganic semiconductor. Both the donor and acceptor materials are required to form highly efficient percolation networks spanning the entire active layer to provide efficient charge transport.[15] The polymers need to have a higher degree of planarity for efficient backbone stacking for a high hole mobility. Through the treatments such as thermal and solvent annealing, the polymers should also be able to self-assemble into a more organized structure.

Collection of charge-carriers (η_{CC})

It is the fraction of the charges transported from the active layer to the electrodes with respect to the total free charges that are supposed to transport to the electrodes. The η_{CC} depends on the energy levels of the active layer, the electrodes and the interface between them.[8]

1.2.2 Characterization of OSCs

Solar cell efficiency can be calculated from its current densityvoltage (*J-V*) characteristic curves. From such curves, open circuit voltage (V_{OC}), short-circuit current density (J_{SC}) and fill factor (FF) can be obtained. Then energy conversion efficiency can be determined by equation 1.1

$$\eta = \frac{J_{sc}\, V_{oc}\, FF}{P_s} \times 100 \quad (1.1)$$

Where P_S is the incident light power density. A standard test condition for solar cells is Air Mass 1.5 global (AM 1.5 G) with an incident power density of 100 mW cm^{-2} at a temperature of 25° C. Equivalent circuit of a solar cell is shown as **Figure 1.2**. A series resistance (R_S) originates from contact and bulk semiconductor, and a shunt resistance (R_{sh}) comes from poor diode contact. The *J-V* characteristics can be described as equation 1.2,[16]

$$J = J_0 \left\{ \exp\left[\frac{q(V-JR_SA)}{nKT}\right] - 1 \right\} + \frac{V-JR_SA}{R_{sh}A} - J_{ph} \quad (1.2)$$

Where k is Boltzmann's constant, T is temperature, q is elementary charge, A is device area, n is ideality factor of the diode, J_0 is reverse saturation current density, J_{ph} is photocurrent, R_S is series resistance and R_{sh} is shunt resistance. The *J-V* curves and photovoltaic parameters including V_{OC} and FF strongly depend on the n, J_0, R_S, and R_{sh}.
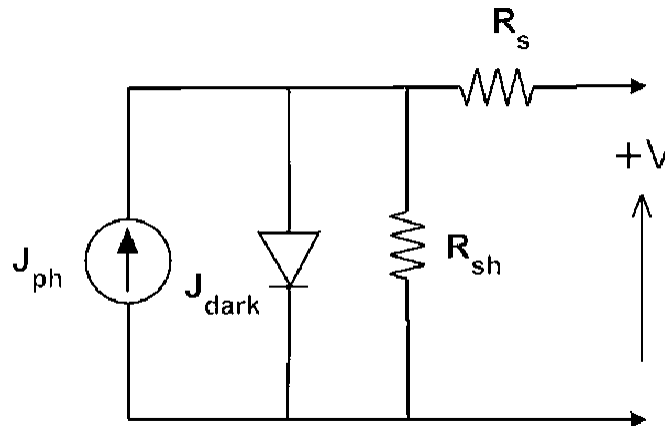
Figure 1.2. The equivalent circuit for solar cell.

Figure 1.3 shows typical dark and illuminated current density-voltage (*J-V*) curves, in which three distinctive regions can be seen.[17] The first (I) is the linear region in negative potentials and low positive potentials, in which the current density is dominated by the shunt resistance (R_{sh}). The second (II) is the region at mediate positive regions where the curve shows an exponential behavior and the

current density is related to the diode. The third (III) is another linear region in high positive potentials where the current density is related to the series resistance (R_S).[17]

The ideality factor (n) is a figure which shows how closely a diode behaves like an ideal diode and it is typically deviated from the ideal by recombination in the junction. In polymer-fullerene solar cells that can be pictured as an ''extended pn junction'', recombination can happen at the DA interface (junction) when the separated electrons and holes meet,[18] causing n to deviate from 1. Thus, the ideality factor (n) can be regarded as an indicator of DA morphology, phase separation and their interfacial area. Waldauf *et al*. reported that bulk heterojunction solar cells with their active layers made from the same production batch have comparable diode idealities, indicated by similar slopes in the exponential regime of their *J-V* curves. It was also found that different solvents led to different morphologies in organic solar cells, resulting in different idealities.[19]

The reverse saturation current density (J_0) is also an important parameter affecting the *J-V* curves in the exponential regimes and thus cell performance. The J_0 is an indicator of how many charges can overcome the energetic barrier in the reverse direction. These charges are regarded as minority charges at the donor/acceptor interface. In a typical pn junction, J_0 can be described as equation 1.3

$$J_0 = J_i \exp\left[\frac{-q\phi}{nKT}\right] \quad (1.3)$$

Where J_i depends on material purity and f is energetic barrier voltage. ϕ was found to be in good agreement with energy difference of the acceptor's LUMO and the donor's HOMO. The J_0 value increases with increasing temperature (T), but decreases as the material quality (purity) and energetic barrier improve.

The series resistance (R_S) is another parameter that affects the *J-V* characteristics and solar cell performance. The R_S results from limited conductivity of organic layer, contact resistance between organic layer and its corresponding electrodes, and connecting resistance between the electrodes and external circuit. The R_S can reduce the FF and it can also reduce the J_{SC} if it is too high. Generally the R_S has no impact on open circuit voltage (V_{OC}) since the entire current flows through the diode at the V_{OC} condition, but no current flows though the R_S. However, at the points close to the V_{OC}, the R_S greatly affects the *J-V* curves, providing a simplified method to estimate the R_S by measuring the slope of the *J-V* curves in the regime close to the V_{OC}. The R_S should be minimized to reduce the energy loss, especially in large area solar cells.[20]

The shunt resistance (R_{sh}) is also a parameter affecting the *J-V* characteristics and solar cell performance. The R_{sh} may be related to the device structure and film morphology. For example, R_{sh} can be lowered by the leakage current through the pinholes and recombination of charge carriers in the devices.[21] The morphology and thickness can be processed with care to reduce the pinholes and

recombination in the devices so that the R_{sh} can be increased. The R_{sh} needs to be maximized to reduce the power loss caused by the current that by passes the solar cell junction and load through an alternate current path from the low R_{sh}. A small R_{sh} lowers the current flowing through the diode (junction) and thus reduces the V_{OC}. A simplified way to approximately calculate the R_{sh} is to measure the slope of the J-V curves in the regime close to the J_{SC}.
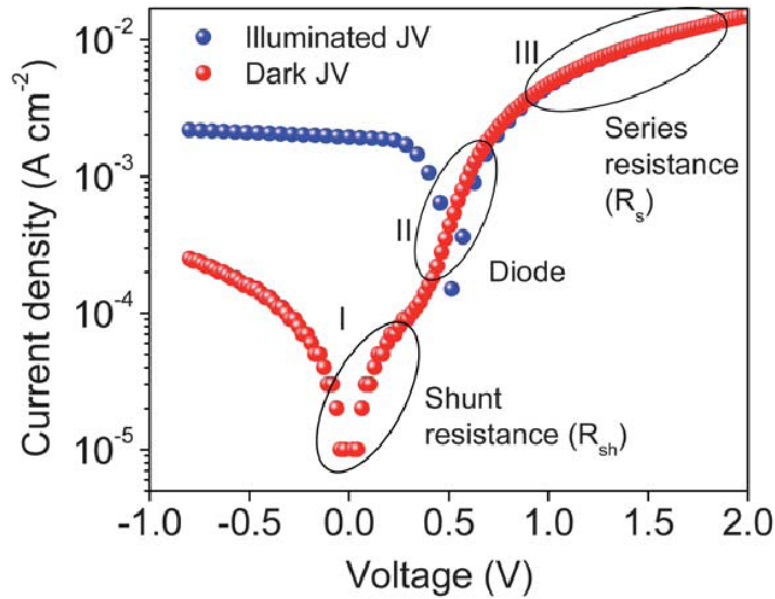
Figure 1.3. *J-V* curves of solar cell.

The above discussed n, J_0, R_s and R_{sh} can strongly affect the photovoltaic parameters including V_{OC}, FF, J_{SC} and cell efficiency (η). V_{OC} is defined as the voltage across the cell under illumination with a zero current at which the dark current and short circuit photocurrent was exactly cancelled out. By solving the current density verse voltage equation (equation 1.3) at $J=0$ and $V= V_{OC}$ can be derived as equation 1.4

$$V_{oc} = \frac{nKT}{q} \ln\left(\frac{J_{ph}}{J_0} + 1 - \frac{V_{oc}}{J_0 R_{sh}}\right) \quad (1.4)$$

Figure 1.4 shows the dependence of V_{OC} on n and J_0, calculated using equation 1.5 that is derived from equation 1.4 by assuming an infinitely large R_{sh}.

$$V_{oc} = \frac{nKT}{q} \ln\left(\frac{J_{ph}}{J_0} + 1\right) \quad (1.5)$$

6

When the R_{sh} is not large enough, it can also affect the V_{OC} of organic solar cells.

The FF is greatly affected by the R_S and R_{sh}. The relationship has been reported previously. High FF can be achieved with low R_S and high R_{sh} (ideally $R_S = 0$, $R_{sh} = \infty$). Therefore, the R_S needs to be minimized and the R_{sh} should be maximized to ensure a high FF. The dependence of FF on R_S and R_{sh} can be approximated as equation 1.6

$$FF(R_s, R_{sh}) = FF(0, \infty)\left[\left(1 - \frac{J_{sc}R_S}{V_{oc}}\right) - \left(\frac{V_{oc}}{J_{sc}R_{sh}}\right)\right] \tag{1.6}$$

Another useful measurement is the incident photon-to-current conversion efficiency (IPCE), which is also called EQE, for monochromatic radiation. The IPCE value is the ratio of the observed photocurrent divided by the incident photon flux, uncorrected for reflective losses during optical excitation through the conducting glass electrode. The IPCE is a percentage of incident photons converted to electrons and predominantly coincident with the absorbance spectrum of the solar cells.

$$\begin{aligned} \text{IPCE} &= \frac{\text{number of electrons through the external circuit}}{\text{number of photons incident}} \\ &= \frac{[1240 \text{ (eV nm)}][\text{photocurrent density}(\mu A \text{ cm}^{-2})]}{[\text{wavelength (nm)}][\text{irradiation}(mW \text{ cm}^{-2})]} \end{aligned} \tag{1.7}$$

Solar irradiance varies with wavelength and roughly traces out a curve in the visible and infrared regions. Additional changes in intensity occur because of different pathways by which the sun's rays traverse through the earth's atmosphere. The property of light illuminated on a solar cell is expressed by Air Mass which is a measure of how absorption in the atmosphere affects the spectral content and intensity of the solar radiation reaching the earth's surface.
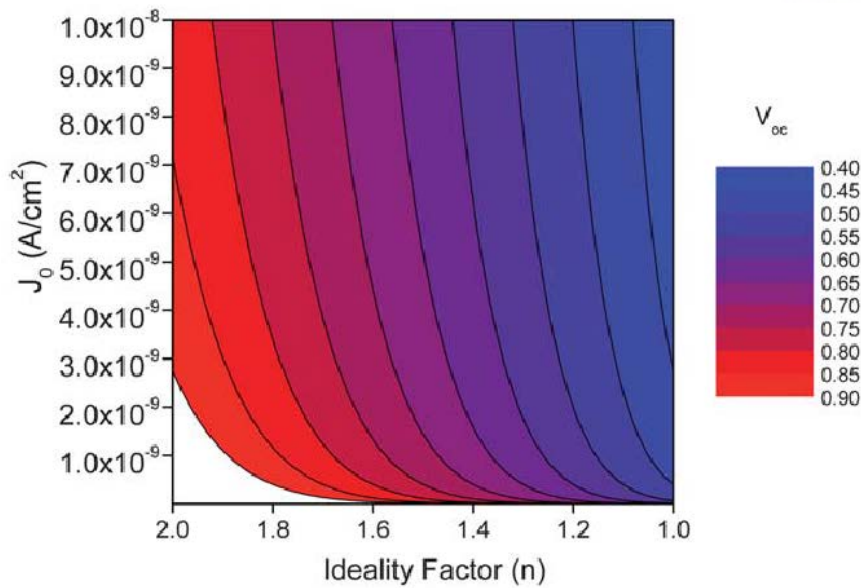
Figure 1.4. Reverse saturation current and ideality factor depending on different V_{OC}.

1.3 Development of Polymer Solar Cells (PSCs)

The polymer solar cells (PSCs) are fabricated through the solution-process and have promising potential to achieve the low-cost solar energy harvesting,due to their many advantages such as various material and easy manufacturing techniques. The PSCs can be possibly applied to the flexible electronic devices and semitransparent solar devices in windows, and also to building applications and even for photon recycling in liquid-crystal displays. Various approaches, such as surface plasmon effect using metal nanoparticels, morphology engineering of bulkheterojunction film, and ternary blend based solar cells, have resulted in enhanced device performance.

1.3.1 Surface plasmon resonace (SPR) effect

Plasmonic metallic structures are characterized by their strong interaction with resonant photons through an excitation of surface plasmon resonance (SPR). SPR can be described as the resonant photon-induced collective oscillation of valence electrons, established when the frequency of photons matches the natural frequency of surface electrons oscillating against the restoring force of positive nuclei. The resonant photon wavelength is different for different metals. For example, gold, silver, and copper nanostructures exhibit resonant behavior when interacting with ultraviolet (UV) and visible (vis) photons. Because a large fraction of the abundant solar flux consists of UV-vis photons, these noble metals are of particular interest. The resonant wavelength and SPR intensity depend not only on

the nature of the metal, but also on the size and shape of metallic nanostructures[22-25] By manipulating the composition, shape and size of plasmonic nanoparticles, it is possible to design nanostructures that interact with the entire solar spectrum and beyond (**Figure 1.5**).[26, 27]
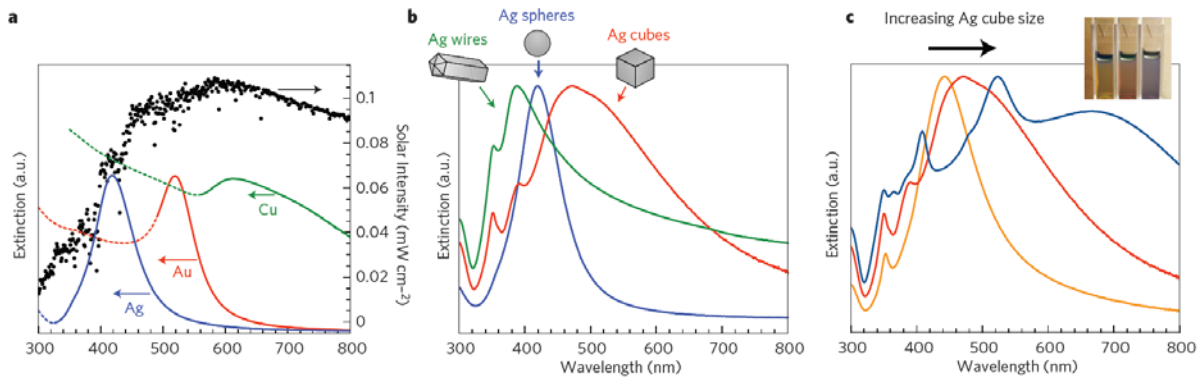
Figure 1.5. Extinction spectra of a) different types of metal nanoparticles, b) different shape of metal nanoparticles, and c) silver nanocubes with different size.

Plasmonic structures can offer at least three ways of reducing the physical thickness of the photovoltaic absorber layers while keeping their optical thickness constant.[28] First, metallic nanoparticles can be used as subwavelength scattering elements to couple and trap freely propagating plane waves from the Sun into an absorbing semiconductor thin film, by folding the light into a thin absorber layer (**Figure 1.6a**). Second, metallic nanoparticles can be used as subwavelength antennas in which the plasmonic near-field is coupled to the semiconductor, increasing its effective absorption cross-section (**Figure 1.6b**). Third, a corrugated metallic film on the back surface of a thin photovoltaic absorber layer can couple sunlight into SPP modes supported at the metal/semiconductor interface as well as guided modes in the semiconductor slab, whereupon the light is converted to photocarriers in the semiconductor (**Figure 1.6c**).
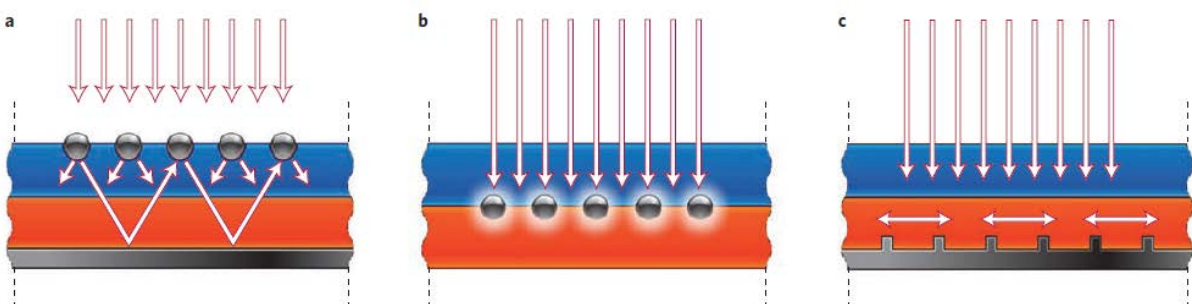
Figure 1.6. a) Light trapping by scattering from metal nanoparticles at the surface of the device. Light is preferentially scattered and trapped into the semiconductor thin film by multiple and high-angle scattering, causing an increase in the effective optical path length in the cell. b) Light trapping by the

excitation of localized surface plasmons in metal nanoparticles embedded in the semiconductor. The excited particles near-field causes the creation of electron–hole pairs in the semiconductor. c) Light trapping by the excitation of surface plasmon polaritons at the metal/semiconductor interface.

Metal nanoparticles

The introduction of metal nanoparticles is an effective strategy for enhancing the performance of polymer solar cells because of its easy application to device fabrication. Various designs using metal nanoparticles have been extensively explored for inorganic solar cells.[28] In OSCs, metal nanoparticles with different types, concentrations, shapes, sizes, distributions, etc. have been introduced into various layers and at interfaces within the devices.[29, 30]

Metal nanoparticles outside the active layer

Device structure of OSC with metallic nanoparticles outside the active layer is as shown in **Figure 1.7a**. Various method such as vapor phase deposition, pulse-current electrodeposition, and thermal annealing, have been used to deposit metal nanoparticles on ITO or inside a PEDOT:PSS buffer layer.[31-33] Metal nanoparticles synthesized by chemical method were assembled on top of or embedded in a PEDOT:PSS layer (**Figure 1.7 b**).[34-36] The dependence of the localized surface plasmon resonance (LSPR) on the size and composition of the nanoparticles have been investigated, and there were many reports on the enhancement in the PCE of OSCs by LSPR of metal nanoparticles. For instance, the PCEs of OSCs based on P3HT:PCBM as the active layer were increased by 20~70% by adding Ag or Au nanoparticles within the PEDOT:PSS buffer layer.[36, 37] As shown in **Figure 1.7c**, LSPR effect of Au nanoparticles enhanced the photocurrent by increasing light absorption in the active layer. The addition of Au nanoparticles (~15 nm in diameter) into PEDOT:PSS layer led to the enhancement in PCE from 1.99% to 2.36% in OSC based on poly(2-methoxy-5(20-ethylhexyloxy)-1,4-phenylenevinylene (MEH-PPV) as the active layer.[38] In order to enhance the plasmon excitation and far-field scattering, Au nanowire and nanomeshes with random distribution were also introduced at the interface between PEDOT:PSS and ITO layers, and improved PCE (Au nanowires: 2.31% → 2.45%, Au mesh: 1.9% → 3.2%).[39] The introduction of a mixture of Ag and Au nanoparticles (40~50 nm in diameter) into PEDOT:PSS layer showed a PCE of 8.67% in OSC based a polythieno[3,4-b]-thiophene/benzodithiophene (PTB7) and $PC_{71}BM$. Cooperative plasmonic effect from dual resonant enhancement of Ag and Au nanoparticles resulted in 20% increase in PCE, and this enhancement was larger than those of devices with only Ag or Au NPs in same buffer layer.[40]
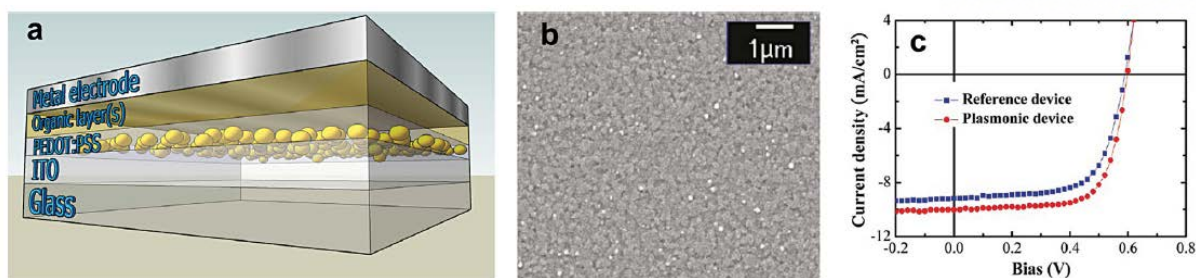
Figure 1.7. Outside type of metal nanoparticles in the active layer for OSCs; a) schemetic of OSC with plasmonic nanoparticles outside the active layer. b) SEM image of PEDOT:PSS layer with embedded gold nanoparticles c) *J-V* cruve of polymer solar cells with (plasmonic device) and without (reference device) Au nanoparticles dispersed in the PEDOT:PSS layer.

Recently, surface modification of metal nanoparticles for manipulating chemical and electrical properties led to the enhancement in PCE and device stability.[41, 42] For example, plasma-polymerized fluorocarbon (CF_x)-modified Ag nanoparticles embedded at the interface between ITO and OSC layers enhanced the PCE of a zinc phthalocyanine (ZnPc): fullerene-based OSCs from 2.7% to 3.5%. This enhancement was attributed to increased light absorption in the active layer due to broadband scattering from the Ag nanoparticles. The CF_x played important role to improve charge collection at the electrode/organic interface due to an increase of 1 eV in the work function of the modified electrode. In addition, metallic nanoparticles or clusters were also applied to enhance the PCE of tandem solar cells. Originally, Forrest's group proposed that metallic clusters (5 nm-diameter Ag clusters) can be effective recombination centers for electrons and holes at multiple junction interfaces of tandem solar cells.[43] More recently, metallic nanoparticles act as a sub-wavelength scattering element which couples and traps freely propagating plane waves in the absorbing OSC layers.[44] For instance, Au nanoparticles (~72 nm in diameter) were deposited in the interconnecting layer of an inverted tandem polymer solar cell consisting of a cell based on a P3HT:indene-C_{60} bis-adduct ($IC_{60}BA$) and another based on poly[(4,4′-bis(2-ethylhexyl)dithieno[3,2-b:2′,3′-d]silole)-2,6-diyl-alt-(2,1,3-benzothiadiazole)-4,7-diyl] (PSBTBT):$PC_{71}BM$, and resulted in an enhancement of PCE from 5.22% to 6.24%.[45] In addition to light scattering effect, the introduction of the metallic nanoparticles can affect the electrical properties of OSC devices. For instance, PEDOT:PSS layer with Ag nanoparticles on top of the ITO substrate remarkably reduced series resistance, and improved the performance of P3HT:PCBM OSCs.[46] Since the nanoparticles were located relatively far from the active organic layer, the absorption enhancement resulted mainly from light concentration/scattering from the LSPR modes of the nanoparticles rather than any near-field enhanced LSPR modes. In summary, when plasmonic materials including metallic nanoparticles, nanowires and nanomeshes were placed outside the active light-harvesting layer, strong localized plasmon field enhancement and/or increased light scattering enhanced device performances.

11

Metal nanoparticles inside the active layer

Incorporation of metallic nanoparticles into the active layers can take advantage of strongly confined field of the LSPR and more efficient light scattering within the active layers, as shown in **Figure 1.8**. It is generally believed that small metallic nanoparticles (usually smaller than 20 nm in diameter) can act as sub-wavelength antennas in which the enhanced near-field is coupled to the absorbing OSC layer(s), increasing its effective absorption cross-section; while large nanoparticles (e.g., larger than 40 nmin diameter) can be used as effective subwavelength scattering elements that significantly increase the optical path length of the sunlight within the active layers.[47-50] Because of solution-processability if OSCs, metallic nanoparticles are easily dispersed into the active layer. Tuning geometric parameters, such as the size and shape of the metal nanoparticles, can promote interaction between longitudinal and transverse SPP modes supported in the embedded nanoparticle array/chain/cluster in the active layer. It can also lead to absorption enhancement in single-junction and multi-junction or tandem solar cells through several different optical and electrical mechanisms.[51-54] For instance, 70 nm Au nanoparticles and 40 nm Ag nanoparticles were blended into bulk heterojunction solutions, increasing the PCE from 3.54% to 4.36% for P3HT:$PC_{71}BM$ OSC devices, from 3.92% to 4.54% for poly[[4,4 -bis(2-ethylhexyl)dithieno(3,2-b:2′,3′-d)silole]-2,6-diyl-alt-[4,7-bis(2-thienyl)-2,1,3-benzothiadiazole]-5,5′-diyl] (Si PCPDTBT) :$PC_{71}BM$ devices, and from 5.77% to 6.45% or from 6.3% to 7.1% for PCDTBT:$PC_{71}BM$ devices at an optimized blend ratio of 5 wt% Au nanoparticles and 1 wt% Ag nanoparticles.[49, 50] These relatively large metal nanoparticles efficiently scatter the incident light, increase the optical path length and therefore enhance the optical absorption as shown in **Figure 1.8b**. In addition, it was proposed that large metallic nanoparticles can transport holes more efficiently, providing an additional contribution to the improved current density (see **Figure 1.8c**) and PCE. Recently, larger Ag nanowires were also mixed with P3HT:PCBM blends and an enhancement in PCE from 3.31% to 3.91% was achieved.[55] Chemically synthesized Ag nanoplates with well-controlled shapes and mixing ratios were also embedded into the active layers of OSC devices and led to the enhancement of PCE from 3.2% to 4.4% in devices based on P3HT:$PC_{71}BM$ and from 5.9% to 6.6% in devices based on PCDTBT:$PC_{71}BM$, respectively, and it was suggested that metallic nanowires and nanoplates can provide greater enhancement than small nanoparticles due to potentially improved electron transport and larger scattering cross-sectional areas.[55, 56] To simultaneously achieve SPR enhancement by small nanoparticles and scattering effect by large nanoparticles, combination of surfactant-free Au NPs (1.5-20nm) and 40nm Au nanoparticles was successfully introduced into the P3HT:PCBM active layer, leading to the enhancement in PCE from 2.64% to 3.71%.[47] In addition, simultaneous benefits of placing metallic nanostructures outside

and inside the active layers can be possible by incorporating metallic nanoparticles into multiple polymer layers (e.g., buffer layers and active layers).[57] Since there is a concern about energy loss (such as non-radiative decay, charge-carrier recombination, and quenching of excitons) caused by direct contact between metal nanoparticles and active layer, it is critical to fine tune the concentration, dispersion, and size of metal nanoparticles when incorporating them into the OSC active layers.[58] It was reported that Ag nanoparticles tended to phase segregate from P3HT:PCBM polymer blends at high concentrations and resulted in decreased carrier extraction.[59] Incorporating Au nanoparticles at the interface between P3HT:PCBM and PEDOT:PSS resulted in PCE enhancement from 1% to 2.4%. However, this very large enhancement in PCE does not seem consistent with the reported P3HT:PCBM absorption of only 30%.[60] Current investigations have focused on the potential benefits of introducing different metallic nanoparticles (e.g., Ag, Al, Au, Cu, etc.) to improve device performance.[61] For example, □□6 nm Ag or □□5 nm in poly(3-octylthiophene) (P3OT):C_{60} active layer, resulting in improved electrical conductivity and an PCE enhancement from 0.7% to 1.9%.[62] Ag nanoparticles in the P3HT:PCBM layer improved the structural and morphological properties of the composite blend, leading to better device performance and device stability under air atmosphere.[63, 64] On the other hand, 20 nm Cu nanoparticles embedded inside P3HT layers reportedly enhanced the dissociation of excitons without increasing the P3HT optical absorption. Although various metallic nanoparticles dispersed in active layer enhanced light absorption, SPR effect of metal nanoparticles on device performance were not fully revealed.[65, 66] Therefore, the mechanism of SPR effect improving the optical and electrical properties of the active layer need to be further investigated when metal nanostructures (e.g., nanoparticles, nanowires, nanoplates, etc.) were introduced inside active layer.
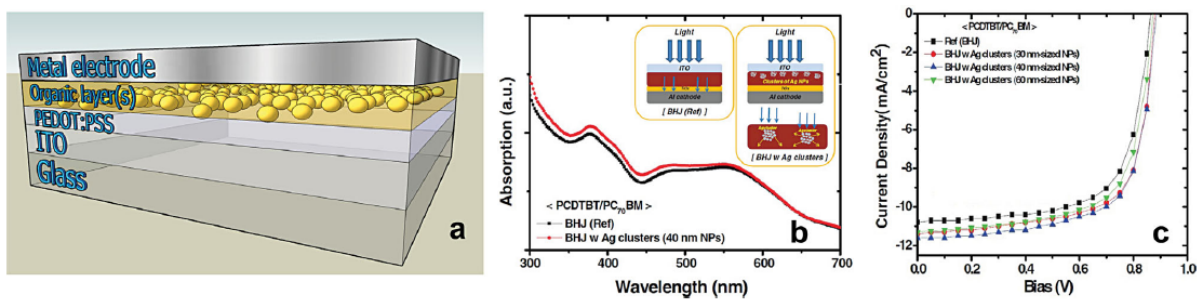
Figure 1.8. Inside type of metal nanoparticles in the active layer for OSCs; a) schematic of OSC with plasmonic nanoparticles inside the active layer. b) Absorption spectra of the plain PCDTBT:$PC_{71}BM$ BHJ film without and with 1wt% Ag clusters (40nm). The insets show light trapping from scattering and excitation of the LSPR. c) the *J-V* curves of PSCs using the PCDTBT:$PC_{71}BM$ blend without and with Ag clusters (1 wt%) with different size of particles.

1.3.2 Morphology Engineering of Bulkheterojunction Film

Development of Materials

The development of polymer solar cells (PSCs) has always been accompanied by innovations in materials science. **Figure 1.9** shows the chemical structures of some representative materials. One of the earliest PSC polymers is poly[2-methoxy-5-(2'-ethylhexyloxy)-*p*-phenylene vinylene] (MEH-PPV), which was developed by Wudl *et al.* Wudl also invented one of the most important fullerene derivatives, PCBM8, which represents a milestone in the development of PSC acceptors and is still widely used today. In 1995, Yu *et al.* blended MEH-PPV with C60 and its derivatives to give the first PSC with a high PCE.[6] This work opened up a new era of polymer materials for use in solar energy conversion. After significant optimization, researchers achieved PCEs of more than 3.0% for PPV-based PSCs.[67, 68] However, further improvement was limited by the relatively low hole mobility and narrow light absorption range. Soluble polythiophenes, especially poly(3-hexylthiphene) (P3HT)[69], with their higher hole mobility[70] and therefore a broader spectrum coverage than MEH-PPV, have become a standard for PSC materials in the 2000s. Morphology optimization[71, 72] has provided PCEs of 4–5%, thus attracting worldwide interests in PSCs.
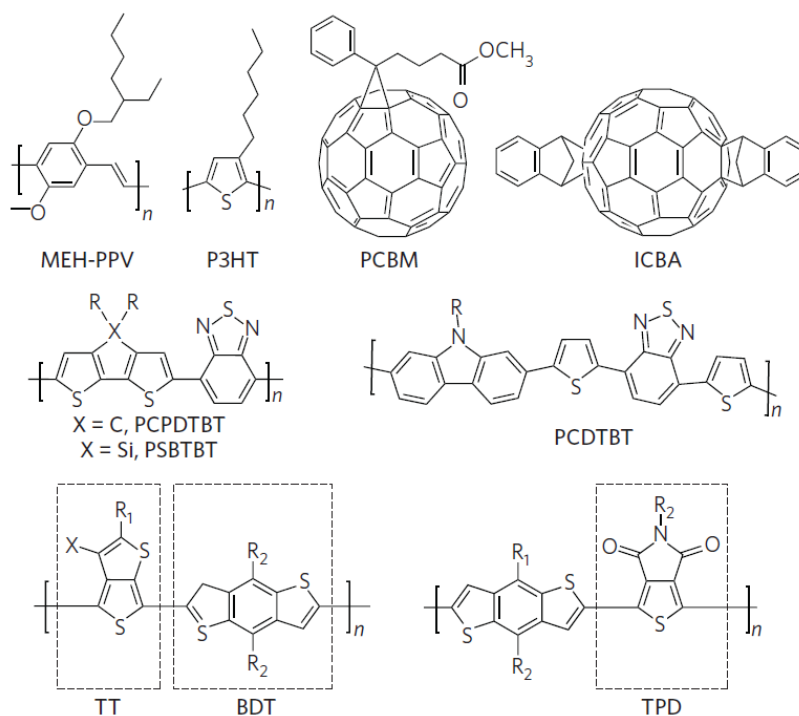
Figure 1.9. Chemical structures of prominent electron donors and acceptors used in PSCs.

Many more high-performance polymers have been developed in recent years. One of these is poly [2,6-(4,4-bis-(2-ethylhexyl)-4*H*-cyclopenta[2,1-*b*;3,4-*b*']dithiophene)-alt-4,7-(2,1,3-benzothiadiazole)]

(PCPDTBT), a low-bandgap polymer whose absorption extends up to 900 nm. PSCs made from this polymer have showed an initial efficiency of around 3%.[73] However, by incorporating alkanedithiol additives, researchers were able to achieve efficiencies of around 5.5%.[74] Leclerc *et al.* developed poly [*N*-9''-hepta-decanyl-2,7-carbazole-alt-5,5-(4',7'-di-2-thienyl-2',1',3'-benzothiadiazole)] (PCDTBT), which gave a PCE of 3.6%.[75] In 2009, researchers increased this to 6.1% by incorporating a titanium oxide (TiO*x*) layer as an optical spacer.[76] The most impressive high-performance polymers are those designed by Yu *et al.*, which are composed of thieno[3,4-*b*]-thiophene (TT) and benzodithiophene (BDT) alternating units.[77-79] This was the first polymer donor system capable of reaching PCEs of 7–8%. Following this work, PCEs of more than 7% were frequently reported with either new materials or novel device optimization techniques.[80-83] Materials innovation is one of the major forces currently driving the performance of PSCs. The key issues of polymer design include[84, 85] engineering the bandgap and energy levels to achieve high J_{SC} and V_{OC}, enhancing planarity to attain high carrier mobility, and materials processability and stability. All of these issues are correlated with each other. In the ideal case, all factors should be optimized in a single polymer, but this remains a significant challenge. The efficiency of a PSC is given by $\eta = V_{OC} \times J_{SC} \times FF$, where FF is the fill factor. Knowledge of the link between the design of a polymer and these parameters has been significantly improved over the past decade.

The value of V_{OC} for a PSC can be expressed by the empirical equation $V_{OC} = e{-}1 \times (|E\text{HOMO}$ donor$| - |E\text{LUMO}$ acceptor$| - 0.3$ eV$)$, where e is the elementary charge, E is the energy level and 0.3 eV is an empirical value for efficient charge separation.[86] A donor polymer with a lower HOMO level will give a higher V_{OC}. P3HT is by far the most popular donor, with a HOMO level of ~4.9 eV,[87] which corresponds to a V_{OC} value of around 0.6 V and serves as a reference for polymer design15. Thiophene is an electron-rich group.[88, 89] The HOMO level of the polymer in a PSC can be effectively lowered by utilizing groups that are less electron-rich.[75, 90-92] For example, fluorene and carbazole are commonly used units in wide-bandgap materials because they are less electron-rich than thiophene. By incorporating these units into a polymer donor, V_{OC} can be significantly increased. Cao *et al.* demonstrated a polymer containing a fluorene unit that achieved $V_{OC} \approx 1.0$ V.[90] Inganas *et al.* also reported a polymer composed of fluorene and quinoxaline alternating units[91] that reached $V_{OC} \approx 1.0$ V. Another example is PCDTBT, which incorporates carbazole units in the polymer chain, from which researchers achieved $V\text{OC} \approx 0.89$ V.[75] V_{OC} is also affected by non-radiative recombination between the donor and the acceptor. Eliminating these non-radiative pathways[93] will help to maximize V_{OC}. However, linking polymer design with such an elimination process remains a significant challenge.

J_{SC} is another important parameter that determines the performance of a PSC. The most powerful strategy for achieving high J_{SC} is to narrow the bandgap (<1.8 eV) for a broader coverage of the solar spectrum.[84, 85, 94] Methods for achieving this include designing an alternating donor–acceptor structure,

stabilizing the quinoid structure, controlling the polymer chain planarity, and tuning the effective conjugation length. Designing an alternating donor–acceptor structure is the most common approach, in which the push–pull driving forces between the donor and acceptor units, together with the photoinduced intramolecular charge transfer, facilitates electron delocalization and the formation of low-bandgap quinoid mesomeric structures over the polymer backbone.[95, 96] According to molecular orbital perturbation theory, electron delocalization leads to the hybridization of molecular orbitals, resulting in electron redistribution throughout the interacting orbitals. This provides two new hybridized orbitals— a higher HOMO level and a lower LUMO level — resulting in a narrower bandgap. One of the most successful examples of this donor–acceptor structure is PCPDTBT.[73, 74] By combining a dialkyl-cyclopentabithiophene donor unit and benzothiadiazole acceptor unit, the bandgap of PCPDTBT spans 1.4 eV (around 900 nm). This donor–acceptor structure is not limited to the polymer main chain. Huang *et al.* demonstrated that a donor–acceptor structure comprising an acceptor-based side chain and a donorbased main chain also results in a lower bandgap.[97] Another successful way of reducing the bandgap is to stabilize the quinoid structure of conjugated units.[77, 94] The ground state of a conjugated structure has two resonance structures: an aromatic form and a quinoidal form.[84] The quinoidal form is energetically less stable because of its smaller bandgap; achieving a stable quinoidal form therefore reduces the bandgap. Yu *et al.* have found that a thieno[3,4-*b*]thiophene unit can stabilize the quinoidal structure through a fused thiophene ring.[77, 78, 94] Polymers containing TT and BDT alternating units have bandgaps of around 1.6 eV.

Narrowing the bandgap alone is not necessarily enough to achieve high J_{SC}. Other parameters, such as carrier mobility, intermolecular interaction and molecular chain packing, also affect JSC. For example, tuning the chemical structure provides effective ways to improve hole mobility. Yang *et al.* developed poly(4,4-dioctyldithieno(3,2-*b*:2',3'-*d*)silole)-2,6-diyl-alt-(2,1,3-benzothiadiazole)-4,7-diyl) (PSBTBT) by replacing the bridging carbon atom in PCPDTBT with a silicon atom.[98, 99] PSBTBT has a higher crystallinity than PCPDTBT and therefore has improved hole mobility, leading to a higher value of J_{SC}. Using a large planar structure can also improve transport by enhancing molecule packing.[100, 101]

Although V_{OC} and J_{SC} can indeed be improved by employing these strategies, it remains a challenge to improve both values simultaneously. Narrowing the bandgap can improve J_{SC}, but V_{OC} may correspondingly be decreased because of the higher HOMO level that results. Researchers recently demonstrated that structural fine-tuning is a powerful approach for improving both V_{OC} and J_{SC} simultaneously. For example, introducing a fluorine atom into the TT unit reduces both HOMO and LUMO levels simultaneously, while also improving V_{OC} and retaining the bandgap.[102, 103] Fine-tuning the side-chain structure can also result in a similar effect. One example is to simultaneously lower both the HOMO and LUMO levels by replacing the electron-rich alkoxy side chain with the

less electron-rich alkyl chain.[79]

The third parameter for achieving high efficiency in a PSC is the FF, which is currently the least understood one among the three. The FF is the ratio between the maximum obtainable power and the product of J_{SC} and V_{OC}. It is affected by many factors, including charge carrier mobility and balance, interface recombination, series and shunt resistances, film morphology and miscibility between the donor and acceptor.[104] However, obtaining a clear understanding and the ability to modulate the FF still remains a hurdle in the development of PSCs. From the materials design point of view alone, molecular planarity, intermolecular interactions, molecular chain packing and crystallinity, and high-mobility units should be taken into consideration in structure designs. Side-chain tuning also has considerable effects on improving the FF. For example, Frechet *et al.* optimized the side-chain patterns for *N*‑alkylthieno[3,4-*c*]pyrrole-4,6-dione (TPD)-based polymers.[105] Side-chain tuning helped to optimize π-stacking, polymer crystallinity and material miscibility, and caused the FF to increase from 55% to 68%. Researchers also recently achieved an efficiency of 7% for a TPD–silole copolymer.[106]

Morphology Control (review napho)

Morphology control is critical in bulk-heterojunction PSCs. Thermal annealing[69] and solvent annealing[71] are currently the most popular methods for controlling morphology. It was not until 2005 that both thermal and solvent annealing were shown to enhance PSC efficiency by a significant amount.[71] Many otherapproaches are also effective for improving polymer–fullerene morphology, such as solvent selection[107] and solvent mixture[108] techniques, and the use of additives.[109]

The Effect of Solvent (ref Morphology_2)

Solution processing has many advantages over other filmfabrication technologies, which usually require complicated instruments as well as costly and time-consuming procedures. Therefore, solution processing has developed into the most favored methodology for fabricating organic optoelectronic devices. Solution processing also allows the freedom to control phase separation and molecular self-organization during solvent evaporation and/or film treatment. The solvent establishes the film evolution environment, and thus has foreseeable impact on the final film morphology. Selection and combination of solvents have been shown to be critical for the morphology in polymer-blend films, and are well-documented in the literature.[13, 110]
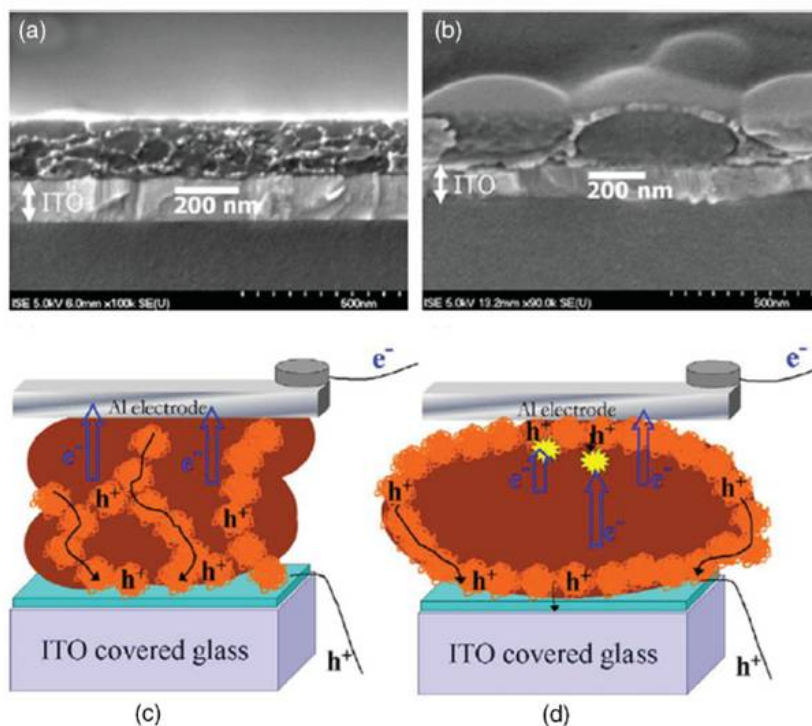
Figure 1.10. SEM cross-sectional images of MDMO-PPV:PCBM blend films on top of ITO from a) CB and b) toluene solution. The brighter objects in a) are polymer nanospheres, whereas the darker embedments are PCBM clusters. Schematic of film morphology of c) CB- and d) toluene-cast MDMO-PPV: PCBM blend active layers. In c), carriers form percolated pathways to reach their respective electrodes. In d), electrons and holes suffer from recombination due to undesirable phase separation.

Spin-coating from single-solvent solutions results in thin films, which possess optoelectronic properties determined by the solution parameters and the spin-coating process, for example concentration, blending ratio, spin speed and time, etc. Meanwhile, solvent properties, such as boiling point, vapor pressure, solubility, and polarity, also have considerable impact on the final film morphology. The wettability of the organic solvents on the poly(3,4-ethylenedioxythiophene) poly(styrenesulfonate) (PEDOT:PSS) surface is usually sufficiently good and not taken into account as a factor on the film morphology. However, it is worth noting that different solution processes have dissimilar requirements for achieving optimal morphology.[111] This article focuses only on the most common spin-coating processes.

In 2001, Shaheen et al. demonstrated the effect of solvent and morphology on device performance for the poly-[2-(3,7-dimethyloctyloxy)-5-methyloxy]-para-phenylene-vinylene(MDMO-PPV):[6,6]-phenyl-C61-butyric acid methyl ester (PCBM) blend system.[107] By replacing toluene with chlorobenzene (CB), the PCE of the device dramatically improved to 2.5%. A more intimate mixing and stronger interchain interaction accounted for this improvement. The solubility of the polymer

blend is much better in chlorobenzene than in toluene; thus, a much more uniform mixing of the donor and acceptor is expected. This improved intermixing is evidenced by the roughness of the polymer-blend film, where the chlorobenzene-based sample has a much smoother film surface. Liu et al. investigated the poly(2-methoxy-5-(20-ethoyl-hexyloxy)-1,4-phenylene vinylene (MEH-PPV):C_{60} blend devices and observed the effect of solvation-induced morphology on device performance.[112] Using nonaromatic solvents, such as tetrahydrofuran (THF) and chloroform, resulted in larger V_{OC} and smaller J_{SC}, due to the fact that MEH-PPV side groups prevented intimate contact and thus efficient charge transfer between the MEH-PPV and C_{60} molecules. Ma et al. also observed that P3HT:PCBM polymer films were smoother and more uniform when chloroform was replaced with CB.[72] The high efficiency is the result of improved morphology, crystallinity, and cathode contact due to better choice of solvent as well as post-annealing treatment. Because of the better solubility of fullerenes in CB, its use instead of toluene resulted in a finer phase separation, while thermal annealing in both cases led to coarsening of the phases.[113] **Figure 1.10a and 10b** show the scanning electron microscopy (SEM) cross-section views of the MDMO-PPV:PCBM system casted from CB and toluene, respectively. One interesting observation is the 20–40nm thick ''skin'' layer observed in the toluene-casted film, in which the PCBM nanocrystallites were generally covered by this ''skin'' layer, identified as polymer nanospheres. However, for most chlorobenzene-cast films, the polymer nanospheres were homogeneously distributed; therefore, only at very-high PCBM loadings can this phenomenon of PCBM clusters surrounded by a ''skin'' layer be perceived. The CB-cast films have a finer phase separation and higher J_{SC} in comparison to the toluene-cast films. However, the J_{SC} of CB-cast films decreased with heavier PCBM loadings, indicating that an optimal phase-separated domain size is imperative for good device performance. Hoppe et al. also measured the localized work function using Kelvin probe force microscopy.[114] CB-cast films showed a uniform work function at the surface but an approximately 0.3 eV decrease upon illumination, while the work function of the toluene-cast films was directly topography-related, increasing in the PCBM clusters under illumination. The work function correlates to the Fermi level, that is, electron density. Under illumination, CB-cast films showed an enrichment of electrons at the surface due to charge generation, while the surface of the toluene-cast films was covered by the polymer skin-layer, causing substantial charge recombination, and a lower J_{SC}.

The proposed film morphology and respective charge transport for CB- and toluene-cast films are depicted in **Figure 1.10c and 1.10d**. The solubility of the fullerene phase can strongly affect the solvent selection. Larger fullerene balls tend to be less soluble, and different solvents have been used for optimal processing conditions. For example, $PC_{84}BM$:MDMO-PPV solar cells were spin-coated from CB and $PC_{71}BM$:MDMO-PPV devices were spin-coated from 1,2-dichlorobenzene (DCB).[23,41] Yao et al. showed that in a new low-band-gap copolymer poly[(9,9-dioctylfluorene)-

19

2,7-diyl-alt-[4,7-bis(3-decyloxythien-2-yl)-2,1,3-benzothiadiazole]-50, 500-diyl] (PF*co*-DTB)/ $PC_{71}BM$ system, DCB resulted in very smooth films (r.m.s. roughness of 0.8 nm) and negligible phase contrast, indicating uniform distribution of the mixture.[115] However, CB produced much rougher films(r.m.s. roughness 4.0 nm) and visible phase separation of 200–300 nm. Based on the exciton diffusion length of approximately 10 nm, CB is not the appropriate solvent for achieving high solar-cell performance in this particular system,anddevice data also reflected this scenario. It is, however, not sufficient for one to judge the quality of the film merely by thefilmroughness. In P3HT:PCBM systems, using both thermal annealing and solvent annealing leads to higher roughness than as-cast films, but the device performance in these two cases is much better. The key point is likely to be the formation of proper nanoscale phase separation.

The Effect of Processing Additives

In general, device performance can be improved with post treatments such as various annealing processes. However, for some material systems, such as the novel low-band-gap polymer poly[2,6-(4,4-bis-(2-ethylhexyl)-4H-cyclopenta[2,1-b;3,4-b0]-dithiophene)-alt-4,7-(2,1,3-benzothiadiazole)] (PCPDTBT), which has a better overlap with the solar spectrum, typical post-treatments are incapable of improving the device characteristics.[73, 116] It has been reported that solvent mixtures have a significant effect on film morphology and device performance, namely on J_{SC}, V_{OC}, and FF in the polyfluorene copolymer/fullerene system.[108] In the poly(2,7-(9,9-dioctyl-fluorene)-alt-5,5-(40,70-di-2-thienyl-20,10,3-benzothiadiazole)):$PC_{61}BM$ blend system, mixing a small volume of CB into chloroform developed a finer and more uniform distribution of domains, which enhanced the J_{SC}. In contrast, adding xylene or toluene into chloroform resulted in larger domain sizes that decreased J_{SC} and caused significant light-intensity-dependent recombination of free charge carriers. Time-resolved spectroscopy on the picosecond scale revealed that charge mobility was considerably improved by adding CB into chloroform, due to an enhanced free-charge-carrier generation from a finer morphology.

Earlier efforts on the solvent-mixture approach concentrated on two miscible solvents, in which both the polymers and fullerenes have considerable solubility. Recently, advances in cooperative effect of solvent mixtures using solvents with distinct solubilities have been obtained.[109, 117] The incorporation of additives into a host solvent represents an innovative method and important trend capable of controlling the BHJ morphology. It also provides a unique viewing angle to study the film-formation dynamics of the spin-coating process. However, it is vital to mention that solvent mixtures introduce a more sophisticated circumstance in both the solution and film evolutions, since the solutions now become multicomponent (phase) systems. Therefore, in order to maintain simplicity,

only two solvents are usually involved in the solution system when studying the fundamental principles and improving the performance. It should also be noted that the solvent-mixture method should not be restricted to only two solvents; ternary- or even quaternary-solvent systems are also realistic approaches. Recently, the mixture-solvent systems have been intensively explored by several groups, bringing a rather clear understanding of solvent-selection rules for desirable morphology.[109, 117-119]

Previously, the formation of fullerene nanocrystallites by "bad"-solvent incorporation was reported by Alargova et al.[120] It was claimed that fullerene molecules tend to crystallize upon contact with a "bad" solvent in order to reduce the overall energy. The narrowly distributed size of these aggregates is proportional to the fullerene concentration and solvent choices, regardless of the volume of the "bad" solvent added. Introduction of alkyl thiols, which are bad solvents for P3HT, to P3HT/PCBM in toluene can increase the photoconductivity and carrier lifetime, due to the enhanced structural order.[24] More recently, Peet et al. reported that by incorporating a few volume percent of alkanedithiols into the PCPDTBT:$PC_{71}BM$ polymer blend solution, the efficiency doubled from 2.8% to 5.5%, with J_{SC} as high as 16.2mAcm^{-2}.[109]
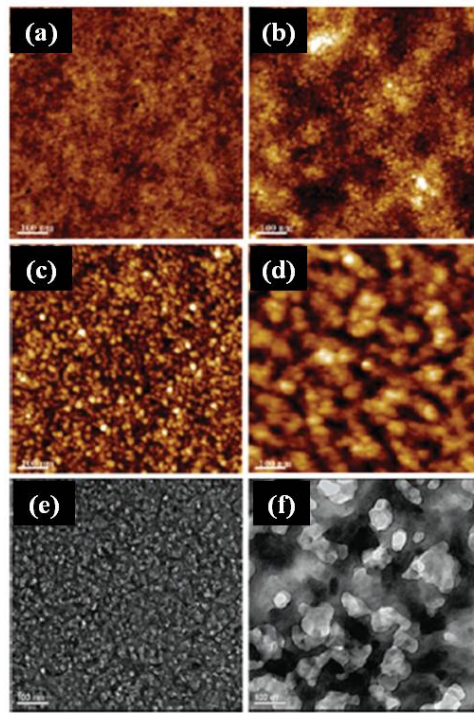
Figure 1.11. AFM and TEM images of PCPCTBT/$PC_{71}BM$ films without and with 1,8-octanedithiol and exposed PCPDTBT networks after removal of $PC_{71}BM$. AFM image of BHJ film a) without and b) with 1,8-octanedithiol. AFM image of exposed polymer networks c) without and d) with 1,8-octanedithiol. TEM image of exposed polymer networks e) without and f) with 1,8-octanedithiol.

The vast improvement was attributed to the enhanced interactions between the polymer chains and/or between the polymer and fullerene phases upon alkanedithiol addition, which was evidenced by the absorption data.

A systematic study of alkanedithiol incorporation was carried out by Lee et al. to elucidate the morphology-controlling mechanism, where the alkanedithiols played the role of "processing additive", without reacting with either the polymer or fullerene components.[121] The alkanedithiol selectively dissolved the fullerene phase, while the PCPDTBT was relatively insoluble. Due to the higher boiling points of the alkanedithiols solvent addition, and indicated a guideline for alternative solvent-additive selection. (b.p. >160. 8°C), the fullerene phase stayed in the solution longer than the polymer, providing more freedom to self-align and crystallize. Consequently, the phase-separation morphology can be manipulated by various alkanedithiols and by tailoring their relative ratios. In addition, the polymer domains are preserved after removal of the fullerene phase, which allowed the direct observation of the exposed polymer network. **Figure 1.11** shows the atomic force microscopy (AFM) and transmission electron microscopy (TEM) images of the PCPDTBT:PC$_{71}$BM films with and without 1,8-octanedithiol (OT), as well as the exposed PCPDTBT network after selective dissolution of the PC$_{71}$BM. These images clearly show larger PCPDTBT and C71-PCBM domains as a result of OT addition, indicating that the improved device performance is related to the better percolating pathways for both carriers from the larger interconnected domains. Carrier-transport analysis also pointed out the enhanced network by the increased electron mobility.[122] Accordingly, two criteria for incorporating alkanedithiols to control the blend-film morphology were proposed: i) selective solubility of the fullerene component and ii) a higher boiling point (lower vapor pressure) than the host solvent. This work provided insight into the mechanism of film-morphology evolution regarding a "bad" solvent addition, and indicated a guideline for alternative solvent-additive selection.

Concluding the results of various works, vertical stratification can be attributed to the different solubilities and surface energies of the blend components as well as the dynamics of the spin-coating process. A volatile solvent is likely to form a more homogeneous film, while a viscous solvent allows vertical phase separation. Upon vertical phase separation, the low-surface-energy component preferentially segregates at the surface or interface to reduce the overall energy. By controlling the film-drying rate via solvent viscosity and spin-coating condition, as well as surface treatment, a closer to optimal, both laterally and vertically segregated morphology can be formed. Furthermore, certain "bad" solvents can function as "processing additives" to preform PCBM aggregates, which assist in the self-organization of both components, and thus induce vertical phase separation. If the vertical segregation can be manipulated to the desired morphology, with a donor-enriched anode and acceptor-enriched cathode, efficient charge dissociation via the interpenetrating network and efficient charge transport along the interconnected pathways are expected to vastly enhance the device performance.

1.3.3 Ternary Blend Solar Cells

Mechanism of Ternery Solar Cells

In general, a ternary solar cell consists of a wide bandgap polymer as the host donor, a near IR sensitizer and a fullerene derivative as the host acceptor. The charge transfer and transport in the ternary blend is more than a simple superposition of the charge transfer and transport properties of the individual phases. It is governed by various mechanisms, depending on the sensitizer content, electronic energy levels and bandgap of the three components, sensitizer location in the binary photoactive layer as well as fi nal microstructure of the film.

Cascade Charge Transfer
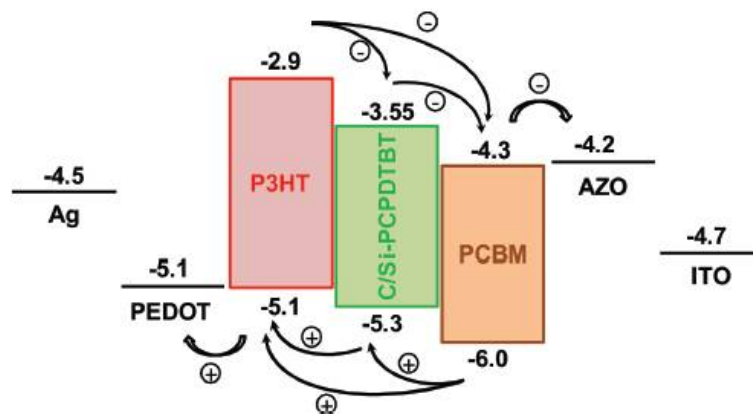
Figure 1.12 . Schematic representation of the cascade charge transfer in a ternary solar cell, where the P3HT:PCBM is employed as the host system and low bandgap material of C-/Si-PCPDTBT as the near IR sensitizer. The electronic energy levels of electrodes and semiconductors are presented in eV unit. Curved arrows indicate allowed charge transfer reactions in the ternary blend.

The relative energetic position of the sensitizer's electronic levels with respect to those of host donor and acceptor determines the feasibility of a cascade exciton dissociation and charge transfer at the donor/sensitizer and sensitizer/acceptor interfaces. Locating the HOMO and LUMO level of the sensitizer between the HOMOs and LUMOs of host components (cascade energy levels), several pathways are energetically relevant for the relaxation of photoexcited states. The photoexcited host donor may transfer an electron to either acceptor or the sensitizer phase instead. In the latter case, the sensitizer subsequently has to transfer an electron to acceptor. Alternatively, a photoexcited sensitizer can transfer a hole to host donor and in parallel an electron to the host acceptor. **Figure 1.12** illustrates

this cascade charge transfer in a ternary blend.

This mechanism was reported by Koppe et al., where P3HT:PCBM blend was employed as the host matrix and the low bandgap polymer of poly[2,6-(4,4-bis-(2-ethylhexyl)-4H-cyclopenta[2,1-b;3,4-b´]-dithiophene)-alt-4,7-(2,1,3-benzothiadiazole)] (PCPDTBT/or C-PCPDTBT) as the near IR sensitizer.[123] Photoinduced absorption spectroscopy studies (PIA) revealed that photoexciting PCPDTBT (pump energy of 1.59 eV) in ternary P3HT:PCPDTBT:PCBM (0.8:0.2:1 wt.%) composites created free charges on P3HT. This near-IR (1.59 eV) photogeneration mechanism was absent in a binary blend made of P3HT:PCBM (1:1), shown in **Figure 1.13**.
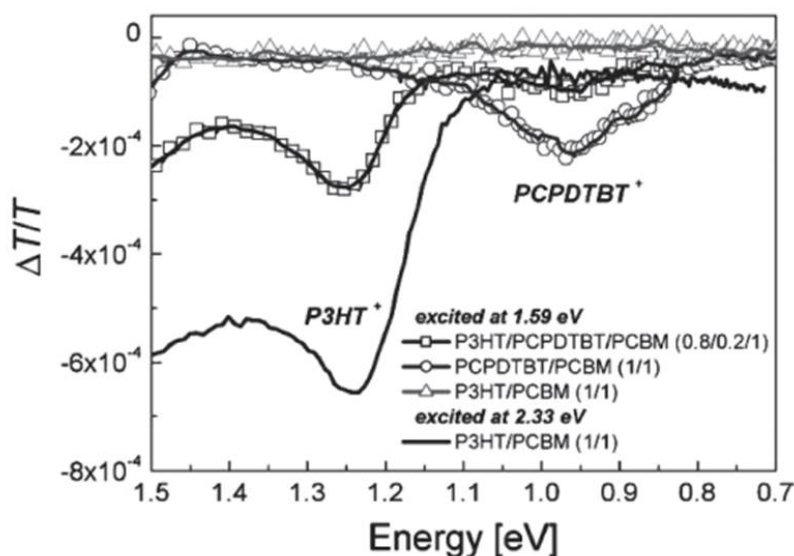
Figure 1.13. Photoinduced absorption spectra of annealed thin films (d $\sim$ 100–150 nm) of P3HT:PCPDTBT:PCBM (0.8:0.2:1) (open squares), PCPDTBT:PCBM (1:1) (open circles), and P3HT:PCBM (1:1) (open triangles) which were all excited at 1.59 eV. P3HT:PCBM (1:1), excited at 2.33 eV (full line), serves as a reference for the spectroscopic positionof the P3HT polaron.

Energy Transfer

Förster (Fluorescence) resonance energy transfer, resonance energy transfer or electronic energy transfer, is a mechanism describing energy transfer between two chromophores.[124] A donor chromophore, initially in its electronic excited state, may transfer energy to an acceptor chromophore in its vicinity through non-radiative dipole–dipole coupling. For an energy transfer to occur, the acceptor molecule needs to have an absorption spectrum that overlaps with the emission spectrum of the donor molecule (**Figure 1.14**). This mechanism can become a relevant relaxation pathway for the primary photoexcited states in the ternary blends, depending on the domains sizes of the individual components. Photoluminescence measurement (PL) is a convenient tool to probe energy transfer.
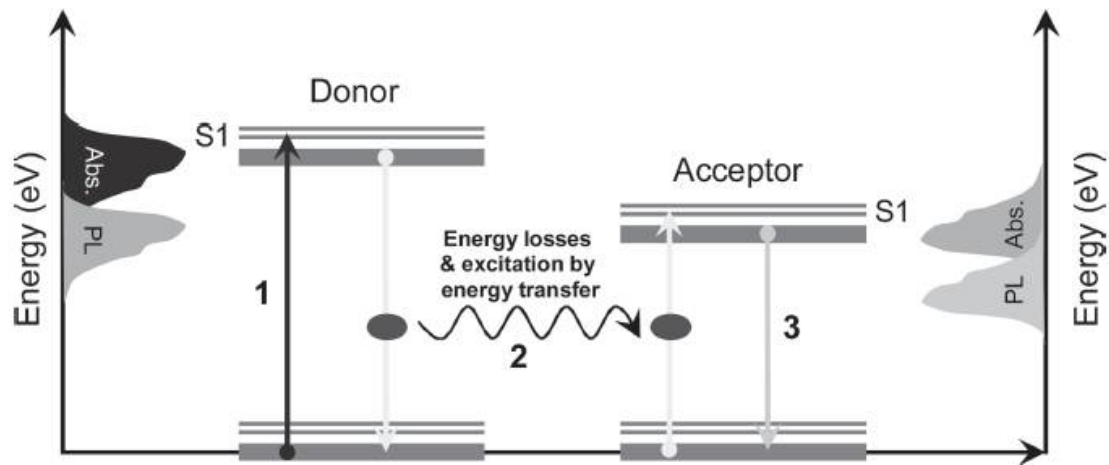
Figure 1.14 . Schematic representation of the resonant energy transfer mechanism, as donor absorbs light (arrow 1) and transfers the energy to acceptor (arrow 2), which fl uoresces (arrow 3). The abbreviations of Abs. and PL represent the absorption and photoluminescence spectra of the donor and acceptor, respectively.

Parallel-Like Charge Trasfer/Transport

Alternative to the cascade charge transfer mechanism, a parallel-like charge transport mechanism of two or more materials (mostly polymers) with different band gaps but similar polarity can be employed for the design of ternary systems. In this mechanism, excitons generated in each individual donor polymer would migrate to the respective polymer/acceptor interface and then dissociate into free electrons and holes. Electrons are transported via the acceptor domains towards the cathode as in normal binary solar cells. In the case that charge transfer between the two polymers is absent; holes will be transported towards the anode via the two parallel percolation pathways formed by the two polymers (**Figure 1.15**). The charge carriers generated in each polymer:acceptor blend (or in each "sub-blend") are collected simultaneously by the same cathode and anode electrodes, suggesting a photocurrent equal to the sum of those of the individual sub-blends. It is conceptually very similar to the parallel architecture of tandem devices and therefore such a single junction ternary system can be called parallel-like composite. The limiting factor of such a parallel-like system is the required transport capacity of both polymer absorbers. Yang et al. reported the most efficient parallel-like BHJ ternary solar cells to date by employing poly(benzodithiophen − dithienyldifluorobenzothiadiazole) (DTffBT) and poly(benzodithiophene – dithienylthiadiaz olopyridine) (DTPyT).[103, 125]
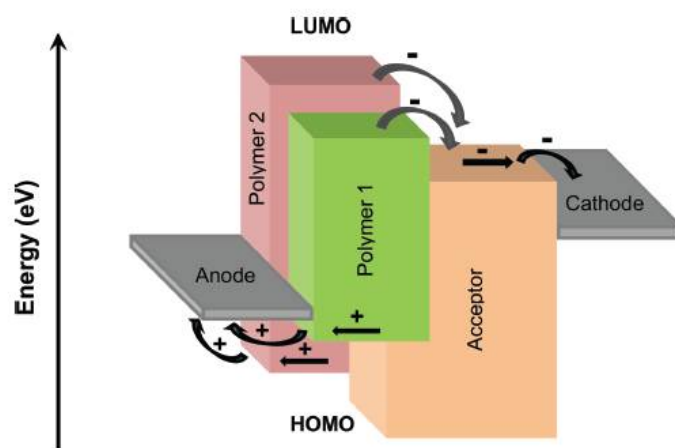
Figure 1.15. Schematic representation of the parallel-like charge transfer in a ternary solar cell, where polymer 1 and 2 are employed as the complementary absorbers blended in an acceptor. Curved arrows indicate charge transfer and linear arrows indicate charge transport in the ternary solar cell.

Two Acceptors

In a BHJ solar cell, V_{OC} is given by the energy of the interface band gap minus the quasi-Fermi energies, where the interface band gap is the energy difference between the donor HOMO and the acceptor LUMO.[126, 127] Hence, while the obvious origin of the continuous change in V_{OC} in ternary blends is the corresponding change in the LUMO or HOMO level, it is possible that the effect reflects a change in the quasi-Fermi energies.

(Tomson paper) In many cases, an increase in the breadth of the spectral response of the ternary blends has been observed relative to the corresponding limiting binary blends, often leading to a larger J_{SC}.[123, 128-132] Conversely, the V_{OC} is proposed to be pinned to the smallest V_{OC} of corresponding binary blends.[123, 132, 133] To this end, it is thought that a limiting $HOMO_D$-$LUMO_A$ interaction controls the V_{OC}, since dominant hole transport and collection occurs through the donor component with the highest-lying HOMO (and analogously, electron transport and collection through the lowest-lying LUMO), independent of the origin of photocurrent generation.[123] However, in a limited number of cases, the V_{OC} seems to be tunable in the three-component system, although at the expense of a marked and steady decrease in the FF as the amount of the third component increases.[134-136]Nonetheless, these isolated observations of composition-tunable V_{OC} suggest that both J_{SC} and V_{OC} are composition-dependent in ternary blend BHJ solar cells and that neither value is necessarily limited to the lesser quantity of the corresponding binary blend solar cells. Khlyabich et al. first reported compositional dependence of V_{OC} using two acceptor polymers with a donor polymer as shown in **Figure 1.16** and **Table 1.1**.[137]
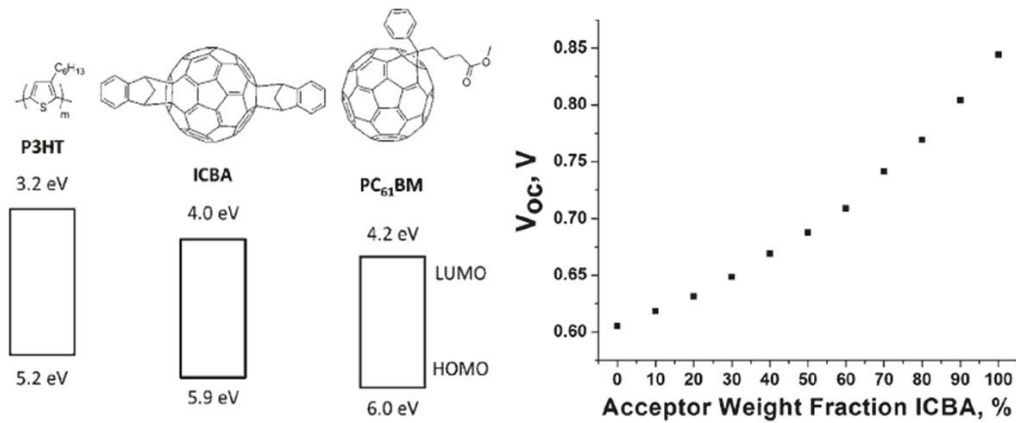
Figure 1.16. Structures and energy levels of P3HT, ICBA, and PC$_{61}$BM and V_{OC} for the ternary blend BHJ solar cells as a function of the amount of ICBA in the blend.

Table 1.1. Photovoltaic properties of P3HT:PC$_{61}$BM:ICBA and ternary blend solar cells at different fullerene Ratios.[a]

P3HT:PC$_{61}$BM:ICBA	J_{sc} (mA/cm^2)	V_{oc} (V)[b]	FF	η (%)
1:1:0[c]	9.90	0.605	0.60	3.57
1:0.9:0.1[d]	9.22	0.618	0.59	3.29
1:0.8:0.2[d]	9.11	0.631	0.57	3.28
1:0.7:0.3[e]	8.58	0.649	0.58	3.22
1:0.6:0.4[f]	8.31	0.669	0.58	3.11
1:0.5:0.5[g]	8.27	0.688	0.57	3.18
1:0.4:0.6[e]	8.18	0.709	0.57	3.22
1:0.3:0.7[h]	8.14	0.741	0.57	3.34
1:0.2:0.8[d]	8.19	0.769	0.59	3.69
1:0.1:0.9[d]	8.18	0.804	0.60	3.91
1:0:1[h]	8.23	0.844	0.58	3.98

[a] Devices were spin-coated from CB and after aluminum deposition were annealed at 150 °C under N$_2$ for the specified times. [b] Standard deviations of less than 0.005 were observed in all cases for averages over eight pixels. [c] 60 min. [d] 20 min. [e] 40 min. [f] 30 min. [g] 50 min. [h] 10 min.

1.4 Research Overview and Objective

Polymer solar cells (PSCs) have great potential as a promising candidate for clean and renewable energy sources. PSCs are attracting increasing attention from both academia and industry, due to the demand for flexible, portable and solution processable low-cost photovoltaic devices to comply with increasing global energy demand. As results of many efforts for developing PSCs, the power conversion efficiency (PCE) of PSCs has been tremendously improved over the past decades. However, the low PCE is still a hurdle to overcome for commercial applications of PSCs. To further optimize PSCs, several challenges have to be considered including maximizing the light absorption capability in the active layer for high-performance PSCs while minimizing the thickness of BHJ films due to low carrier mobility of organic semiconductors, and development of highly soluble and crystalline photovoltaic polymers to enable thick film production without damage in the fill factor. In addition, limitations of binary BHJ solar cells can be solved by developing ternary BHJ solar cells.

In this thesis, I focused on various engineerings which are surface plasmon resonance (SPR) effect using PEDOT:PSS electrode doped with silver nanoparticels, morphology control using diphenly ether (DPE) as a novel processing additive with conjugated polymers (PPDT2FBT and P2), and ternary blend using a $PC_{61}BM$ and $PC_{71}BM$ mixture with a donor polymer resulting in enhaced electromagnetic field to provide light confinement to active layer, well-formed phase separation to make good pathway for electron and holes, and overcoming problem of binary BHJ solar cells (lower J_{SC} and FF), respectively, for the highly efficient light harvesting of polymer solar cells.

Chapter 2. Highly Efficient Plasmonic Organic Optoelectronic Devices Based on a Conducting Polymer Electrode Incorporated with Silver Nanoparticles

2.1 Research background

Organic semiconductor-based optoelectronic devices, such as polymer solar cells (PSCs) and polymer light-emitting diodes (PLEDs), have attracted considerable attention due to their advantages such as solution-based low-cost and large-area fabrication using printing techniques.[138-141] On the other hand, the performance of these polymer based optoelectronic devices has not reached the level needed for commercialization. Although power conversion efficiencies (PCEs) of ~8% have been demonstrated for PSCs,[76, 142, 143] there are still many limitations for practical applications. Indium tin oxide (ITO) is used widely as a transparent electrode for optoelectronic devices because of its good electrical conductivity and appropriate transparency.[144] However, ITO has many disadvantages, such as intrinsic brittleness, poor transparency in the near IR regions, chemical instability under acid or basic conditions, increasing cost of indium due to the limited reserves on the earth, and costly preparative methods, such as sputtering, evaporation and pulsed laser deposition, etc.[145, 146] Therefore, devices with an ITO electrode with the conventional structure of PSCs and PLEDs are unsuitable for cost-effective and flexible device applications. To overcome these problems, many efforts have been made to replace the conducting oxide electrode with a transparent conducting polymer electrode.[146-153] A conducting polymer, poly(3,4-ethylenedioxythiophene):poly(styrenesulfonate) (PEDOT:PSS), has been widely exploited in PSCs and PLEDs by modulating and improving its intrinsic conformation as well as electrical and optical properties.[154-157] For example, Na and Yim et al. reported the feasibility of replacing the ITO electrode with a PEDOT:PSS electrode doped with dimethyl sulfoxide (DMSO).[146, 153]

To improve the performance of PSCs, it is important to maximize the light absorption of the photoactive layer. Simply increasing the thickness of an active layer can allow more sunlight absorption but also increases the series resistance, often resulting in a poor fill factor (FF).[158] The surface plasmon resonance (SPR) effect may offer a solution to improving the short circuit current density (J_{SC}) in PSCs by the incorporation of metal nanoparticles (NPs) in organic electronic devices without increasing the active layer thickness.[159-165] The SPR effect arises from a localized electromagnetic surface wave at the metal and dielectric interface, which enables the active layer to absorb more photons from irradiated light via field enhancement near metal NPs.[28, 159, 166, 167] Similarly, the SPR effect supports the improved device performance in PLEDs by enhancing light emission by accelerating the radiative decay process.[162-165, 168]

Silver (Ag) and gold (Au) NPs are used widely to induce the SPR effect due to strong light absorption and excellent air stability, etc.[49, 50, 169-172] In particular, Ag-based nanostructures, such as Ag nanospheres, nanoholes, gratings, and grids, have been studied extensively as an electrode for optoelectronic devices.[35, 148, 150, 173, 174] Despite the desirable SPR effect of these Ag nanomaterials, complicated processes, such as photolithography and nano-imprinting, are required to prepare nano-patterned Ag electrodes, resulting in high-cost fabrication. To overcome this problem, methods for the simple and low-cost synthesis of metal NPs have been introduced to all solution-based fabrication of PSCs and PLEDs.[159-161, 163]

In this paper, we successfully demonstrated the highly efficient ITO-free PSCs and PLEDs by replacement of the ITO electrode with a PEDOT:PSS/Ag NPs composite film. The Ag NPs in PEDOT:PSS contribute simultaneously to enhancing the device performance via the SPR effect and increasing the conductivity of the PEDOT:PSS electrode. These enhanced optical and electrical properties resulted in PCE increases by 32% for PSCs and 124% increment of light-emitting efficiency for PLEDs, compared to the devices without Ag NPs

2.2 Experimental

Materials and instruments: Silver nitrate ($AgNO_3$, 99.9999%) and N-methyl-2-pyrrolidone (NMP, 99.5%) were purchased from Sigma-Aldrich Co. and used as without further purification. Poly(3,4-ethylenedioxythiophene):poly(4-styrenesulfonate) (PEDOT:PSS PH500) was acquired from H. C. Starck (Germany). Poly(5,6-bis(octyloxy)-4-(thiophen-2-yl)benzo[c][1,2,5]thiadiazole) (PTBT) (M_n = 30,000 g mol^{-1}) was synthesized in our laboratory.[175] Regio-regular P3HT (M_n = 55,000 g mol^{-1}) and [6,6]-phenyl-C61-butyric acid methyl ester ($PC_{61}BM$) were purchased from Electronic Materials (EM) Index Co., Ltd. Poly(phenylene vinylene)-based light-emitting copolymer, Super Yellow (SY, M_n = 1,950,000 g mol^{-1}) was supplied by Merck Co. The transmission electron microscope (TEM) images were obtained using a JEOL JEM-2100 TEM operated at 200 kV. The samples for TEM analysis were prepared by placing a few drops of the Ag NPs in NMP on a carbon-coated copper grid, and dried in a vacuum oven at room temperature for 1 h. The optical properties of Ag NPs were analyzed using a UV-vis spectrophotometer (Varian Carry 5000) in a range of 300 ~ 800 nm. The PL quantum efficiency was measured on a Jasco (FP-6500) spectrofluorometer with a Xenon lamp excitation source and an integration sphere. The fluorescence image was obtained by confocal laser scanning microscopy using a white light source (Olympus Mercury 100W). The laser beam was focused on a sample through a microscope objective (100x [oil]) mounted in an inverted microscope (Olympus IX 81). The conductivity was evaluated from the resistivity measured using a four-point-probe technique (CMT-SR1000N)

Preparation of Ag NPs: Ag NPs were synthesized by reducing silver nitrate ($AgNO_3$) using NMP as a reducing agent, where NMP has been also found to increase the conductivity of PEDOT:PSS.[176,177] Briefly 3 mg of $AgNO_3$ was added into 3 mL of NMP (stock solution, Ag@NMP). The vial was shaken for 1 min and then exposed to UV irradiation for 1h. The Ag NPs in NMP (50 μL) were added to 1 mL of PEDOT:PSS (PH500) solution and the resulting mixture was stirred at room temperature over 2 h. For preparation of a reference electrode (NMP:PH500), pure NMP (50 μL) without Ag NPs was mixed with 1 mL PH500. A transparent anode with low series resistance is required for sufficient light absorption/emission and better charge extraction/injection in PSCs and PLEDs, respectively. As a replacement for ITO, pristine PH500, NMP:PH500 (1:20 v/v%), and Ag@NMP:PH500 (1:20 v/v%) were prepared on glass substrates by spin casting the above solutions at 2000 rpm for 60s.

Device Fabrication characterization of PSCs and PLEDs: The device structures of solar cells are glass/NMP:PH500/PTBT:$PC_{61}BM$/Al for the reference and glass/Ag@NMP:PH500/PTBT:$PC_{61}BM$/Al for the testing device. The devices were fabricated using the following procedures. First, the glass substrates were cleaned with a detergent, ultra-sonicated sequentially in acetone and isopropyl alcohol, and then dried in an oven overnight at 100 °C. NMP:PH500 and Ag@NMP:PH500 layers, which were used as the anode, were spin-coated (after

passing through a 0.45 µm filter) onto a glass substrate at 2000 rpm for 60 s, baked at 120 °C for 15 min in air and moved to a glove box. The top of the NMP:PH500 and Ag@NMP:PH500 layers was spin-coated with mixed solution of PTBT:PC$_{61}$BM (1:2, 0.68 wt.%) a in o-dichlorobenzene at 1000 rpm for 60s. The devices were pumped down in a vacuum(< 10^{-6} torr), and a 100 nm thick Al electrode was deposited on top of the active layer. The deposited Al electrode area defined the active area of the devices as 13.5 mm^2. The measurements of photovoltaic characteristics were taken with the solar cells inside a glove box using a high quality optical fiber to guide the light from the solar simulator equipped with a Keithley 2635A source measurement unit. The *J-V* curves for the devices were measured under AM 1.5G illumination at 100 mW cm^{-2} with a mask. The IPCE measurements were carried out in ambient air using an IPCE system (Model QEX7) by PV measurements Inc. (Boulder, Colorado). For the PLEDs, the device structures were glass/NMP:PH500/SY/LiF/Al and glass/Ag@NMP:PH500/SY/LiF/Al for the reference and testing device, respectively. A SY solution dissolved in chlorobenzene (0.8 wt.%) was spin-cast at 2000 rpm for 45 s on top of the electrodes. Finally, a 1 nm-thick LiF layer and a 100 nm-thick Al layer were thermally evaporated on top of the SY layer. The current density and luminance versus the applied voltage characteristics were measured using a Keithley 2400 source measurement unit and a Konica Minolta spectroradiometer (CS-2000).

2.3 Results and discussion

Figure 2.1 shows a transmission electron microscopy (TEM) image and UV-vis absorption spectra of the Ag NPs in solution (NMP) and in the film substrate. As shown in **Figure 2.1a**, the Ag NPs were dispersed randomly with a diameter of 3 to 9 nm.

The surface plasmon absorption band of Ag NPs was observed around 420 nm (**Figure 2.1b**), which clearly indicates the formation of Ag NPs.[178] Figure c shows the optical transmittance of the ITO, NMP:PH500 and Ag@NMP:PH500 films measured in air. The transparency of the NMP:PH500 and Ag@NMP:PH500 films is comparable to that of ITO. As shown in the inset in **Figure 2.1c**, the Ag@NMP:PH500 film exhibited greater absorbance than NMP:PH500 in the vicinity of the Ag plasmonic peak around 420 nm. We also simulated the extinction and electromagnetic field enhancement near Ag NPs using a three dimensional finite-difference time-domain (3D FDTD) method (**Figure 2.4**). By comparing the near-field enhancement by Ag NPs with a diameter of 3 to 9 nm, the 9 nm-sized Ag NP was calculated to show the strongest electromagnetic field enhancement. In addition, Ag NPs at the bottom and center positions in the PEDOT:PSS film showed almost identical electromagnetic field distribution around particles. The pristine PH500, NMP:PH500 and Ag@NMP:PH500 films showed conductivities (by a four point-probe method)[179] of 0.48 S cm^{-1}, 322 S cm^{-1}, and 450 S cm^{-1}, respectively. As reported previously, the conductivity could be improved significantly over that of the pristine PH500 film by adding a small amount of NMP (5 vol%) to the

(a)

(b)

(c)
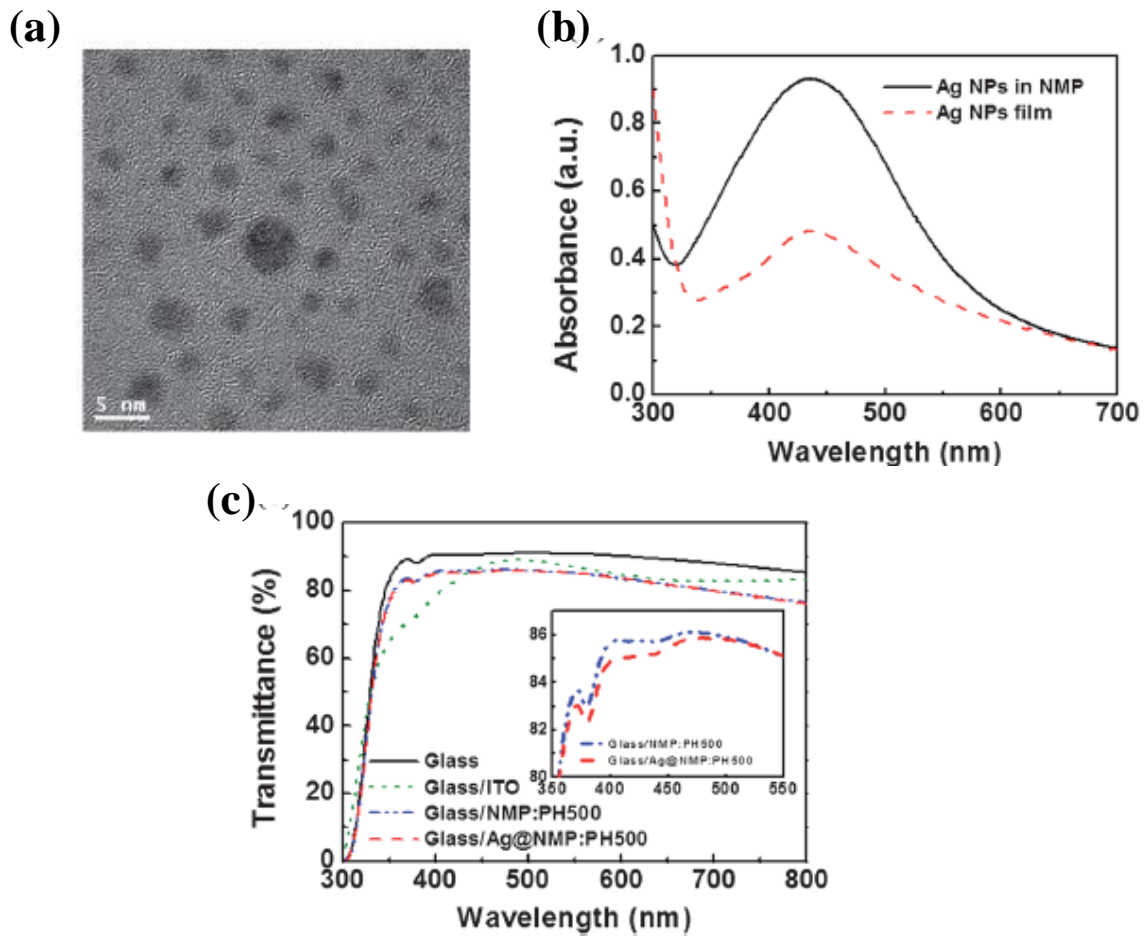
Figure 2.1. a) TEM image of spin-coated Ag NPs film, b) UV-vis absorption spectra of Ag NPs in solution and in the film and c) transmittance of glass, ITO, NMP-PH500 and Ag@NMP-PH500 films. (Inset shows a clearly enhanced absorption around 420 nm for Ag@NMP-PH500 compared to NMP-PH500).

PEDOT:PSS solution.[180, 181] Furthermore, the conductivity of the Ag@NMP:PH500 film was increased by ~ 40% compared to that of NMP:PH500. This enhancement was attributed to the well dispersed electrically conductive Ag NPs.[171]
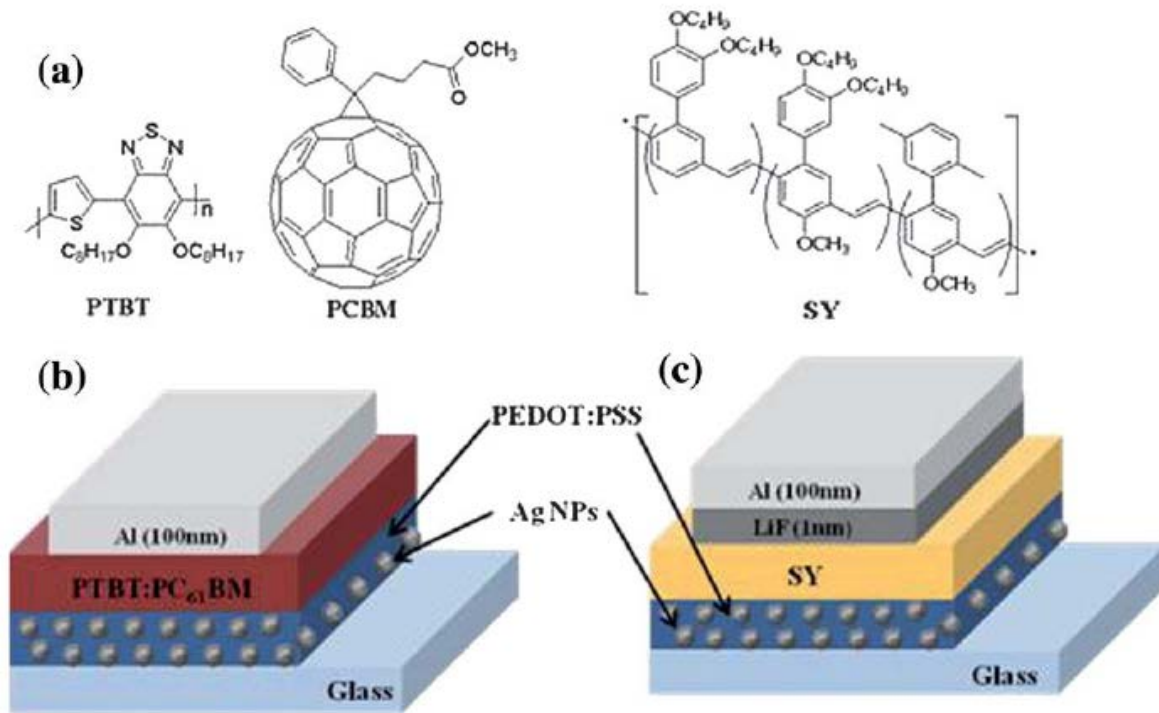
Figure 2.2. (a) Chemical structures of PTBT, PC$_{61}$BM and SY, (b) and (c) schematics of ITO-free PSCs and PLEDs based on PTBT:PC$_{61}$BM and SY with an Ag NPs containing PEDOT:PSS electrode, respectively.
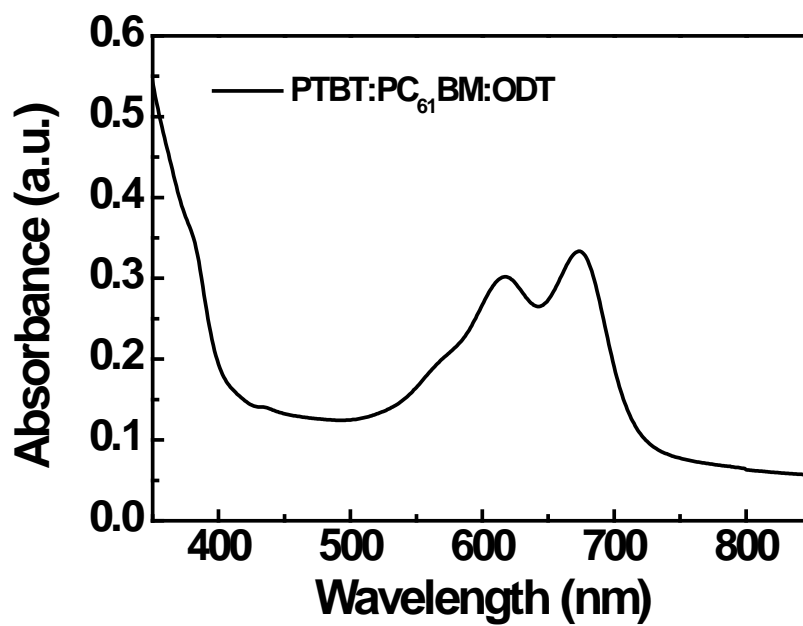
Figure 2.3. Absorption spectra of active layer (PTBT:PC$_{61}$BM:ODT).
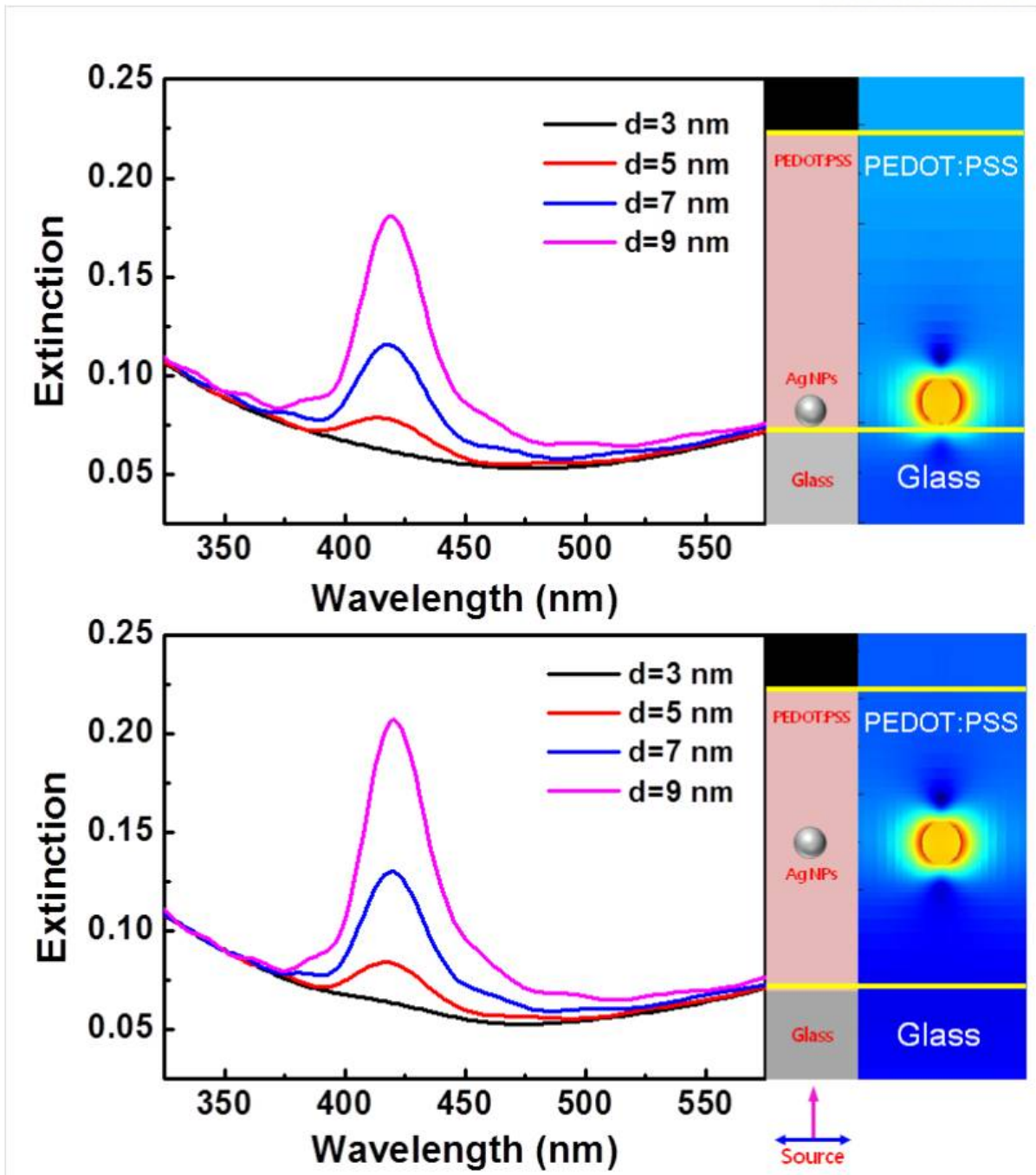
Figure 2.4. Simulated extinction spectra of Ag NPs with a size of 3-9 nm and electromagnetic field distribution around Ag NPs at the bottom and center position from a glass substrate.
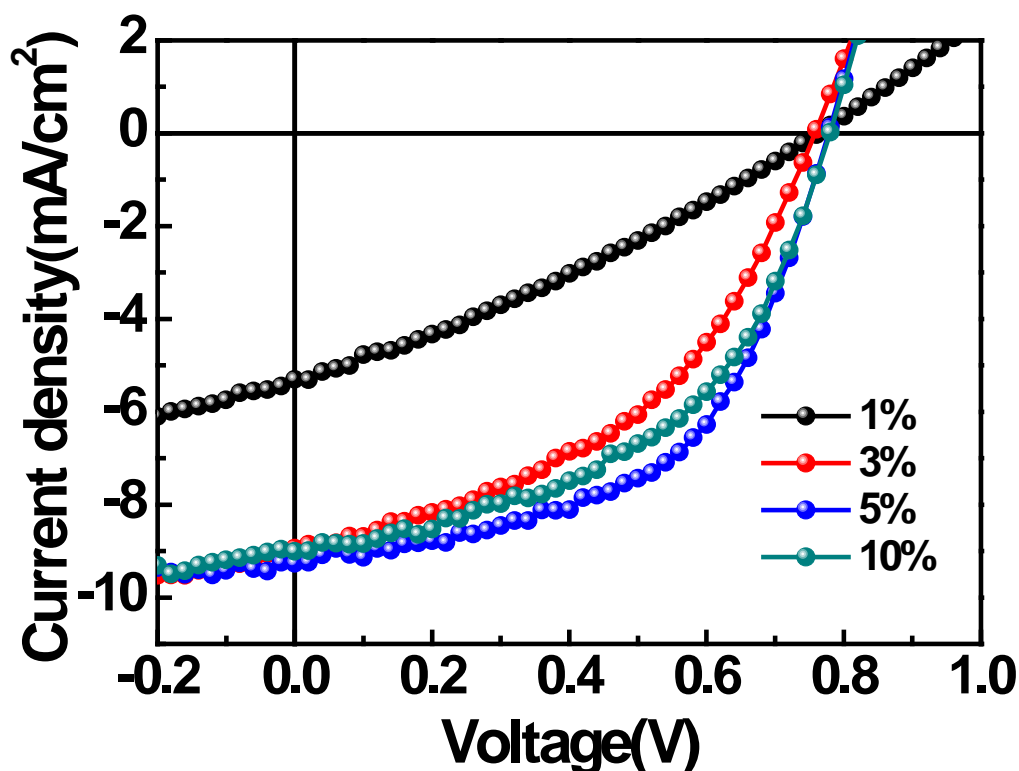
Figure 2.5. *J-V* characteristics of ITO-free PTBT:PC$_{61}$BM-based PSCs with Ag@NMP:PH500 electrodes by increasing concentration of Ag NPs.

Table 2.1 Summary of device properties of ITO-free PTBT:PC$_{61}$BM-based PSCs with Ag@NMP:PH500 electrodes by increasing concentration of Ag NPs.

Device configuration	Concentration of Ag NPs	J_{SC} (mA cm^{-2})	V_{OC} (V)	*FF*	PCE (%)
	1%	5.30	0.76	0.30	1.21
Glass/Ag@NMP :PH500/PTBT:PC$_{61}$BM/Al	3%	8.93	0.76	0.45	3.03
	5%	9.26	0.78	0.53	3.85
	10%	9.00	0.78	0.49	3.44
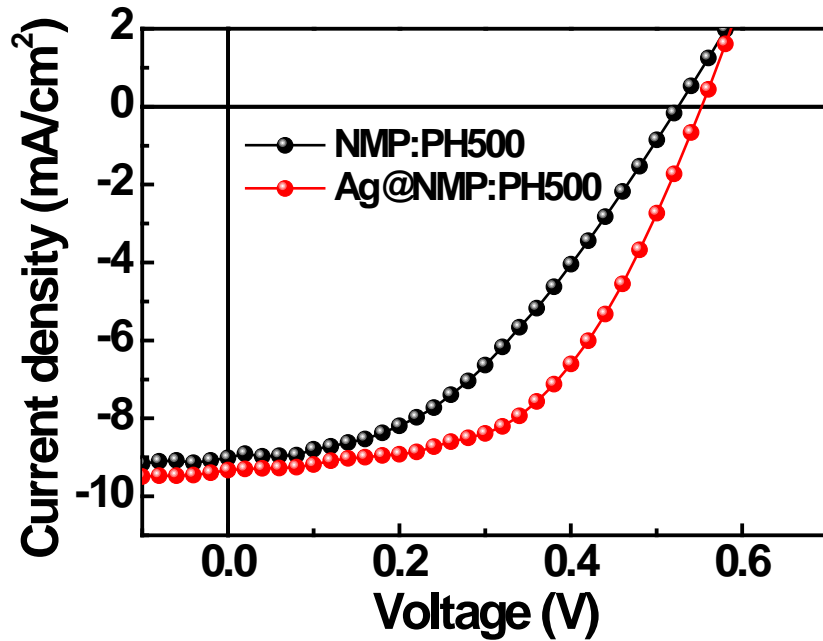
Figure 2.6. *J-V* characteristics of ITO-free P3HT:PC$_{61}$BM-based PSCs with NMP:PH500 and Ag@NMP:PH500 electrodes.
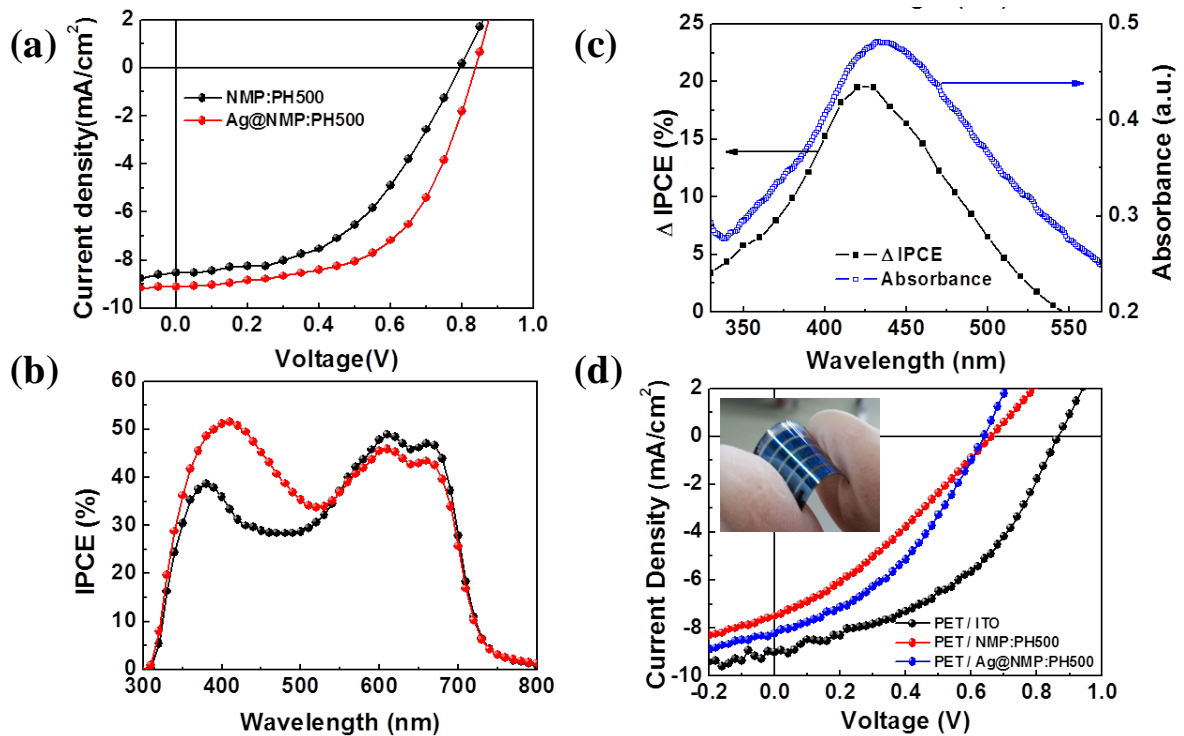
Figure 2.7. (a) *J-V* characteristics, (b) IPCE curves for PSCs with NMP:PH500 and Ag@NMP:PH500 electrodes, (c) comparison of ΔIPCE and absorbance of Ag NPs, and (d) *J-V* characteristics of ITO-coated and ITO-free flexible PSCs on PET substrate. The inset of (d) shows a picture of the flexible PSC with Ag@NMP:PH500 electrode.

An ITO-free bulk heterojunction solar cell was prepared by blending a low band gap polymer, PTBT as a donor and $PC_{61}BM$ as an acceptor for the active layer (**Figure 2.2a**). The synthesis of PTBT and its photovoltaic properties were reported recently.[43] The donor–acceptor (D–A) type alternating copolymer, PTBT exhibited broad absorption covering the whole visible region, with the absorption maxima at 605 nm and 652 nm in the film. The optical band gap (Eg) of the polymer was estimated to be 1.72 eV based on the onset point of the absorption spectrum in the film. However, PTBT shows a weak absorption in a wavelength range of 400–500 nm (**Figure 2.3**). Hence, the incident photon to electron conversion efficiency (IPCE) is relatively poor at this wavelength range. Therefore, light absorption of the $PTBT:PC_{61}BM$-based photovoltaic device is expected to be enhanced by incorporating Ag NPs via the plasmonic effect around 420 nm. To optimize the device fabrication condition, more than 100 PSC and PLED devices with the NMP:PH500 and Ag@NMP:PH500 electrodes (as anodes) were tested. We first fabricated $PTBT:PC_{61}BM$-based PSCs by changing the concentration of Ag@NMP from 1 to 10 vol% to get the optimum concentration of Ag NPs in PEDOT:PSS. **Figure 2.5** and **Table 2.1** show that 5 vol% of Ag NPs is the optimized concentration for device fabrication. **Figure 2.7a** shows the current density–voltage (*J–V*) characteristics of the ITO-free PSCs with NMP:PH500 and Ag@NMP:PH500 as anodes.
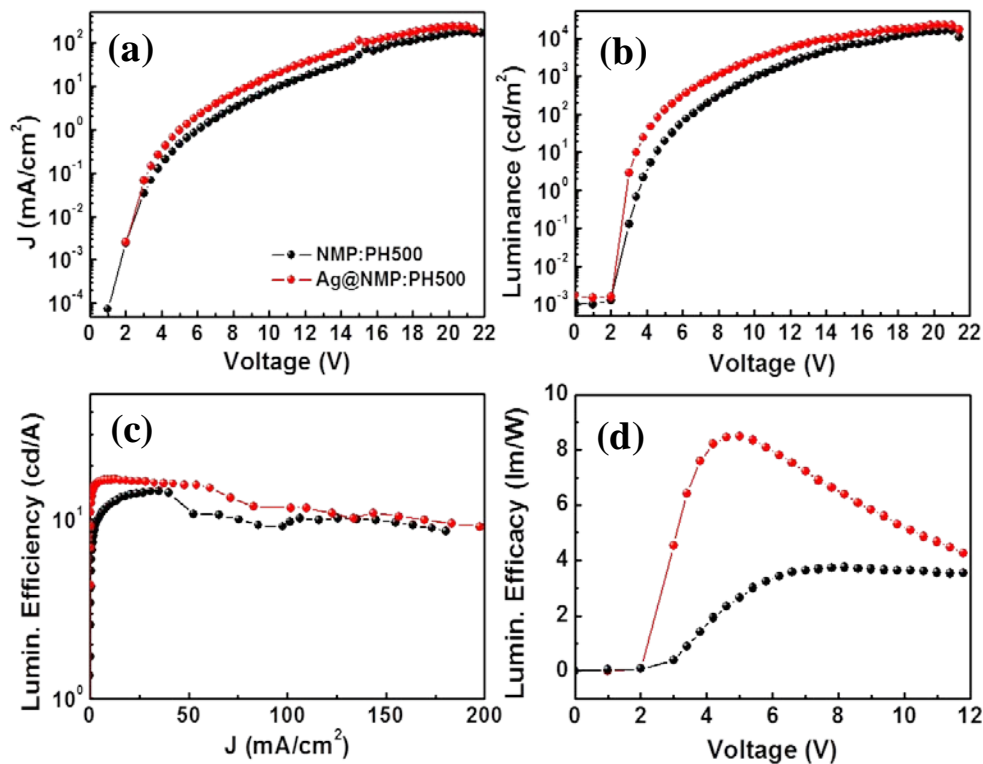
Figure 2.8. Light-emitting characteristics. (a) current density vs. applied voltage, (b) luminance vs. applied voltage, (c) EL efficiency vs. current density   and (d) power efficiency vs. voltage curves.

The reference device with the NMP:PH500 electrode exhibited a J_{SC}, open-circuit voltage (V_{OC}), FF, and best PCE of 8.52 mA cm^{-2}, 0.79 V, 0.48, and 3.27%, respectively. In contrast, the J_{SC}, V_{OC}, FF and best PCE values of the device with Ag@NMP:PH500 were improved remarkably to 9.11 mA cm^{-2}, 0.84 V, 0.56, and 4.31%, respectively, as summarized in **Table 2.2**. The PSC device with Ag@NMP:PH500 leads to a ~32% increase in PCE compared to the device without Ag NPs. To elucidate the effect of the Ag NPs on improving the J_{SC}, the IPCE was measured for the devices with NMP:PH500 and Ag@NMP:PH500 electrodes (**Figure 2.7b**). The IPCE values of the device with Ag@NMP:PH500 were higher than those of the NMP:PH500-based reference device in a range of 380 nm–520 nm. In **Figure 2.7c**, the ΔIPCE (which represents the difference between IPCE of the devices with NMP-PH500 and Ag@NMP:PH500) spectrum almost overlapped with the Ag plasmonic band, suggesting enhanced light absorption via the SPR effect of Ag NPs. This clearly supports the increased J_{SC} resulting from amplified light absorption by the localized electromagnetic field enhancement. The FF of the device with Ag@NMP:PH500 (0.56) was also increased compared to that of the reference device (0.48), as shown in **Table 2.3**. The FF is related to the active layer thickness and series resistance (R_S), which is the sum of the bulk resistance and contact resistance at the interfaces.[158]

Table 2.2. Summary of device properties of ITO-free P3HT:PC$_{61}$BM-based PSCs.

Device configuration	J_{SC} (mA cm^{-2})	V_{OC} (V)	FF	PCE (%)
Glass/NMP:PH500/ P3HT:PC$_{61}$BM/Al	8.89	0.54	0.43	2.00
Glass/Ag@NMP:PH500/P3HT:PC$_{61}$BM/Al	9.34	0.55	0.53	2.74

Table 2.3. Device characteristics of PTBT:PC$_{61}$BM-based PSCs and SY-based PLEDs with NMP:PH500 and Ag:NMP:PH500 electrodes.

Electrodes for PSCs	J_{SC} (mA cm-2)	V_{OC} (V)	FF	Best PCE (%)
NMP:PH500	8.52	0.79	0.48	3.27
Ag@NMP:PH500	9.11	0.84	0.56	4.31
Electrodes for PLEDs	**Maximum luminance (cd m^{-2}) (at voltage)**	**Maximum EL efficiency (cd A^{-1}) (at voltage)**	**Maximum power efficiency (lm W^{-1}) (at voltage)**	**Turn on voltage (V)**
NMP:PH500	15582 (21.0V)	14.43 (14.2V)	3.75 (8.2V)	2.0
Ag@NMP:PH500	22402 (20.2V)	16.77 (9.4V)	8.4 (5.0V)	2.0

Therefore, the sheet resistance of the electrode (R_{sheet} = 1/ $\sigma \times$d, where σ is the conductivity and d is the layer thickness) is closely related to the FF and R_S. Note that all the processes for fabricating the active layer and electrodes were performed under identical conditions; a similar thickness for both devices is expected. Since the enhanced conductivity by the Ag NPs results in reduced R_{sheet} ((638 Ω sq^{-1} for NMP-PH500 $\rightarrow$ 444 Ω sq^{-1} for NMP-PH500), the increased FF of the device can be attributed to the reduced R_S. Therefore, the Ag NPs enhance optical and electrical properties, resulting in the increases in J_{SC} and FF.[174] Devices based on poly(3-hexylthiophene) (P3HT):PC$_{61}$BM were also fabricated with the NMP:PH500 and Ag@NMP:PH500 electrodes. The results also exhibited a similar trend (J_{SC} and *FF* were improved from 8.89 mA cm^{-2} and 0.43 to 9.34 mA cm^{-2} and 0.53, respectively), as shown in **Figure 2.6 and Table 2.2**. It indicates our electrode system with Ag NPs and PEDOT:PSS can be extended to other polymeric photovoltaic devices.

For practical application of Ag@NMP:PH500 as the electrode, we evaluated long-term stability under ambient condition and fabricated flexible PSCs on a poly(ethyleneterephthalate) (PET) substrate. As shown in **Figure 2.9**, the devices with PH500 electrodes showed a similar temporal stability compared with the the conventional ITO-based one. The PCE value was decreased by ~66% for all devices within 200 h in air.
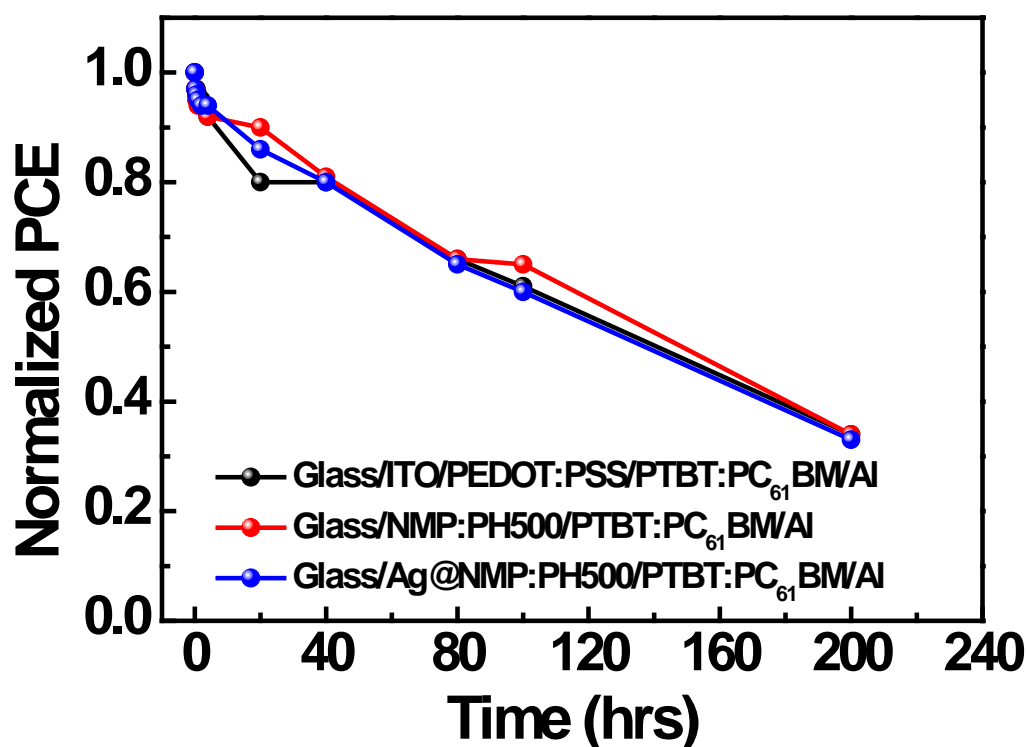
Figure 2.9. Temporal stabilities of devices with ITO, NMP:PH500 and Ag@NMP:PH500 electrodes.

Table 2.4. Summary of device properties of ITO-coated and ITO-free PTBT:PC$_{61}$BM-based PSCs on PET substrate.

Device configuration	J_{SC} (mA cm^{-2})	V_{OC} (V)	FF	PCE (%)
PET/ITO/PEDOT:PSS/PTBT:PC$_{61}$BM/Al	9.00	0.87	0.44	3.40
PET/NMP:PH500/PTBT:PC$_{61}$BM/Al	7.50	0.66	0.31	1.55
PET/Ag@NMP:PH500/PTBT:PC$_{61}$BM/Al	8.22	0.64	0.39	2.06

Compared to the NMP:PH500 electrode, a flexible PSC with Ag@NMP:PH500 exhibited a substantially enhanced device efficiency (PCE: 1.55→ 2.06%) (**Figure 2.7d** and **Table 2.4**). Although we obtained the lower device properties using Ag@NMP:PH500 as an anode (relative to the device with ITO), our approach offers possibility of Ag@NMP:PH500 as a flexible plastic anode.

To assess the applicability to PLEDs, ITO-free PLEDs were also fabricated using the PEDOT:PSS electrodes with and without Ag NPs. The poly(phenylene vinylene)-based copolymer, Super Yellow (SY), was used as an emitting material and the device configuration was NMP:PH500 (or Ag@NMP:PH500)/SY/LiF/Al, as shown in **Figure 2.2**. **Figure 2.8** shows the light-emitting characteristics of the PLEDs with NMP:PH500 and Ag@NMP:PH500 electrodes. As shown in **Figure 2.8a**, charge injection in the device with Ag@NMP:PH500 was improved compared to the reference device with NMP:PH500. The reference device with NMP:PH500 exhibited a maximum luminance, electroluminescence (EL) efficiency, and power efficiency of 15,582 cd m^{-2} (at 21.0 V), 14.43 cd A^{-1} (at 14.2 V), and 3.75 lm W^{-1} (at 8.2 V), respectively. In contrast, the device with Ag@NMP:PH500 showed substantially improved light-emitting characteristics with a maximum luminance, EL efficiency, and power efficiency of 22,402 cd m^{-2} (at 20.2 V), 16.77 cd A^{-1} (at 9.4 V), and 8.4 lm W^{-1} (at 5.0 V), respectively. Fluorescence emission enhancement of the SY film with Ag NPs supports the improved device performance, which was confirmed by solid-dtate photoluminescence (PL) measurements and confocal laser scanning microscopy. The SY film with Ag@NMP:PH500 exhibited enhanced photoluminescence (PL) quantum efficiency (7.1 → 18.6%) via the incorporation of Ag NPs (**Figure 2.10a**). Similarly, a confocal laser scanning microscopy image showed the stronger SY fluorescence intensity around Ag NPs. (**Figure 2.10b**). The power efficiency of the device with Ag@NMP:PH500 was increased remarkably by 124% (**Table 1**). This must be related closely to SPR-assisted acceleration of the radiative recombination because the spontaneous emission rate increases through strong resonance coupling between the exciton in the emitting material and the SPR mode of Ag NPs.
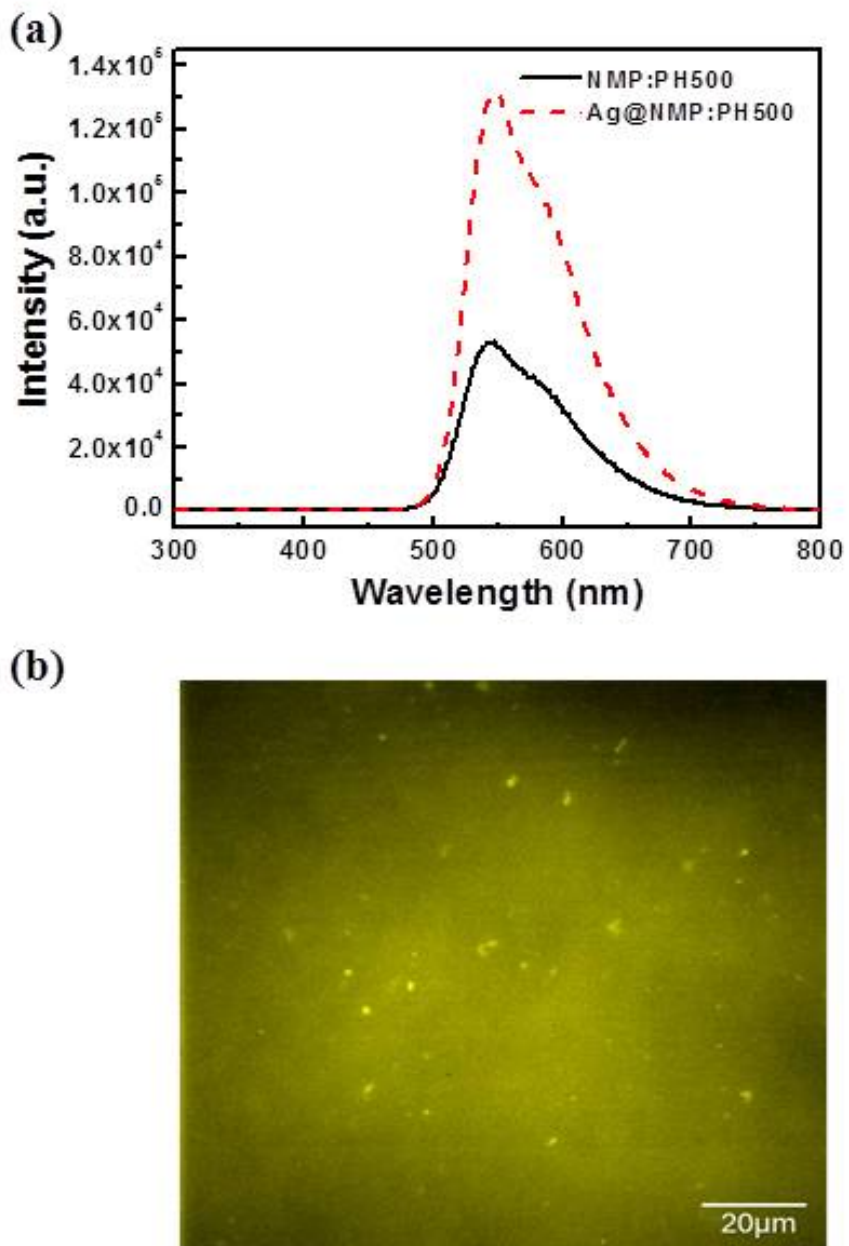
Figure 2.10. (a) Photoluminescence spectra of SY films on NMP:PH500 and Ag@NMP:PH500 electrodes and (b) confocal laser scanning microscopy image of SY film on Ag@NMP:PH500.

2.4 Conclusion

In summary, this study successfully demonstrated ITO-free PSCs and PLEDs with the SPR effect and the possibility of solution-processed PEDOT:PSS containing Ag NPs as a flexible plastic electrode. The Ag NPs-incorporated Ag@NMP:PH500 electrode exhibited a high conductivity of 450 S cm^{-1} with similar transparency to ITO. The PSC device based on PTBT:PC61BM with the Ag@NMP:PH500 electrode showed a 1% absolute enhancement in the power conversion efficiency (3.27 to 4.31%), whereas the power efficiency of the PLEDs was improved by 124% (3.75 to 8.4 lm W^{-1}) compared to the reference devices without Ag NPs. The SPR effect and improved electrical conductivity by the Ag NPs clearly contributed to increments in light absorption/emission in the active layer as well as the conductivity of the PEDOT:PSS electrode in PSCs and PLEDs. The solution-processable conducting polymer-based electrode, Ag@NMP:PH500 with Ag NPs, is a promising candidate as a flexible electrode for large area and flexible optoelectronic devices with a low-cost fabrication process.

Chapter 3. Semi-crystalline photovoltaic polymers with efficiency exceeding 9% in a ~300 nm thick conventional single-cell device

3.1 Research background

Over the past few decades, polymer solar cells (PSCs) have made significant progress, showing their potential in low-cost, flexible, lightweight, portable and large-area energy-harvesting devices.[182, 183] Considerable efforts have been dedicated toward the design of new materials, device architectures and processing techniques in order to improve the power conversion efficiency (PCE).[184-187] Recently, bulk heterojunction (BHJ) PSCs, consisting of low band gap (LBG) polymers (as an electron donor) mixed with C60 or C70 fullerene derivatives (as an electron acceptor), have shown promising performance with PCEs of 8–9% in single junction devices.[188] Cao et al. reported highly efficient (9.2% PCE) inverted-type PSCs based on the benzodithiophene–thienothiophene copolymer (PTB7) with an amine-functionalized polymer interlayer as an indium tin oxide (ITO) surface modifier.[189] With regard to a single cell having conventional geometry, Yu et al. further optimized PTB7 by replacing thiophene with thienothiophene in the benzodithiophene moiety to yield a dithieno[2,3-*d*:2',3'-*d'*]benzo[1,2-*b*:4,5-*b'*]dithiophene-based polymer (PTDBD2) with a PCE of 7.6%.[190] Chou et al. reported a new fluorinated quinoxaline-based copolymer (PBDT-TFQ) showing 8% PCE.[191]

To further improve PCEs, first and foremost, the molecular structure of LBG polymers should be carefully designed by considering their close relationship with the photovoltaic parameters, including short-circuit current density (J_{SC}), open-circuit voltage (V_{OC}) and fill factor (FF). Recently, highly efficient photovoltaic materials have been designed by introducing fluorine (F) atoms onto the polymeric chain.[192, 193] Fluorine has a small van der Waals radius (~1.35 Å) and is the most electronegative element with a Pauling electronegativity of 4.0. The introduction of fluorine onto the periphery of an electron-deficient unit is a versatile strategy, because it not only minimizes any undesired steric hindrance along the polymer chains but also effectively stabilizes the highest occupied molecular orbital (HOMO) and lowest unoccupied molecular orbital (LUMO) levels. Furthermore, hole mobility improves upon fluorination, though a reverse trend has been observed in some cases.[194] The fluorine substituent often has a great influence on inter- and intramolecular interactions,[195-197] which play important roles in the solid-state polymer organization with a cofacial π-π stacking. An effective approach to planarize a polymer chain (without losing its solution processability) is to create a noncovalent attractive interaction between neighboring moieties via intramolecular hydrogen bonds, dipole–dipole interactions, etc. Noncovalent intramolecular O···S interactions between alkoxy substituents and thiophene rings have been demonstrated to be effective for minimizing torsional angles within polymer backbones.[175, 198, 199] On increasing the coplanarity of a polymer chain with close solid-state π-π stacking, both polaron and exciton delocalization and their

transport characteristics can be improved.[200-202]

This study reports highly efficient new LBG polymer structures with a planar polymeric backbone formed via noncovalent intra- and interchain hydrogen bonds and dipole–dipole interactions, leading to highly ordered film morphologies, deep HOMO level, balanced electron and hole mobilities (a hole/electron mobility ratio of 1–2) and exceptional device stability. Devices based on these polymers exhibit outstanding long-term thermal stability at 130°C for over 200 h and the highest PCE over 9% in a conventional PSC having a single-cell device structure with a ~300 nm thick active layer.

3.2 Experimental

General: A microwave reactor (Biotage Initiator™) was used to synthesize the polymers. ^{1}H and ^{13}C NMR spectra were recorded on a JEOL (JNM-AL300) FT NMR system operating at 300 MHz and 75 MHz, respectively. UV-vis spectra were obtained with a JASCO V-630 spectrophotometer. The number- and weight-average molecular weights of the polymers were determined by gel-permeation chromatography (GPC) with o-dichlorobenzene as an eluent at 80 °C on an Agilent GPC 1200 series, relative to polystyrene standards. Cyclic voltammetry (CV) experiments were performed with a Versa STAT 3 analyzer. All CV measurements were carried out in 0.1 M tetrabutylammoniumtetrafluoroborate (Bu$_4$NBF$_4$) in acetonitrile with a conventional three-electrode configuration employing a platinum wire as a counter electrode, platinum electrode coated with a thin polymer film as a working electrode, and Ag/Ag$^+$ electrode as a reference electrode (scan rate: 50 mV s^{-1}). Thermogravimetric analysis (2050 TGA V5.4A) and differential scanning calorimetry (DSC Q200 V24.4) measurements were performed at a heating and cooling rate of 10 °C min^{-1} under nitrogen (purity, 99.999%). The nanoscale morphology of the polymer films was investigated using high-resolution transmission electron microscopy (HR-TEM) (JEM-2100, Cs corrector). Atomic force microscopy (AFM) images (1.5 mm x 1.5 mm) were obtained using a Veeco AFM microscope in tapping mode. Carrier mobilities were calculated by the space charge limited current method using hole-only (ITO/PEDOT:PSS/active layer/Au) and electron-only (FTO/active layer/Al, FTO: fluorine-doped tin oxide) diodes by fitting their J–V characteristics with the Mott–Gurney equation (eqn (1)).[37,38] Corrections were made for the built in potential (V_0) of the devices due to differences in the work functions of the electrodes and for the loss in potential due to the series resistance (V_{RS}) using the equation $V_{RS} = I$ x R_S. The thickness (L) of each device was measured after collecting J–V data using an atomic force microscope and a value of 3 was assumed for ε_r.

Synthesis of polymers: In a glove box, M1 (0.230 g, 0.32 mmol), M4 (0.263 g, 0.32 mmol), tris(dibenzylideneacetone)dipalladium(0) (4 mol%), tri(o-tolyl)phosphine (8 mol%) and 1 mL chlorobenzene were added in a 5 mL microwave vial. The polymerization reaction mixture was heated at 80 °C (65 W, 10 min), at 100 °C (70 W, 10 min) and at 140 °C (80 W, 40 min) in a microwave

reactor. The polymer was end-capped by addition of 2-tributylstannylthiophene (0.05 g, 0.14 mmol) and the mixture was further reacted at 140 °C for 20 min. The solution was cooled down and 2-bromothiophene (0.09 g, 0.53 mmol) was added by a syringe. The reaction solution was heated at 140 °C for another 20 min. After the reaction was ⬚hished, the cr precipitated into the mixture of methanol and HCl (36%) (350 mL : 10 mL) and further purified by Soxhlet extraction with acetone, hexane and chloroform. The extracted PPDTBT polymer in chloroform was precipitated into MeOH, filtered and dried under vacuum. PPDTFBT and PPDT2FBT were synthesized by following the same procedure as PPDTBT.

Poly[(2,5-bis(2-hexyldecyloxy)phenylene)-alt-(4,7-di(thiophen-2-yl)benzo[c][1,2,5]-thiadiazole)] (PPDTBT). Yield: 70%. Number average molecular weight (M_n) = 17.8 kDa, polydispersity index (PDI) = 2.4. δ_H (300 MHz; CDCl$_3$) 0.86–2.02 (62H, br), 4.10 (4H,br), 7.48 (2H, br), 7.69 (2H, br), 7.91 (2H, br), 8.19 (2H, br).

Poly[(2,5-bis(2-hexyldecyloxy)phenylene)-alt-(5-fluoro-4,7-di-(thiophen-2-yl)benzo[c][1,2,5]-thiadiazole)] (PPDTFBT). Yield: 65%. M_n = 29.8 kDa, PDI = 2.4. δ_H (300 MHz; CDCl$_3$) 0.86–2.02 (62H, br), 4.06 (4H, br), 7.06–8.20 (7H, br).

Poly[(2,5-bis(2-hexyldecyloxy)phenylene)-alt-(5,6-difluoro-4,7-di(thiophen-2-yl)benzo[c][1,2,5]-thiadiazole)] (PPDT2FBT). Yield: 67%. M_n = 42.6 kDa, PDI = 2.8. δ_H (300 MHz; CDCl3) 0.86–2.02 (62H, br), 4.00 (4H, br), 7.06–8.20 (6H, br).

Fabrication and characterization of polymer solar cells: ITO-coated glass substrates were cleaned by ultrasonication in deionized water, acetone and iso-propanol, and then dried in an oven for 12 h. After UV-ozone treatments for 10 min, PEDOT:PSS solution (Baytron P VPAI 4083, H. C. Starck) was spin-coated onto the ITO substrate at 5000 rpm for 40 s and then baked at 140 °C for 10 min. For deposition of the active layer, blend solutions of polymer (1 wt%):PC$_{71}$BM (1.5 wt%) dissolved in DCB or in CB (with/without 2 vol% diphenyl ether) were spin-cast on top of the PEDOT:PSS layer in a nitrogen-filled glove box. For methanol (MeOH) treatment, MeOH was spin-cast at 1000 rpm for 40 s on top of the active layer. Subsequently, an Al (100 nm) electrode was deposited on top of the active layer under vacuum (<10^{-6} Torr) by thermal evaporation. The area of the Al electrode defines the active area of the device as 13.0 mm^2. For the characterization of PSCs, their current density–voltage (*J–V*) characteristics were measured using a Keithley 2635A Source Measure Unit. Solar cell performance was tested with an Air Mass 1.5 Global (AM 1.5 G) solar simulator under an irradiation intensity of 100 mW cm^{-2}. EQE measurements were performed using a PV measurement QE system using monochromatic light from a xenon lamp under ambient conditions. The monochromatic light was chopped at 100 Hz and intensity was calibrated relative to a standard Si photodiode using a lock-in-amplifier. A mask (13.0 mm^2) made of thin metal was used for *J–V* characteristics and EQE measurements.

Fabrication and characterization of polymer solar cells: GIWAXS measurements were carried out at the PLS-II 9A U-SAXS beam line of Pohang Accelerator Laboratory. X-ray coming from the in-vacuum undulator (IVU) was monochromated (E_k = 11.24 keV, λ = 1.103 Å) using a Si(111) double crystal monochromator and focused horizontally and vertically at the sample position (450 (H) x 60 (V) μm^2 in FWHM) using a K–B-type focusing mirror system. The GIWAXS sample stage was equipped with a 7-axis motorized stage for the fine alignment of the thin sample and the incidence angle of X-rays was adjusted to 0.12–0.14°. GIWAXS patterns were recorded with a 2D CCD detector (Rayonix SX165, USA), and X-ray irradiation time was 0.5–5 s depending on the saturation level of the detector. The diffraction angle was calibrated with a sucrose standard (monoclinic, $P21$, a = 10.8631 Å, b = 8.7044 Å, c = 7.7624 Å, β = 102.938°) and the sample-to-detector distance was approximately 232 mm. Samples for GIWAXS measurements were prepared by spin-coating polymer or polymer:$PC_{71}BM$ blend solutions on top of the Si substrates. We also checked GIWAXS data on top of the PEDOT:PSS/Si layer. We obtained same morphologies with and without PEDOT:PSS layer on the Si substrate.

3.3 Results and discussion

The dialkoxylphenylene and benzothiadiazole (BT)-based monomers were prepared according to the procedures reported in the literature.[203-205] 1,4-Dibromo-2,5-bis(2-hexyldecyloxy) benzene was reacted with three BT-based monomers, 4,7-bis(5-trimethylstannylthiophen-2-yl)-2,1,3-benzothiadiazole (M1), 4,7-bis(5-trimethylstannyl-thiophen-2-yl)-5-fluoro-2,1,3-benzothiadiazole (M2) and 4,7-bis(5-trimethylstannylthiophen-2-yl)-5,6-difluoro-2,1,3-benzothiadiazole (M3), to yield poly[(2,5-bis(2-hexyldecyloxy)phenylene)-*alt*-(4,7-di(thiophen-2-yl)-benzo[c][1,2,5]thiadiazole)] (PPDTBT), poly[(2,5-bis(2-hexyldecyloxy) phenylene)-alt-(5-fluoro-4,7-di(thiophen-2-yl)benzo-[c][1,2,5]thiadiazole)] (PPDTFBT) and poly[(2,5-bis(2-hexyldecyloxy) phenylene)-alt-(5,6-difluoro-4,7-di(thiophen-2-yl)benzo[c]-[1,2,5]thiadiazole)] (PPDT2FBT), respectively, via Stille cross-coupling with $Pd_2(dba)_3$ as a catalyst in chlorobenzene using a microwave reactor (65–70% yield). The chemical structures and synthetic scheme for three polymers are shown in **Figure 3.1a** and **Figure 3.2**, respectively. The number average molecular weight and molecular weight distribution were measured to be 17.8 (polydispersity index, PDI = 2.4), 29.8 (2.4) and 42.6 kDa (2.8) for PPDTBT, PPDTFBT, PPDT2FBT, respectively (**Table 3.1**).

Three different types of dialkoxyphenylene and BT-based LBG copolymers were designed by carefully considering the planarity, chain curvature[206] and the resulting intermolecular orientations. The noncovalent attractive interactions between S (in thiophene) and O (in alkoxy groups), between S (in thiophene) and F, and between C–H (in thiophene) and N (in BT) minimize the torsional angle,
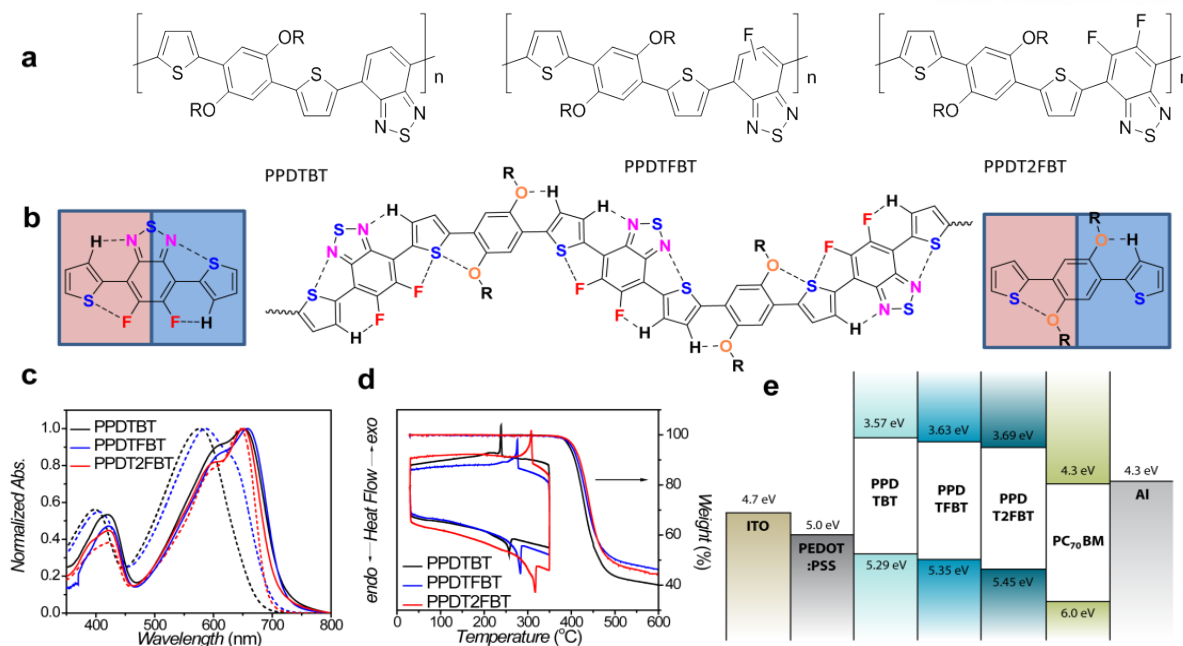
Figure 3.1. (a) Chemical structures, (b) noncovalent attractive interactions within the polymer chain, (c) UV-vis absorption spectra (dashed: in chloroform, solid: in the film), (d) TGA and DSC thermograms of PPDTBT, PPDTFBT and PPDT2FBT and (e) energy-band diagram.
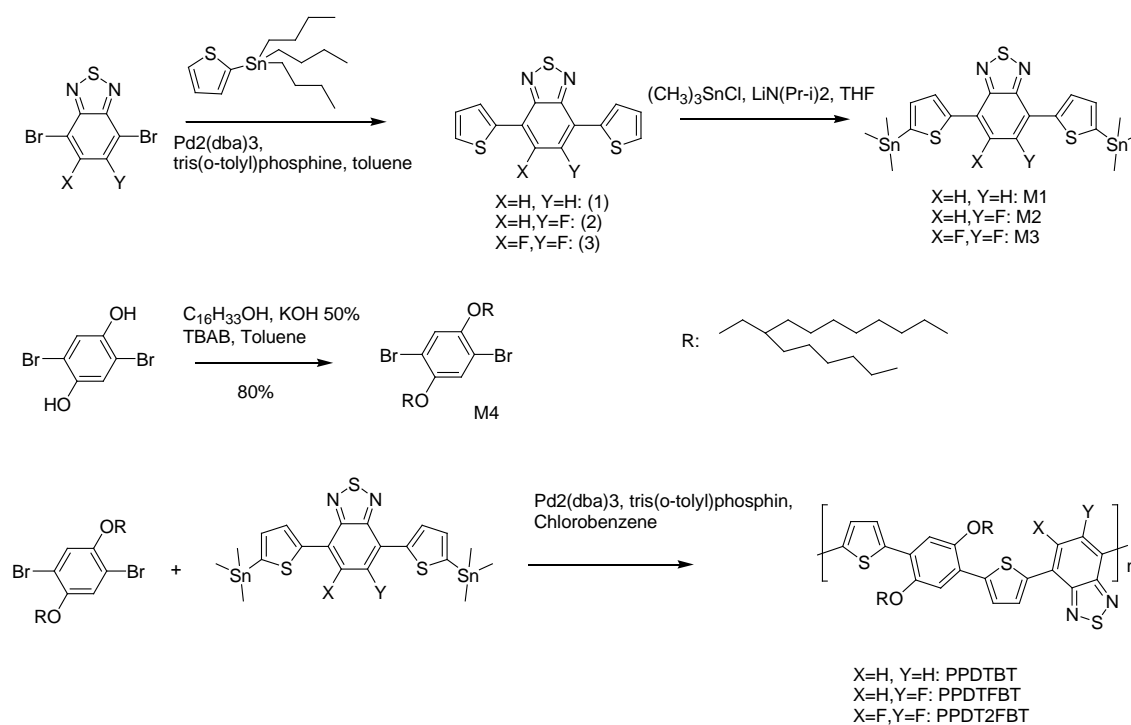
Figure 3.2. Synthetic routes to the monomers and polymers. Reagents and reaction conditions: (i) 2-tributylstannylthiophene, Pd2(dba)3, tris(o-tolyl)phosphine, toluene; (ii) (CH3)3SnCl, LiN(Pr-i)2, THF; (iii) C16H33Br, KOH, 50% TBAB, toluene; (iv) Pd2(dba)3, tris(o-tolyl)phosphine chlorobenzene.

Table 3.1. Summary of photophysical-, electrochemical- and thermal properties of polymers.

Polymers	M_n [Kg mol^{-1}][a]	PDI	λ_{onset} (film) [nm]	E^{opt}_g [eV][b]	HOMO [eV][c]	LUMO [eV][b]	T_d [°C][d]	T_c [°C][e]	T_m [°C][e]
PPDTBT	15	1.5	720	1.72	-5.29	-3.57	396	239	257
PPDTFBT	10	1.2	720	1.72	-5.35	-3.63	397	276	283
PPDT2FBT	16	2.4	705	1.76	-5.45	-3.69	402	308	317

[a] Number-average molecular weight (M_n) determined by GPC in chloroform at room temperature. [b] Optical bandgap and LUMO level was estimated form the onset of UV-vis spectra of the polymer films (LUMO = HOMO + E^{opt}_g). [c] HOMO level was estimated from the onset of the oxidation peaks of cyclic voltammogram. [d] Decomposition temperature (T_d) was determined by TGA. [e] Crystallization (T_c) and melting (T_m) temperature were obtained by DSC.
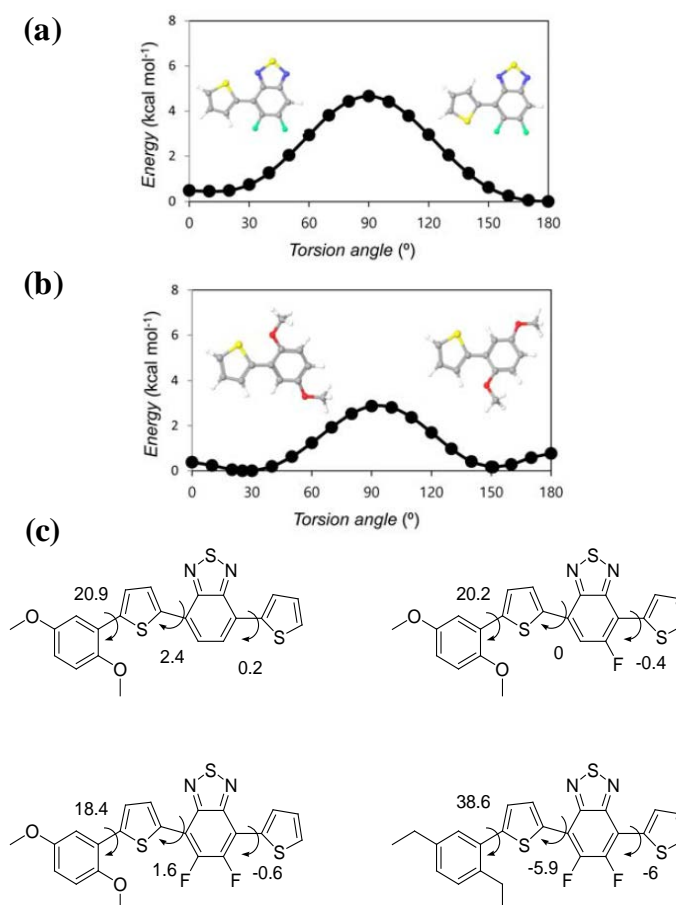
Figure 3.3. Torsional profiles for (a) thiophene-difluoro BT and (b) thiophene-dimethoxybenzene (yellow:sulfur, green: fluorine, red: oxygen). (c) The most stable conformation for PPDTBT, PPDTFBT and PPDT2FBT. (*) Methoxy substituents are replaced by ethyl groups in PPDT2FBT.

thus maximizing the planarity of the polymer chain (**Figure 3.1b**).[175, 195-199, 207, 208] Noncovalent coulomb interactions have been utilized to increase the planarity and ordering of polymer chains. Guo et al. demonstrated the use of noncovalent S···O attractive interactions to fix the chain conformation with improved planarity in methoxy-substituted thiophene and bithiazoles (dihedral angle, ~0°) compared to unsubstituted (~22°) and methyl-substituted thiophene-containing analogues (~68°).[198] S···F interactions have been emphasized in controlling the stacking orientation in fluorinated benzobisbenzothiophenes by single-crystal X-ray analyses.[195] Recently, Ratner and coworkers reported the role of nonbonding interactions in determining conformations of conjugated polymers and small molecules.[209] In this paper, the binding energy was calculated to be 2.2, 0.51 and 0.44 kcal mol^{-1} for CH···N, O···S and F···S nonbonding interactions, respectively. The branched 2-hexyldecyloxy substituents endow great solubility in common organic solvents with little influence on the intermolecular packing in the film by keeping the branching point away from the main chain. Additionally, by changing the number of fluorine substituents, the electronic structures (such as frontier orbital energy levels) of the polymers can be fine-tuned, which significantly influences the thermal, electrical properties and temporal stabilities of the resulting devices.

Computational studies using density functional theory (DFT, Jaguar quantum chemistry software, M06-2X/6-31G** level) were performed.[210-214] As shown in **Figure 3.3**, torsional profiles obtained by the introduction of fluorine atoms (in PPDTFBT and PPDT2FBT) were expected to be similar with that of PPDTBT because of the small size of fluorine atoms and intrachain F···S interactions. The introduction of alkoxy substituents on the phenylene ring was observed to decrease the torsional angle (18.4°–20.9°) *via* the S···O noncovalent interaction compared to the alkyl-substituted structure (38.6°). **Figure 3.3** shows the minimum energy conformations of PPDTBT, PPDTFBT and PPDT2FBT. According to the torsional profiles for PPDT2FBT, there are two minimum energy conformations for the thiophene–dialkoxybenzene linkage. This means that the S···O interaction is comparable with that of the O···H–C interaction (**Figure 3.3b**). The same argument can be applied to the thiophene–difluoro BT linkage (**Figure 3.3a**). We guess that these minimum energy conformations are expected to repeat randomly in the polymeric backbone for the polymers, as displayed in **Figure 3.1b**. In order to estimate interchain packing interactions, the binding energies were calculated by considering three types of cofacial interactions.[99] The head-to-tail (HT) configuration was found to be the most stable among the various possible configurations for all the polymers (**Figure 3.4**). The calculated binding energies of HT-type cofacial dimers were -18.7, -22.5, and -24.2 kcal mol^{-1} for PPDTBT, PPDTFBT and PPDT2FBT, respectively. In particular, the introduction of fluorine substituents greatly affected the interchain packing by way of attractive C–F···H, F···S and C–F/···π_F interactions in the adjacent polymeric chains.[215, 216] As shown in **Figure 3.4**, the replacement of methoxy substituents on the phenylene ring with ethyl groups destabilized the structure by ~3 kcal mol^{-1} because of the twisting in

50

the main chain caused by the absence of S···O or O···H–C interactions. The HOMO levels were measured to be -5.29, -5.35 and -5.45 eV for PPDTBT, PPDTFBT and PPDT2FBT by cyclic voltammetry (CV) (**Figure 3.5**), respectively. The LUMO levels were estimated to be -3.57, -3.63 and -3.69 eV for PPDTBT, PPDTFBT and PPDT2FBT, respectively, from the HOMO values and the optical band gaps of the films. Though the HOMO and LUMO electronic structures were calculated to be similar for the three polymers (**Figure 3.6**), their energies were clearly stabilized upon fluorine substitution. The resulting energy band structures are also summarized in **Figure 3.1e**.
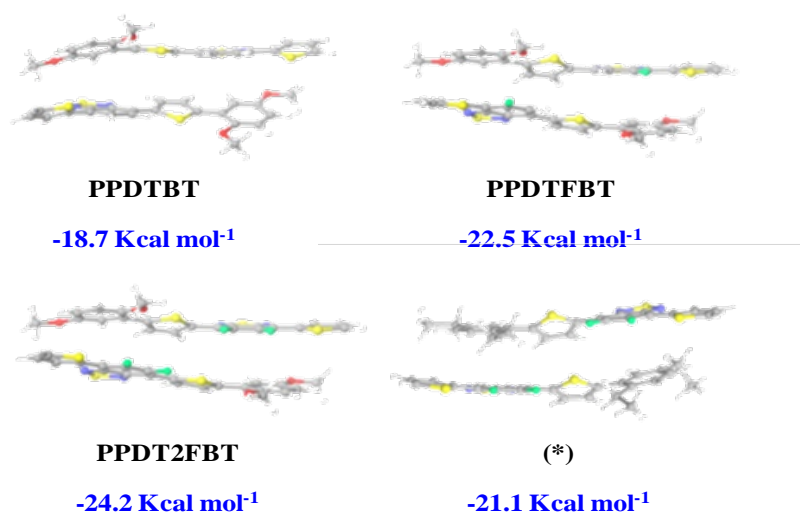
PPDTBT

-18.7 Kcal mol⁻¹

PPDTFBT

-22.5 Kcal mol⁻¹

PPDT2FBT

-24.2 Kcal mol⁻¹

(*)

-21.1 Kcal mol⁻¹

Figure 3.4. Calculated binding energies of HT-type cofacial dimeric structures for PPDTBT, PPDTFBT and PPDT2FBT. (*) Methoxy substituents are replaced by ethyl groups in PPDT2FBT. (red: oxygen, yellow:sulfur, green: fluorine)

Figure 3.5. Cyclic voltammogram of three polymers.

PPDTBT   **PPDTFBT**   **PPDT2FBT**

HOMO

LUMO
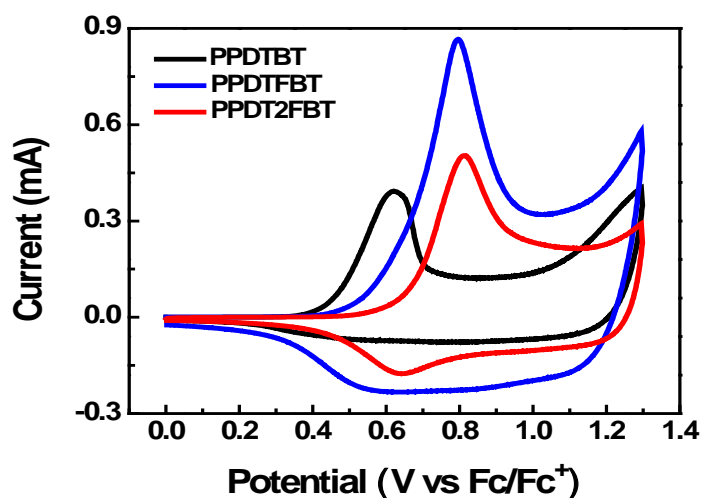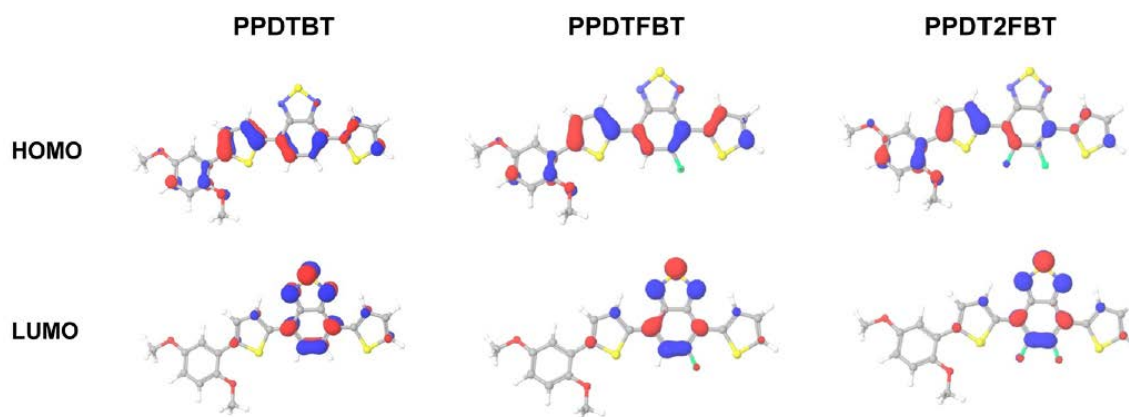
Figure 3.6. Calculated electronic structure of frontier orbitals.

Figure 3.1c shows the normalized UV-vis absorption spectra of the polymers in chloroform and in the film. All the polymers exhibit broad absorption in the range of 350–750 nm with two distinct high and low energy bands attributed to the localized π-π* and internal charge transfer transitions, respectively. In chloroform, the maximum absorption was measured at λ_{abs} = ~575 nm, ~585 nm and ~650 nm for PPDTBT, PPDTFBT and PPDT2FBT, respectively. More importantly, the shoulder peak at 650 nm was gradually enhanced with increasing fluorine substitution. In the film, three polymers show similar UV-vis profiles, where the spectra are red-shifted and the shoulder peak is substantially intensified, relative to those in solution. The differences in UV-vis spectra in the solution and film emphasize the facile interchain organization in the solid state. Optical band gaps were determined to be 1.72–1.76 eV for the polymer films. Thermal stability of the polymers was analyzed by thermogravimetric analysis (TGA) and differential scanning calorimetry (DSC) (**Figure 3.1d**). PPDTBT, PPDTFBT and PPDT2FBT showed the decomposition onset temperatures with 5% weight loss at 396, 397 and 402 °C, respectively. Clear melting temperatures (T_m) at 257, 283 and 317 °C, and recrystallization points (T_c) at 239, 276 and 308 °C were measured for PPDTBT, PPDTFBT and PPDT2FBT, respectively, indicating clear crystalline nature of the polymers. This clearly indicates that the introduction of fluorine atoms has a significant effect on the thermal properties of the polymers. Detailed optical, electrochemical and thermal properties of the three polymers are summarized in **Table 3.1**.

We investigated the photovoltaic properties of the polymers with a simple device architecture of ITO/PEDOT:PSS/polymer:PC$_{71}$BM/Al (PEDOT:PSS, poly(3,4-ethylenedioxythiophene):polystyrene sulfonic acid; PC$_{71}$BM, [6,6]-phenyl-C71 butyric acid methylester). To optimize the donor and acceptor (D : A) blend ratio, polymer:PC$_{71}$BM blend films were processed using o-dichlorobenzene (DCB) as a solvent (**Figure 3.7** and **Table 3.2**).
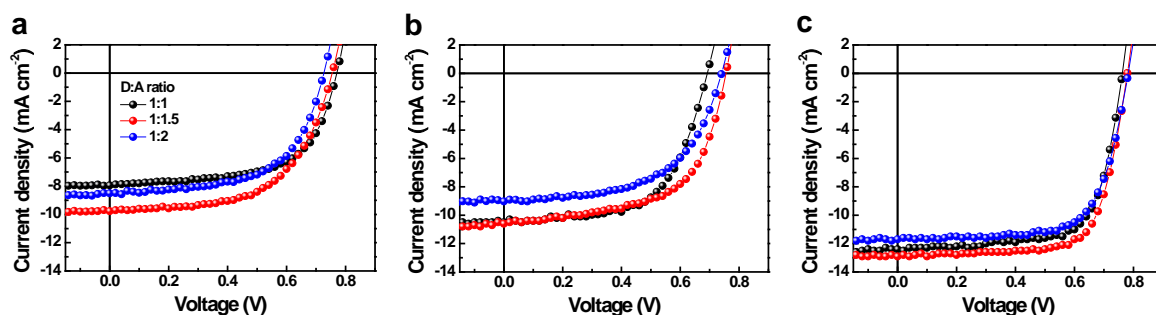
Figure 3.7. *J-V* characteristics of (a) PPDTBT, (b) PPDTFBT and (c) PPDT2FBT based PSCs with different polymer:PC70BM blend ratios (solvent: o-dichlorobenzene).

Table 3.2. Device characteristics of polymer:PC$_{71}$BM PSCs with different D:A blend ratios (solvent: odichlorobenzene).

Polymer	D:A ratio	J_{SC} (mA/cm^2)	V_{OC} (V)	*FF*	PCE (%)
	1:1	7.94	0.77	0.62	3.77
PPDTBT	1:1.5	9.77	0.76	0.58	4.27
	1:2	8.50	0.73	0.59	3.63
	1:1	10.5	0.69	0.60	4.38
PPDTFBT	1:1.5	10.6	0.76	0.59	4.72
	1:2	9.03	0.74	0.57	3.80
	1:1	12.5	0.79	0.71	6.94
PPDT2FBT	1:1.5	12.9	0.78	0.71	7.18
	1:2	11.7	0.78	0.69	6.34

For all polymers, devices with a D : A weight ratio of 1 : 1.5 showed the best performance (PCE: 4.27%, 4.72% and 7.18% for PPDTBT, PPDTFBT and PPDT2FBT, respectively). The device using PPDT2FBT exhibited the highest PCE of 7.18% with a J_{SC} of 12.9 mA cm^{-2}, V_{OC} of 0.78 V and FF of 0.71. This is one of the highest PCE values reported so far for conventional PSCs without any post-treatments (i.e., thermal, solvent annealing and additives, etc.). Upon thermal annealing (130 _C for 10 min), V_{OC} and FF were substantially improved for the three polymer systems (**Figure 3.8a** and **Table 3.3**). The V_{OC} increased from 0.76–0.78 V to 0.81– 0.86 V and the FF improved by ~0.03. This must be due to morphological changes in the photoactive layer and improved contact between the active layer and the electrode. Similar results have been reported.[217, 218]
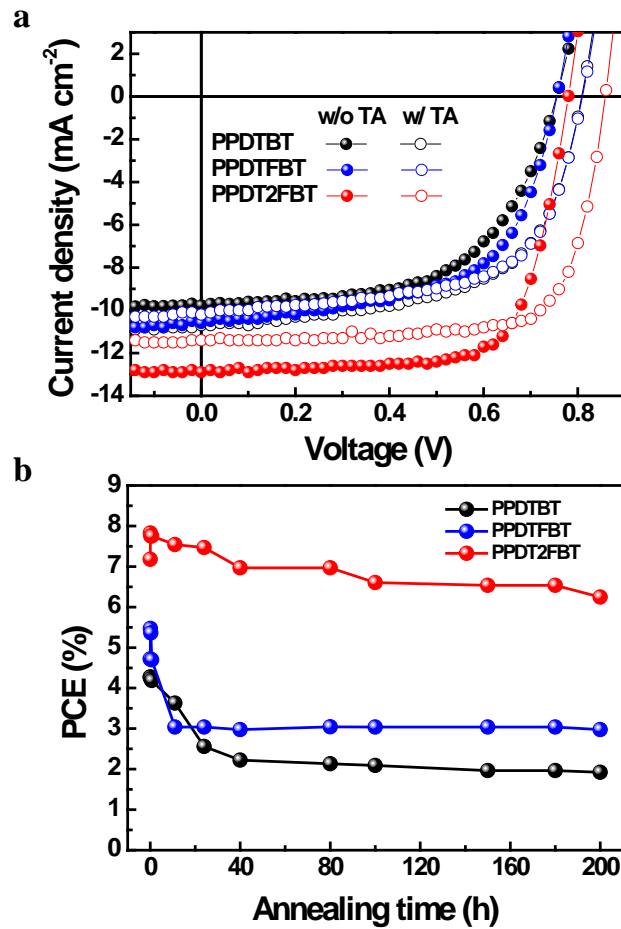
Figure 3.8. (a) Current density versus voltage (J–V) characteristics (w/o TA: without thermal annealing, w/TA: with thermal annealing) and (b) temporal stability (at an annealing temperature of 130 °C) of polymer: $PC_{71}BM$ PSCs. All devices were prepared from o-dichlorobenzene solutions.

Table 3.3. Device characteristics of polymer:$PC_{71}BM$-based PSCs with thermal annealing (solvent: DCB, blend ratio: 1 : 1.5)

Polymer	Thermal annealing [a]	J_{SC} (mA/cm^2)	V_{OC} (V)	FF	PCE (%) Best/Ave.
PPDTBT	No	9.77	0.76	0.58	4.27/4.12
	Yes	10.40	0.81	0.61	5.08/4.89
PPDTFBT	No	10.6	0.76	0.59	4.72/4/38
	Yes	10.2	0.81	0.62	5.11/5.02
PPDT2FBT	No	12.9	0.78	0.71	7.18/6.94
	Yes	11.40	0.86	0.74	7.26/7.06

[a] Thermal annealing at 130 °C for 10 min.

Temporal stabilities of the devices were also characterized by annealing at 130 °C for 200 h under nitrogen (**Figure 3.8b**). After thermal annealing for 200 h, the PPDTBT device showed a ~55% decrease in PCE. Interestingly, the PSCs based on PPDTFBT and PPDT2FBT showed a substantial improvement in temporal stability, showing 37% and 13% reductions in PCE, respectively. This remarkable device stability must be closely related to the stronger intermolecular interaction and higher interchain ordering, which is also consistent with the TGA and DSC measurements. Furthermore, relatively small morphological changes were detected for the PPDT2FBT:PC$_{71}$BM blend film after thermal annealing, compared to those of other two polymers and P3HT blends by atomic force microscopy (AFM) (**Figure 3.9**). Until now, there have been few reports on conjugated polymers achieving both high efficiency of over 7% and long-term thermal stability for over 200 h in PSCs (**Table 3.4** and **3.5**).
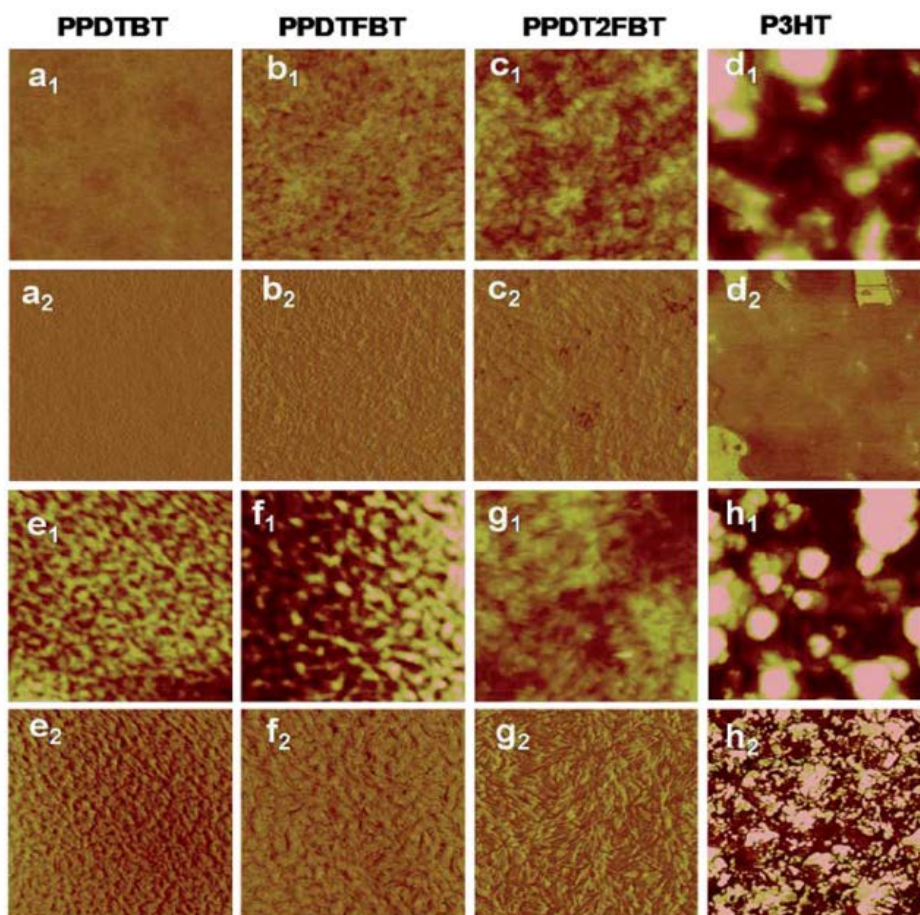
Figure 3.9. Tapping-mode AFM topography and phase images of polymer:PC$_{71}$BM blend films (solvent: DCB) before and after thermal treatment at 130°C for 200 h. Before thermal treatment: PPDTBT (a$_1$ and a$_2$), PPDTFBT (b$_1$ and b$_2$), PPDT2FBT (c$_1$ and c$_2$), P3HT (d$_1$ and d$_2$). After thermal treatment: PPDTBT (e$_1$ and e$_2$), PPDTFBT (f$_1$ and f$_2$), PPDT2FBT (g$_1$ and g$_2$), P3HT (h$_1$ and h$_2$). The size of all images is 1.5 mm x 1.5 mm.

Table 3.4. Comparison of photovoltaic characteristics and device stability.

Active layer	J_{SC} (mA cm^{-2})	V_{OC} (V)	FF	Initial PCE (%)	TA time[a] (hours)	Final PCE after TA (%)	PCE decrement after TA (%)	Reference
P3HT:PC$_{60}$BM	8.93	0.54	0.65	3.11	10	1.00	67	S7
P3HNT:PC$_{60}$BM	7.55	0.64	0.63	3.03	10	1.74	43	S7
TPD-Br16:PC$_{70}$BM	11.70	0.73	0.66	5.60	72	4.00	26	S8
P3HT:NC70BA	10.73	0.83	0.66	5.88	20	4.89	17	S9
PPDT2FBT:PC$_{70}$BM[b]	12.9	0.78	0.71	7.18	200	6.25	13	Current work

[a] TA: Thermal annealing at 130 °C. [b]Device was prepared using a o-dichlorobenzene solvent.

Table 3.5. Thermal cycling test protocol.

		ISOS-T-1 (thermal cycling)
Testing setup	Test environment	Dark
	Load	Open circuit
	Storage temperature	Cycle between RT and 130°C by cycling on/off hot plate
	Storage R.H.	Nitrogen-filled glove box
	Characterization light source	Solar simulation
Testing protocol	Temperature	130°C
	JV measurement	Intermediate procedure
	Min. measurement interval	Gradually increased annealing time (See Table R1)
	Characterization temperature	Room temperature
	Characterization irradiation level	Monitor
	IPCE	None
Output	Time	200 hours
	Characterization light source	AM 1.5G (100 mW/cm^2)
	Instantaneous performance parameters	PCE
	Stability performance parameters	See Fig. 2b
	Storage temperature/R.H.	Thermal annealing at 130°C and measurement at RT under nitrogen atmosphere
	IPCE	None
	Description of measurement protocol and setup	See experimental section 4.3 for detailed description
Required equipment	Characterization light source	AM 1.5G reference spectral irradiation
	Temperature	RTD
	R.H. monitoring	Nitrogen
	Storage	Hot plate with capability to cycle between RT and 130°C
	JV measuring setup	Intermediate procedure
	IPCE measuring system	None

Processing additives offer an efficient way to control the morphology of the active layer by selectively solvating one of the components in BHJ systems.[105, 109, 219, 220] Several additives were tested to modulate the morphology of the blend films prepared from a 1wt% chlorobenzene (CB) solution, where the clearer additive effects were observed compared to the films from DCB solutions. In contrast to poor performances of the devices fabricated without processing additives (**Figure 3.11** and **Table 3.7**), devices with additives showed substantial improvements in photovoltaic properties. Among the tested additives, diphenyl ether (DPE) was found to be an appropriate processing additive for our polymers. The addition of DPE to CB (CB : DPE = 98 : 2 by volume) led to remarkable enhancements in device performances for the three polymeric structures, showing ca. 5–8% PCE values (**Figure 3.10**).
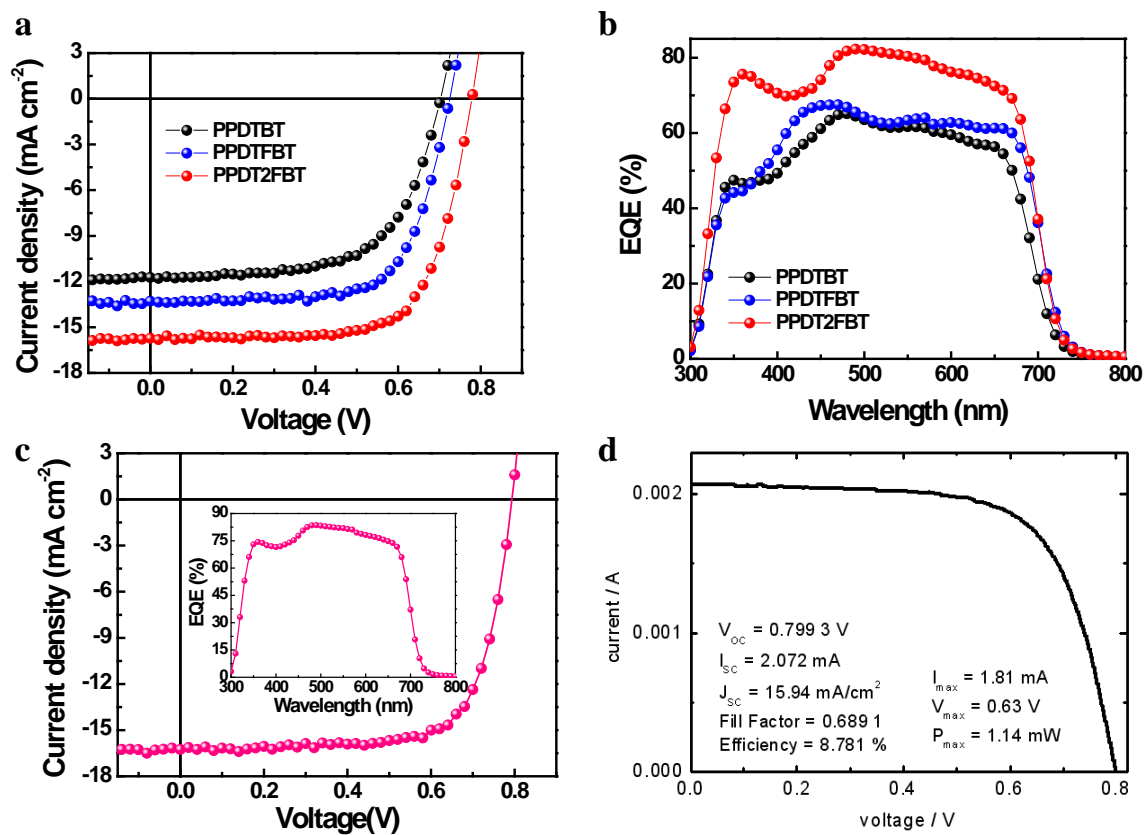
Figure 3.10. Photovoltaic characteristics of polymer:PC$_{71}$BM-based devices fabricated using a CB:DPE solvent mixture. (a) Current density versus voltage (*J–V*) characteristics and (b) external quantum efficiency (EQE) of polymer:PC$_{71}$BM-based PSCs. (c) *J–V* characteristics of the optimized PPDT2FBT:PC70BM-based PSC obtained from our laboratory and (d) certified by the KIER, respectively (c and d: with MeOH treatment). The inset of **Figure 3.10c** shows the EQE values over 80% in the range of 460–570 nm with the maximum EQE of 83.6% at 490 nm.

Table 3.6. Summary of photovoltaic characteristics (prepared from a solvent mixture of CB and DPE).

Polymer	Active layer Thickness (nm)	MeOH treatment	J_{SC} (mA cm^{-2})	V_{OC} (V)	FF	J_{SC} [Cal.][a] (mA/cm^2)	PCE (%) Best	PCE (%) Ave
PPDTBT	170	No	11.73	0.70	0.63	11.77	5.17	5.04
PPDTFBT	175		13.29	0.73	0.69	12.88	6.64	6.45
PPDT2FBT	290		15.73	0.78	0.71	15.59	8.64	8.39
PPDT2FBT	290	Yes	16.30	0.79	0.73	15.94	9.39	9.21

[a] J_{SC} [cal.], calculated J_{SC} from a EQE curve.
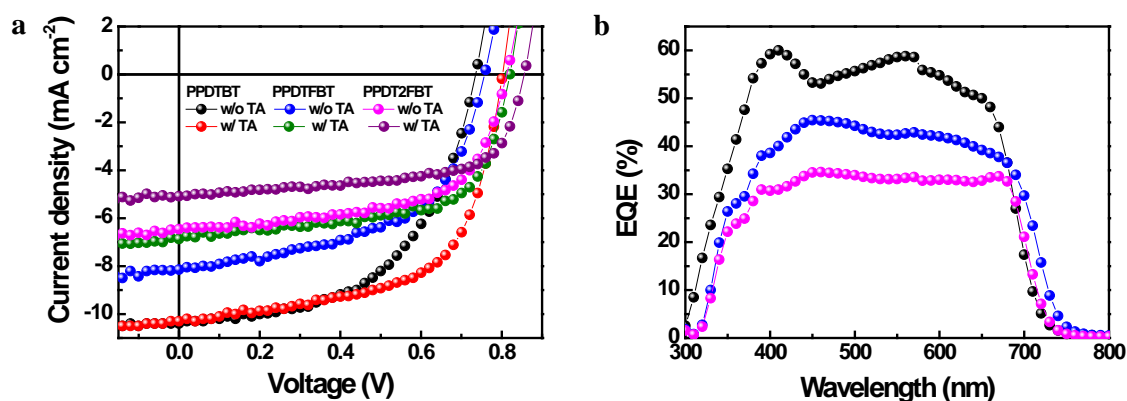
Figure 3.11. (a) *J-V* characteristics (w/o TA: without thermal annealing, w/ TA: with thermal annealing) and (b) EQE of polymer:PC$_{71}$BM PSCs prepared from a chlorobenzene solution without processing additives.

Table 3.7. Device characteristics of polymer:PC$_{71}$BM PSCs (solvent: chlorobenzene).

	Thermal annealing[a]	J_{SC} (mA/cm^2)	V_{OC} (V)	FF	PCE (%)
PPDTBT	No	10.40	0.74	0.54	4.13
	Yes	10.30	0.80	0.61	5.02
PPDTFBT	No	8.14	0.76	0.55	3.36
	Yes	6.87	0.82	0.64	3.58
PPDT2FBT	No	6.46	0.81	0.61	3.22
	Yes	5.08	0.86	0.64	2.78

PPDTBT:PC_{71}BM and PPDTFBT:PC_{71}BM devices showed the best PCE with a film thickness of ~170 nm. Interestingly, the PPDT2FBT blend film exhibited the best efficiency using a thick (290 nm) film (as shown in **Figure 3.12** and **Table 3.8**). **Figure 3.10a and b** show the J–V characteristics and external quantum efficiency (EQE) of the devices with DPE. **Table 3.6** summarizes the detailed photovoltaic parameters. The PPDT2FBT device showed the highest PCE of 8.64% with a J_{SC} of 15.73 mA cm^{-2}, V_{OC} of 0.78 V and FF of 0.71, reaching EQE values of over 80% in the range of 470– 550 nm with a maximum EQE of 82.5% at 490 nm (**Figure 3.10b**). These enhancements in J_{SC} and FF by the addition of DPE are closely related to the strong interchain ordering with the recovery of the strong shoulder peak (originating from strong intermolecular packing and/or π–π stacking) of polymer:PC_{71}BM blend films in UV-vis spectra (**Figure 3.13**). In addition, we also measured a remarkable temporal stability of PPDTFBT- and PPDT2FBT-blend films (in CB without DPE) at 130 °C for 200 h, compared to PPDTBT and P3HT based devices (**Figure 3.14a**). For devices with the processing additive (DPE), poor thermal stability was measured, showing a gradual decrease in PCE, compared to the devices without DPE (**Figure 3.14b**). It has been recognized previously that thermal treatment induces agglomeration with a concomitant decrease in device performance with processing additives. The solvent additive allows the components to remain partially dissolved, thus affecting the morphology and diffusion rate of fullerene molecules in the polymer matrix, and promoting the growth of fullerene agglomerates. This can accelerate phase separation between the polymer and fullerene moieties during heat treatment, adversely affecting device performance.[221]
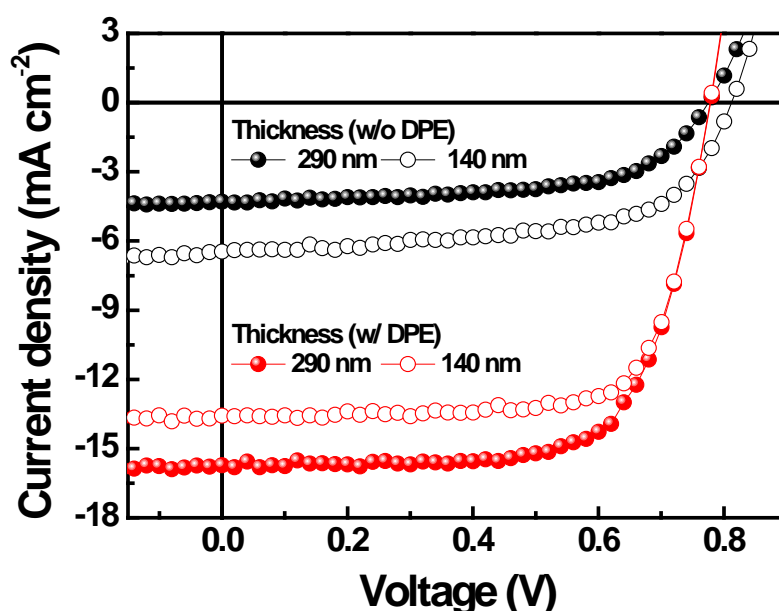
Figure 3.12. *J-V* characteristics of PPDT2FBT:PC_{71}BM PSCs with variable film thickness.

Table 3.8. Device characteristics of PPDT2FBT:PC$_{71}$BM PSCs with variable film thickness.

Polymer	DPE	Thickness of active layer (nm)	J_{SC} (mA cm^{-2})	V_{OC} (V)	FF	PCE (%)
PPDT2FBT	No	290	4.30	0.78	0.26	2.07
		140	6.46	0.81	0.61	3.22
	Yes	290	15.73	0.78	0.71	8.64
		140	13.57	0.78	0.74	7.79
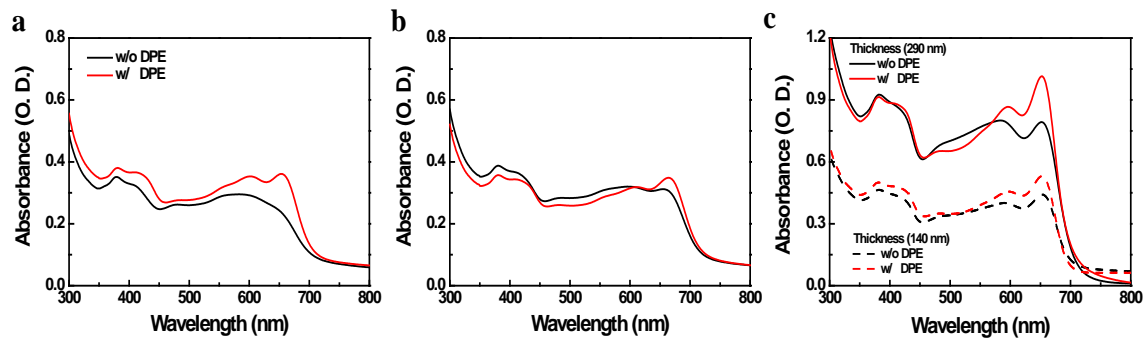
Figure 3.13. UV-vis absorption spectra of polymer:PC$_{71}$BM blend films based on (a) PPDTBT, (b) PPDTFBT and (c) PPDT2FBT. The films were prepared with CB (w/o DPE) and mixed CB:DPE (98 : 2 vol%, w/DPE) as a solvent.
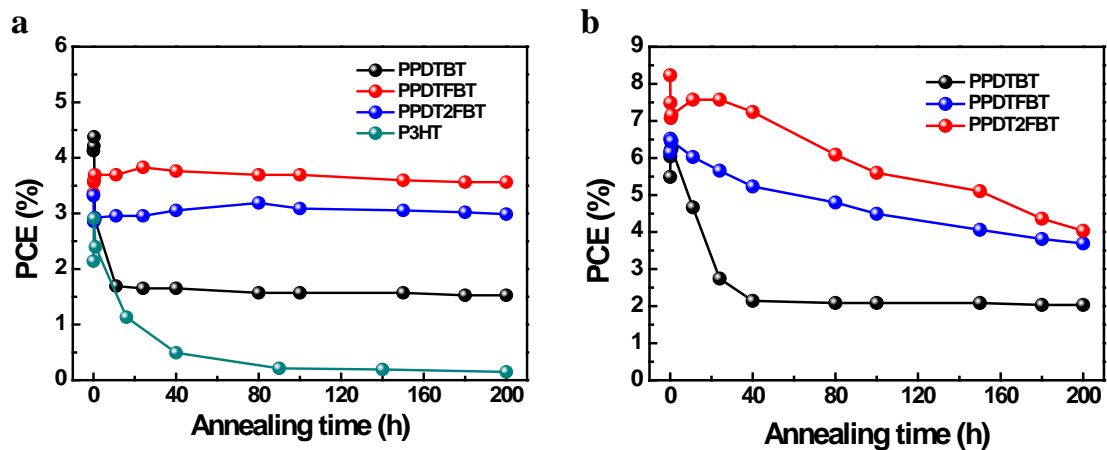
Figure 3.14. Temporal stability of polymer:PC$_{71}$BM PSCs (a) without and (b) with DPE at an annealing temperature of 130 °C for 200 h (P3HT-based device for comparison). All devices were prepared from chlorobenzene.

To further optimize the PPDT2FBT device, the top of the active layer was treated with methanol (MeOH). Solvent treatments can be an effective strategy for simultaneously enhancing all device parameters.[222, 223] **Figure 3.10c** and **10d** show J–V characteristics of optimized, MeOH treated, PPDT2FBT:PC$_{71}$BM devices as measured in our laboratory and certified by the Korea Institute of Energy Research (KIER), respectively. More than 50 devices were fabricated for device optimization. The best performing device exhibited a PCE of 9.39% (average PCE = 9.21%) with a J_{SC} of 16.30 mA cm^{-2}, V_{OC} of 0.79 V and FF of 0.73 (**Table 3.6**). The EQE values of these devices are above 80% in the range of 460–570 nm with a maximum EQE of 83.6% at 490 nm (inset of **Figure 3.10c**). The surface morphologies of PPDT2FBT:PC$_{71}$BM films with and without MeOH treatments were characterized by AFM (**Figure 3.15**). There were no observable changes in the AFM images, indicating that the effects of MeOH treatment do not arise from reconstruction of the film surface. Similar data and the detailed studies on the MeOH treatment effects have been reported previously. Bazan and Heeger et al. reported that MeOH treatment enhanced the photovoltaic efficiency by increasing the internal electric field and surface potential by Kelvin probe force microscopy (KPFM) and impedance measurements. Additionally, the series resistance decreased and the shunt resistance increased after methanol treatment, in good agreement with the observed improvements in J_{SC} and FF.[222, 223] A certified PCE of 8.78% was obtained by the KIER (**Figure 3.10d** and **3.16**) from a UV-epoxy encapsulated sample. This PCE was ~5% lower than the average PCE as measured in our laboratory, which could be attributed to non-ideal encapsulation.[79, 189] The certified results confirm that the measured PCE values of over 9%, as obtained in our laboratory, are reasonable.
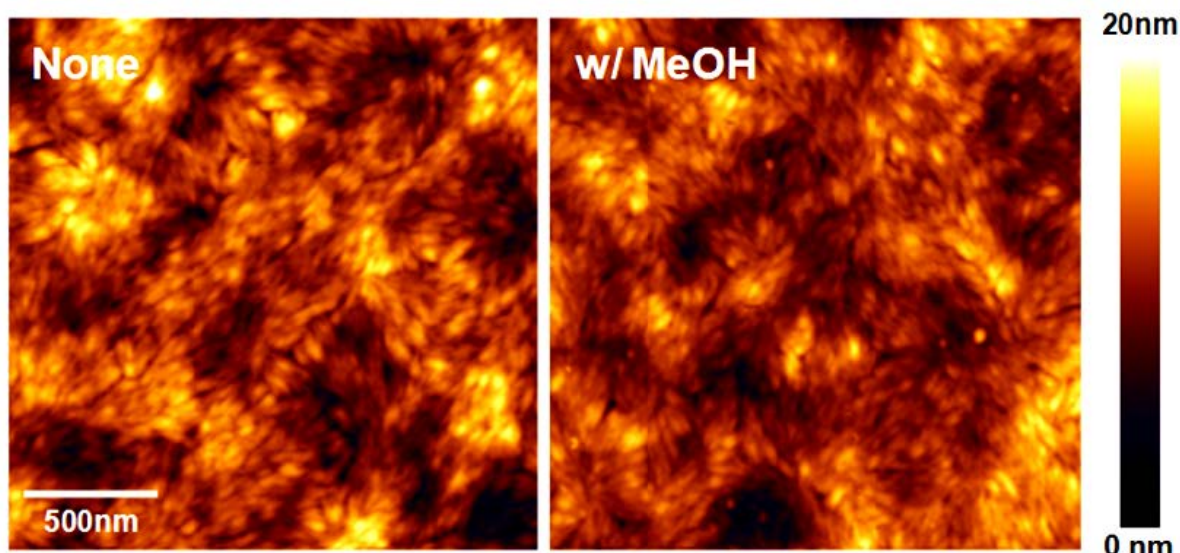
Figure 3.15. AFM topography images of PPDT2FBT:PC70BM without (left) and with (right) MeOH treatments. (solvent: CB:DPE, 98:2 vol%).
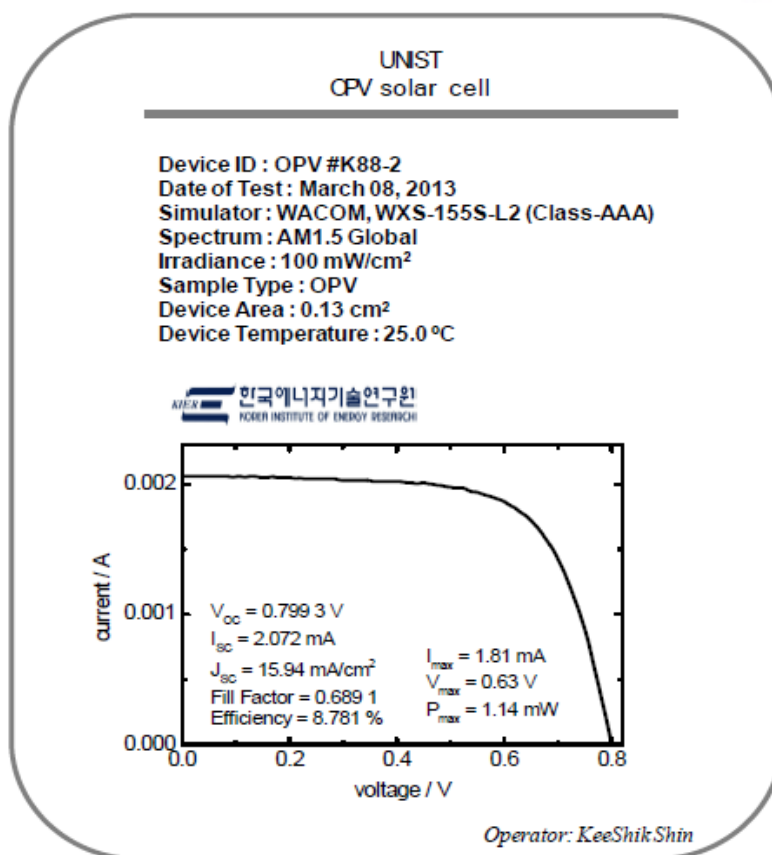
Figure 3.16. Photovoltaic data of PPDT2FBT:PC$_{71}$BM-based PSCs certified by KIER (solvent: CB:DPE (98:2 vol%), MeOH treatment on top of the active layer).

Furthermore, this work is the first report that showcases efficiency over 9% with a conventional type, 290 nm thick, single cell structure without any additional interfacial layer (**Table 3.9**). The high PCE and device thickness also suggest a meaningful approach for real commercial applications of PSCs. Although remarkable improvements in PCE have been reported in PSCs, the device thickness is on the order of ~100 nm. It is of great importance to develop photovoltaic materials which can function effectively at the greater film thickness. It is not currently viable to fabricate uniform and defect-free films on the order of 100 nm thickness using industrial solution casting techniques. Most previous PSCs showed that the performance degrades with the concomitant decrease in FF, with increasing film thickness. This must be closely related to space charge accumulation and charge recombination losses which become stronger with thicker films. It is noteworthy to emphasize that a ~300 nm thick active layer in the PPDT2FBT:PC$_{71}$BM device attenuates incident light almost completely without damage in the fill factor (0.71–0.73), showing a high J_{SC} of 15.7–16.3 mA cm^{-2}. These superior properties are closely related to the molecular structures and pronounced crystalline morphology in the film.

Table 3.9. Comparison of photovoltaic characteristics with previously reported high-efficiency PSCs.

Solvent (additive)[a]	Active layer	J_{SC} (mA cm^{-2})	V_{OC} (V)	FF	Best EQE (%)	Best PCE (%)	Ref.
CB (DIO)	PBDTTT-CF:PC$_{71}$BM	15.20	0.76	0.67	69	7.73	[7]
CB (DIO)	PTB7:PC$_{71}$BM	14.5	0.74	0.69	68	7.40	[8]
DCB (DIO)	PBDTTT-C-T:PC$_{71}$BM	17.48	0.74	0.59	75	7.59	[9]
CB (DIO)	PTDBD2:PC$_{71}$BM	13.0	0.89	0.65	-	7.60	[10]
DCB (DIO)	PBDTTT-ST:PC$_{71}$BM	16.35	0.69	0.66	75	7.81	[11]
DCB (DIO)	PBDT-TFQ:PC$_{71}$BM	17.90	0.76	0.58	86	8.00	[12]
CB (CN)	PBDTTPD:PC$_{71}$BM	12.60	0.97	0.70	N/A	8.50	[13]
CB (DPE)	PPDT2FBT:PC$_{71}$BM	15.73	0.78	0.71	82	8.64	Current work

[a]CB: chlorobenzene; DCB: *o*-dichlorobenzene; DIO: 1,8-diiodooctane; CN: 1-chloronaphthalene; DPE:diphenyl ether.
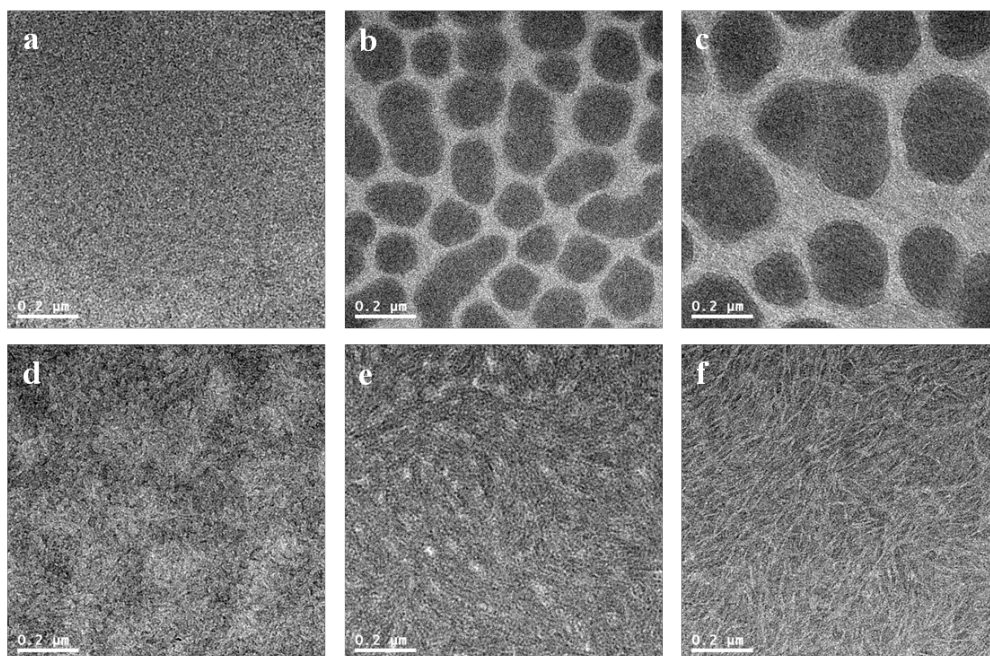
Figure 3.17. HR-TEM images of polymer:PC70BM films without (a–c) and with DPE (d–f). PPDTBT (a and d), PPDTFBT (b and e) and PPDT2FBT (c and f).

The nanoscale morphology of polymer:PC71BM blend films (in CB) was studied by high-resolution transmission electron microscopy (HR-TEM) and tapping mode AFM. In **Figure 3.17**, TEM images show large domains with diameters of 100–300 nm for the PPDTFBT and PPDT2FBT blend films fabricated without DPE, whereas the PPDTBT films show featureless morphologies. Macrophase separation in the PPDTFBT and PPDT2FBT blend films limits the probability for exciton dissociation by reducing donor/acceptor interfacial areas, leading to poor J_{SC} and FF values by charge recombination loss.[142, 191] In contrast, the blend films with DPE show a clear morphological change for all polymers, forming well-distributed nano-fibrillar structures where a bicontinuous interpenetrating network may be formed in BHJ films with PC71BM. These fibrillar structures are expected to enhance the charge-carrier mobility, J_{SC}, FF and the resulting photovoltaic performance of PSCs.[79, 224] Surface topography and phase images of the three blend films obtained from AFM measurements are consistent with morphologies observed in HR-TEM images (**Figure 3.18**).
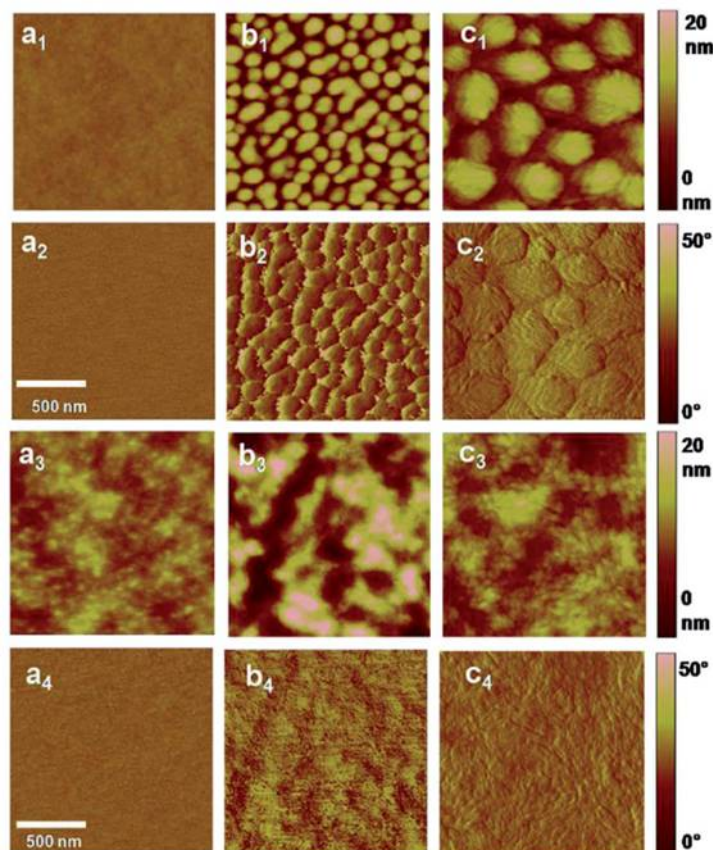
Figure 3.18. Tapping-mode AFM topography (a_1–c_1, a_3–c_3) and phase (a_2–c_2, a_4–c_4) images of polymer:PC$_{71}$BM blend films. Without DPE: PPDTBT (a_1 and a_2), PPDTFBT (b_1 and b_2) and PPDT2FBT (c_1 and c_2). With DPE: PPDTBT (a_3 and a_4), PPDTFBT (b_3 and b_4) and PPDT2FBT (c_3 and c_4). The size of all images is 1.5 mm x 1.5 mm.

In order to quantify charge carrier mobilities, hole-only (ITO/PEDOT:PSS/polymer:PC70BM/Au) and electron-only (FTO/polymer:PC$_{71}$BM/Al, FTO: fluorine-doped tin oxide) diodes were prepared[47] using optimized BHJ films (CB : DPE = 98 : 2 vol%) with various film thicknesses (200–1000 nm) and their *J–V* characteristics were analyzed by the space charge limited current (SCLC, J_{SCL}) method. The potential loss due to the series resistance of the ITO and the built-in potential were carefully considered in order to ensure accuracy in the measurements. The *J–V* characteristics show a quadratic dependence on voltage over a range of several volts and an inverse cubic dependence on the film thickness, consistent with the Mott–Gurney relationship (eqn (1)),[225, 226] where ε_0 is the free-space permittivity, ε_r is the dielectric constant of the semiconductor, μ is the mobility, V is the applied voltage and L is the thickness of the active layer.

$$J_{SCL} = 9\varepsilon_0\varepsilon_r\mu V^2/(8L^3) \tag{1}$$
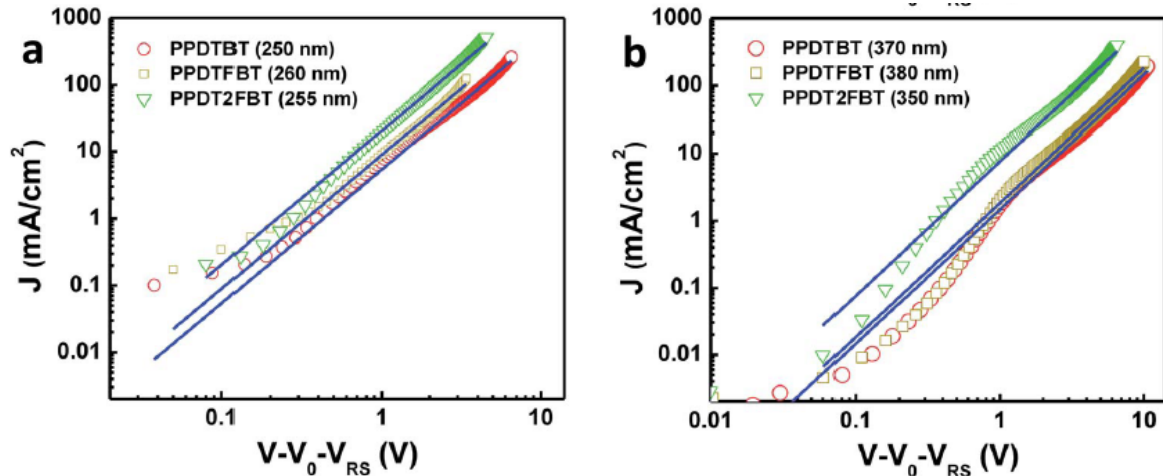
Figure 3.19. *J–V* characteristics of (a) hole- and (b) electron-only devices based on polymer:PC$_{71}$BM blend films (solvent: CB : DPE = 98 : 2 vol%). Blue lines represent fits of the curves using the Mott–Gurney relationship.

The average hole and electron mobilities were determined to be μ (hole) = 3.2 x 10^{-4}, 5.5 x 10^{-4} and 3.0 x 10^{-3} cm^2 V^{-1} s^{-1}, and μ (electron) = 2.8 x 10^{-4}, 4.2 x 10^{-4} and 1.5 x 10^{-3} cm^2 V^{-1} s^{-1} for PPDTBT, PPDTFBT and PPDT2FBT devices, respectively. Plots of films with similar thickness are found in **Figure 3.19**, while additional plots with films of various thicknesses are found in **Figure 3.20** and **Table 3.10**. All the polymers showed well balanced hole/electron mobility ratios in the range of 1–2 with various film thicknesses. PPDT2FBT showed ~1 order higher hole and electron mobilities relative to other two polymers. Notably, PPDT2FBT showed negligible changes in the carrier mobility even at ~1 μm film thickness. These SCLC results are consistent with the PCE data of PPDT2FBT,

showing no decrease in V_{OC} and FF with a 290 nm thick active layer, resulting in a high J_{SC} of 15.7–16.3 mA cm^{-2} due to the increased light absorption.
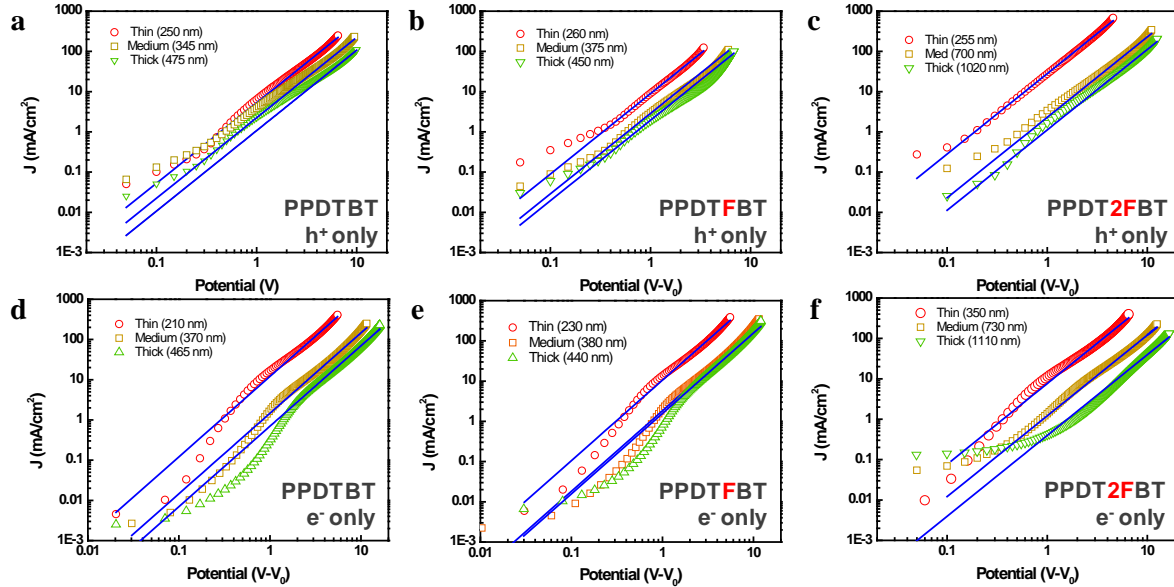
Figure 3.20. *J-V* characteristics of (a)~(c) hole-only and (d)~(f) electron-only devices based on polymer:PC$_{71}$BM blend films with various film thickness (solvent: CB:DPE = 98:2 vol%). Blue lines represent fits of the curves using the Mott-Gurney relationship.

Table 3.10. Electron and hole mobilities of electron- and hole-only devices based on polymer:PC$_{71}$BM films measured using a space-charge-limited current method.

Material	Hole-Only		Electron-Only		
	Film Thickness (nm)	μ_h (cm^2/Vs)	Film Thickness (nm)	μ_e (cm^2/Vs)	μ_h/μ_e
PPDTBT	250	2.7×10^{-4}	210	3.7×10^{-4}	0.7
	345	3.1×10^{-4}	370	2.4×10^{-4}	1.3
	475	3.8×10^{-4}	465	2.4×10^{-4}	1.6
PPDTFBT	260	5.4×10^{-4}	230	4.3×10^{-4}	1.3
	375	5.1×10^{-4}	380	3.7×10^{-4}	1.4
	450	6.0×10^{-4}	440	4.5×10^{-4}	1.3
PPDT2FBT	255	2.3×10^{-3}	350	1.1×10^{-3}	2.1
	700	2.6×10^{-3}	730	1.6×10^{-3}	1.6
	1020	4.0×10^{-3}	1110	1.8×10^{-3}	2.2

To further understand the detailed film morphology of the three polymers with/without PC$_{71}$BM and before/after additive treatments, the molecular arrangements and packing characteristics of the thin films were studied by grazing incidence wide angle X-ray scattering (GIWAXS).[223, 227, 228] **Figure 3.21** shows GIWAXS patterns for pristine polymer and polymer:PC$_{71}$BM blend films prepared from CB solutions with and without DPE. From the GIWAXS profiles, packing parameters were extracted and are listed in **Table 3.11**.
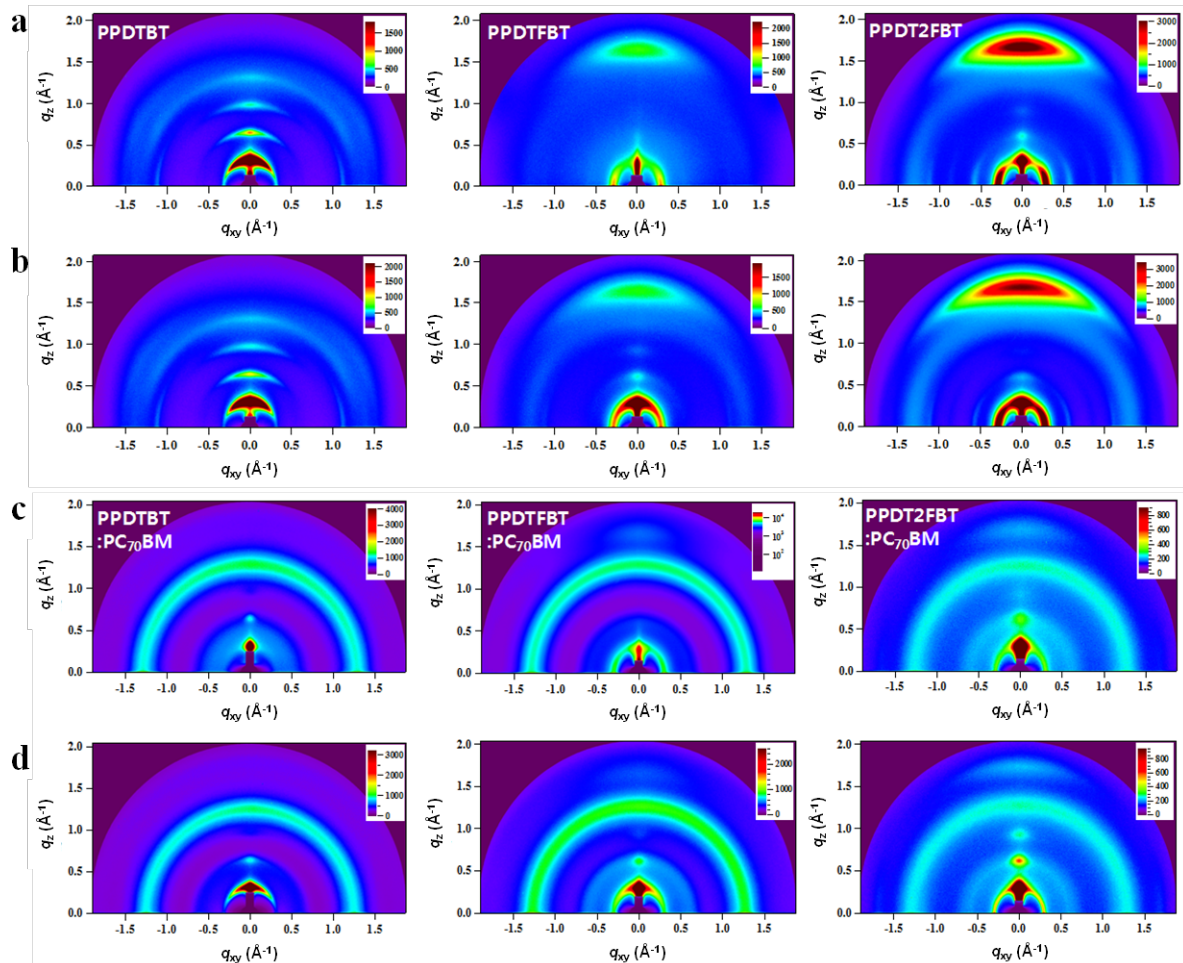
Figure 3.21. Grazing incidence wide angle X-ray scattering (GIWAXS) images. GIWAXS images of pristine polymer films (upper two rows) (a) without and (b) with DPE, and polymer:PC$_{71}$BM blend films (lower two rows) (c) without and (d) with DPE. Left, middle and right panels show the images for PPDTBT, PPDTFBT and PPDT2FBT, respectively.

Table 3.11. Packing parameters derived from GIWAXS measurements.

Films	Polymers	Additive (DPE)	Crystallographic parameters			
			Lamellar spacing		π-π stack (q_z direction)	
			q (Å^{-1})	d-spacing (Å)	q (Å^{-1})	d-spacing (Å)
Pristine polymer	PPDTBT	X	0.3324	18.9	-	-
		O	0.3312	19.0	-	-
	PPDTFBT	X	0.3035	20.7	1.6614	3.78
		O	0.3036	20.7	1.6706	3.76
	PPDT2FBT	X	0.3036	20.7	1.6873	3.72
		O	0.3000	20.9	1.6901	3.72
Polymer:PC$_{71}$BM blend	PPDTBT	X	0.3297	19.1	-	-
		O	0.3332	18.9	-	-
	PPDTFBT	X	0.3182	19.7	1.6925	3.71
		O	0.3178	19.8	1.7590	3.57
	PPDT2FBT	X	0.3164	19.9	1.7089	3.68
		O	0.3133	20.1	1.7514	3.59
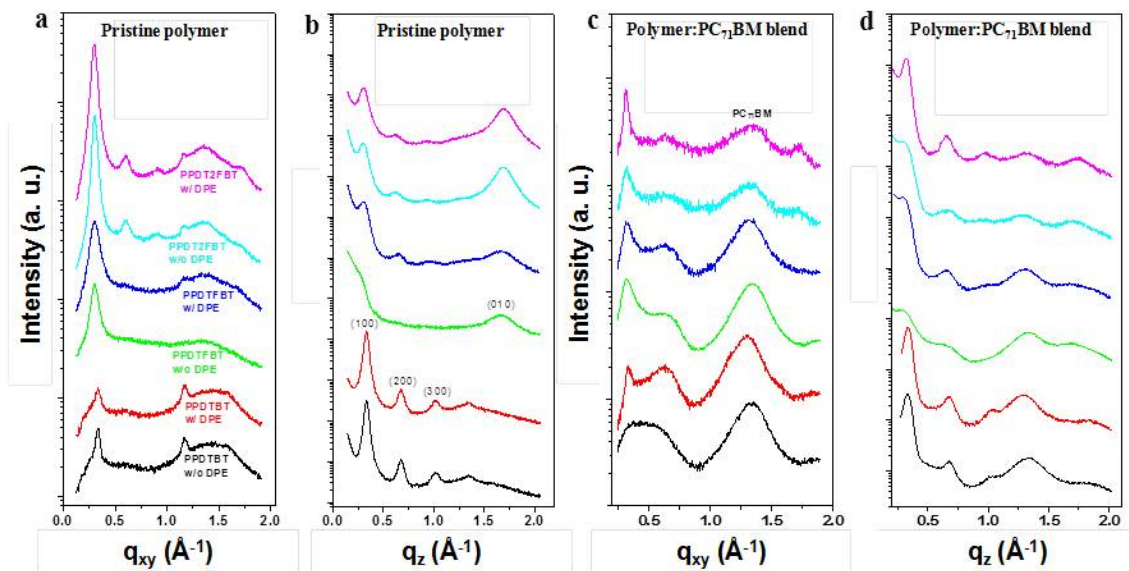
Figure 3.22. In-plane (a and c) and out-of-plane (b and d) GIWAXS data for pristine polymers (a and b) and polymer:PC$_{71}$BM (c and d) films with and without DPE.

Pronounced reflection peaks of (100), (200), and (300) in the out-of-plane direction were observed in the pristine PPDTBT film, showing a lamellar spacing of 18.9 Å (**Figure 3.21a** and **3.22**). For the pristine PPDTFBT and PPDT2FBT films, the lamellar spacing calculated from the (100) diffraction peak was slightly increased to 20.7 Å. On increasing the number of fluorine substituents on the BT unit, the in-plane lamellar diffraction peak was also intensified (strongest in PPDT2FBT). Therefore, the presence of fluorine atom may induce a face-on lamellar orientation coexisting with the edge-on lamellar stacks, which may facilitate an effective three-dimensional charge transport. The PPDTBT sample showed no π–π stacking (010) peak in the out-of-plane direction. Interestingly, the (010) peak (d = ~3.7 Å) in the out-of-plane direction becomes pronounced by the introduction of fluorine substituents. The π–π stacking distance was shorter in PPDT2FBT (3.72 Å) than in PPDTFBT (3.78 Å), which indicates a stronger cofacial interchain orientation between the neighboring chains. Upon addition of DPE to the pristine polymer films, similar trends were observed with increased scattering intensity, indicating more pronounced interchain orientation with DPE. The GIWAXS patterns of polymer:$PC_{71}BM$ blend films are shown in **Figure 3.21c** and **d**. The lamellar spacing for polymer:$PC_{71}BM$ blend samples was measured to be 19.1–19.9 Å for the three structures, showing similar spacings in the pristine polymer films. Upon addition of DPE, the diffraction patterns are clearer without noticeable changes in the lamellar spacing. We also observed a further reduction in the π–π stacking distance (3.57–3.59 Å) for the PPDTFBT:$PC_{71}BM$ and PPDT2FBT:$PC_{71}BM$ films with DPE, indicating an intensified interchain orientation upon addition of DPE. Interestingly, the blend films with DPE show shorter π–π stacking distances than those of the pristine polymers (PPDTFBT: 3.78 Å and PPDT2FBT: 3.72 Å). The solvent additive allows the components to remain partially dissolved and affects the morphology and diffusive rate of $PC_{71}BM$ in the polymer matrix. This may allow a longer time for polymer chains to self-organize into highly ordered intermolecular structures.[229]

3.4 Conclusion

In summary, a series of dialkoxyphenylene-BT containing semicrystalline LBG polymers were synthesized with noncovalent conformational locking to enhance chain planarity, intermolecular ordering and thermal stability without losing solution processability. The polymers formed well-distributed interpenetrating nano-fibrillar networked morphologies with $PC_{71}BM$, showing well-balanced hole and electron mobilities. Notably, PSCs based on these polymers exhibited PCEs of up to 9.39% in a 290 nm thick conventional single-cell device structure without any additional interfacial layer. The thick active layer (290 nm) in the $PPDT2FBT:PC_{71}BM$ device enabled strong light absorption, yielding a high J_{SC} of 15.7–16.3 mA cm^{-2} without the loss in V_{OC} and FF. It is of great importance to develop photovoltaic materials which can function effectively at the thicker film which can absorb solar light completely and is viable to be produced using industrial solution processing techniques. These remarkable device characteristics with the great thickness are closely related to the highly ordered organization of polymer chains via noncovalent attractive interactions, showing nano-fibrillar structures in TEM with tight interchain packing (a π–π stacking distance of 3.57–3.59 Å) in the blend films. In addition, we also measured clear molecular weight dependence on the photovoltaic properties. We synthesized more than 20 batches of PPDT2FBT to optimize the photovoltaic characteristics. Among them, the high molecular weight batches (with ~40 kDa) showed the PCE over 8–9% but small molecular weight batches showed the relatively lower PCE values (~7%). The detailed study on the molecular weight dependence is now under investigation. Furthermore, this work also demonstrates a high PCE of over 7% (without any post-treatments) with long-term thermal stability at 130 °C for ~200 h. These new polymers provide a great possibility to overcome the efficiency barrier of 10% and accelerate the real application of plastic solar cells.

Chapter 4. Photocurrent Extraction Efficiency Near Unity in a Thick Polymer Bulk Heterojunction

4.1 Research background

Polymeric bulk heterojunction (BHJ) solar cells have the potential to revolutionize the solar industry due to their low cost and ability to be processed like inks.[140, 230] While organic BHJ films are able to deliver substantial power conversion efficiencies using films as thin as 100 nm,[3-7] it is nonetheless of vital importance to develop materials which are able to function effectively at greater film thicknesses. The need for thicker active layers is an often overlooked, but important consideration,[140, 231, 232] for the future commercialization of organic solar technologies. Although organic semiconductors exhibit large absorption coefficients, it is impossible to completely absorb incident sunlight using 100 nm thick films[233]; thus a significant amount of energy is lost as light passes through films which are too thin. Using films on the order of 250-300 nm, however, allows nearly complete attenuation of incident light[i]. Additionally, the production of defect-free films with ~100 nm thickness is not currently possible using industrial solution coating equipment,[140, 231] posing intractable problems from a manufacturing perspective. Again, this problem can be resolved using thick active layers.

In practice, most reported BHJ systems achieve optimal performance using films close to 100 nm thick, corresponding to the first constructive interference maximum in the active layer.[231, 233, 234] There are a number of reasons why performance degrades for thicker BHJ films including low charge carrier mobilities, space charge accumulation and charge carrier recombination losses which all become stronger with thicker films[233, 235, 236] and preclude thick active layers in most BHJ materials.

Here, we have investigated the unique properties of the photovoltaic polymer poly[(2,5-bis(2-hexyldecyloxy)phenylene)-alt-(5,6-difluoro-4,7-di(thiophen-2-yl)benzo[c][1,2,5]thiadiazole)] (PPDT2FBT)[237], which exhibits optimal performance using exceptionally thick films. Unlike the widely studied polymers poly-3-hexylthiophene (P3HT), PCDTBT[75] and PTB7,[142] we found that this system closely tracked theoretical short circuit current (J_{SC}) generation as the active layer thickness approached 1 μm in both conventional and inverted architectures. The structures of PPDT2FBT and PC$_{71}$BM are shown in **Figure 4.1a**, together with the conventional (**Figure 4.1b**) and inverted device architectures used in this study (**Figure 4.1c**). Optimal current density – voltage (*J-V*) curves and external quantum efficiency plots of PPDT2FBT:PC$_{71}$BM devices are shown in **Figure 4.1d and 1e**, respectively, corresponding to devices with active layer thicknesses of 290 nm (conventional) and 260 nm (inverted).

4.2 Experimental

Materials: Poly(3,4-ethylenedioxythiophene):poly(4-styrenesulfonate) (PEDOT:PSS) (Baytron AI 4083 and PH500) was purchased from H. C. Starck (Germany). Regio-regular P3HT (Medium M_W 55,000 g/mol) was purchased from Rieke Metals, Inc. [6,6]-phenyl-C61-butyric acid methyl ester ($PC_{61}BM$)   and [6,6]-phenyl-C71-butyric acid methyl ester ($PC_{71}BM$) were purchased from Electronic Materials (EM) Index Co., Ltd. Poly[[4,8-bis[(2-ethylhexyl)oxy]benzo[1,2-b:4,5-b']dithiophene-2,6-diyl][3-fluoro-2-[(2-ethylhexyl)carbonyl]thieno[3,4-b] thiophenediyl]] (PTB7) and poly[N-9′-heptadecanyl-2,7-carbazole-alt-5,5-(4′,7′-di-2-thienyl-2′,1′,3′-benzothiadiazole)] (PCDTBT) were purchased from 1-material (Canada). Poly[(2,5-bis(2-hexyldecyloxy)phenylene)-alt-(5,6-difluoro-4,7-di(thiophen-2-yl)benzo[c][1,2,5]-thiadiazole)] (PPDT2FBT) was synthesized according to reference.[237]

Instruments: Transmission electron microscopy (TEM) images were obtained using a JEOL JEM-2100 transmission electron microscope operated at 200 kV. UV-vis spectra were measured using a Varian Carry 5000 spectrophotometer in the range 300 to 1200 nm with 1 nm resolution. Atomic force microscopy (AFM) images were collected using a Veeco Multimode microscope with 300 kHz silicon tips operating in tapping mode. UV-Vis total reflectance was measured using a Varian Cary 5000 spectrophotometer equipped with a specular reflectance assembly.

Optical Simulations: Optical constants of ITO, PEDOT and ZnO layers were calculated from ellipsometric data in the range of wavelengths from 370 to 1200 nm. Optical constants for Al, Au and MoO_3 were taken from the literature.[238] For bulk heterojunction films, **n** and **k** values were calculated from absorption coefficients (α) of each film using the Kramers-Kronig relationship.[239] Transfer matrix simulations were performed using a modified Matlab script introduced by Burkhard, *et al.*.[240] For each material, α values were calculated based on the average absorption spectra taken from films with four different thicknesses. The thickness of each film was taken as the average of 9 measurements using a recently calibrated atomic force microscope. Bulk heterojunction films were observed to vary in thickness by approximately 5% between different locations on the same film. To account for this, transfer matrix simulations were taken as the average of 3 calculations for optical stacks in which the active layer thickness was varied by + 5% and - 5%, resulting in a better match between simulated active layer absorption and the observed EQE. To correct for absorption tails in α which extend well beyond the absorption onset (caused by scattering effects, etc.), the absorption onset of each material was fit with a Gaussian curve resulting in an accurate match between the calculated onset of light absorbed in the active layer and the onset observed in the EQE.

Fabrication and characterization of solar cells: Devices were fabricated according to the following procedures. First, the glass/ITO substrates were cleaned with detergent, then ultra-sonicated in acetone and isopropyl alcohol and subsequently dried in an oven overnight at 100 °C. PEDOT:PSS

hole transport layers were spin-coated (after passing through a 0.45 µm cellulose acetate syringe filter) at 5000 rpm for 40s followed by baking at 140 °C for 15 min in air and then moved into a glove box. For deposition of the active layer, blend solutions of PPDT2FBT (1 wt%):$PC_{71}BM$ (1.5 wt%) dissolved in CB (with 2 vol% diphenylether), P3HT (2.5 wt%): $PC_{61}BM$ (2 wt%) dissolved in DCB, PCDTBT (1.2 wt%):$PC_{71}BM$ (4.7 wt%) dissolved in DCB, and PTB7 (1.2 wt%):$PC_{71}BM$ (1.8 wt%) (with 3 vol% 1,8-diiodooctane) were spin-cast on top of the PEDOT:PSS layer in a nitrogen-filled glove box. The device was pumped down in vacuum ($< 10^{-6}$ torr; 1 torr $\sim$ 133 Pa), and a 100 nm thick Al electrode for conventional architecture or a 80 nm thick Au electrode for inverted architecture was deposited on top of the active layer by thermal evaporation. The deposited Al or Au electrode area defined the active area of the devices as 13 mm^2. Measurements were carried out with the solar cells inside the glove box by using a high quality optical fiber to guide the light from the solar simulator equipped with a Keithley 2635A source measurement unit. *J-V* curves for devices were measured under AM 1.5G illumination at 100 $mWcm^{-2}$ using an aperture to define the illuminated area. EQE measurements were conducted in ambient air using an EQE system (Model QEX7) by PV measurements Inc. (Boulder, Colorado).

Two dimensional-grazing incident wide angle X-ray scattering (2D-GIWAXS): GIWAXS measurements were carried out at the PLS-II 9A U-SAXS beam line of Pohang Accelerator Laboratory, Korea. An X-ray beam from the in-vacuum undulator (IVU) was monochromated ($E_k = 11.24$ keV, $\lambda = 1.103$ Å) using a Si(111) double crystal monochromator and focused horizontally and vertically at the sample position (450 (H) × 60 (V) μm^2 in FWHM) using K-B-type focusing mirror system. The GIWAXS sample stage was equipped with a 7-axis motorized stage for the fine alignment of the thin sample and the incidence angle of X-rays was adjusted to 0.12º–0.14º. GIWAXS patterns were recorded with a 2D CCD detector (Rayonix SX165, USA) and X-ray irradiation time was 0.5–5 s depending on the saturation level of the detector. The diffraction angle was calibrated using a pre-calibrated sucrose crystal (monoclinic, P21, $a = 10.8631$ Å, $b = 8.7044$ Å, $c = 7.7624$ Å, $\square\square=$ 102.938°) and the sample-to-detector distance was approximately 232 mm. Samples for GIWAXS measurements were prepared by spin-coating polymer:$PC_{71}BM$ blend solutions on top of Si substrates.

Transient photocurrent (TPC) measurements: TPC measurements were carried out with a custom built, fully-automated setup. A Stanford Research Systems NL100 nitrogen laser with an attached Rhodamine 6G dye cell provided the excitation source with 4 ns wide, $\lambda = 590$ nm pulses and a repetition rate of 10 Hz. A set of computer controlled variable neutral density filters regulated the incident light intensity, and a 50/50 beam splitter simultaneously sent every pulse to a Coherent J-10Si-le energy sensor as well as the solar cell under test. Active monitoring of the fluence of every pulse allowed a typical measurement to consist of 500 current transients averaged together, where no pulse deviated by more than 2% from the target fluence of 0.05 $\mu J/cm^2$. The external voltage bias was

applied to the cell with an Agilent 33519B waveform generator operating in DC mode, connected to the cell through a wideband bias tee. The time-resolved photocurrent was recorded with a Tektronix DPO3034 oscilloscope by measuring the voltage drop across a 5 ohm RF sensor resistor in series with the solar cell.

.

4.3 Results and discussion
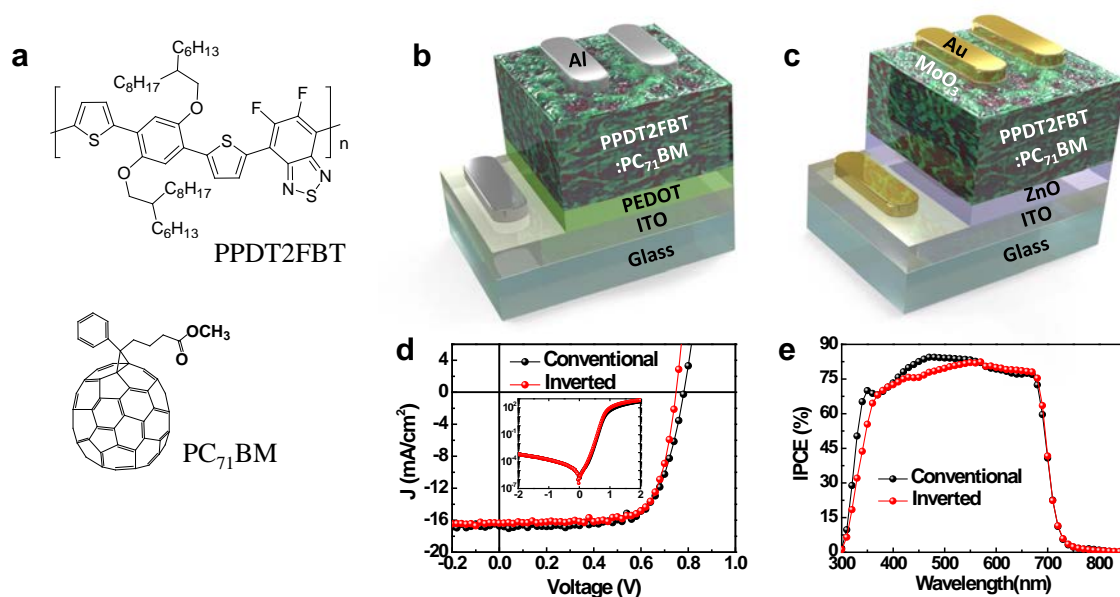
Figure 4.1. Materials and schematic device architectures. (**a**) Molecular structures of PPDT2FBT and PC$_{71}$BM. (**b** and **c**) Conventional and inverted solar cell architectures, respectively. The top and side surface textures are constructed from re-colored AFM and cross-sectional TEM data, respectively. (**d** and **e**) Current density-voltage characteristics and incident photon conversion efficiency (IPCE), respectively, of optimized PPDT2FBT:PC$_{71}$BM devices in conventional and inverted BHJ solar cells; the inset shows the dark currents for each device.

The effects of thickness on the solar cell characteristics of the polymers P3HT, PCDTBT and PTB7 were investigated compared to PPDT2FBT. For each material a suite of solar cell devices with thicknesses in the range of 35 to 450 nm was prepared in both conventional and inverted architectures. An estimate of the maximum obtainable J_{SC} was made based on the optical properties of each device (J_{opt}), assuming each photon absorbed in the active layer can be extracted as an electron-hole pair. The amount of light absorbed by each active layer was calculated based on the optical constants of each material via transfer matrix modeling (**Figure 4.2**).

Table 4.1. Characteristics of solar cells based on PPDT2FBT, P3HT, PCDTBT and PTB7.

Material	Geometry	Thickness (nm)	J_{SC} (mA cm-2)	V_{OC} (V)	FF	BEST PCE (%)	Average PCE (%)
PPDT2FBT	Conventional	290	16.72	0.78	0.69	9.07	8.84±0.23
		1150	15.40	0.74	0.54	6.15	6.11±0.04
	Inverted	260	16.37	0.75	0.73	8.91	8.78±0.13
		1050	15.66	0.67	0.53	5.58	5.54±0.04
P3HT	Conventional	170	9.35	0.55	0.64	3.32	3.21±0.11
	Inverted	210	10.20	0.54	0.63	3.49	3.34±0.15
PCDTBT	Conventional	85	10.20	0.90	0.54	4.98	4.83±0.15
	Inverted	80	8.10	0.89	0.58	4.22	3.93±0.29
PTB7	Conventional	100	16.39	0.74	0.66	8.06	7.88±0.18
	Inverted	90	14.14	0.74	0.68	7.05	6.76±0.29
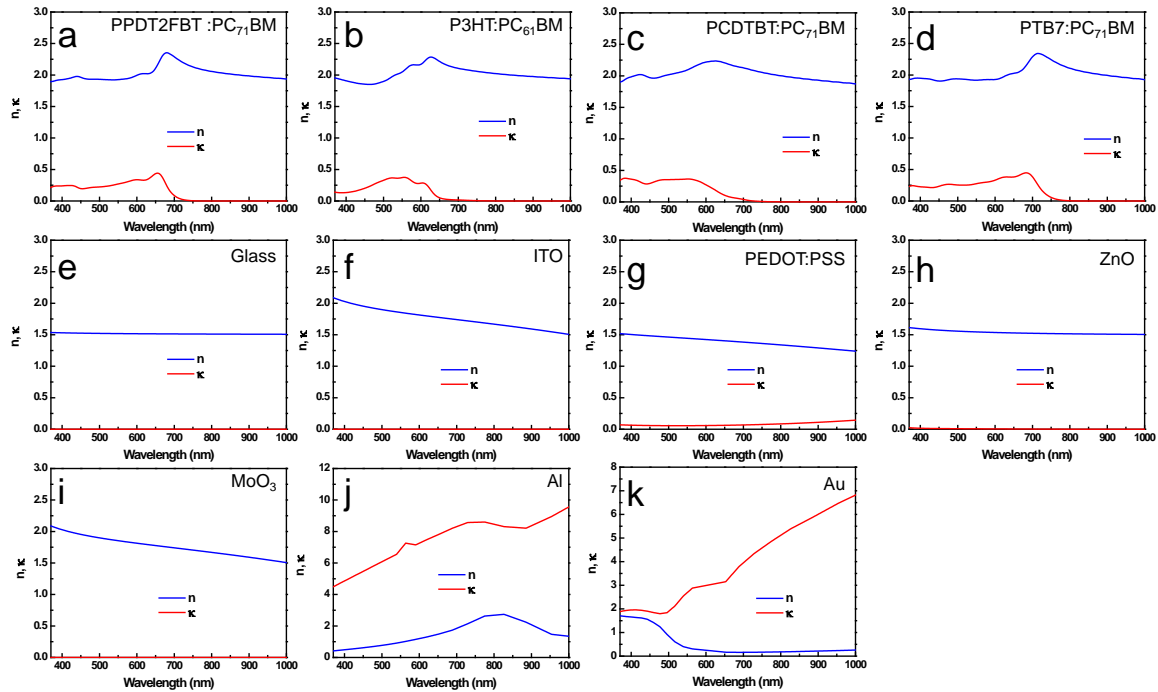
Figure 4.2. Optical constants. n and κ values used for (a) PPDT2FBT:PC$_{71}$BM, (b) P3HT:PC$_{61}$BM, (c) PCDTBT:PC$_{71}$BM, (d) PTB7:PC$_{71}$BM, (e) glass, (f) ITO, (g) PEDOT:PSS, (h) ZnO, (i) MoO$_3$, (j) Al and (k) Au. Blue traces represent n values while red traces represent κ values.

Exceptional care was taken in measuring the extinction coefficients and thicknesses of the active layer materials in order to make photocurrent estimates as accurate as possible. Plots of J_{opt} and

observed J_{SC} values vs film thickness are reported in **Figure 4.3**, while optimal device characteristics are summarized in **Table 4.1** and the effects of thickness on other device parameters are summarized in **Figure 4.4**.

Figure 4.3. Observed J_{SC} compared to theoretical maximum photocurrent. (a and e) show data for PPDT2FBT; (b and f) show data for P3HT; (c and g) show data for PCDTBT; (d and h) show data for PTB7. (a to d) show data for conventional devices while (e to h) show data for inverted devices. Optically modeled currents appear as red and blue solid lines in conventional and inverted architectures, respectively, while observed J_{SC} values are plotted as blue-green circles.

Figure 4.4. Solar cell parameters vs. active layer thickness. (a) Ratio of observed J_{SC} (J_{OBS}) to optically modeled J_{SC} (J_{OPT}) (spectrally averaged IQE), (b) Fill factor, (c) power conversion efficiency observed for PPDT2FBT:PC$_{71}$BM (blue), P3HT:PC$_{61}$BM (red), PCDTBT:PC$_{71}$BM (purple) and PTB7:PC$_{71}$BM (green).

For each device, J_{opt} increases with thickness and exhibits local maxima where constructive interference between incident light and reflected light coincides with absorption bands in the active layer. As the active layer becomes thicker, most of the incident light is absorbed before being reflected and interference effects become smaller, causing the plots to flatten out and approach a maximum value based on the absorption onset of each material. In all cases, the active layers absorb additional light as the film thickness exceeds the first and second constructive maxima, however, PCDTBT and PTB7 exhibit peak performance with thin active layers near the first maximum (80 – 100 nm). Among the four materials, PPDT2FBT followed J_{opt} most closely in both the conventional and inverted architectures and showed the lowest decrease in FF, leading to the highest PCE and greatest optimal active layer thickness. In contrast P3HT, PCDTBT and PTB7 showed pronounced decreases in performance as film thicknesses reached 300 nm.
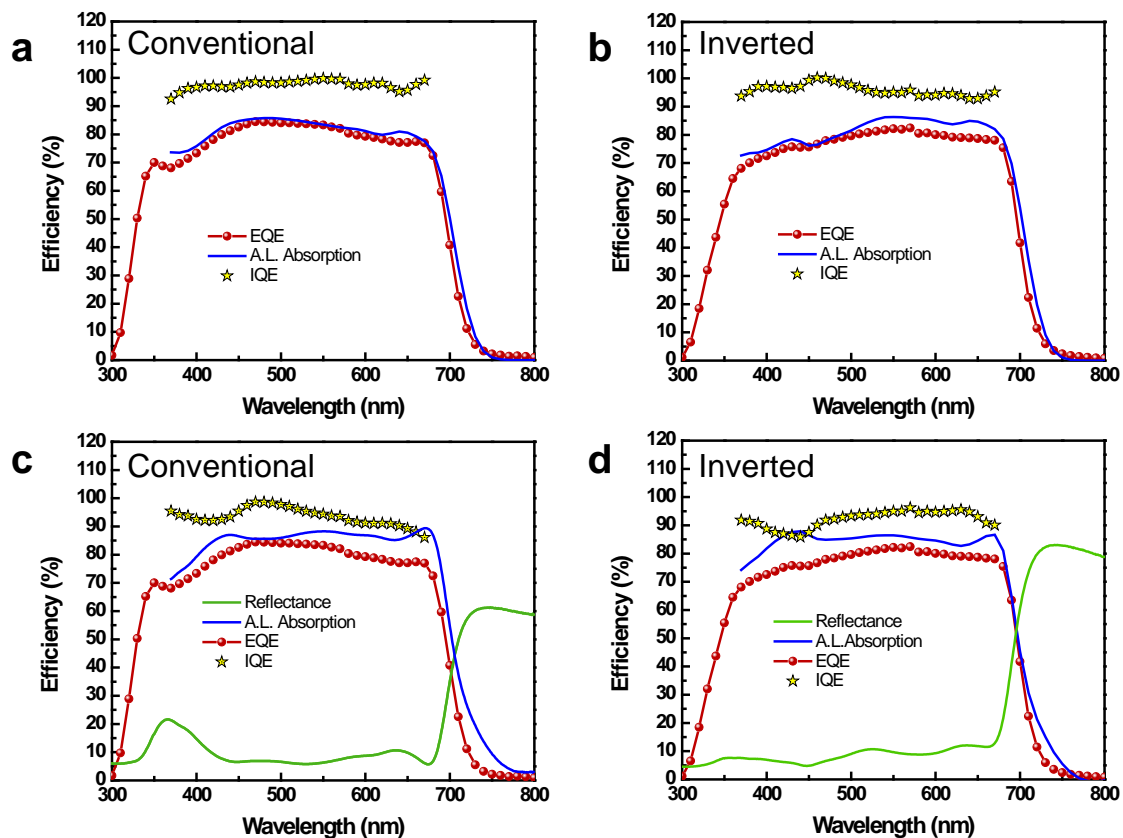
Figure 4.5. Internal Quantum Efficiency for Conventional and Inverted Type PPDT2FBT Devices. Plots of external quantum efficiency (red lines / spheres), active layer absorption (blue trace) and internal quantum efficiency (yellow stars) for devices (**a**) in the conventional architecture and (**b**) in the inverted architecture calculated based on optical constants alone. (**c**) and (**d**) show internal quantum efficiencies calculated from active layer absorptions derived from reflectance spectra (green traces) with corrections for parasitic absorption.

Comparing the number of photons absorbed in the active layer (J_{opt}) to the observed J_{SC} provides an estimate of the efficiency with which charges can be extracted from a solar cell. Thus, the ratio J_{SC} / J_{opt} estimates the average internal quantum efficiency (IQE) of the device.[76] Spectrally resolved J_{SC} / J_{opt} (IQE derived via transfer matrix alone) of optimized PPDT2FBT devices were calculated and compared to IQEs calculated from reflectance data (**Figure 4.5**)[240], showing good agreement. PPDT2FBT exhibits a J_{SC} / J_{opt} of 97.6% for optimized devices (290 nm) in the conventional architecture and 95.9% for optimized devices (270 nm) in the inverted architecture, while average IQEs of 93.5% and 92.2% were obtained for the same devices in conventional and inverted architectures, respectively.
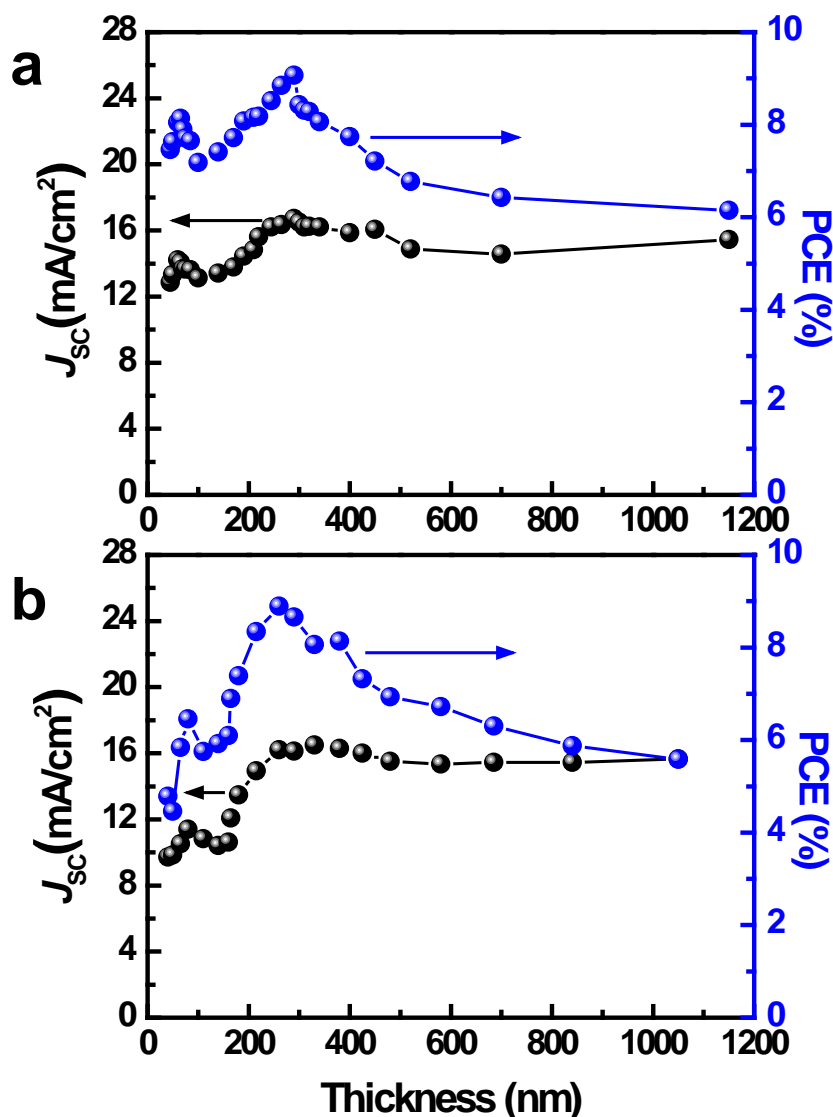
Figure 4.6. Solar cell parameters vs. active layer thickness. Power conversion efficiency and J_{SC} observed for PPDT2FBT:PC$_{71}$BM in (**a**) conventional and (**b**) inverted architectures with different active layer thickness (from 40 nm to over 1000 nm).

PPDT2FBT BHJs greater than 1000 nm thick were prepared in order to determine the thickness at which performance degrades significantly. These device characteristics are summarized in **Table 4.1**, while plots of J_{SC} and PCE for film thicknesses in the range of 300-1200 nm are shown in **Figure 4.6**. We found that the J_{SC} decreased only slightly as film thickness increased from 300 to 1200 nm, remaining in the range of 15 - 16 mA cm^{-2} in conventional devices or 14.5 - 16 mA cm^{-2} in the case of inverted devices. Conventional devices with active layer thickness of 1150 nm were found to yield a PCE of 6.15% while inverted devices of 1050 nm thickness produced a PCE of 5.58%. To our knowledge, this material is among few organic BHJ materials known to function effectively with active layer thicknesses over 1 μm and currently the most efficient.
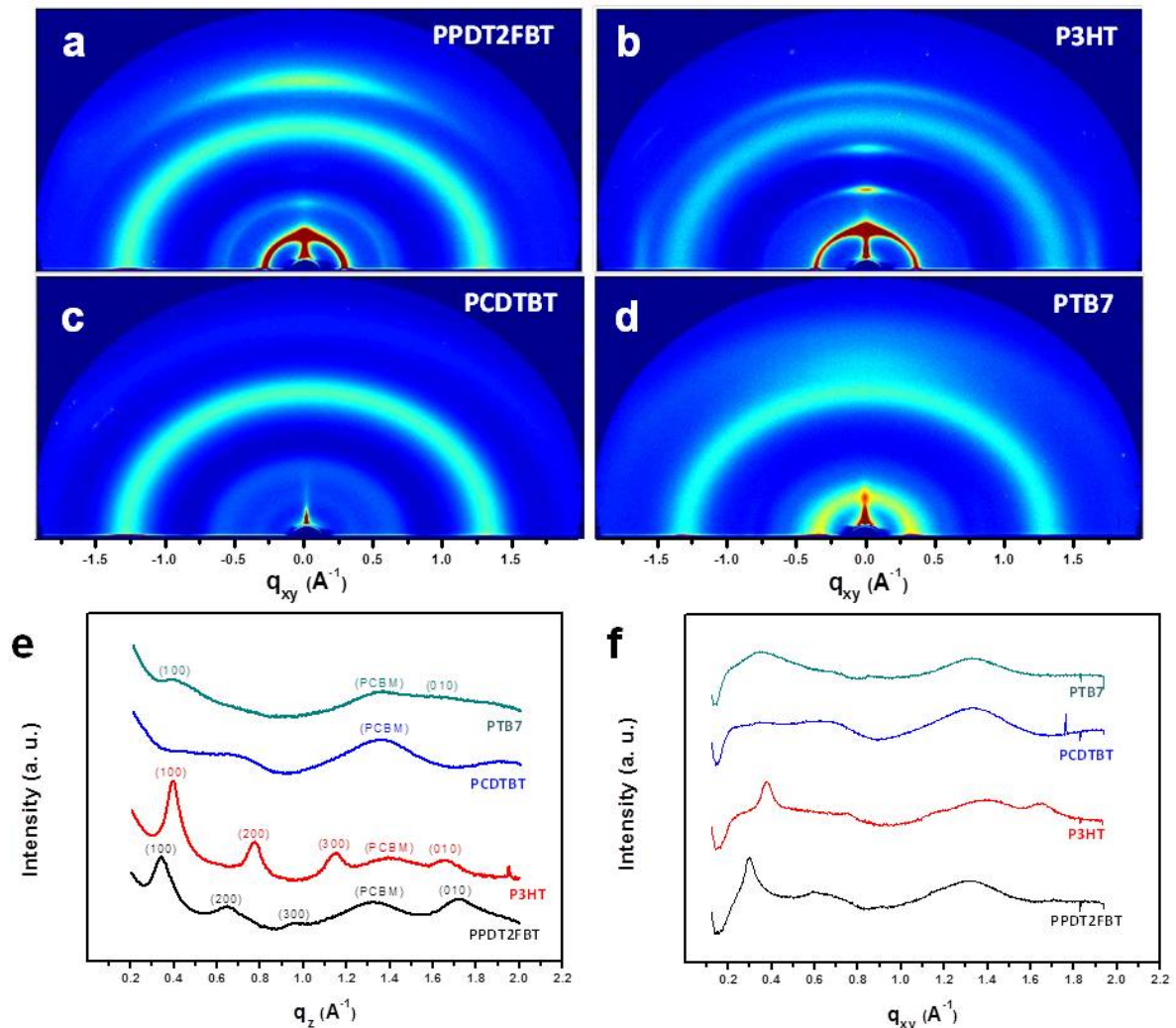
Figure 4.7. Grazing incidence wide angle X-ray scattering plots. (a) PPDT2FBT:PC_{71}BM, (b) P3HT:PC_{61}BM, (c) PCDTBT:PC_{71}BM and (d) PTB7:PC_{71}BM. Cross sectional profiles in the out-of-plane (e) and in-plane (f) directions.

Table 4.2 . Packing parameters derived from GIWAXS measurements.

Crystallographic parameters		PPDT2FBT	P3HT	PCDTBT	PTB7
(100) Lamellar spacing	q (Å^{-1})	0.3402	0.3960	0.3881	0.3880
	d-spacing (Å)	18.47	15.87	16.19	16.19
π-π stack from q_{xy} profile	q (Å^{-1})	-	1.6504	-	-
	d-spacing (Å)	-	3.81	-	-
π-π stack from q_z profile	q (Å^{-1})	1.7173	1.6570	-	1.5907
	d-spacing (Å)	3.66	3.79	-	3.95

The performance of BHJ solar cells is strongly correlated to the internal structure of the donor and acceptor materials.[241, 242] The packing and physical structure of the films were studied via grazing incidence wide angle X-ray scattering (GIWAXS), atomic force microscopy (AFM) and cross-sectional transmission electron microscopy (TEM). The ability of PPDT2FBT and P3HT to generate increasing photocurrent without suffering a decrease in FF (**Figure 4.4b**) in thick films appears to be correlated to the semi-crystalline nature of these polymers, which is evident in the clear lamellar and π-π stacking scattering peaks exhibited by these polymers (**Figure 4.7**). Notably, PPDT2FBT shows strong π-π stacking predominantly in the vertical direction, with the shortest π-π stacking distance of 3.66 Å (**Table 4.2**). Atomic force microscopy (AFM) was used to probe the surface structure of the PPDT2FBT:PC$_{71}$BM BHJ, (**Figure 4.9-4.16**), revealing radiating fibril-like structures on PPDT2FBT film surfaces. These features were not observed in P3HT, PCDTBT or PTB7, however, are strikingly similar to surface features of another polymer which exhibits peak performance using a thick (220 nm) active layer.[232]

The internal structure of PPDT2FBT:PC$_{71}$BM was investigated by TEM using cross-sectional specimens of optimized PPDT2FBT devices. These images are reported in **Figure 4.8**. Similar images for P3HT, PCDTBT and PTB7 devices can be found in **Figure 4.17-4.19**. **Figures 4.8a and 8d** show the entire device stack with layers corresponding to Glass/ITO/PEDOT:PSS/PPDT2FBT:PC$_{71}$BM/Al and Glass/ITO/ZnO/PPDT2FBT:PC$_{71}$BM/ MoO$_3$/Au for the conventional and inverted architectures, respectively. Wispy features are apparent in the active regions of both conventional and inverted architectures. High-angle annular dark-field (HAADF) images (**Figure 4.8f and8 g**) confirmed the structural features observed in the bright-field images. The distribution of sulfur in the active layer was quantified by energy dispersive X-ray spectroscopy (EDS), revealing a relatively uniform distribution of sulfur throughout the active layer, indicating an isotropic distribution of donor and

acceptor phases through the film thickness and demonstrating that the high FF observed in this system was not due to vertical phase gradation.[229]
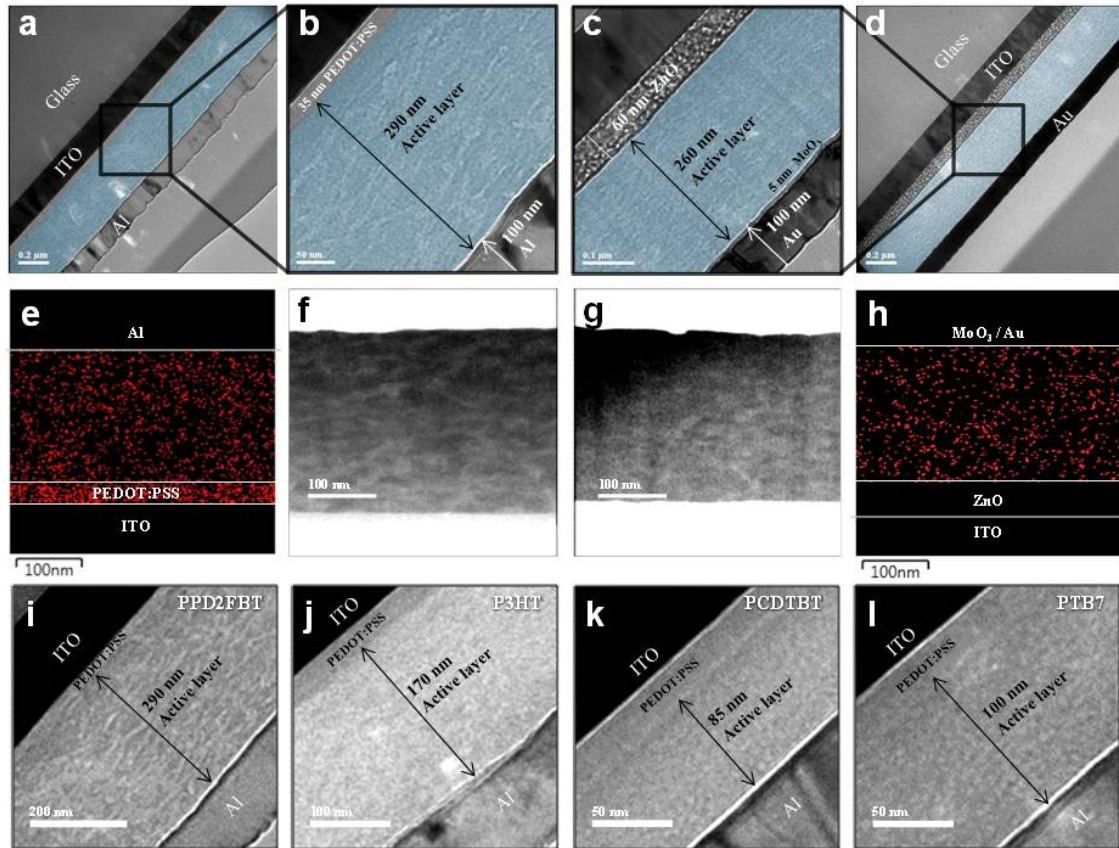
Figure 4.8. Cross-sectional TEM images of PPDT2FBT devices. (a, and b) Defocused, bright-field images of the conventional architecture. (c and d) Defocused, bright-field images of the inverted architecture. (b and c) are magnified active regions from images (a and d), respectively. For clarity, active regions in the images have been tinted blue. (e and h) EDS spectra showing the distribution of sulfur in the active layer of conventional and inverted architectures, respectively. (f and g) HAADF images of conventional and inverted structures, respectively. (i to l) Defocused, bright-field images comparing the active layer morphology of optimized conventional devices using PPDT2FBT, P3HT, PCDTBT and PTB7, respectively.

Images comparing close-ups of the active layers for optimized, conventional structure PPDT2FBT, P3HT, PCDTBT and PTB7 devices are shown in **Figure 4.8i, 8j, 8k and 8l**, respectively. The internal structure of PPDT2FBT is unique compared to the other polymers, exhibiting a clear network of wisp-like structures with length scales on the order of 50 nm. It can be presumed that these structural features act to facilitate the extraction of charge carriers and play a critical role in determining the semiconducting properties of PPDT2FBT BHJs.
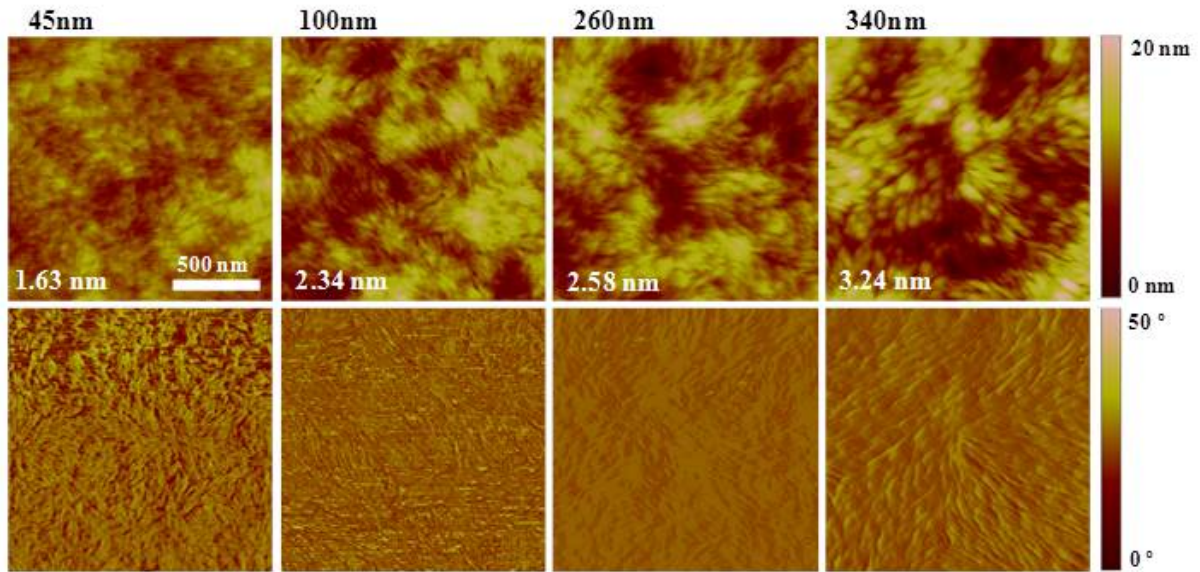
Figure 4.9. AFM images of PPDT2FBT:PC$_{71}$BM films with different thicknesses on ITO/PEDOT substrates. The top images are topographic images while the bottom images are phase images. RMS roughness values are included for each topographic image. All scan sizes are 2 μm × 2 μm.
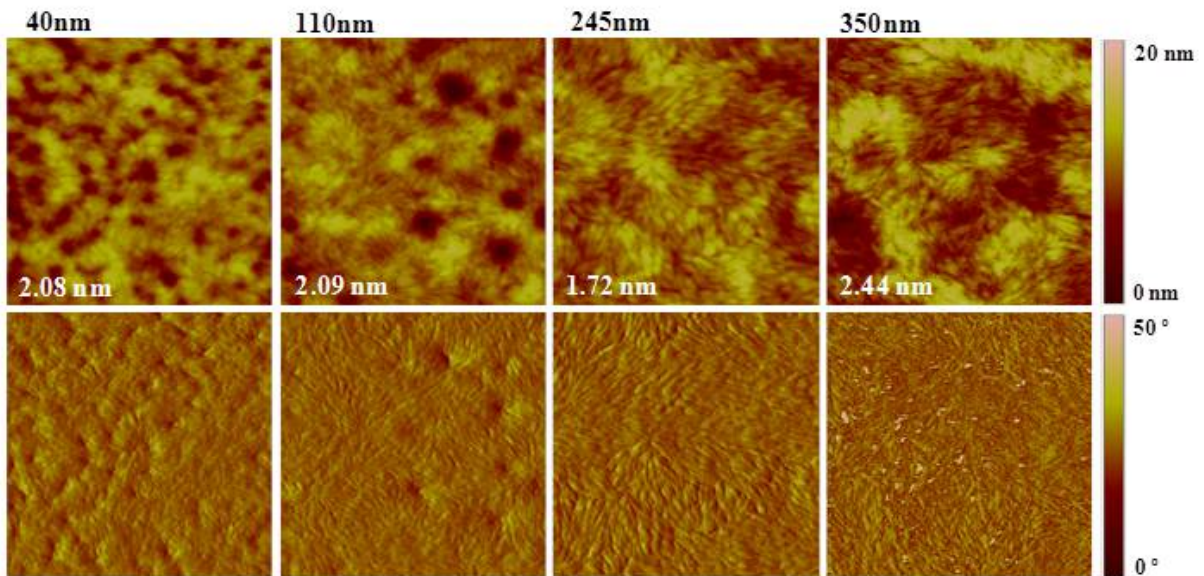
Figure 4.10. AFM images of PPDT2FBT:PC$_{71}$BM films with different thicknesses on ITO/ZnO substrates. The top images are topographic images while the bottom images are phase images. RMS roughness values are included for each topographic image. All scan sizes are 2 μm × 2 μm.
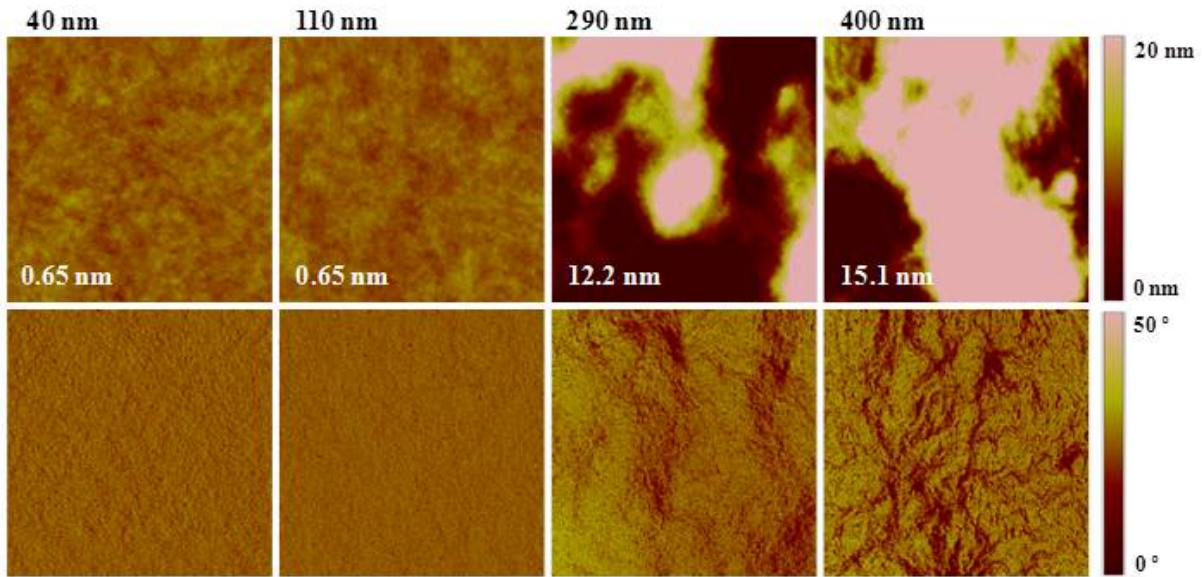
Figure 4.11. AFM images of P3HT:PC$_{61}$BM films with different thicknesses on ITO/PEDOT substrates. The top images are topographic images while the bottom images are phase images. RMS roughness values are included for each topographic image. All scan sizes are 2 μm × 2 μm.
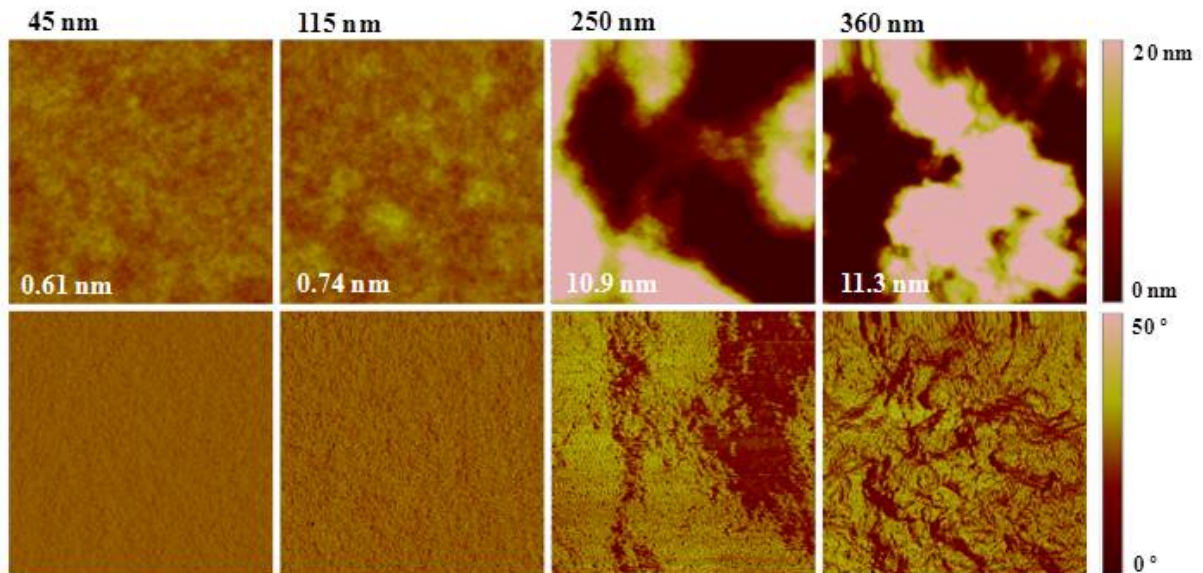
Figure 4.12. AFM images of P3HT:PC$_{61}$BM films with different thicknesses on ITO/ZnO substrates. The top images are topographic images while the bottom images are phase images. RMS roughness values are included for each topographic image. All scan sizes are 2 μm × 2 μm.

45nm	130 nm	240 nm	390 nm
0.28 nm	0.32 nm	0.33 nm	0.50 nm
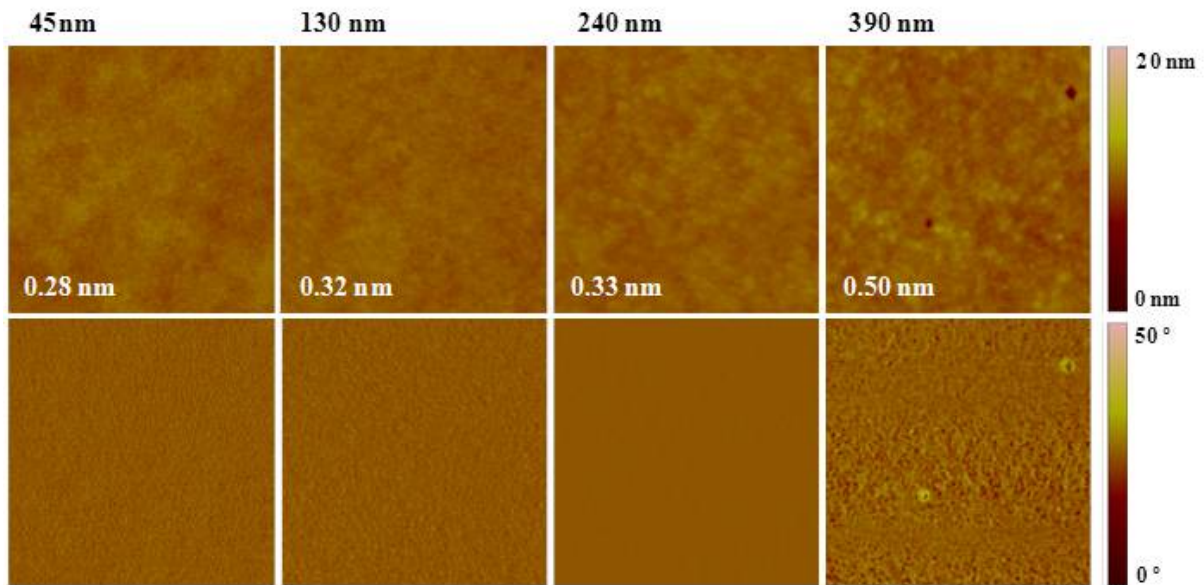
Figure 4.13. AFM images of PCDTBT:PC$_{71}$BM films with different thicknesses on ITO/PEDOT substrates. The top images are topographic images while the bottom images are phase images. RMS roughness values are included for each topographic image. All scan sizes are 2 μm × 2 μm.

50nm	105nm	235nm	390nm
1.86 nm	1.08 nm	0.51 nm	0.48 nm
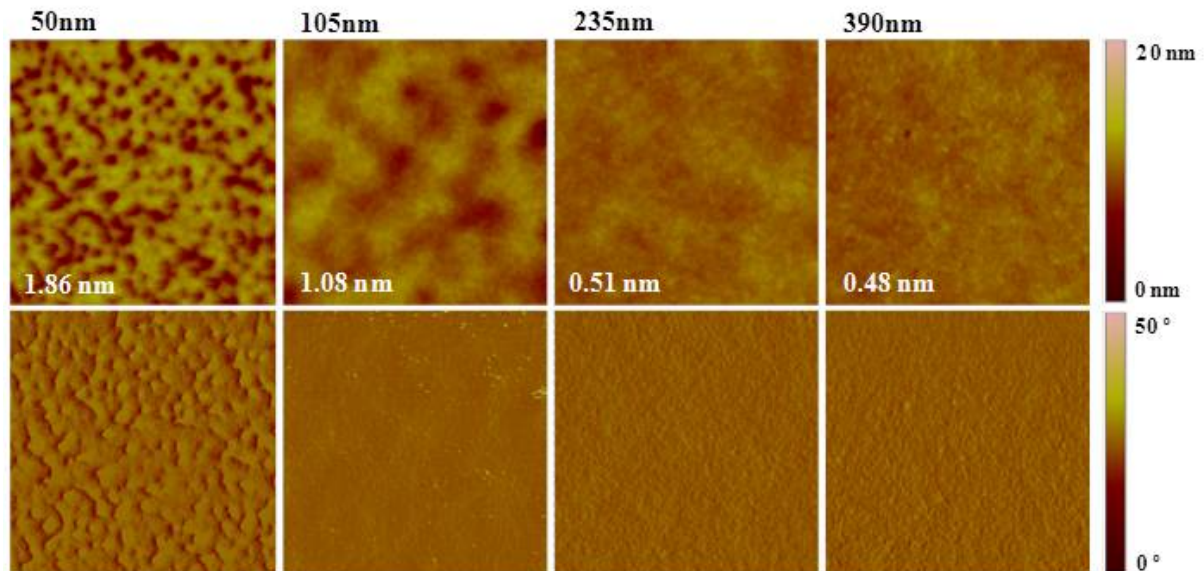
Figure 4.14. AFM images of PCDTBT:PC$_{71}$BM films with different thicknesses on ITO/ZnO substrates. The top images are topographic images while the bottom images are phase images. RMS roughness values are included for each topographic image. All scan sizes are 2 μm × 2 μm.
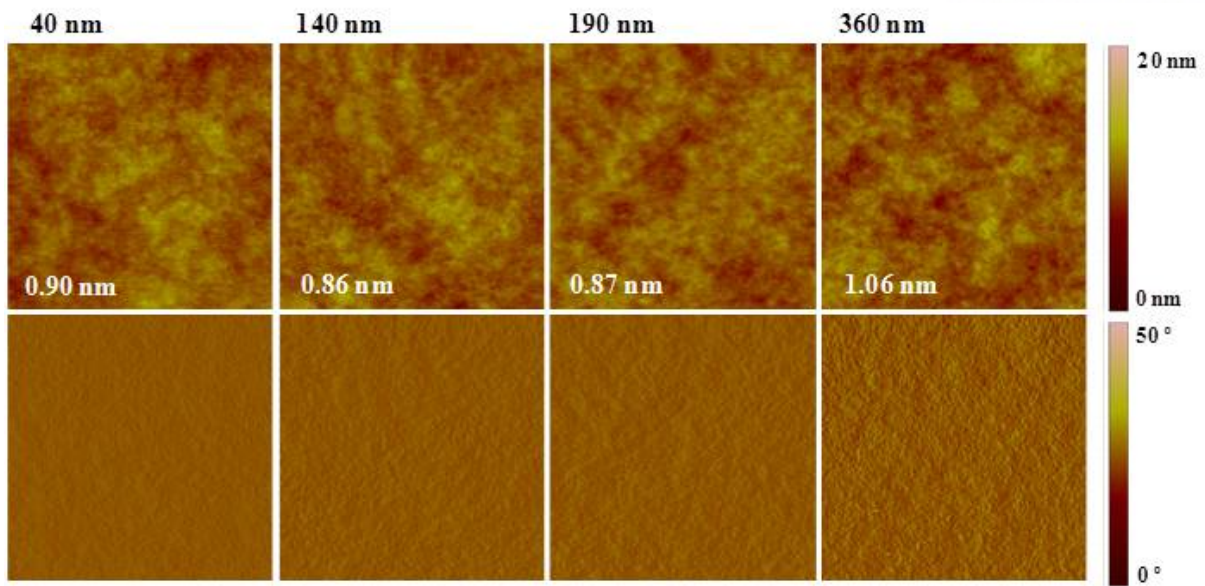
Figure 4.15. AFM images of PTB7:PC$_{71}$BM films with different thicknesses on ITO/PEDOT substrates. The top images are topographic images while the bottom images are phase images. RMS roughness values are included for each topographic image. All scan sizes are 2 μm × 2 μm.
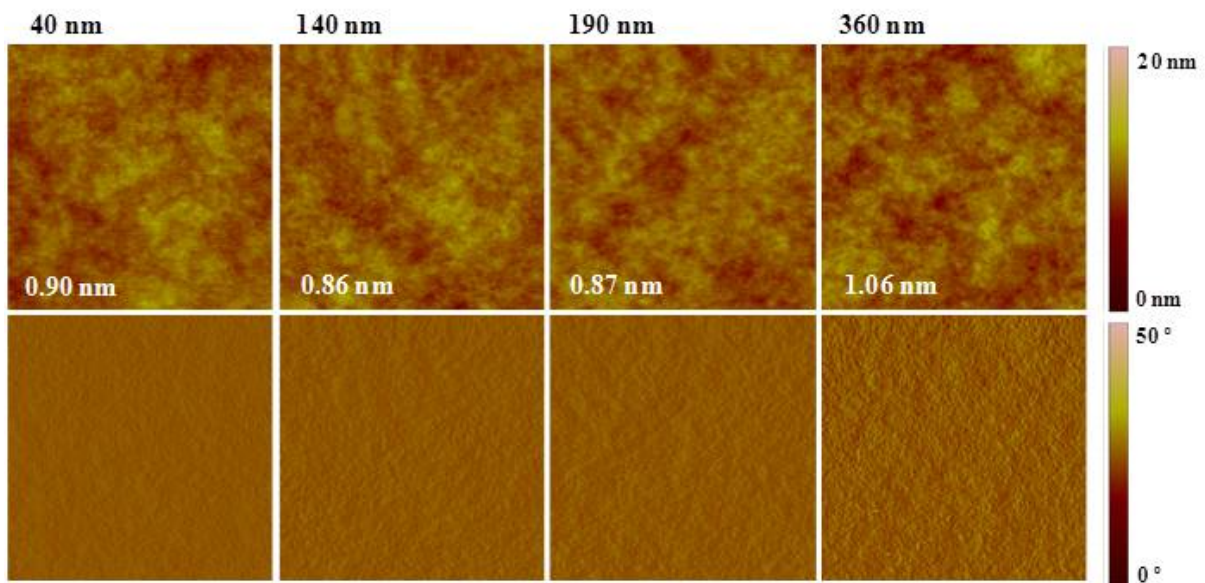
Figure 4.16. AFM images of PTB7:PC$_{71}$BM films with different thicknesses on ITO/ZnO substrates. The top images are topographic images while the bottom images are phase images. RMS roughness values are included for each topographic image. All scan sizes are 2 μm × 2 μm.
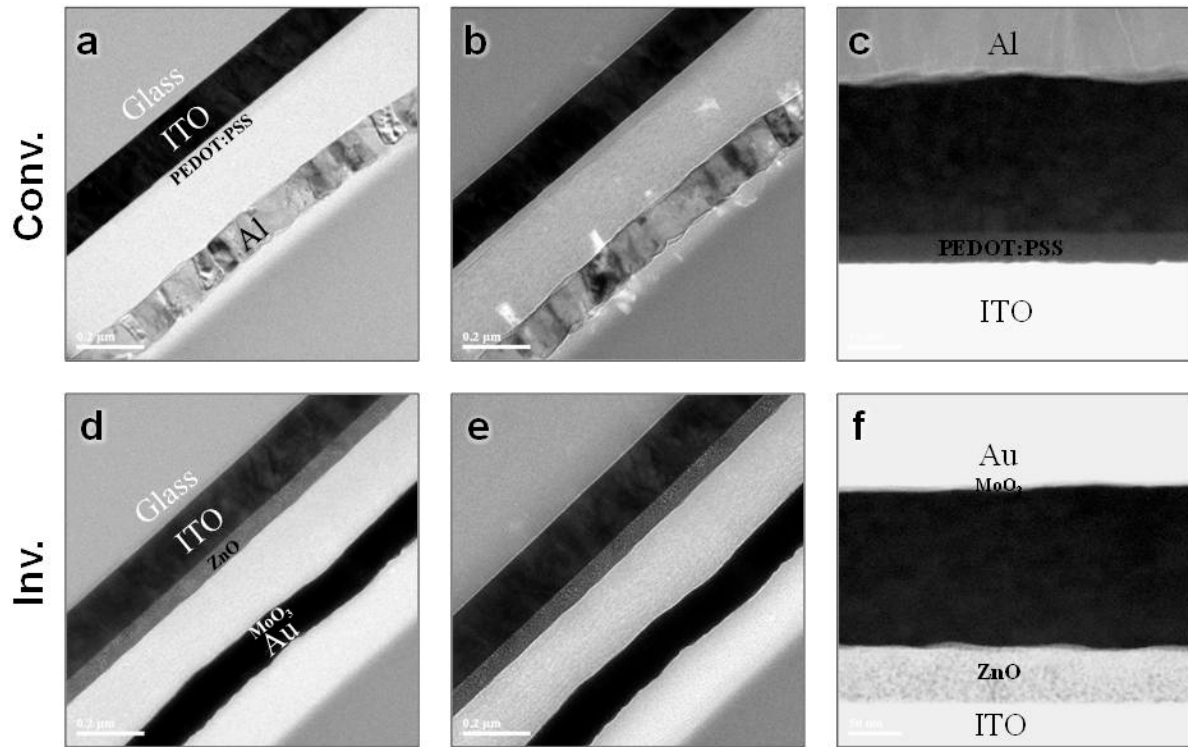
Figure 4.17. Cross-sectional TEM images of optimized P3HT:PC$_{61}$BM devices. The top images (a, b, c) show conventional devices with the architecture of ITO/PEDOT/P3HT:PC$_{61}$BM/Al. The bottom images (d, e, f) show inverted devices with the architecture of ITO/ZnO/P3HT:PC$_{61}$BM/MoO$_3$/Au. Images (a and b) are in focus while images (d and e) are defocused. Images (c and f) show high-angle annular dark-field images of the conventional and inverted structures, respectively.
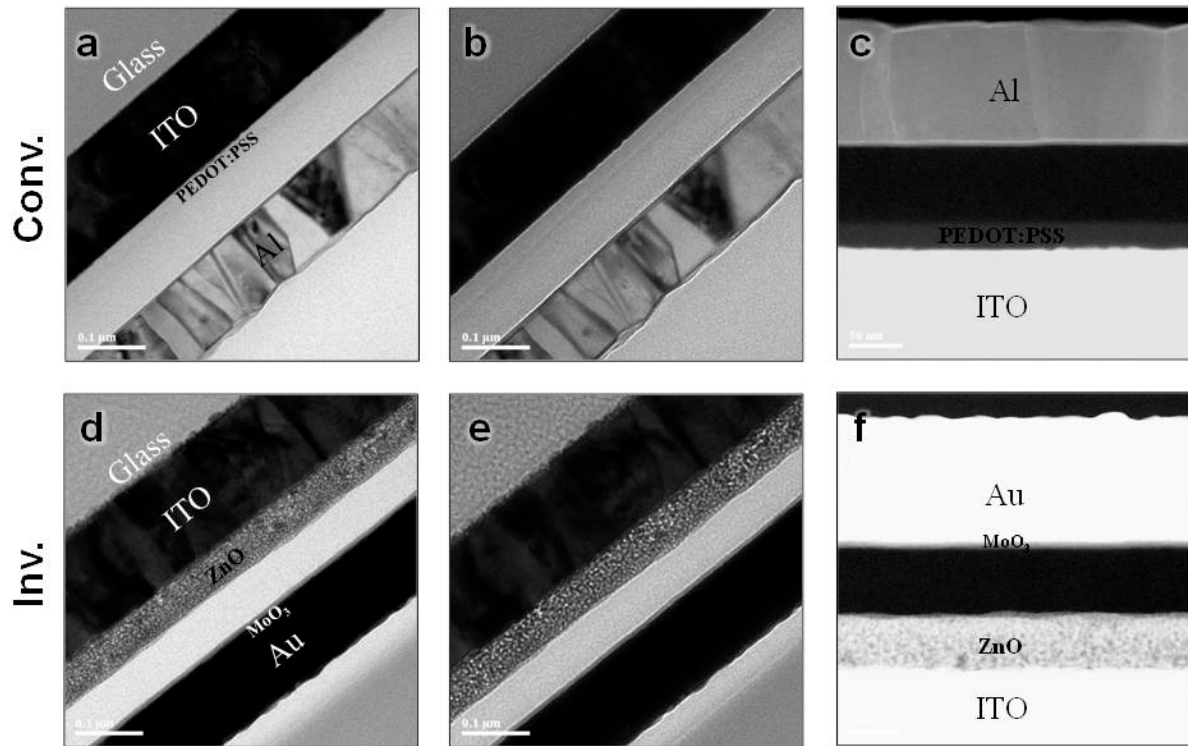
Figure 4.18. Cross-sectional TEM images of optimized PCDTBT:PC$_{71}$BM devices. The top images (a, b, c) show conventional devices with the architecture of ITO/PEDOT/PCDTBT:PC$_{71}$BM/Al. The bottom images (d, e, f) show inverted devices with the architecture of ITO/ZnO/PCDTBT:PC$_{71}$BM/MoO$_3$/Au. Images (a and b) are in focus while images (d and e) are defocused. Images (c and f) show high-angle annular dark-field images of the conventional and inverted structures, respectively.
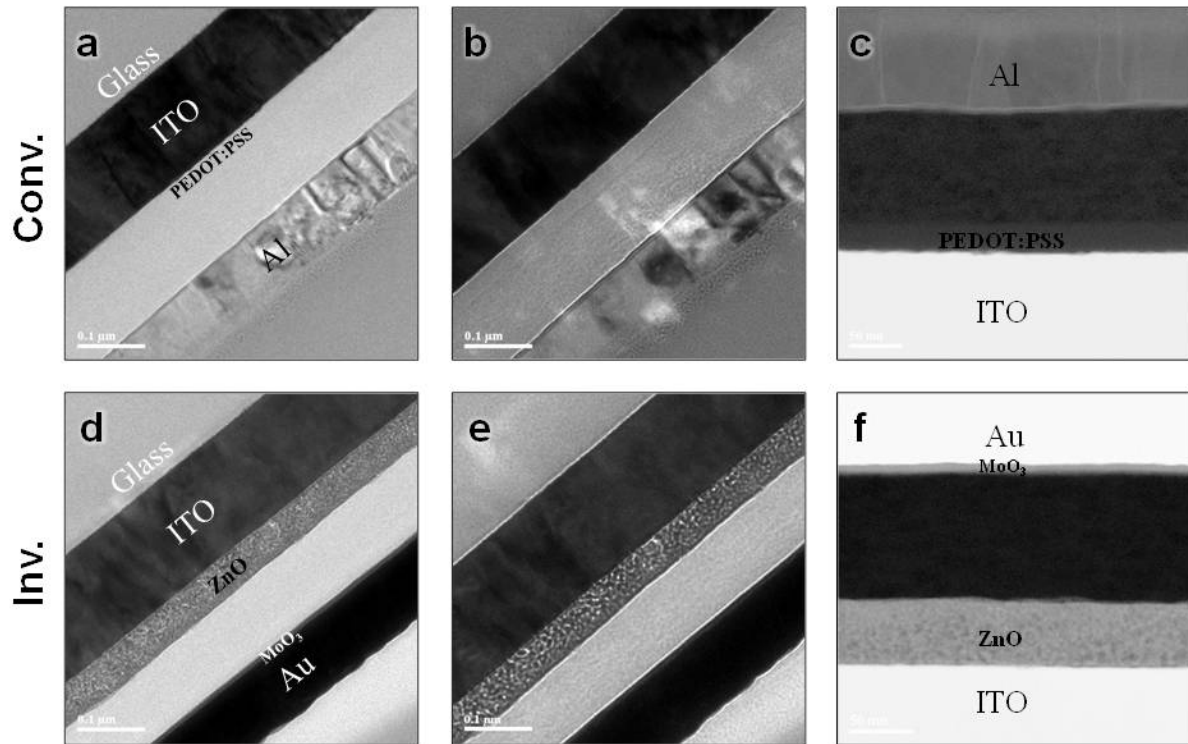
Figure 4.19. Cross-sectional TEM images of optimized PTB7:PC$_{71}$BM devices. The top images (a, b, c) show conventional devices with the architecture of ITO/PEDOT/PTB7:PC$_{71}$BM/Al. The bottom images (d, e, f) show inverted devices with the architecture of ITO/ZnO/PTB7:PC$_{71}$BM/MoO$_3$/Au Images (a and b) are in focus while images (d and e) are defocused. Images (c and f) show high-angle annular dark-field images of the conventional and inverted structures, respectively.
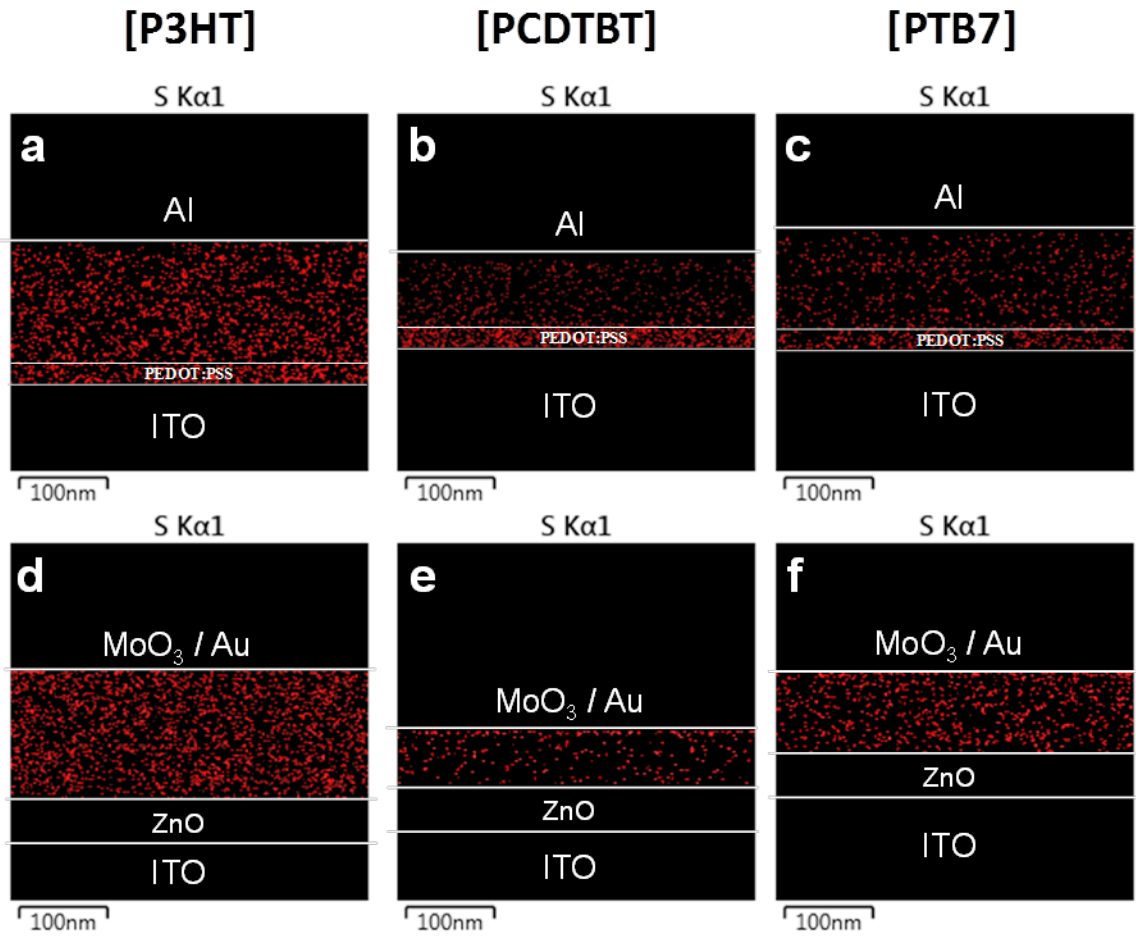
Figure 4.20. Energy dispersive X-ray spectroscopy of cross-sections. Vertical S atom distribution in cross sections of P3HT (a, d), PCDTBT (b, e) and PTB7 (c, f) devices in conventional (a, b, c) and inverted (d, e, f) architectures.
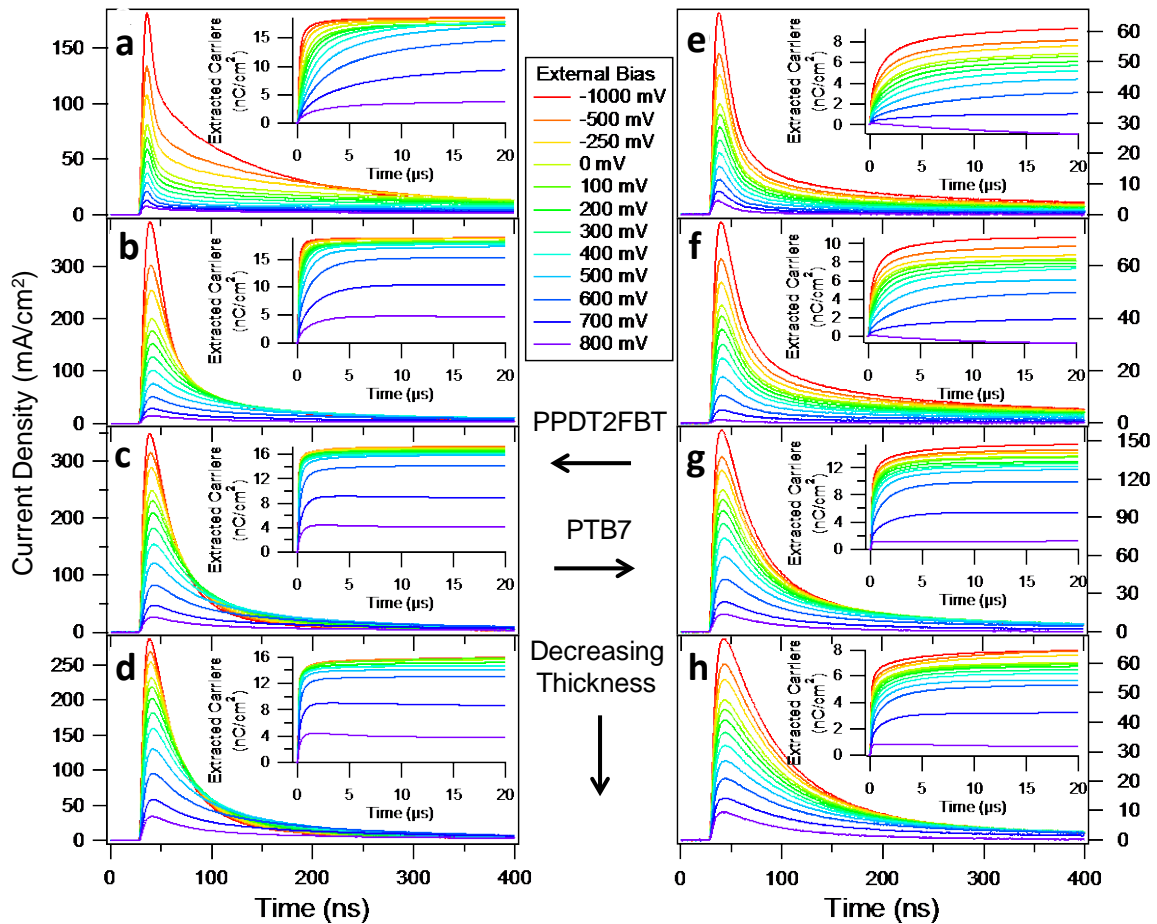
Figure 4.21. TPC measurements of solar cells with active layers consisting of (a) 650 nm PPDT2FBT, (b) 350 nm PPDT2FBT, (c) 130 nm PPDT2FBT, (d) 70 nm PPDT2FBT, (e) 215 nm PTB7, (f) 185 nm PTB7, (g) 100 nm PTB7, and (h) 60 nm PTB7. Insets show the integrated charges collected as a function of time. Note that a negative voltage corresponds to an increased internal field in the solar cell.

The photocurrent extraction of PPDT2FBT:PC$_{71}$BM was further probed by transient photocurrent (TPC) measurements. TPC measurements involved exciting charge carriers with an ultra-short pulse of laser light and quantifying their extraction as a function of time under variable electric fields. By systematic variation of the internal field, one can influence the carrier drift velocities and transit times, allowing quantification of carrier recombination and carrier mobility.[243-247]

Figure 4.21 shows bias-dependent TPC traces for PPDT2FBT and PTB7 devices of varying thickness. Insets show the corresponding time-integrals of the photocurrent curves, which yield the number of carriers collected as a function of time. In efficient solar cells, saturation is reached at reverse bias, where further increasing the internal field in the device has little to no effect on the total number of carriers extracted. At large internal fields in such devices, recombination is minimal and

90

the vast majority of carriers are quickly swept out. As can be seen in the insets to **Figure 4.21a-d**, PPDT2FBT cells clearly exhibit this trend for all thicknesses. PTB7 based cells, however, do not saturate as BHJ thickness increases (**Figure 4.21e-h**). This implies significantly faster carrier sweep-out and lower recombination rates in PPDT2FBT.

In order to explain this observation, the maximum vertical carrier mobility for each of these devices was determined by fitting the slope of the linear regime of the TPC traces following the method outlined by Heeger and coworkers.[243] Calculated values are shown in **Table 4.3**, showing that the carrier mobility of optimized PPDT2FBT cells is roughly an order of magnitude greater than that of the PTB7 devices. Due to the thickness-squared dependence of the carrier transit time, recombination losses become severe if BHJ thickness is increased without a corresponding increase in carrier mobility. Thus, the higher mobility of PPDT2FBT is seen here to allow for efficient operation at active layer thicknesses largely inaccessible to PTB7.

Table 4.3. Calculated maximum carrier mobility for PPDT2FBT and PTB7 solar cells.

Material	Thickness (nm)	Mobility ($cm^2 V^{-1}s^{-1}$)
PPDT2FBT	650	2.2×10^{-2}
PPDT2FBT	350	2.6×10^{-2}
PPDT2FBT	130	5.3×10^{-3}
PPDT2FBT	70	2.1×10^{-3}
PTB7*	215	6.9×10^{-3}
PTB7*	185	5.6×10^{-3}
PTB7	100	2.2×10^{-3}
PTB7	60	7.1×10^{-4}

*Note that the starred PTB7 devices overestimate their respective mobility, since the high reverse bias condition does not yield an adequate assessment of initial carrier density. However, this overestimation error is less than a factor of two.

4.4 Conclusion

The high carrier mobilities and complete carrier extraction from thick active layers evidently result from the strong out-of-plane π-π stacking and unique internal structure observed in PPDT2FBT:PC$_{71}$BM films. We conclude that these physical characteristics allow photo-dissociated electron-hole pairs to be collected from the active layer with almost 100% efficiency using exceptionally thick films. This economy of charge carrier extraction from thick films has thus far only been achieved in crystalline inorganic solar cells and has constituted a major hurdle limiting the application of organic solar cells. The energy band structure of PPDT2FBT allows near complete attenuation of incident photons with wavelengths up to 700 nm coupled with a V_{OC} of almost 0.8 V and a PCE of over 9%. We envision that if the same approach to engineering polymer self-assembly can be accomplished with a conjugated polymer having a narrower band gap (and thus higher J_{SC}), or deeper HOMO band (and thus higher V_{OC}), efficiencies of over 10% can be readily achieved, paving the way to commercially profitable organic solar cells.

Chapter 5. Improved Small bandgap polymer solar cells with unprecedented short-circuit current density and high fill factor

5.1 Research background

Polymer solar cells (PSCs) with polymer:fullerene bulk-heterojunction (BHJ) structure have been regarded as next-generation solar cells because of their low cost of materials and processes and easy production of flexible device.[187, 248, 249] Considerable efforts developing new polymer donors and fullerene acceptors[188, 191, 237, 250], device architectures[251-253][3], and morphology engineering[109, 254, 255] have enhanced power conversion efficiencies (PCEs) of PSCs up to 10%. However, most polymer donors that exhibit high PCEs over 8% can absorb the light in the wavelength region of 300-800 nm, thereby limiting further enhancement of photo-current. In addition to insufficient light absorption, their optimum thicknesses of the active layer are very thin (90-160 nm) which are challenging to produce defect-free large-area device via roll-to-roll process. Although thick BHJ films can absorb large amount of the light and are suitable for printing solar cells, increased bimolecular recombination induced by low charge-carrier mobility of BHJ components reduces fill factor and device performance.[232, 256] Therefore, it is required to synthesize novel semiconducting polymers with small bandgap (SBG) and high charge-carrier mobility as well as develop morphology engineering for bicontinuous interpenetrating donor:acceptor (D:A) network in both lateral and vertical direction of thick BHJ film.

A diversity of SBG polymers have been successfully designed to extend the absorption of solar spectrum from UV-visible to near infrared (NIR) region for high short-circuit current density (J_{SC}) while maintaining deep highest occupied molecular orbital (HOMO) level for high open-circuit voltage (V_{OC}). However, although PCEs of the devices based on these SBG polymers have increased up to 7%[257-262], their optimum thicknesses are restricted to about 100 nm and their device efficiencies are still lower than those of the devices with high-performance polymers with medium bandgap (1.5-1.8 eV).[188, 191, 237, 263] Recently, Janssen group designed diketopyrrolopyrrole (DPP)-based SBG polymer, DT-PDPP2T-TT, with high charge-carrier mobility and achieved a PCE of 6.9% in conjunction with high fill factor (FF) of 0.70 for the device with thick BHJ film of 220 nm.[232] While increasing active layer thickness from 200 nm to 400 nm led to slight increase in J_{SC}, significant decrease in FF was observed, which is consistent with tendencies observed in common BHJ PSCs. To the best of our knowledge, there have been no reports on SBG PSCs possessing thick active layer over 300 nm and achieving high PCEs over 9% at the same time.

Here, we report highly efficient SBG PSCs with thick BHJ film of ~340 nm and best PCEs of 9.40% by controlling lateral and vertical morphology of active layer through the addition of diphenyl ether (DPE) as the optimum processing additive into blend system of DT-PDPP2T-TT (P2) and [6,6]-

phenyl-C_{71} butyric acid methyl ester ($PC_{71}BM$).

5.2 Experimental

Materials and preparation for P2 polymer: All reagents and chemicals compounds were purchased from Aldrich, Alfa Aesar, or TCI America and used without any further purification. 2,5-bis(trimethylstannyl)-thieno[3,2-*b*]thiophene 97% was purchased from Sigma-Aldrich and recrystallized twice from MeOH (5 g/20 ml). 3,6-Bis(5-bromo-2-thienyl)-2,5-dihydro-2,5-di(2´-decyltetradecyl)-pyrrolo[3,4c]pyrrolo-1,4-dione has been synthesized following already published literature.[232] The P2 was prepared following Janssen's protocol.[232] A 20 ml microwave vial was charged with 0.19864 g (0.17557 mmol, 1eq) 3,6-Bis(5-bromo-2-thienyl)-2,5-dihydro-2,5-di(2´-decyltetradecyl)-pyrrolo[3,4c]pyrrolo-1,4-dione, 0.08179 g (0.17557 mmol, 1 eq) of 2,5-bis(trimethylstannyl)-thieno[3,2-*b*]thiophene, 8ml of dry toluene and 0.8 ml of dry DMF. The solution was degassed for 30 min after which 4.8 mg of Pd_2dba_3 (3%) and 5.4mg (12%) was added. The vial was sealed and the reaction mixture was vigorously stirred for 18 h in an 115 °C oil bath. The reaction was cooled at room temperature and the polymer was precipitated in methanol, filtered through 0.45 µm nylon filter and washed on Soxhlet apparatus with acetone, hexanes, dichloromethane and then chloroform. The chloroform fraction was reduced to 20-30 mL and then precipitated in methanol, filtered through 0.45 µm nylon filter and vacuum-dried to give 175 mg of the desired polymer (90% yield). Mn: 209 kDa, Mw: 449 kDa, PDI: 2.1.

Polymer characterizations: Number-average (M_n) and weight-average (M_w) molecular weights were determined by size exclusion chromatography (SEC) using a high temperature Varian Polymer Laboratories GPC220 equipped with an RI detector and a PL BV400 HT Bridge Viscometer. The column set consists of 2 PL gel Mixed C (300 x 7.5 mm) columns and a PL gel Mixed C guard column. The flow rate was fixed at 1.0mL/min using 1,2,4-trichlorobenzene (TCB) (with 0.0125% BHT w/v) as eluent. The temperature of the system was set to 110 °C. All the samples were prepared at concentrations of nominally 1.0 mg/ml in TCB. Dissolution was performed using a Varian Polymer Laboratories PL-SP 260VC sample preparation system. The sample vials were held at 110 °C with shaking for 1 h for complete dissolution. The solutions were filtered through a 2 mm porous stainless steel filter used with the 0.40 µm glass filter into a 2 ml chromatography vial. The calibration method used to generate the reported data was the classical polystyrene method using polystyrene narrow standards Easi-Vials PS-M from Varian Polymer Laboratories which were dissolved in TCB.

Film characterizations: TEM images were obtained using a JEOL JEM-2100 transmission electron microscope (TEM) operated at 200 kV. Atomic force microscope (AFM) images were collected using a Asylum MFP-3D standard system AFM microscope operating in tapping mode. UV-vis-NIR absorption was measured using a OLIS 14 spectrophotometer.

GIWAXS: GIWAXS measurements were carried out at PLS-II 9A U-SAXS beam line of Pohang

Accelerator Laboratory. An X-ray beam from the in-vacuum undulator (IVU) was monochromated (E_k = 11.24 keV, λ = 1.103 Å) using a Si(111) double crystal monochromator and focused horizontally and vertically at the sample position (450 (H) $\times$ 60 (V) μm^2 in FWHM) using K-B-type focusing mirror system. The GIWAXS sample stage is equipped with a 7-axis motorized stage for the fine alignment of the thin sample and the incidence angle of X-rays was adjusted to 0.12°–0.14°. GIWAXS patterns were recorded with a 2D CCD detector (Rayonix SX165, USA), and X-ray irradiation time was 0.5–5 s depending on the saturation level of the detector. The diffraction angle was calibrated using a pre-calibrated sucrose crystal (monoclinic, P21, a = 10.8631 Å, b = 8.7044 Å, c = 7.7624 Å, β = 102.938°) and the sample-to-detector distance was approximately 232 mm. Samples for GIWAXS measurements were prepared by spin-coating blend solutions on top of PEDOT:PSS-coated Si substrates.

Optical simulation: In order to investigate the optical properties and photocurrent generation capacity of P2, optical constants (n and κ) were calculated and transfer matrix modeling (TMM) was carried out. κ values were derived from the absorption coefficient, α, via the relationship $\kappa = \lambda\alpha/4\pi$. n values were similarly derived from α via the Kramers-Kronig relationship as described in a previous report.[239] J_{SC} was estimated based on the active layer absorption (ALA), assuming that each photon absorbed in the active layer leads to the generation and extraction of one electron-hole pair. Bulk heterojunction films were observed to vary in thickness by approximately 5% between different locations on the same film. To account for this, transfer matrix simulations were taken as the average of 3 calculations for optical stacks in which the active layer thickness was varied by $\pm$ 5%, resulting in a better match between simulated active layer absorption and the observed EQE. Plots of simulated J_{SC}, (based on ALA) vs. film thickness can be found in **Figure 5.8**.

Solar cell fabrication and characterization: We fabricated the PSCs with device configuration of ITO/PEDOT:PSS/P2:PC$_{71}$BM/Al by using the following procedure: PEDOT:PSS solution was spin-cast at 5000 rpm on cleaned ITO substrates after UV-ozone treatment for 10 min and dried at 150 °C for 15 min. For depositing the active layer, we prepared solution consisting of P2 (0.5 wt. %), PC$_{71}$BM (1.5 wt. %), and diphenyl ether (3 vol. %) and spin-cast on top of PEDOT:PSS layer in a nitrogen-filled glove box. Subsequently, Al (100 nm) electrode was deposited on the active layer under vacuum ($<10^{-6}$ Torr) by thermal evaporation. The area of the Al electrode defines the active area of the device as 3.3 mm^2.

The *J-V* characteristics of the solar cells were measured by a Keithley 2400 Source Measure Unit. The solar cell performance was tested with an Air Mass 1.5 Global (AM 1.5 G) solar simulator with an irradiation intensity of 100 mW cm^{-2}. EQE measurements were obtained using the PV measurement QE system by applying monochromatic light from a xenon lamp under ambient conditions. The monochromatic light intensity was calibrated using a Si photodiode and chopped at

100 Hz. Masks (1.70 mm^2) made of thin black plastic were attached to each cell before measurement of the J-V characteristics and the EQE to accurately measure the performance of solar cells. All devices were tested in ambient air after UV-epoxy encapsulation.

5.3 Results and discussion

Unlike common tendencies in BHJ PSCs, where poor device performances are observed for the PSCs with thick BHJ film of over 300 nm due to significant decrease in *FF* in spite of slight increase in J_{SC}, we show that the P2:PC$_{71}$BM devices exhibit extremely high J_{SC} of 20.07 mA cm^{-2} for thick active layer over 300 nm while maintaining high FF of 0.70. This high performance of SBG PSCs results from high charge carrier mobility of P2 and successful formation of bicontinuous interpenetrating D:A network in both lateral and vertical direction of thick BHJ film through morphology engineering with processing additive.

The devices were fabricated using simple and conventional device structure of indium tin oxide (ITO) / poly(3,4-ethylenedioxythiophene):polystyrene sulfonate (PEDOT:PSS) / P2:PC$_{71}$BM / Al (**Figure 5.1b**). The P2 was prepared following synthetic method in previous literature[232] and has electrical bandgap of 1.42 eV (optical bandgap: 1.35 eV) in conjunction with HOMO level of -5.10 eV and lowest unoccupied molecular orbital (LUMO) level of -3.68 eV (**Figure 5.1c**). Although Janssen group reported the P2:PC$_{71}$BM PSCs prepared from mixed solvent of chloroform (CF) and 1,2-dichlorobenzene (DCB) as a function of thickness[232], we systematically investigated the effect of D:A ratio, solvent, and processing additives on device performance (**Figure 5.2 -5.4 and Table 5.1-5.3**). We found that optimum D:A ratio and solvent are 1:3 and mixed solvent of chlorobenzene (CB) and DPE (97:3 vol. %), respectively (**Figure 5.2, 5.3 and Table 5.1, 5.2**). Among various additives such as 1,8-diiodooctane (DIO), 1,8-octanedithiol (ODT), chloronaphthalene (CN), the devices processed with DPE exhibited highest PCE of 9.40% compared to those of the devices with other additives (DIO: 7.75%, ODT: 6.01%, and CN: 7.34%) (**Figure 5.4 and Table 5.3**).
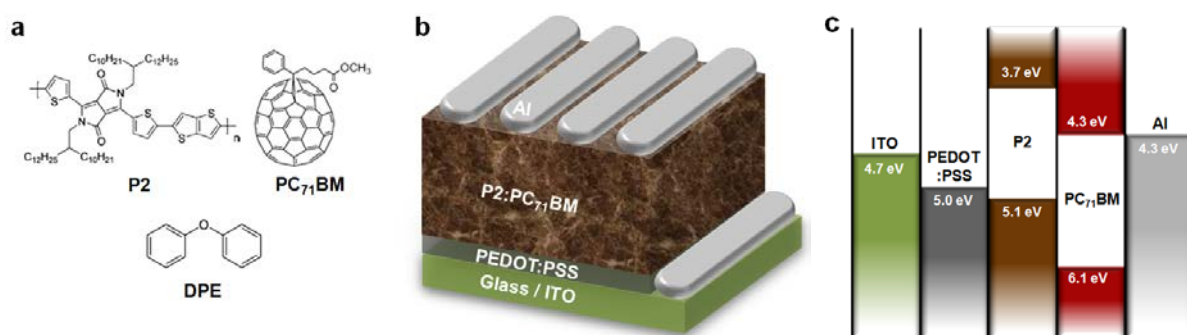
Figure 5.1. (a) Chemical structures of components of the active layer. (b) Device structure of solar cells. (c) Energy band diagram of materials used in solar cells.

The DPE was the best additive to form nanofibrillar morphology of P2:PC$_{71}$BM BHJ film, which may lead to bicontinuous interpenetrating D:A network (**Figure 5.6**). We also fabricated two types of reference devices for comparison: (1) the device prepared from solvent mixture of CF and DCB (92.5:7.5 vol.%) used in previous report[232]; (2) the device prepared from pure CB to understand DPE effect on device performance.
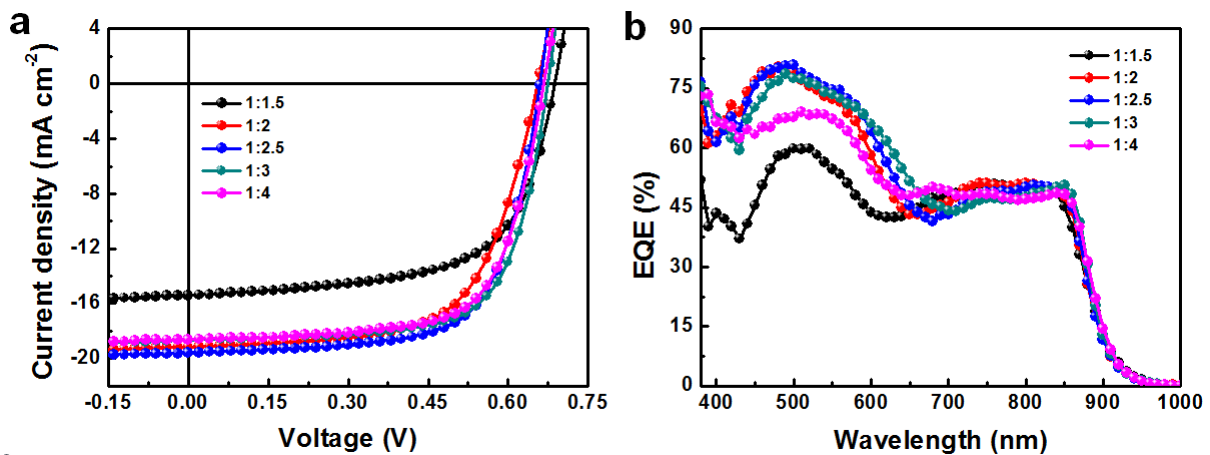
Figure 5.2. (a) *J-V* curves and (b) EQE of P2:PC$_{71}$BM PSCs with different D:A ratio.

Table 5.1. Device characteristics for P2:PC$_{71}$BM PSCs with different D:A ratio.

D:A ratio	J_{SC} (mA cm^{-2})	V_{OC} (V)	FF	PCE (%)	J_{SC} [Cal.] (mA cm^{-2})
1:1.5	15.40	0.69	0.63	6.67	15.57
1:2	19.19	0.66	0.64	8.03	18.41
1:2.5	19.61	0.66	0.68	8.79	18.58
1:3	20.07	0.67	0.70	9.40	18.70
1:4	18.62	0.67	0.68	8.47	17.65
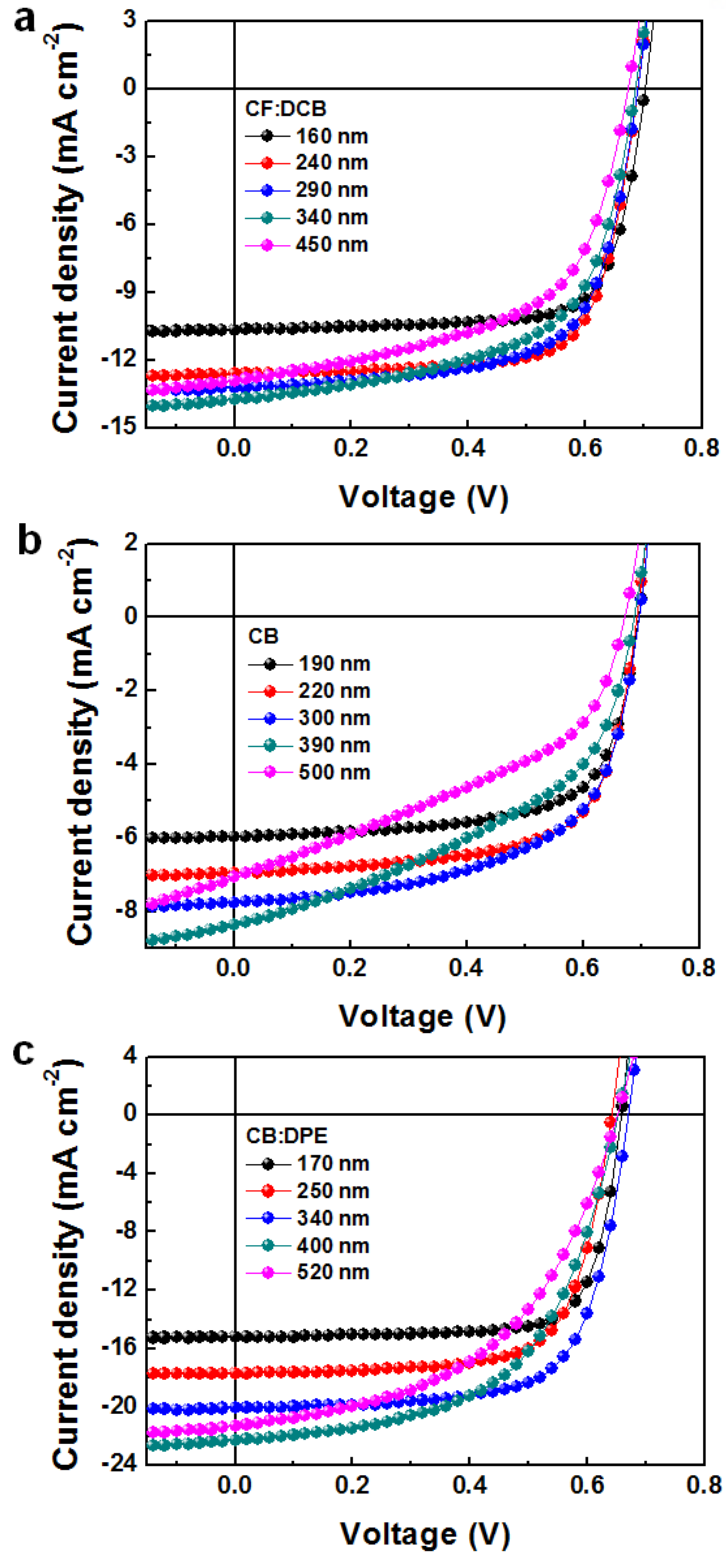
Figure 5.3. Current density-voltage (*J-V*) curves of P2:PC$_{71}$BM PSCs prepared from (a) CF:DCB, (b) CB, and (c) CB:DPE as a function of thicknesses.

Table 5.2. Device characteristics for P2:PC$_{71}$BM PSCs as a function of solvents and thicknesses.

Solvent	Thickness (nm)	J_{SC} (mA cm^{-2})	V_{OC} (V)	FF	PCE (%)
CF:DCB	160	10.65	0.70	0.75	5.58
	240	12.61	0.69	0.73	6.33
	290	13.21	0.69	0.67	6.11
	340	13.74	0.69	0.60	5.66
	450	12.91	0.67	0.57	4.93
CB	190	5.97	0.70	0.68	2.81
	220	6.95	0.69	0.67	3.21
	300	7.76	0.70	0.60	3.24
	390	8.37	0.69	0.45	2.60
	500	7.08	0.67	0.41	1.97
CB:DPE	170	15.19	0.66	0.76	7.60
	250	17.71	0.64	0.71	8.07
	340	20.07	0.67	0.70	9.40
	400	22.30	0.65	0.56	8.19
	520	21.34	0.65	0.50	6.93
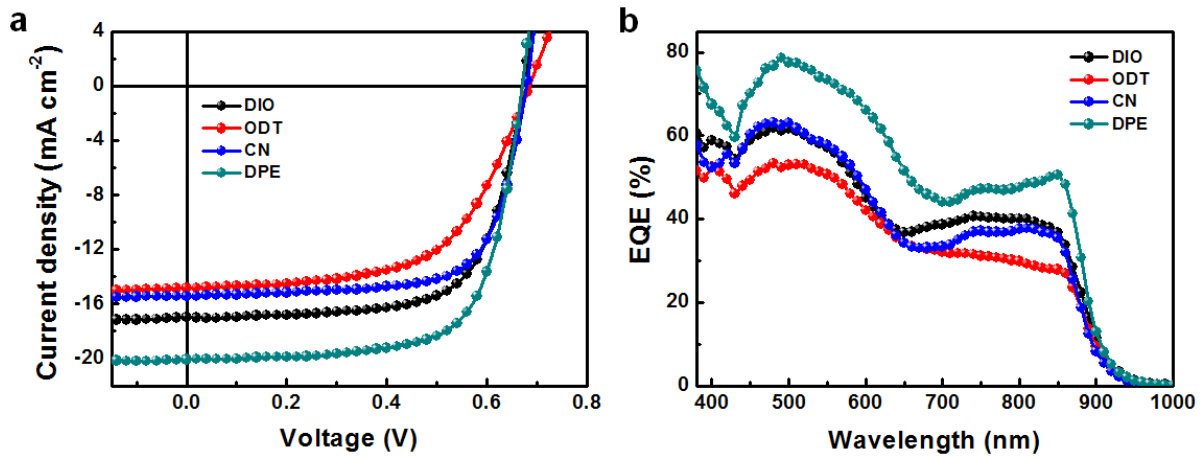
Figure 5.4. (a) *J-V* curves and (b) EQE of P2:PC$_{71}$BM PSCs with different additives.

Table 5.3. Device characteristics for P2:PC$_{71}$BM PSCs with different additives.

Additive	Thickness (nm)	J_{SC} (mA cm^{-2})	V_{OC} (V)	FF	PCE (%)	J_{SC} [Cal.] (mA cm^{-2})
DIO	340	15.67	0.69	0.72	7.75	14.72
ODT	290	14.84	0.69	0.59	6.01	12.50
CN	330	15.44	0.65	0.70	7.34	14.20
DPE	320	20.07	0.67	0.70	9.40	18.70
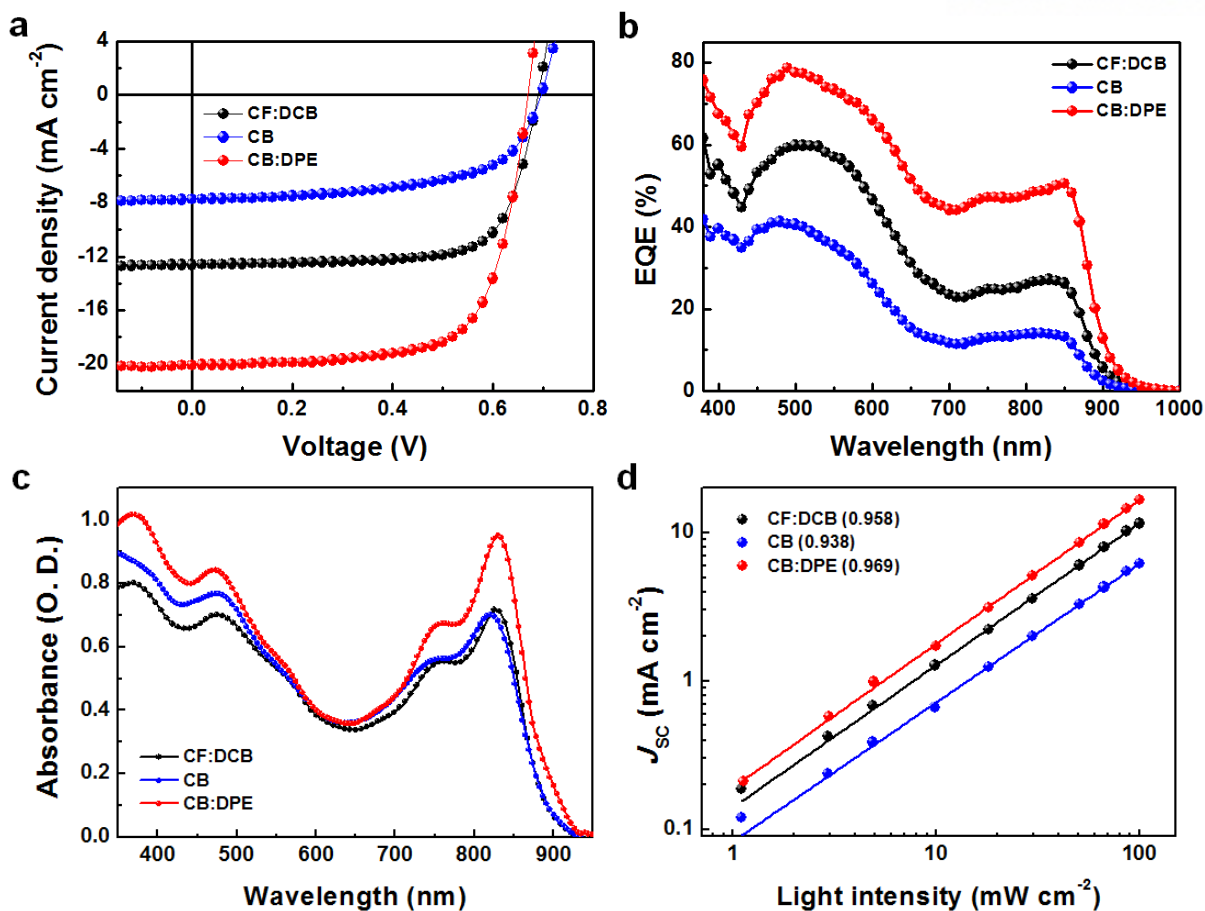
Figure 5.5. (a) Current density-voltage (*J-V*) curves, (b) external quantum efficiency (EQE), (c) UV-vis absorption spectra, and (d) J_{SC} dependence on light intensity of optimum devices prepared from different solvents.

Table 5.4. Device parameters for optimum P2:PC$_{71}$BM PSCs prepared from different solvents.

Solvent	Optimum thickness (nm)	J_{SC} (mA cm^{-2})	V_{OC} (V)	FF	Average PCE (%)	Best PCE (%)
CF:DCB	240	12.61	0.69	0.73	5.98	6.33
CB	300	7.76	0.70	0.60	3.01	3.24
CB:DPE	340	20.07	0.67	0.70	9.03	9.40

As shown in **Figure 5.5a**, device parameters for optimized devices from CF:DCB was J_{SC} = 12.61 mA cm^{-2}, V_{OC} = 0.69 V, and FF = 0.73, and best PCE of 6.33%, and for the device from pure CB was J_{SC} = 7.76 mA cm^{-2}, V_{OC} = 0.70 V, and FF = 0.60, and best PCE of 3.24%. These results of the devices from CF:DCB were in good agreement with previous literature.[232] It is surprising that the addition of DPE into CB solution led to remarkable PCE enhancement. Optimized device from CB:DPE achieved best PCE of 9.40% with J_{SC} = 20.07 mA cm^{-2}, V_{OC} = 0.67 V, and FF = 0.70. The detailed device characteristics are listed in **Table 5.4**. Enhanced device efficiency by incorporation of DPE is fully ascribed to unprecedented J_{SC} up to 20 mA cm^{-2} owing to thick BHJ film over 300 nm. Although optimum film thickness for the device from CB:DPE was thicker than those of the devices from CF:DCB and pure CB (CB:DPE = 340 nm, CB = 300 nm, CF:DCB = 240 nm), the device from CB:DPE still maintained high FF of 0.70.

To investigate the effect of active layer thickness on device performance, we fabricated P2:PC$_{71}$BM PSCs as a function of solvents and thicknesses. Regardless of solvents, thicker devices (above 300 nm) exhibited higher J_{SC} and lower FF, whereas thinner devices (below 200 nm) showed diametrical tendencies (**Figure 5.3 and Table 5.2**). It is noticeable that increasing the thickness of BHJ film prepared from CB:DPE (from 170 to 340 nm) led to remarkable increase in J_{SC} (from 15.19 to 20.07 mA cm^{-2}) while maintaining high FF up to 0.70.
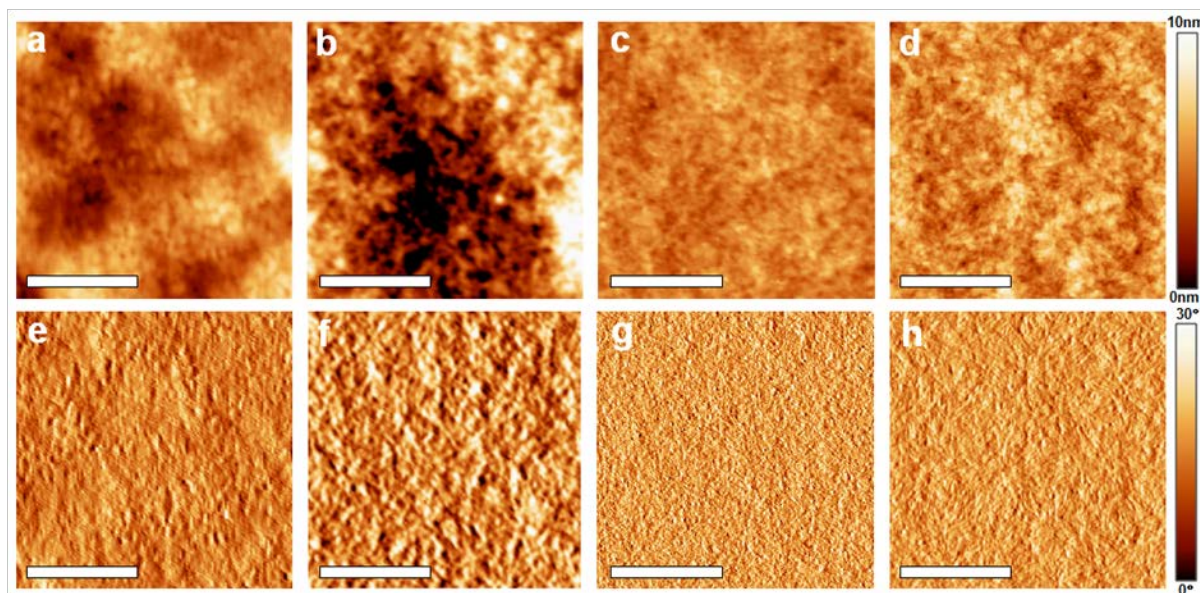
Figure 5.6. AFM topography (upper row) and phase images (lower row) of P2:PC$_{71}$BM BHJ films with different additives, (a, e) DIO, (b, f) ODT, (c, g) CN, and (d, h) DPE. Scale bar is 1 μm.

Furthermore, J_{SC} of the device with BHJ film of 400 nm (22.30 mA cm^{-2}) is the highest value in the PSCs reported to date[188, 255, 259], as well as comparable to those of highly efficient perovskite solar cells.[264-266] In contrast, the devices from CF:DCB and CB simultaneously exhibited significant increase in J_{SC} and decrease in FF by increasing film thickness, giving rise to resulting reduction in device efficiency. We speculated that high performance of the devices from CB:DPE are attributed to maximized light absorption by thick BHJ film and improved film morphology by optimum additive.

To understand the differences in device performance as a function of solvents, we measured external quantum efficiency (EQE) and UV-Vis-NIR absorption of optimum devices prepared from different solvents. Compared to EQE values of the device from CF:DCB and CB, the devices from CB:DPE exhibited higher EQE curve over the whole wavelength region with two peaks of 78.7% at 490 nm and 50.6% at 850 nm (**Figure 5.5b**). These differences in EQE values were partly related to optical density (OD) of BHJ films. Thicker BHJ film from CB:DPE (thickness: 340 nm) had higher OD of 0.84 at 470 nm and 0.95 at 830 nm, whereas BHJ films from CF:DCB and CB showed relatively lower OD due to their thinner thicknesses (CF:DCB: 240 nm and CB: 300 nm) (**Figure 5.5c**). Increasing BHJ film thickness enhances photogeneration of charge carriers by maximizing light absorption within the active layer. However, although thicker devices have higher light absorption, this does not assure high EQE value due to high probability of recombination loss by low charge-carrier mobilities of BHJ components.
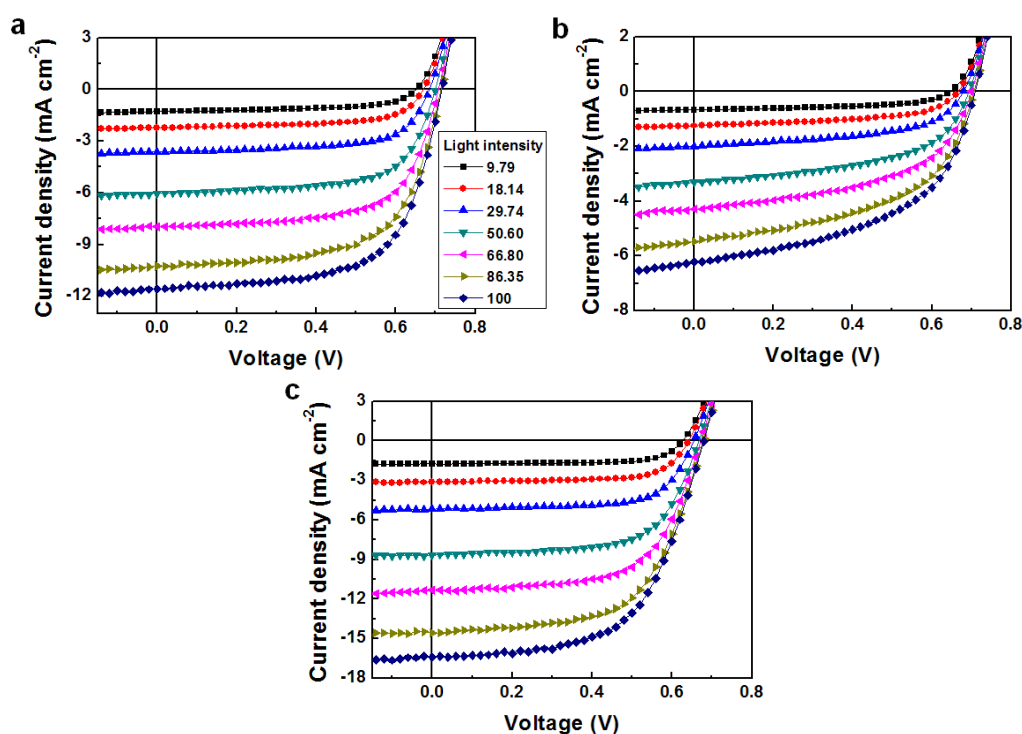
Figure 5.7. *J-V* characteristics of the devices prepared from (a) CF:DCB, (b) CB, and (c) CB:DPE as a function of light intensity.

To find the origin of unprecedented J_{SC} and high *FF* for thick PSCs, we investigated bimolecular recombination dynamics by measuring the dependence of J_{SC} on light intensity for devices prepared from different solvents (**Figure 5.7**). The J_{SC} dependence on light intensity measurements provide the information on bimolecular recombination.[255, 267, 268] Linear slope in the plot on dependence of J_{SC} on light intensity indicates weak bimolecular recombination, while sublinear slope suggests partial bimolecular recombination loss during charge transport process.[263] As shown in **Figure 5.5d**, logarithmic plots between J_{SC} and light intensity exhibited a slope of 0.958, 0.938, and 0.969 for devices prepared from CF:DCB, CB, and CB:DPE, respectively. These results reveal that weakest bimolecular recombination occurred in the devices prepared from CB:DPE, which were also confirmed by optical simulation results for photocurrent estimation. Among three devices, measured J_{SC} values of the devices from CB:DPE most closely follow theoretically maximum J_{SC} (**Figure 5.8**). These imply that thick active layer maximizes light absorption and optimized nanoscale morphology by addition of DPE minimizes bimolecular recombination, simultaneously leading to unprecedented J_{SC} and high FF.
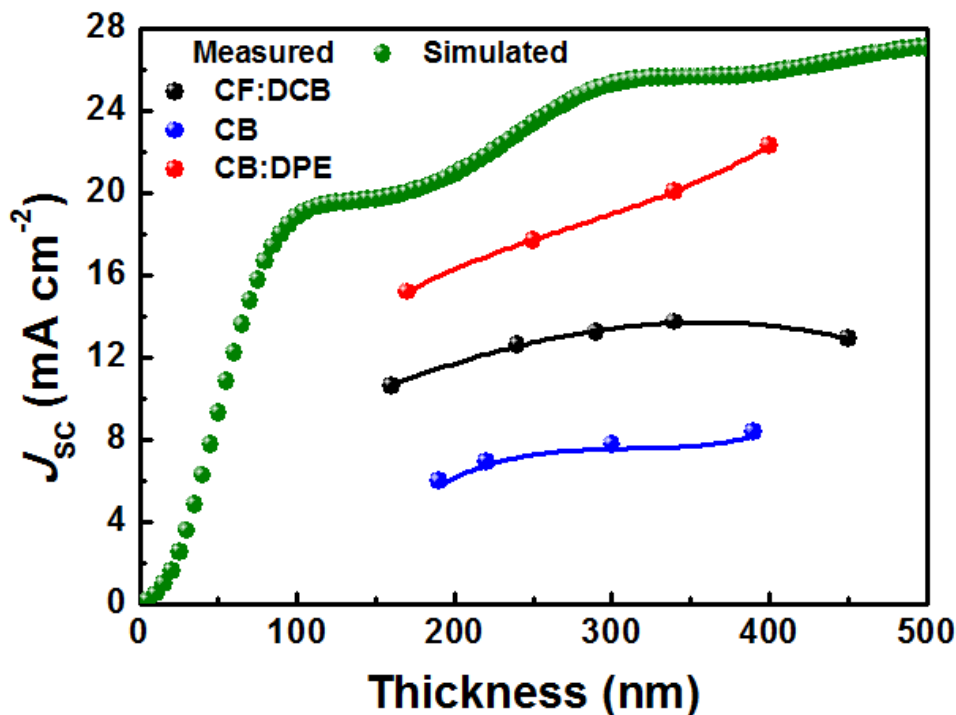
Figure 5.8. Comparison of measured J_{SC} from *J-V* characteristics and estimated J_{SC} from optical simulation of P2:PC$_{71}$BM PSCs with structure of ITO/PEDOT:PSS/active layer/Al as a function of active layer thickness.
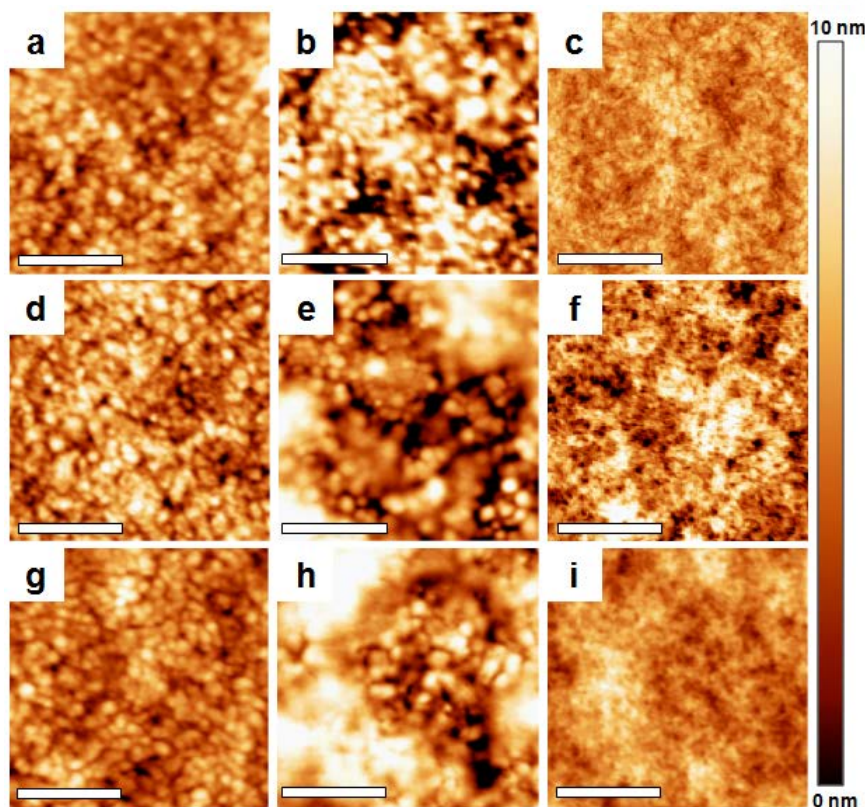
Figure 5.9. AFM topography images of BHJ films with optimum (top row), thin (middle row), and thick (bottom row) thickness that were prepared from CF:DCB (a, d, g), CB (b, e, h), and CB:DPE (c, f, i). The scale bar is 1 μm.

To investigate lateral and vertical morphology of BHJ films prepared from different solvents, we measured atomic force microscopy (AFM) and transmission electron microscopy (TEM). **Figure 5.9** exhibits AFM images of BHJ films as a function of solvents and thicknesses. Optimum films prepared from CF:DCB and CB:DPE exhibited uniform surface with smooth root-mean-square (rms) roughness of 1.3 nm and 1.1 nm, respectively, whereas the film from CB was uneven with rough rms roughness of 3.4 nm (**Figure 5.9a-c**). It is noticeable that the film from CB:DPE only showed well-distributed fibrilar-featured structure. This morphology is beneficial to formation of bicontinuous interpenetrating D:A network, enhancing charge-carrier mobility and device performance.[79, 224, 237] Although decreasing film thickness below optimum thickness (thickness: 160 ± 10 nm) resulted in larger domains and slight increase in rms roughness, there were negligible changes in morphology for all BHJ films (**Figure 5.9d-f**). Increasing film thickness over optimum thickness (thickness: 490 ± 30 nm) also led to slight increase in surface roughness for films from CF:DCB and CB:DPE (**Figure 5.9g** and **5.9i**). It is noteworthy that the film from CB:DPE still maintained fibrilar morphology in spite of its thick film of 520 nm (**Figure 5.9i**). In contrast, thick film from CB exhibited uneven surface with high rms roughness of 5.1 nm and big islands with size of 100-150 nm (**Figure 5.9h**).
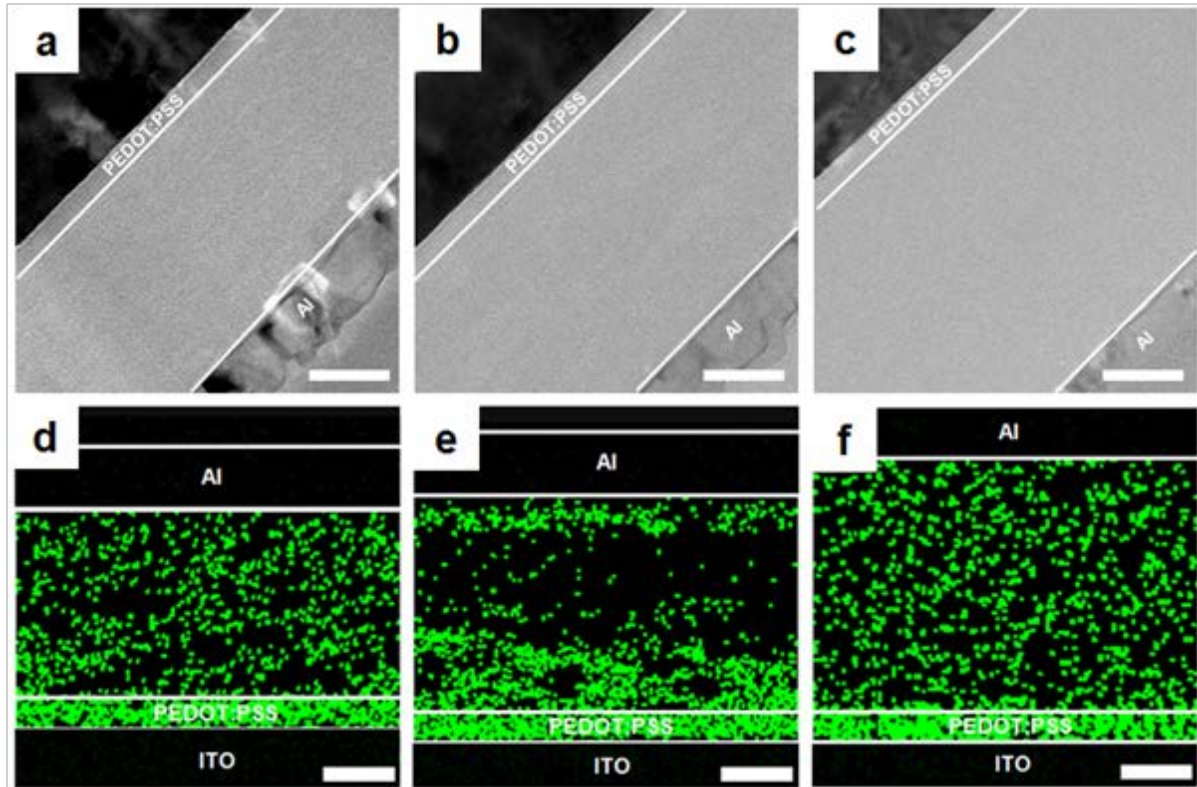
Figure 5.10. Cross-sectional TEM images (a-c) and EDS S mapping (d-f) of optimum devices prepared from CF:DCB (a, d), CB (b, e), and CB:DPE (c, f), respectively. Scale bar is 100 nm.

AFM results reveal that optimized lateral morphology of thick active layer by the addition of DPE remarkably enhances J_{SC} and maintains high FF by improving exciton dissociation probability and reducing non-geminated recombination.

Figure 5.10 presents cross-sectional TEM images and energy dispersive X-ray spectroscopy (EDS) results of optimum devices prepared from different solvents. Component layers of the device were clearly seen in these images (**Figure 5.10a-c**). Thicknesses of optimum devices measured from TEM images were in good agreement with those measured by surface profiler (CF:DCB: 240 nm, CB: 300 nm, and CB:DPE: 340 nm). We performed EDS carbon (C) and sulfur (S) mapping of these cross-sections to investigate vertical distribution of polymer chains and $PC_{71}BM$ within BHJ film (**Figure 5.10d-f** and **Figure 5.11**). In EDS S mapping images, BHJ film prepared from CB had discontinuous network of polymer chains (**Figure 5.10e**), whereas films from CF:DCB and CB:DPE exhibited continuous and evenly distributed polymer network from bottom PEDOT:PSS to top Al electrode (**Figure 5.10d** and **5.10f**). This optimized vertical morphology promotes hole and electron transport along respective pathways of polymers and fullerenes in vertical direction, leading to high FF.
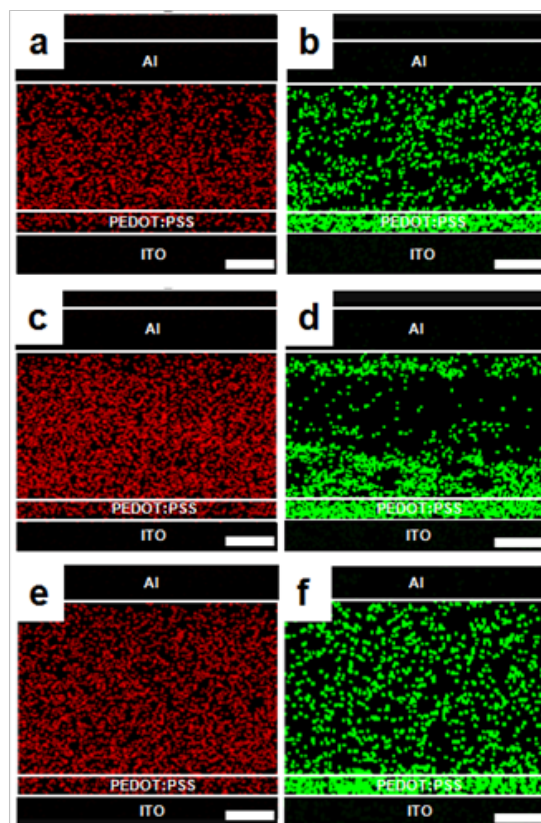
Figure 5.11. EDS C (red dots, left column) and S mapping (green dots, right column) of optimum BHJ film prepared from (a, b) CF:DCB, (c, d) CB, and (e, f) CB:DPE, respectively. Scale bar of EDS mapping is 100 nm.

To further study molecular orientation and packing characteristics of pristine polymer and blend films, we measured grazing incidence wide angle X-ray scattering (GIWAXS). **Figure 5.12** presents GIWAXS patterns of pristine polymer (**Figure 5.12a-c**) and BHJ films (**Figure 5.12d-f**) prepared from different solvents. The detailed GIWAXS profiles and parameters are shown in **Figure 5.13** and **Table 5.5**, respectively. We observed pronounced reflection peaks of (h00) in out-of-plane direction for pristine polymer films from CF:DCB and CB:DPE (**Figure 5.12a** and **5.12c**) and weak peaks for film from CB (**Figure 5.12b**). Corresponding inter-lamellar stacking distances of pristine polymer films from CF:DCB, CB, and CB:DPE were 21.16, 21.44, and 21.89 Å, respectively. All pristine polymer films showed π-π stacking peaks in both in-plane and out-of-plane directions, indicating mixed π-π edge-on and face-on orientation. However, weak π-π stacking peak in in-plane direction was only observed for film from CB. Resultant π-π edge-on and face-on stacking distances were 3.75 Å and 3.71 Å for film from CF:DCB, 3.83 Å and 3.70 Å for film from CB, 3.75 Å and 3.72 Å for films from CB:DPE, respectively. These π-π edge-on and face-on orientations of P2 polymer chains are favorable to high hole mobility in lateral and vertical directions.

For $P2:PC_{71}BM$ BHJ films prepared from CF:DCB and CB, lamellar stacking distances were

slightly increased to 21.44 Å and 21.58 Å, respectively, compared to those of pristine polymers. In contrast, blend film from CB:DPE exhibited shorter lamellar stacking distance of 21.16 Å, implying closer packing distance between side chains of neighboring polymer backbones by addition of DPE. In spite of disappearance of π-π stacking peaks in in-plane direction, all blend films still showed π-π stacking peaks in out-of-plane direction, corresponding to π-π stacking distances of 3.71, 3.72, and 3.62 Å for films from CF:DCB, CB, and CB:DPE, respectively. Notably, this π-π stacking distance of blend film from CB:DPE is shorter than those observed in BHJ films achieving high device performance (3.65-3.90 Å).[105, 269, 270] Shorter π-π stacking distance of polymer chains and dominant face-on orientation by addition of $PC_{71}BM$ and DPE are beneficial to charge-carrier mobility and charge transport in vertical direction[229], thereby leading to high J_{SC} and FF.
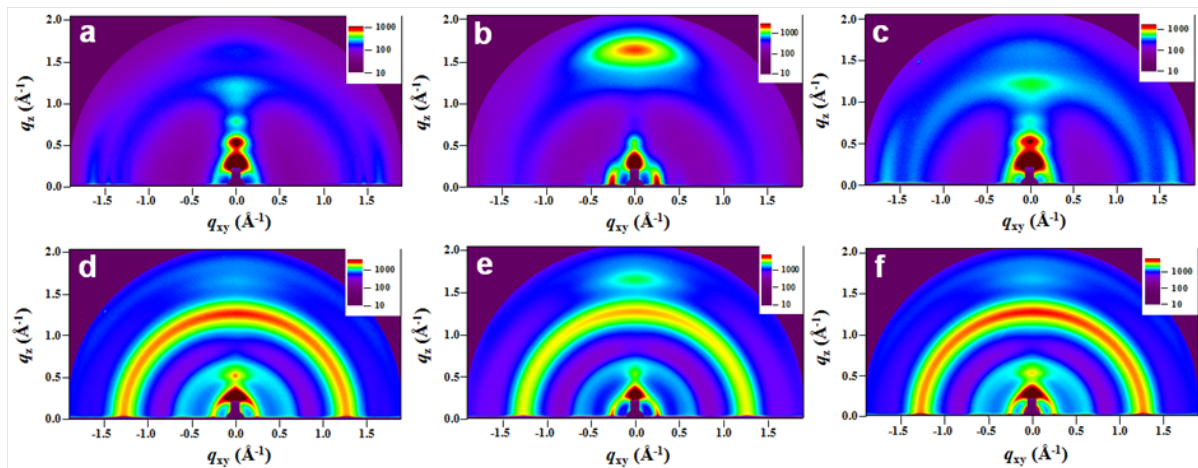
Figure 5.12. GIWAXS patterns of pristine polymer films prepared from CF:DCB (a), CB (b), and CB:DPE (c). d-f, GIWAXS patterns of $P2:PC_{71}BM$ BHJ films prepared from CF:DCB (d), CB (e), and CB:DPE (f).
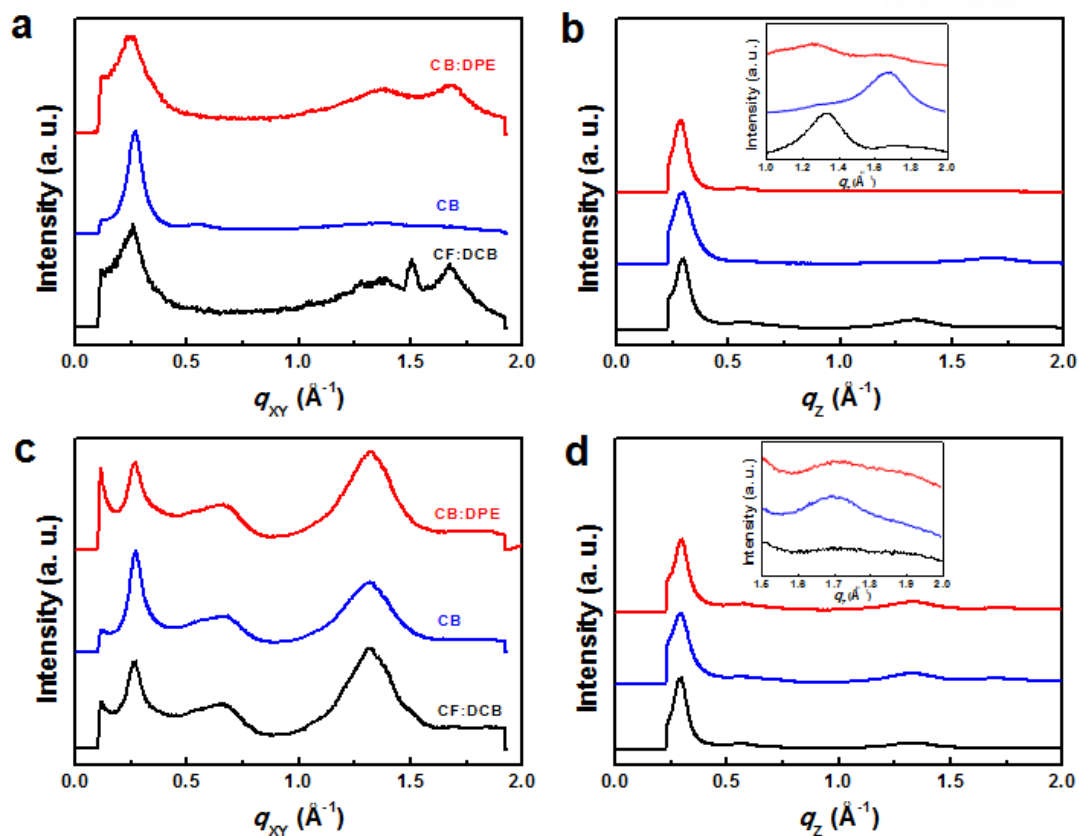
Figure 5.13. (a, c) In-plane and (b, d) out-of-plane linecuts of GIWAXS for pristine polymer (upper row) and blend films (lower row) prepared from different solvents. The Insets of Figure 5.13(b) and (d) indicate expanded out-of-plane linecuts for visualizing π-π face-on orientation.

Table 5.5. Summary of GIWAXS measurements for pristine polymer and BHJ films.

Films	Solvents	GIWAXS parameters					
		Lamellar spacing		π-π stack (q_{xy} direction)		π-π stack (q_z direction)	
		q ($Å^{-1}$)	d-spacing (Å)	q ($Å^{-1}$)	d-spacing (Å)	q ($Å^{-1}$)	d-spacing (Å)
Pristine Polymer	CF:DCB	0.2970	21.16	1.6776	3.75	1.6960	3.71
	CB	0.2931	21.44	1.6418	3.83	1.6960	3.70
	CB:DPE	0.2871	21.89	1.6758	3.75	1.6908	3.72
BHJ	CF:DCB	0.2931	21.44	-	-	1.6943	3.71
	CB	0.2911	21.58	-	-	1.6891	3.72
	CB:DPE	0.2970	21.16	-	-	1.7335	3.62
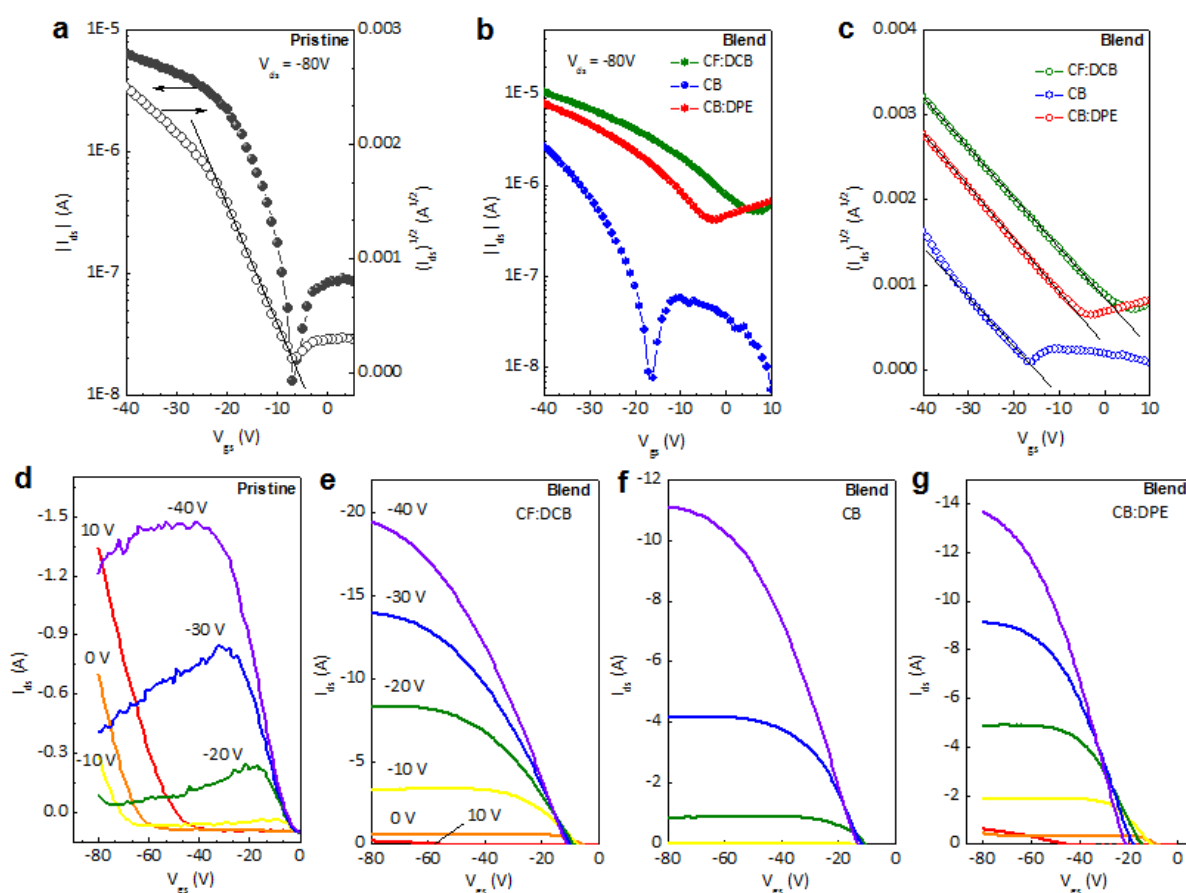
Figure 5.14. Transfer (upper row) and output (lower row) characteristics of OFET based on (a, d) pristine polymer prepared from CB and (b, c, e-g) blend films prepared from different solvents. Bottom-gate/bottom-contact on a Si/SiO$_2$ substrate with a channel length of 160 μm and a channel width of 1000 μm are used for OFET characterization. n-decyltrichlorosilane (DTS) was used as the self-assembled monolayer on Si/SiO$_2$ substrate.

Table 5.6. Device parameters of OFETs based on pristine polymer and blend films. Bottom gate/bottom-contact device geometry was used and mobility was calculated at the saturation region using a standard device formalism.

Films	Solvents	Mobility (cm^2 V^{-1}s^{-1})	V$_{th}$ (V)	I$_{on}$/I$_{off}$
Pristine	CB	0.37	-8.6	5.3 x 10^2
Blend	CF:DCB	0.09	1.7	17
	CB	0.16	-19.1	31
	CB:DPE	0.11	-5.3	18

We performed organic field-effect transistor (OFET) fabrication and space charge-limited current (SCLC) measurement to investigate lateral and vertical charge-carrier mobilities, respectively. Transfer and output characteristics of OFET with pristine polymer and blend films were shown in **Figure 5.14** and detailed OFET parameters were listed in **Table 5.6**. Hole mobility obtained from OFET results was 0.37 cm^2 V^{-1} s^{-1} for pristine polymer film at room temperature. This high hole mobility is consistent with pronounced π-π edge-on orientation of pristine polymer film observed in GIWAXS results. After blending with PC$_{71}$BM, there were no significant decreases in hole mobility for BHJ films prepared from different solvents (CF:DCB: 0.09 cm^2 V^{-1} s^{-1} CB: 0.16 cm^2 V^{-1} s^{-1}, and CB:DPE: 0.11 cm^2 V^{-1} s^{-1}). These imply that addition of PC$_{71}$BM into polymer chains has minor effect on formation of polymer pathways for hole transport in lateral direction. However, lateral mobility from OFET is insufficient to prove high performance of PSCs.

Since vertical charge-carrier mobility is one of critical factors for determining device efficiency, we fabricated hole- and electron-only devices for vertical mobility from SCLC measurements. *J-V* characteristics and detailed parameters of hole- and electron-only devices prepared from different solvents were shown in **Figure 5.15** and **Table 5.7**, respectively. Hole (μ_h) and electron mobilities (μ_e) obtained from SCLC measurements were 8.0 × 10^{-3} cm^2 V^{-1} s^{-1} and 7.6 × 10^{-3} cm^2 V^{-1} s^{-1} for the devices from CF:DCB, 6.0 × 10^{-3} cm^2 V^{-1} s^{-1} and 8.8 × 10^{-4} cm^2 V^{-1} s^{-1} for the devices from CB, 2.1 × 10^{-2} cm^2 V^{-1} s^{-1} and 1.8 × 10^{-2} cm^2 V^{-1} s^{-1} for the devices from CB:DPE, respectively. The devices from CB:DPE exhibited considerably higher μ_h and μ_e than those of the devices from CF:DCB and CB. Furthermore, well-balanced μ_h/μ_e ratios were observed in the devices from CF:DCB and CB:DPE (CF:DCB: 1.05, CB: 6.81, and CB:DPE: 1.17). To the best of our knowledge, vertical μ_h and μ_e of the devices from CB:DPE measured by SCLC method are the highest values among high performance BHJ PSCs reported to date.[229, 237, 269] These high vertical charge-carrier mobility is in good agreement with bicontinuous interpenetrating D:A network in vertical direction (**Figure 5.10**) and close π-π face-on orientation of polymer backbones (**Figure 5.12**), thereby confirming unprecedented *J*$_{SC}$ and high FF of the devices from CB:DPE. Moreover, this polymer shows all features to fabricate highly efficient tandem solar cells.
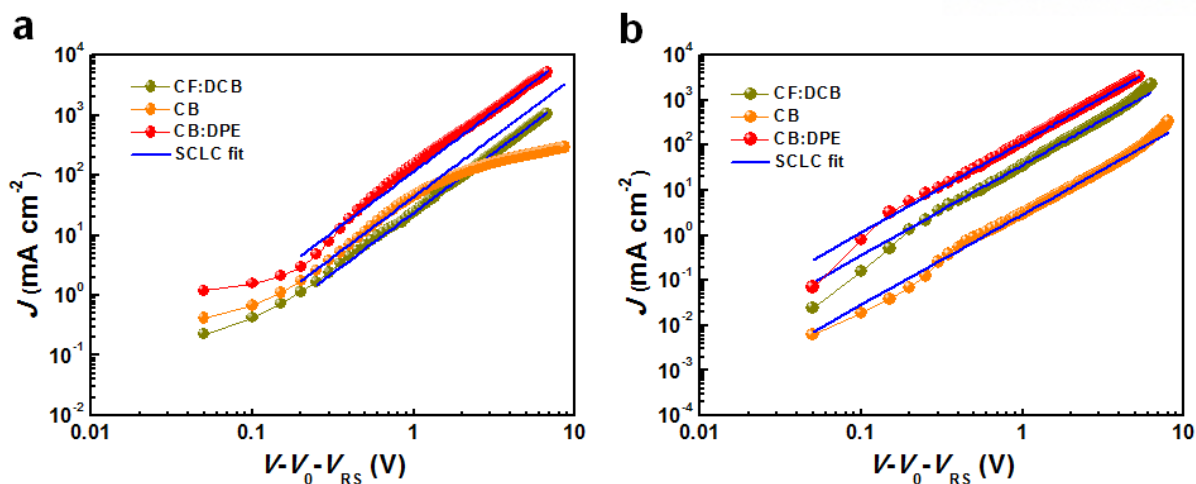
Figure 5.15. *J-V* characteristics of (a) hole- and (b) electron-only devices using P2:PC$_{71}$BM BHJ films prepared from different solvents. Blue lines indicate SCLC fits of curves based on Mott-Gurney relationship.

Table 5.7. Hole and electron mobilities obtained from hole- and electron-only devices using P2:PC$_{71}$BM BHJ films prepared from different solvents.

Solvent	Hole-only device		Electron-only device		μ_h/μ_e ratio
	Thickness (nm)	μ_h (cm^2 V^{-1}s^{-1})	Thickness (nm)	μ_e (cm^2 V^{-1}s^{-1})	
CF:DCB	465	8.0×10^{-3}	395	7.6×10^{-3}	1.05
CB	345	6.0×10^{-3}	455	8.8×10^{-4}	6.81
CB:DPE	385	2.1×10^{-2}	360	1.8×10^{-2}	1.17

Table 5.8. Comparison of our work with previous reports on small bandgap polymer solar cells.

Polymer [a]	Optical bandgap (eV)	Active layer thickness (nm)	J_{SC} (mA cm^{-2})	V_{OC} (V)	FF	PCE (%)	Ref. (journal /year)
PDPP	1.35	-[b]	14.84	0.63	0.60	5.62	*Adv. Mater.* 2012
DT-PDPP2T-TT	1.41	220	14.80	0.66	0.70	6.90	*Adv. Mater.* 2013
DT-PDPP4T	1.43	115	16.00	0.64	0.69	7.10	*J. Am. Chem. Soc.* 2013
DPPTT-T	1.40	-	19.00	0.56	0.59	5.60	*Adv. Funct. Mater.* 2013
PR2	1.40	-	13.52	0.77	0.58	6.04	*Energy Environ. Sci.* 2013
PBTT-TBDTT	1.45	-	12.63	0.75	0.53	5.10	*Chem. Mater.* 2014
PDPPFTF	1.38	100	11.35	0.71	0.58	4.70	*Adv. Energy Mater.* 2014
DT-PDPP2T-TT (P2)	1.41	340	20.07	0.67	0.70	9.40	**Our work**

[a] Small bandgap polymers are defined as conjugated polymers that have optical bandgap lower than 1.45 eV.

[b] "-" indicates that there is no mention about the thickness of the active layer.

5.4 Conclusion

In conclusion, based on a simple and conventional device structure of ITO/PEDOT:PSS/ P2:PC$_{71}$BM/Al, we have demonstrated high-performance small bandgap PSCs simultaneously yielding unprecedented J_{SC} and high FF for thicknesses over 300 nm. In comparison with the devices processed from other solvents, the device prepared from CB:DPE exhibits the highest PCEs of 9.40% with high J_{SC} of 20.07 mA cm^{-2} and FF of 0.70. This high device efficiency results from maximized light absorption by thick active layer, minimized recombination loss by bicontinuous interpenetrating D:A network, and high vertical charge-carrier mobility by close π-π face-on orientation. This work is a first report on bulk heterojunction PSCs based small bandgap (< 1.45 eV) polymers approaching device efficiency of 10% (**Table 5.8**), as well as provides new morphology engineering technique for further improvements of high-performance single-junction and conventional tandem PSCs consisting of small and large bandgap polymers.

Chapter 6. Improved Performance in Polymer Solar Cells Using Mixed PC$_{61}$BM / PC$_{71}$BM Acceptors

6.1 Research background

Considerable efforts have been made to improve the power conversion efficiencies (PCEs) of polymer/fullerene composite PSCs by various strategies including the synthesis of new materials,[175, 271-274] surface modification via interfacial engineering,[223, 251, 275-277] advanced device architectures,[278-281] and morphology control via processing solvents.[74, 117] These efforts have led to a better understanding of PSCs and recently have allowed record PCEs of 8-9% to be achieved.[256, 280, 282, 283]

Despite remarkable advances in recent years, there is still a room for further improvements in the PCE of PSCs. To increase the short-circuit current density (J_{SC}), broad light absorption into the near infrared region is desirable; this has been accomplished using small band gap conjugated donor materials.[232] However, the use of low band gap donor materials often results in low open-circuit voltages (V_{OC}) when donor:acceptor bulk heterojunction (BHJ) systems are formed with fullerene derivatives as acceptors. To overcome the limitations of binary blend PSCs, several studies have focused on ternary blend PSCs including two donors:one acceptor or one donor:two acceptors for the active layer.[125, 284] For instance, Thompson and coworkers reported both ternary blend systems. First, a BHJ consisting of two donor polymers with different ranges of light absorption and one acceptor resulted in an improvement in J_{SC} via increased light absorption.[285] Second, a blend system of one donor polymer and two acceptors allowed tuning of the V_{OC} by changing the blend ratio of acceptors.[137, 286] In the case of two acceptor blends, [6,6]-phenyl-C$_{61}$-butyric acid methyl ester (PC$_{61}$BM) and indene-C$_{60}$ bisadduct (ICBA) were chosen as acceptors with different lowest unoccupied molecular orbital (LUMO) energy levels. This study revealed that the V_{OC} could be controlled by adjusting the relative amounts of PC$_{61}$BM and ICBA. Although these studies demonstrated the potential of ternary blends to increase the light absorption and control V_{OC} with two-donor and two-acceptor systems, respectively, the overall PCEs in these ternary systems showed little or slight improvement relative to each binary blend.

[6,6]-phenyl-C$_{71}$-butyric acid methyl ester (PC$_{71}$BM) is an acceptor which is almost identical to PC$_{61}$BM in terms of its molecular structure, frontier orbital energy levels, electron mobility and electronic properties. However, the distorted geometry of PC$_{71}$BM relative to PC$_{61}$BM endows it with a much greater absorption coefficient in the visible region, allowing it to produce larger photocurrents compared to PC$_{61}$BM. In the past several years, PC$_{71}$BM has emerged as a highly effective acceptor and found widespread use in a variety of BHJ solar cells. Despite the ubiquitous use of PC$_{61}$BM and PC$_{71}$BM in BHJ solar cells, the investigation of ternary blend systems containing PC$_{61}$BM / PC$_{71}$BM mixtures with a donor material has yet to be reported, presumably because of the similar chemical

structures and electronic properties of $PC_{61}BM$ and $PC_{71}BM$, in which the V_{OC} does not change significantly, and the larger size and extinction coefficient of $PC_{71}BM$ (relative to $PC_{61}BM$) are the only apparent differences.

This paper reports a new approach to realize efficient ternary PSCs via the incorporation of both $PC_{61}BM$ and $PC_{71}BM$ as mixed acceptors and the conjugated polymer, poly(5,6-bis(octyloxy)-4-(thiophen-2yl)benzo[c][1,2,5]thiadiazole) (PTBT) as a donor. This report shows that the ternary blend of $PTBT:PC_{61}BM:PC_{71}BM$ results in remarkable improvement in the PCEs compared to binary mixtures of the components, via enhanced light absorption by $PC_{71}BM$ and balanced charge transport by $PC_{61}BM$.

6.2 Experimental

General: Poly(3,4-ethylenedioxythiophene):poly(4-styrenesulfonate) (PEDOT:PSS) (Baytron AI 4083 and PH500) were purchased from H. C. Starck (Germany). [6,6]-phenyl-C61-butyric acid methyl ester ($PC_{61}BM$) and [6,6]-phenyl-C71-butyric acid methyl ester ($PC_{71}BM$) were purchased from Electronic Materials (EM) Index Co., Ltd. The optical properties of composite films were analyzed using a UV-vis spectrophotometer (Varian Carry 5000). The atomic force microscopy (AFM) images (2 μm × 2 μm) were obtained using a Veeco AFM microscope in a tapping mode.

2D-GIXRD measurement: GIXRD measurements were carried out at PLS-II 9A U-SAXS beam line of Pohang Accelerator Laboratory, Korea. The X-ray coming from the in-vacuum undulator (IVU) was monochromated ($E_k = 11.24$ keV, $\lambda = 1.103$ Å) using a Si(111) double crystal monochromator and focused horizontally and vertically at the sample position (450 (H) x 60 (V) μm^2 in FWHM) using K-B type focusing mirror system. The GIXRD sample stage was equipped with a 7-axis motorized stage for the fine alignment of the thin sample and the incidence angle of X-ray was adjusted to 0.12 ° ~ 0.14 °. GIXRD patterns were recorded with a 2D CCD detector (Rayonix SX165, USA) and X-ray irradiation time was 0.5 ~ 5 s dependent on the saturation level of the detector. The diffraction angle was calibrated by a pre-calibrated sucrose (Monoclinic, P21, $a = 10.8631$ Å, $b = 8.7044$ Å, $c = 7.7624$ Å, $\beta = 102.938°$) and the sample-to-detector distance was about 232 mm.

Coherence length: Coherence length is given by the Scherrer equation;

$$\tau = \frac{K\lambda}{\beta \cos\theta}$$

Where:

- τ is the mean size of the ordered (crystalline) domains, which may be smaller or equal to the grain size;

- K is a dimensionless shape factor, with a value close to unity. The shape factor has a typical value of about 0.9, but varies with the actual shape of the crystallite;

- λ is the X-ray wavelength;

- β is the line broadening at the full width at half maximum (FWHM), after subtracting the instrumental line broadening, in radians. This quantity is also sometimes denoted as $\Delta(2\theta)$;

- θ is the Bragg angle.

Fabrication and characterization of PSCs: The PSC device was fabricated with a configuration of ITO/PEDOT:PSS/PTBT:PC$_{61}$BM:PC$_{71}$BM/Al. The devices were fabricated according to the following procedures: First, ITO-coated glass substrates were cleaned with detergent, then sequentially ultra-sonicated in acetone and isopropyl alcohol and dried in an oven overnight at 100 °C. The PEDOT:PSS layer was spin-coated (after filtration through a 0.45 µm filter) at 5000 rpm for 40 s, baked at 140 °C for 10 min in air and then moved into a nitrogen filled glove box. A mixed solution (0.68 wt%) of PTBT:PC$_{61}$BM (or PTBT:PC$_{71}$BM or PTBT:(PC$_{61}$BM+PC$_{71}$BM)) (blend ratio = 1:2 by weight) in chlorobenzene: 1,8-octanedithiol (98:2 vol%) was spin-coated at 1000 rpm for 60 s on top of the PEDOT:PSS layers. Devices were then brought under vacuum ($< 10^{-6}$ torr), and a 100 nm thick Al electrode was deposited on top of the active layer by thermal evaporation. The deposited Al electrode area defined the active area of the devices as 13 mm^2. Measurements were carried out inside a glove box using a high quality optical fiber to guide the light from the solar simulator. *J-V* characteristics were measured under AM 1.5G illumination (100 mWcm^{-2}) with a Keithley 2635A source measurement unit. EQE measurements were conducted in air using an EQE system (Model QEX7) by PV measurements Inc. (Boulder, Colorado).

PFET device fabrication: Highly doped n+-Si wafers were used as the substrates, and a layer of 200 nm of SiO$_2$ (grown by wet chemical process) was used as the gate dielectric. The substrates were cleaned by ultrasonic cleaning in high purity (Mili-Q) deionised water, acetone and isopropanol followed by drying overnight at 100 °C. The organic semiconductor layer was deposited by spin coating at 1000-1400 rpm. All the fabrication processes were carried out in a glove box filled with nitrogen. An 80 nm thick Ag layer was evaporated through a shadow mask to obtain the source and drain electrodes. An inter-digitated structure of source-drain contacts was used having a channel length of 50 μm and a channel width of 2,950 μm. Electrical characterization of the polymers was performed using a Keithley semiconductor parameter analyzer (Keithley 4200-SCS) under nitrogen.

6.3 Results and discussion

Figure 6.1 presents a schematic diagram of the ternary blend PSCs (ITO/PEDOT:PSS/active layer/Al, ITO: indium tin oxide, PEDOT:PSS: poly(3,4-ethylenedioxythiophene):poly(4-styrenesulfonate)) and the chemical structures of the donor and two acceptors, respectively. The conjugated polymer, PTBT, was synthesized and its photovoltaic properties were reported previously (number-average molecular weight, M_n = 30,000 g/mol).[175] The PTBT:$PC_{61}BM$ blend device exhibited a relatively low J_{SC} resulting from limited light absorption in the 400~600 nm range. Therefore, $PC_{71}BM$ was considered as a strategy to improve the J_{SC} by absorbing more photons in this range. Unfortunately, the binary blend of PTBT:$PC_{71}BM$ showed only slight improvement in PCE compared to the PTBT:$PC_{61}BM$ system. Although the J_{SC} improved substantially (from 9.82 to 12.39 mA·cm^{-2}) using $PC_{71}BM$ as an acceptor instead of $PC_{61}BM$, the fill factor (FF) was reduced (from 0.65 to 0.53), while the V_{OC} remained almost the same (0.89 vs. 0.90 V), resulting in similar PCEs of 5.68 and 5.91% for PTBT:$PC_{61}BM$ and PTBT:$PC_{71}BM$, respectively (**Table 6.1**). To overcome the decrease in FF, ternary blends containing both $PC_{61}BM$ and $PC_{71}BM$ were explored as a strategy to exploit the advantages of both acceptors.
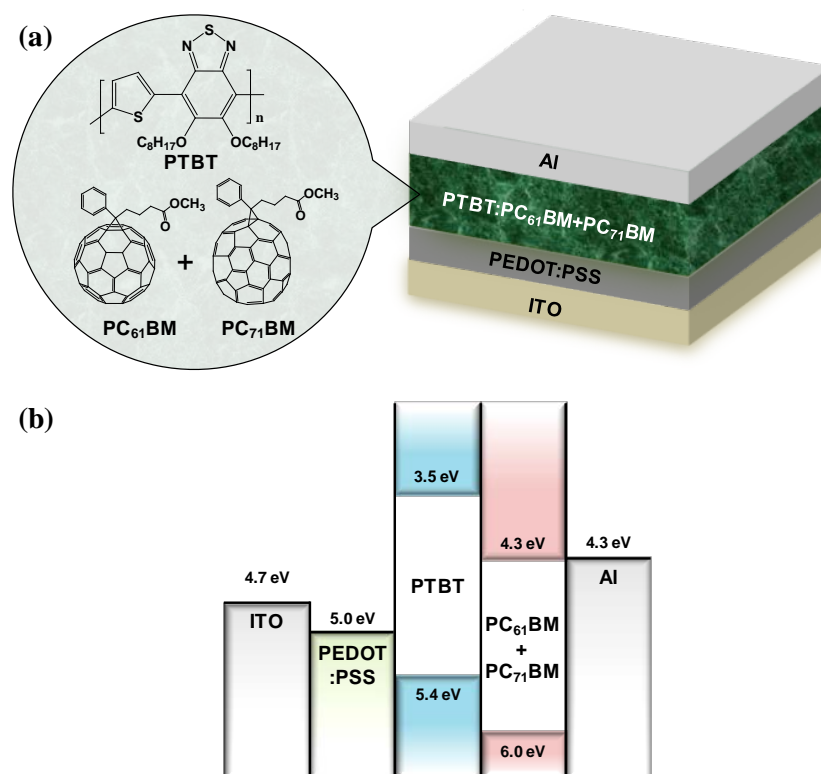
Figure 6.1. a) Schematics of a ternary blend BHJ solar cell with chemical structures of PTBT, $PC_{61}BM$, and $PC_{71}BM$ and b) energy band diagram of the ternary blend device.
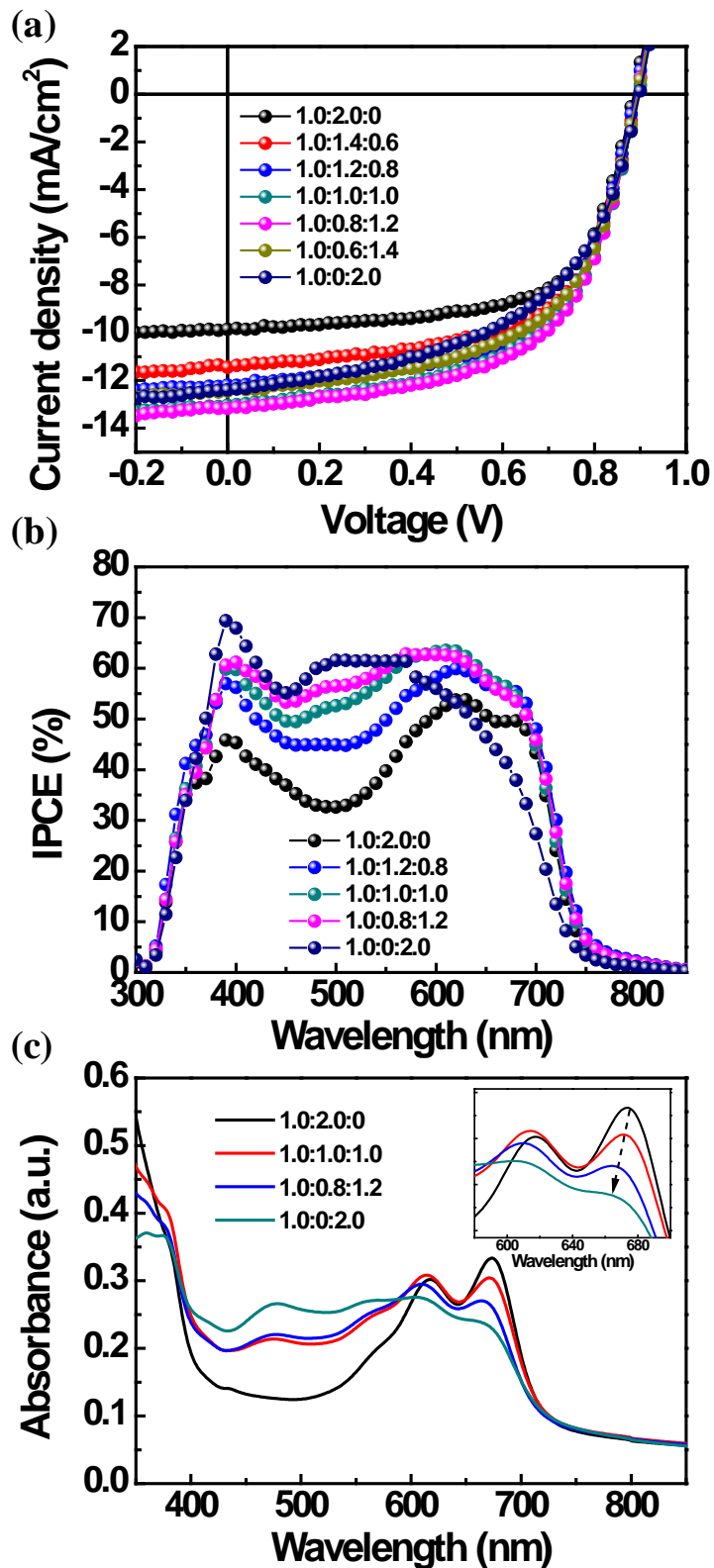
Figure 6.2. a) *J-V* characteristics, b) IPCE curves, and c) absorption spectra of ternary blend BHJ solar cells with changing a blend ratio of PTBT:$PC_{61}BM$:$PC_{71}BM$.

Table 6.1. Photovoltaic parameters of ternary blend BHJ solar cells with changing a blend ratio (PTBT:PC$_{61}$BM:PC$_{71}$BM).

PTBT : PC$_{61}$BM : PC$_{71}$BM	J_{SC} [mA cm^{-2}]	V_{OC} [V]	FF	PCE [%]	Calculated J_{SC} [mA cm^{-2}]
1:2 (1:2:0)	9.82	0.89	0.65	5.68	9.56
1:2 (1:1.4:0.6)	11.44	0.89	0.62	6.31	10.87
1:2 (1:1.2:0.8)	12.18	0.89	0.60	6.50	11.53
1:2 (1:1:1)	13.03	0.90	0.59	6.91	12.28
1:2 (1:0.8:1.2)	13.20	0.90	0.59	7.00	12.57
1:2 (1:0.6:1.4)	12.58	0.90	0.57	6.45	12.05
1:2 (1:0:2)	12.39	0.90	0.53	5.91	11.50

Figure 6.2a and **b** show the current density-voltage (*J-V*) characteristics and incident photon-to-current efficiency (IPCE) of binary and ternary blend PSCs upon changing the ratio of the two acceptors. The PTBT:PC$_{61}$BM binary device showed a J_{SC} of 9.82 mA·cm^{-2}, V_{OC} of 0.89 V, FF of 0.65, and a resulting PCE of 5.68%. As the amount of PC$_{71}$BM in the ternary blends increased, the FF decreased gradually and the J_{SC} reached a peak at a ratio of 1.0:0.8:1.2 (**Figure 6.3** and **Table 6.1**). A peak PCE of 7% was obtained with the composition PTBT:PC$_{61}$BM:PC$_{71}$BM = 1.0:0.8:1.2, showing a J_{SC} of 13.2 mA·cm^{-2}, V_{OC} of 0.9 V, and FF of 0.59, whereas the binary PTBT:PC$_{71}$BM device showed a PCE of only 5.91% (J_{SC}: 12.39 mA·cm^{-2}, V_{OC}: 0.9 V, FF: 0.53). These results show that the addition of PC$_{71}$BM improves light absorption, resulting in an enhanced J_{SC}, but possibly appears to promote geminate- and/or non-geminate recombination, which reduces the FF and J_{SC} as the PC$_{71}$BM concentration becomes too high (see **Figure 6.3a**). Fine-tuning of the ternary blend ratio allowed realization of the advantages of both PC$_{61}$BM (high FF) and PC$_{71}$BM (high J_{SC}).

Figure 6.2c shows the UV-vis absorption spectra of the binary and ternary blend films with different PTBT:PC$_{61}$BM:PC$_{71}$BM blend ratios in the photoactive layer. The shoulder peak at approximately 670 nm, which originates from the π-π inter-chain interactions in a solid thin film, decreases gradually, whereas the absorption around 400-600 nm increases with increasing PC$_{71}$BM content. The increase of PC$_{71}$BM in the mixture clearly enhances the light absorption but might disrupt the intermolecular ordering and π-π interactions.
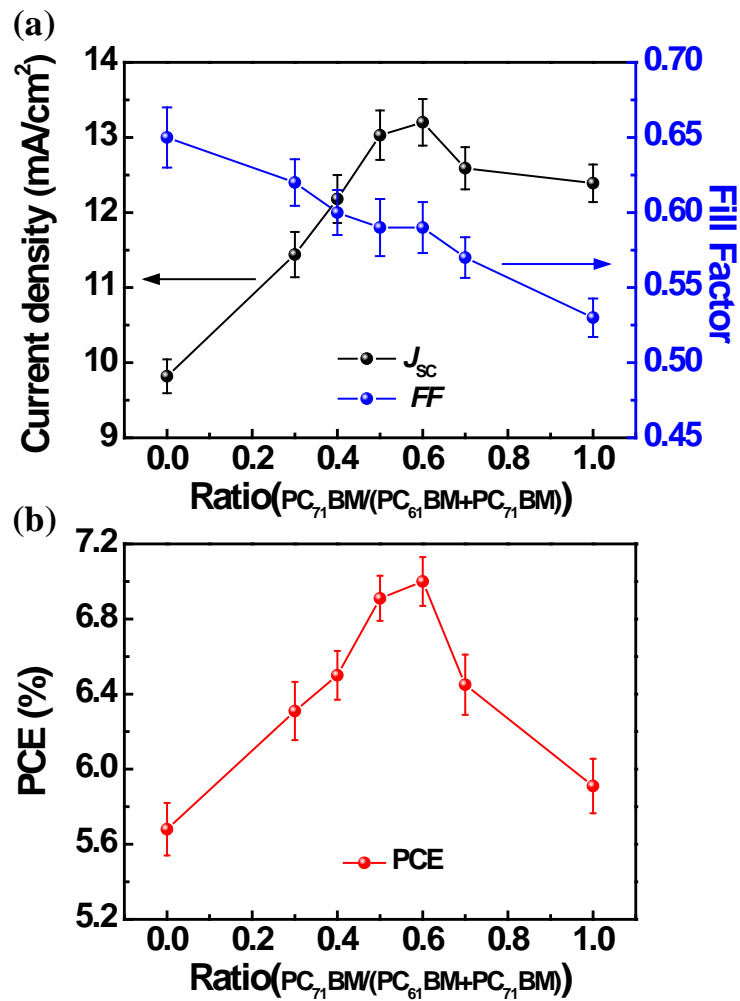
Figure 6.3. a) J_{SC}, FF, and b) PCE for the ternary blend BHJ solar cells with changing the composition in the photoactive layer.
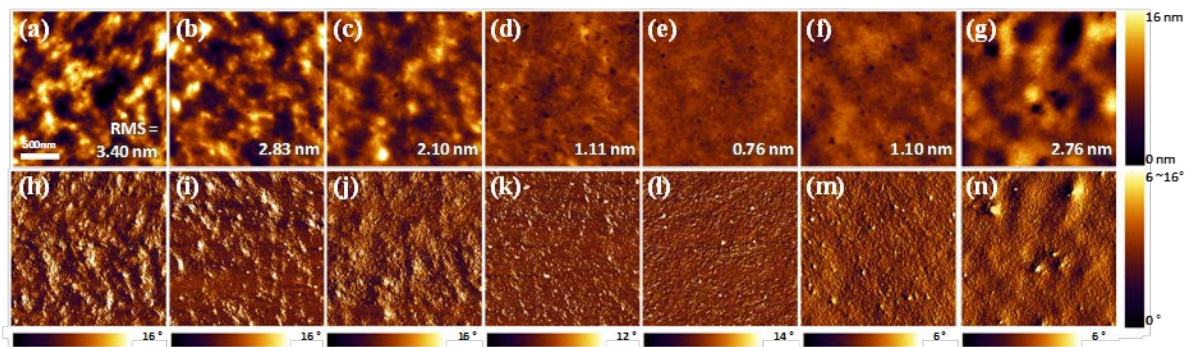
Figure 6.4. AFM images of PTBT:PC$_{61}$BM:PC$_{71}$BM blend films. a), h) 1.0:2.0:0, b), i) 1.0:1.4:0.6, c), j) 1.0:1.2:0.8, d), k) 1.0:1.0:1.0, e), l) 1.0:0.8:1.2, f), m) 1.0:0.6:1.4, and g), n) 1.0:0:2.0 (top: topograph images, bottom: phase images).

To examine the effects of $PC_{71}BM$ addition on the FF, the film morphology was examined by atomic force microscopy (AFM) and two-dimensional grazing incidence X-ray diffraction (2D-GIXRD) for the binary and ternary blend systems. AFM and 2D-GIXRD samples were prepared using silicon substrates under the same processing conditions used for device fabrication. The film morphology of the ternary blends showed significant differences compared to each binary blend, as shown in AFM images (**Figure 6.4**). The ternary blended films showed much smoother surfaces (root mean square (RMS) roughness, 0.76~2.83 nm) than those of the two binary blends (2.76 and 3.40 nm). For the ternary BHJ systems with increasing the $PC_{71}BM$ content, the crystalline intermolecular ordering may be hindered, inducing a featureless film morphology. Although the reason why the $PC_{61}BM$ and $PC_{71}BM$ mixture induces the smoother surface is not very clear at a present stage, the smooth surface may improve the contact between the active layer and cathode (Al), yielding better charge transport to the cathode in the ternary blend system.
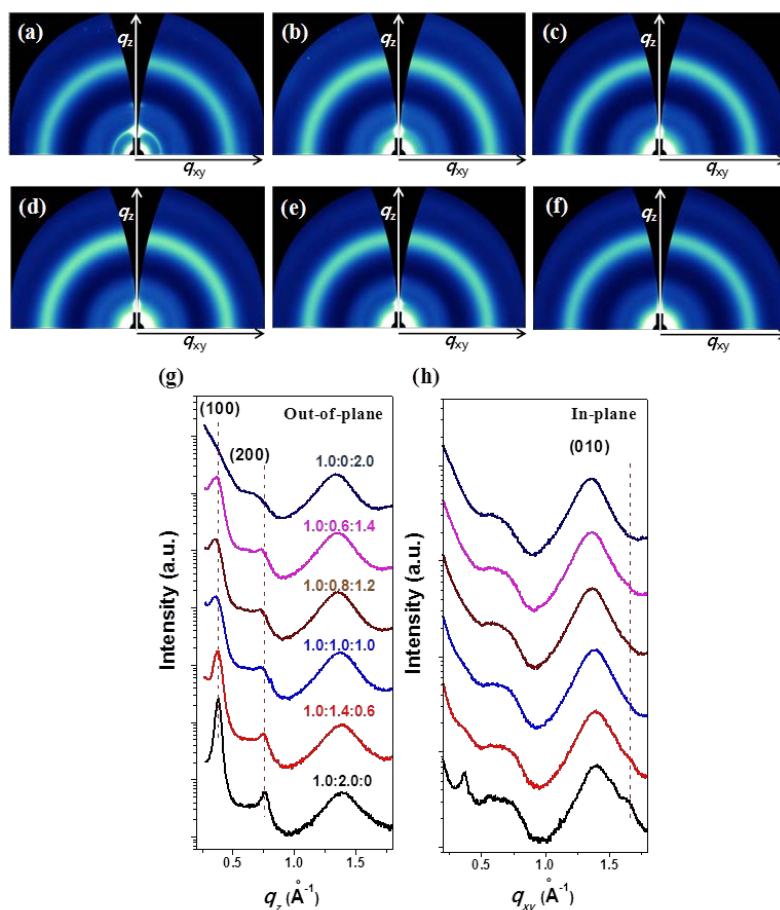
Figure 6.5. 2D-GIXRD images with changing the $(PTBT:PC_{61}BM:PC_{71}BM)$ blend ratio. a) 1.0:2.0:0, b) 1.0:1.4:0.6, c) 1.0:1.0:1.0, d) 1.0:0.8:1.2, e) 1.0:0.6:1.4, and f) 1.0:0:2.0. g) out-of-plane and h) in-plane scattering profiles along the q_z and q_{xy} axis, respectively

Table 6.2. 2D-GIXRD packing parameters along the in-plane and out-of-plane directions.

	1.0:2.0:0	1:1.4:0.6	1.0:1.0:1.0	1.0:0.8:1.2	1.0:0.6:1.4	1.0:0:2.0
$q_{z(100)}$ (Å^{-1})	0.3820	0.3770	0.3655	0.3619	0.3671	n/a
$d_{(100)}$-spacing (Å)	16.45	16.67	17.19	17.36	17.12	
FWHM$_{(100)}$ (Å^{-1})	0.0433	0.0616	0.0757	0.0743	0.0805	
Coherence length (Å) (L_{100})	130.6	91.8	74.7	76.1	70.3	
$q_{xy(010)}$ (Å^{-1})	1.6390	1.6463	n/a			
$d_{(010)}$-spacing (Å)	3.83	3.82	n/a			

Figure 6.5 and **Table 6.2** show the 2D-GIXRD scattering patterns and detailed interference profiles along the in-plane and out-of-plane directions for the binary and ternary blend films. The PTBT:PC$_{61}$BM binary blend exhibited well resolved first (100) and second order (200) inter-lamellar reflections peaks along the out-of-plane direction (q_z = ~0.38 Å^{-1}, d-spacing = ~16.45 Å) and a weak π-π stacking peak (010) along the in-plane direction (q_{xy} = ~1.64 Å^{-1}, d-spacing = ~3.83 Å), indicating a preferential edge-on orientation. A weak inter-lamellar scattering (100) along the in-plane direction was also observed, indicating that an isotropic structure also exists. The broad scattering peak at q_{xy} = ~1.35 Å^{-1} originates from fullerene moieties. However, the scattering intensity of inter-lamellar (100 and 200) and π-π stacking (010) peaks clearly decreased with increasing PC$_{71}$BM content and almost vanished with the PTBT:PC$_{71}$BM binary system (**Figure 6.5g** and **6.5h**). We also calculated coherence length (L_{100}) deduced from the full width at half maximum (FWHM) of inter-lamellar peaks (100), which indicates the mean size of the polymer crystallites. The values substantially decreased with increasing the PC$_{71}$BM content from 130.6 Å (1.0:2.0:0) to 74.7 Å (1.0:1.0:1.0), and further decreased to 70.3 Å (1.0:0.6:1.4) before the disappearance of the inter-lamellar peak (100) in the PTBT:PC$_{71}$BM binary blend (**Table 6.2**). Interestingly, inter-lamellar distance gradually increased with increasing PC$_{71}$BM content, and decreased again in the PTBT:PC$_{71}$BM binary blend. This might be correlated to the decreased crystalline ordering in the ternary blends with the smoother film surface relative to the binary systems (see AFM images in **Figure 6.4**). According to the 2D-GIXRD data, PC$_{71}$BM decreases crystalline ordering of the donor polymer and induces morphological changes on a molecular scale, which is related closely to the decrease in FF. The fullerene derivatives lead to disruption in the intermolecular packing structure, which is more prominent for PC$_{71}$BM than PC$_{61}$BM. The trend in the 2D-GIXRD measurements shows a good agreement with that in UV-vis spectra in **Figure 6.2c**.

Table 6.3. Charge carrier mobility for ternary BHJ films with different blend ratios (PTBT:PC$_{61}$BM:PC$_{71}$BM) via SCLC measurements

PTBT : PC$_{61}$BM : PC$_{71}$BM	Electron mobility (cm^2 V^{-1}s^{-1})	Hole mobility (cm^2 V^{-1}s^{-1})	Electron/Hole fraction
1:2 (1:2:0)	9.8 x 10^{-4}	1.8 x 10^{-4}	5.44
1:2 (1:1:1)	9.6 x 10^{-4}	1.4 x 10^{-4}	6.64
1:2 (1:0.8:1.2)	9.7 x 10^{-4}	1.2 x 10^{-4}	7.92
1:2 (1:0:2)	9.5 x 10^{-4}	7.5 x 10^{-5}	12.67

Electron and hole mobilities were also examined to understand the compositional dependence of the photovoltaic characteristics using the space-charge-limited current (SCLC) technique and the fabrication of polymer field effect transistors (PFETs). We fabricated the hole (ITO/PEDOT:PSS/active layer/Au) and electron (FTO/active layer/Al, FTO: fluorine doped tin oxide) only devices, from which the charge carrier mobilities were extracted based on the SCLC model. The device based on the PTBT:PC$_{61}$BM blend exhibited an electron mobility of 9.8×10^{-4} cm$^2 \cdot$V$^{-1} \cdot$s^{-1} and a hole mobility of 1.8×10^{-4} cm$^2 \cdot$V$^{-1} \cdot$s^{-1} with an electron/hole mobility ratio of 5.44, as shown in **Table 6.3**. With increasing PC$_{71}$BM content, the electron mobility showed little change ($9.3 \sim 9.5 \times 10^{-4}$ cm$^2 \cdot$V$^{-1} \cdot$s^{-1}) but the hole mobility decreased gradually, suggesting decreased inter-chain ordering in the ternary blend system. In the PTBT:PC$_{71}$BM device, the electron/hole mobility ratio was 12.67, showing an enhanced imbalance in the carrier mobility ($\mu_e = 9.5 \times 10^{-4}$ and $\mu_h = 7.5 \times 10^{-5}$ cm$^2 \cdot$V$^{-1} \cdot$s^{-1}, respectively). These SCLC results are also consistent with the UV-vis and 2D-GIXRD data. Therefore, the imbalance between the electron and hole mobilities must be related to the decrease in FF.

To confirm the in-plane ordering and resulting charge carrier mobility, PFET devices were also fabricated and characterized under the same conditions used for PSCs fabrication. **Figure 6.6** and **Table 6.4** summarize the transfer and output characteristics for the neat polymer film as well as the binary and ternary blend films. The hole mobility of PTBT itself was measured to be 1.15×10^{-2} cm$^2 \cdot$V$^{-1} \cdot$s^{-1} from a 1 wt.% solution in chlorobenzene:1,8-octanedithiol (98:2 vol%). Upon blending with the fullerene derivatives, the composites exhibited ambipolar characteristics (both p-channel and n-channel operation), showing a substantial decrease in the hole mobility ($\sim 10^{-4}$ cm$^2 \cdot$V$^{-1} \cdot$s^{-1}) compared to that of PTBT itself. Interestingly the electron mobility of all blends remained fairly constant in the range of 2.1 to 2.5×10^{-3} cm$^2 \cdot$V$^{-1} \cdot$s^{-1}, the hole mobility was significantly lower for the binary PTBT:PC$_{71}$BM blend film with a larger imbalance in the electron and hole mobilities ($\mu_e/\mu_h = 48.9$).

With compared to PTBT:PC$_{71}$BM, the binary PTBT:PC$_{61}$BM and ternary blend systems showed the relatively small values of μ_e/μ_h = 9.3~12.0.
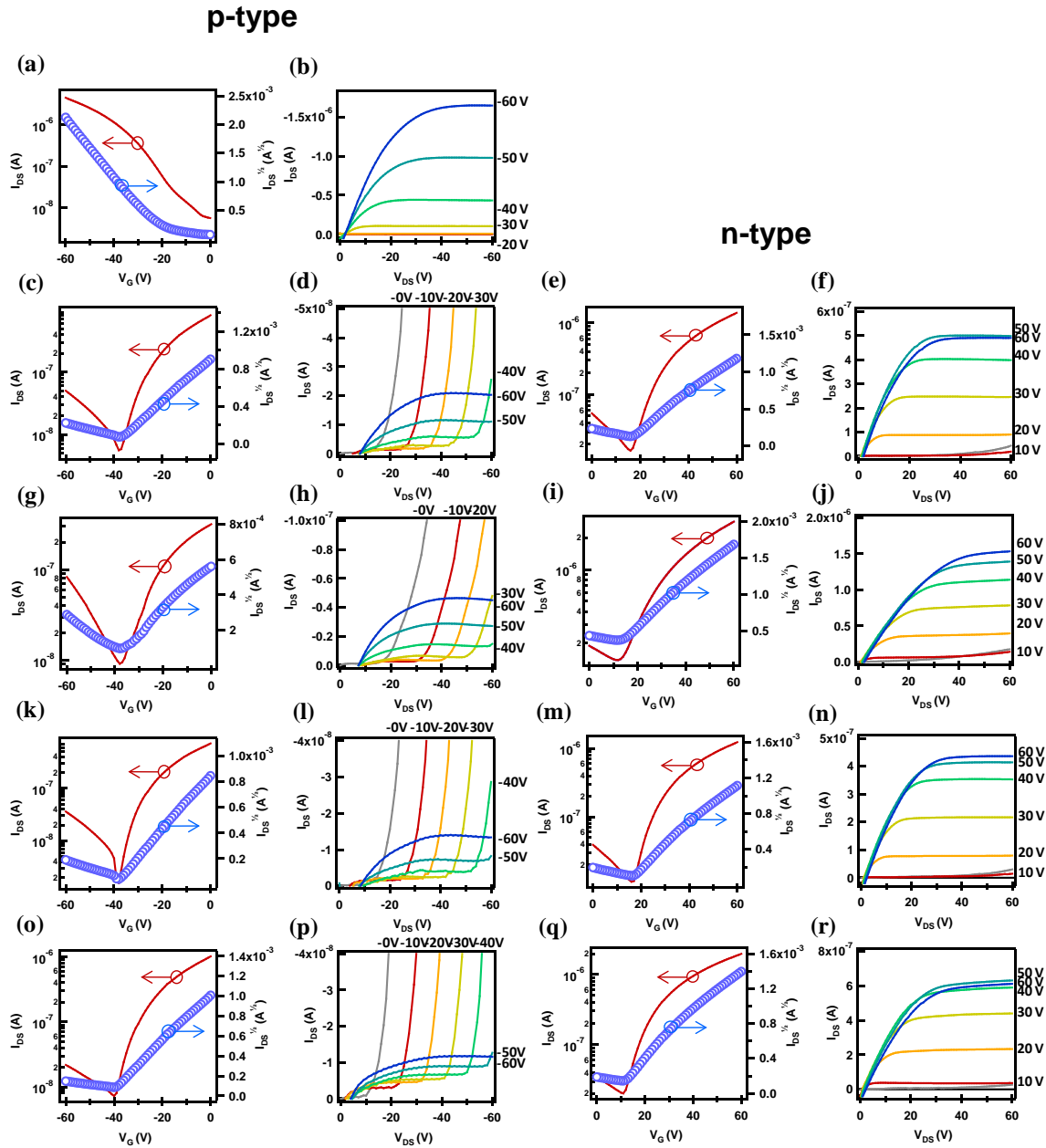
Figure 6.6. FET characteristics of PTBT itself (a, b) and composite films with changing a blend ratio, 1.0:2.0:0 (c~f), 1.0:1.0:1.0 (g~j), 1.0:0.8:1.2 (k~n) and 1.0:0:2.0 (o~r). Transfer characteristics for p-channel operation are displayed in a), c), g), k) and o). Output characteristics for p-channel operation are displayed in b), d), h), l) and p). Transfer characteristics for n-channel operation are displayed in e), i), m) and q). Output characteristics for n-channel operation are displayed in f), j), n) and r).

Table 6.4. Ambipolar device parameters of ternary blend BHJ FETs via different blend ratio ($PTBT:PC_{61}BM:PC_{71}BM$).

$PTBT : PC_{61}BM : PC_{71}BM$	Electron mobilities ($cm^2 V^{-1} s^{-1}$)	Hole mobilities ($cm^2 V^{-1} s^{-1}$)	Electron/Hole fraction
Only PTBT(w/o ODT)	/	9.59×10^{-3}	/
PTBT (w/ ODT)	/	1.15×10^{-2}	/
1:2 (1:2:0)	2.46×10^{-3}	2.13×10^{-4}	11.5
1:2 (1:1:1)	2.14×10^{-3}	2.31×10^{-4}	9.3
1:2 (1:0.8:1.2)	2.10×10^{-3}	1.75×10^{-4}	12.0
1:2 (1:0:2)	2.35×10^{-3}	4.81×10^{-5}	48.9

Taking all of the experimental observations (UV-vis, 2D-GIXRD, SCLC and FET measurements) into account, it becomes apparent that the bigger size, lower symmetry and oblong shape of $PC_{71}BM$ lead to substantial decrease in the crystalline organization of PTBT. The decreased inter-chain ordering gives rise to the reduced hole mobility and imbalance in the electron / hole mobility ratio, deteriorating the FF values in $PC_{71}BM$-rich devices. $PC_{71}BM$ improves J_{SC} by virtue of its larger extinction coefficient in the visible region, compared to $PC_{61}BM$. However, $PC_{71}BM$ also disrupts the crystalline morphology of PTBT with decreased FF. It is important to fine-tune the composition of ternary BHJ films to fully utilize the enhanced light absorption of $PC_{71}BM$ with the minimized FF deterioration. The optimal ternary device was achieved with the compositon of $PTBT:PC_{61}BM:PC_{71}BM$ = 1:0.8:1.2. Consequently, by mixing the two acceptors, the weak points of each binary system PSC containing only $PC_{61}BM$ (low J_{SC}) and $PC_{71}BM$ (low FF) were successfully compensated using the ternary blend system (**Figure 6.3**), demonstrating the device optimization by fine-controlling the $PC_{61}BM:PC_{71}BM$ composition of ternary blends.

6.4 Conclusion

In summary, an efficient ternary blend PSC was reported using a single donor (PTBT) and two acceptors ($PC_{61}BM$ and $PC_{71}BM$). By combination of $PC_{61}BM$ and $PC_{71}BM$ as an acceptor, we fully utilized advantages of both $PC_{61}BM$ (high FF) and $PC_{71}BM$ (high J_{SC}) by fine-controlling the ternary composition and the resulting photovoltaic characteristics. With increasing the $PC_{71}BM$ fraction in the ternary blend systems, the light absorption (in a range of 400 ~ 600 nm) substantially increases and the resulting J_{SC} was maximized at the $PTBT:PC_{61}BM:PC_{71}BM$ = 1:0.8:1.2. The V_{OC} showed a negligible change with different compositions due to the same electronic structures of two fullerene derivatives. However, the FF gradually decreased due to the disruption of inter-chain ordering of PTBT (with decreased hole mobility and increased e-h recombination), via the bigger, lower symmetry and oblong shaped $PC_{71}BM$. Here, we emphasize that it is possible to optimize the ternary blend PSC by fine-control the composition to take advantage of strong light absorption by $PC_{71}BM$ with minimizing the damages in the polymer chian ordering. The optimized ternary blend (1:0.8:1.2) PSC exhibited 7% PCE with clearly improved J_{SC} (13.20 mA·cm^{-2} relative to 9.82 mA·cm^{-2} of $PTBT:PC_{61}BM$) and FF (0.59 relative to 0.53 of $PTBT:PC_{71}BM$).   This shows a successful example of a ternary BHJ PSC showing a substantial PCE improvement (from 5.68 and 5.91 to 7.0%) with compared to the corresponding binary systems. Although ternary systems do not always guarantee the higher device efficiency than the binary systems, ternary systems suggest a great potential to further improve the device properties. By judicious consideration of weak points of binary systems, it may be possible to improve poor device parameters via synergistic interactions between multiple donors or multiple acceptors in ternary systems.

Chapter 7. Summary

In this thesis, I focused on various engineerings which are surface plasmon resonance (SPR) effect using PEDOT:PSS electrode doped with silver nanoparticels, morphology control using diphenly ether (DPE) as a novel processing additive with conjugated polymers (PPDT2FBT and P2), and ternary blend using a $PC_{61}BM$ and $PC_{71}BM$ mixture with a donor polymer resulting in enhaced electromagnetic field to provide light confinement to active layer, well-formed phase separation to make good pathway for electron and holes, and overcoming problem of binary BHJ solar cells (lower J_{SC} and FF), respectively, for the highly efficient light harvesting of polymer solar cells.

First, I successfully demonstrated ITO-free PSCs and PLEDs with the SPR effect and the possibility of solution-processed PEDOT:PSS containing Ag NPs as a flexible plastic electrode. The Ag NPs-incorporated Ag@NMP:PH500 electrode exhibited a high conductivity of 450 S cm^{-1} with similar transparency to ITO. The PSC device based on PTBT:PC61BM with the Ag@NMP:PH500 electrode showed a 1% absolute enhancement in the power conversion efficiency (3.27 to 4.31%), whereas the power efficiency of the PLEDs was improved by 124% (3.75 to 8.4 lm W^{-1}) compared to the reference devices without Ag NPs. The SPR effect and improved electrical conductivity by the Ag NPs clearly contributed to increments in light absorption/emission in the active layer as well as the conductivity of the PEDOT:PSS electrode in PSCs and PLEDs. The solution-processable conducting polymer-based electrode, Ag@NMP:PH500 with Ag NPs, is a promising candidate as a flexible electrode for large area and flexible optoelectronic devices with a low-cost fabrication process.

Second, I successfully demonstrate efficient morphology control of active layer using efficient processing additive, DPE. ; 1) A series of dialkoxyphenylene-BT containing semicrystalline LBG polymers were synthesized with noncovalent conformational locking to enhance chain planarity, intermolecular ordering and thermal stability without losing solution processability. The polymers formed well-distributed interpenetrating nano-fibrillar networked morphologies with $PC_{71}BM$, showing well-balanced hole and electron mobilities. Notably, PSCs based on these polymers exhibited PCEs of up to 9.39% in a 290 nm thick conventional single-cell device structure without any additional interfacial layer. The thick active layer (290 nm) in the PPDT2FBT:$PC_{71}BM$ device enabled strong light absorption, yielding a high J_{SC} of 15.7–16.3 mA cm^{-2} without the loss in V_{OC} and FF. It is of great importance to develop photovoltaic materials which can function effectively at the thicker film which can absorb solar light completely and is viable to be produced using industrial solution processing techniques. These remarkable device characteristics with the great thickness are closely related to the highly ordered organization of polymer chains via noncovalent attractive interactions, showing nano-fibrillar structures in TEM with tight interchain packing (a π–π stacking distance of 3.57–3.59 Å) in the blend films. In addition, we also measured clear molecular weight dependence on the photovoltaic properties. We synthesized more than 20 batches of PPDT2FBT to optimize the

photovoltaic characteristics. Among them, the high molecular weight batches (with ~40 kDa) showed the PCE over 8–9% but small molecular weight batches showed the relatively lower PCE values (~7%). The detailed study on the molecular weight dependence is now under investigation. Furthermore, this work also demonstrates a high PCE of over 7% (without any post-treatments) with long-term thermal stability at 130 °C for ~200 h. These new polymers provide a great possibility to overcome the efficiency barrier of 10% and accelerate the real application of plastic solar cells; 2) the high carrier mobilities and complete carrier extraction from thick active layers evidently result from the strong out-of-plane π-π stacking and unique internal structure observed in PPDT2FBT:PC$_{71}$BM films. We conclude that these physical characteristics allow photo-dissociated electron-hole pairs to be collected from the active layer with almost 100% efficiency using exceptionally thick films. This economy of charge carrier extraction from thick films has thus far only been achieved in crystalline inorganic solar cells and has constituted a major hurdle limiting the application of organic solar cells. The energy band structure of PPDT2FBT allows near complete attenuation of incident photons with wavelengths up to 700 nm coupled with a V_{OC} of almost 0.8 V and a PCE of over 9%. We envision that if the same approach to engineering polymer self-assembly can be accomplished with a conjugated polymer having a narrower band gap (and thus higher J_{SC}), or deeper HOMO band (and thus higher V_{OC}), efficiencies of over 10% can be readily achieved, paving the way to commercially profitable organic solar cells; 3) I have demonstrated high-performance small bandgap PSCs simultaneously yielding unprecedented J_{SC} and high FF for thicknesses over 300 nm. In comparison with the devices processed from other solvents, the device prepared from CB:DPE exhibits the highest PCEs of 9.40% with high J_{SC} of 20.07 mA cm^{-2} and FF of 0.70. This high device efficiency results from maximized light absorption by thick active layer, minimized recombination loss by bicontinuous interpenetrating D:A network, and high vertical charge-carrier mobility by close π-π face-on orientation. This work is a first report on bulk heterojunction PSCs based small bandgap (< 1.45 eV) polymers approaching device efficiency of 10% (**Table 5.8**), as well as provides new morphology engineering technique for further improvements of high-performance single-junction and conventional tandem PSCs consisting of small and large bandgap polymers.

Finally, I demonstrated an efficient ternary blend PSC was reported using a single donor (PTBT) and two acceptors (PC$_{61}$BM and PC$_{71}$BM). By combination of PC$_{61}$BM and PC$_{71}$BM as an acceptor, we fully utilized advantages of both PC$_{61}$BM (high FF) and PC$_{71}$BM (high J_{SC}) by fine-controlling the ternary composition and the resulting photovoltaic characteristics. With increasing the PC$_{71}$BM fraction in the ternary blend systems, the light absorption (in a range of 400 ~ 600 nm) substantially increases and the resulting J_{SC} was maximized at the PTBT:PC$_{61}$BM:PC$_{71}$BM = 1:0.8:1.2. The V_{OC} showed a negligible change with different compositions due to the same electronic structures of two fullerene derivatives. However, the FF gradually decreased due to the disruption of inter-chain

ordering of PTBT (with decreased hole mobility and increased e-h recombination), via the bigger, lower symmetry and oblong shaped $PC_{71}BM$. Here, we emphasize that it is possible to optimize the ternary blend PSC by fine-control the composition to take advantage of strong light absorption by $PC_{71}BM$ with minimizing the damages in the polymer chian ordering. The optimized ternary blend (1:0.8:1.2) PSC exhibited 7% PCE with clearly improved J_{SC} (13.20 mA·cm^{-2} relative to 9.82 mA·cm^{-2} of $PTBT:PC_{61}BM$) and FF (0.59 relative to 0.53 of $PTBT:PC_{71}BM$). This shows a successful example of a ternary BHJ PSC showing a substantial PCE improvement (from 5.68 and 5.91 to 7.0%) with compared to the corresponding binary systems. Although ternary systems do not always guarantee the higher device efficiency than the binary systems, ternary systems suggest a great potential to further improve the device properties. By judicious consideration of weak points of binary systems, it may be possible to improve poor device parameters via synergistic interactions between multiple donors or multiple acceptors in ternary systems.

Chapter 8. References

1. Becquerel, A., Recherches sur les effets de la radiation chimique de la lumière solaire au moyen des courants électriques. *C. R. Acad. Sci.* **1839**, 9, 145-149.
2. Volmer, M., Die verschiedenen lichtelektrischen Erscheinungen am Anthracen, ihre Beziehungen zueinander, zur Fluoreszenz und Dianthracenbildung. *Annalen der Physik* **1913**, 345, 775-796.
3. Tang, C. W., Two-layer organic photovoltaic cell. *Applied Physics Letters* 1986, 48, 183-185.
4. Sariciftci, N. S.; Smilowitz, L.; Heeger, A. J.; Wudl, F., Photoinduced Electron Transfer from a Conducting Polymer to Buckminsterfullerene. *Science* **1992**, 258, 1474-1476.
5. Morita, S.; Zakhidov, A. A.; Yoshino, K., Doping effect of buckminsterfullerene in conducting polymer: Change of absorption spectrum and quenching of luminescene. *Solid State Commun.* **1992**, 82, 249-252.
6. Yu, G.; Gao, J.; Hummelen, J. C.; Wudl, F.; Heeger, A. J., Polymer Photovoltaic Cells: Enhanced Efficiencies via a Network of Internal Donor-Acceptor Heterojunctions. *Science* **1995**, 270, 1789-1791.
7. Siddiki, M. K.; Li, J.; Galipeau, D.; Qiao, Q., A review of polymer multijunction solar cells. *Energy Environ. Sci.* **2010**, 3, 867-883.
8. Saunders, B. R.; Turner, M. L., Nanoparticle–polymer photovoltaic cells. *Advances in Colloid and Interface Science* 2008, **138**, 1-23.
9. Heremans, P.; Cheyns, D.; Rand, B. P., Strategies for increasing the efficiency of heterojunction organic solar cells: material selection and device architecture. *Acc. Chem. Res.* **2009**, 42, 1740-1747.
10. Brédas, J.-L.; Norton, J. E.; Cornil, J.; Coropceanu, V., Molecular understanding of organic solar cells: the challenges. *Acc. Chem. Res.* **2009**, 42, 1691-1699.
11. Peumans, P.; Yakimov, A.; Forrest, S. R., Small molecular weight organic thin-film photodetectors and solar cells. *J. Appl. Phys.* **2003**, 93, 3693-3723.
12. Brabec, C. J.; Cravino, A.; Meissner, D.; Sariciftci, N. S.; Fromherz, T.; Rispens, M. T.; Sanchez, L.; Hummelen, J. C., Origin of the open circuit voltage of plastic solar cells. *Advanced Functional Materials* **2001**, 11, 374-380.
13. Li, G.; Shrotriya, V.; Yao, Y.; Huang, J.; Yang, Y., Manipulating regioregular poly (3-hexylthiophene):[6, 6]-phenyl-C 61-butyric acid methyl ester blends—route towards high efficiency polymer solar cells. *J. Mater. Chem.* **2007**, 17, 3126-3140.
14. Ameri, T.; Dennler, G.; Lungenschmied, C.; Brabec, C. J., Organic tandem solar cells: a review. *Energy Environ. Sci.* **2009**, 2, 347-363.
15. Gur, I.; Fromer, N. A.; Chen, C.-P.; Kanaras, A. G.; Alivisatos, A. P., Hybrid solar cells with prescribed nanoscale morphologies based on hyperbranched semiconductor nanocrystals. *Nano Letters* **2007**, 7, 409-414.
16. Schilinsky, P.; Waldauf, C.; Hauch, J.; Brabec, C. J., Simulation of light intensity dependent current characteristics of polymer solar cells. *J. Appl. Phys.* **2004**, 95, 2816-2819.
17. Waldauf, C.; Scharber, M. C.; Schilinsky, P.; Hauch, J. A.; Brabec, C. J., Physics of organic bulk heterojunction devices for photovoltaic applications. *J. Appl. Phys.* **2006**, 99, 104503.
18. Novotny, C. J.; Yu, E. T.; Yu, P. K., InP nanowire/polymer hybrid photodiode. *Nano Lett.* **2008**, 8, 775-779.
19. Schilinsky, P.; Waldauf, C.; Brabec, C. J., Performance analysis of printed bulk heterojunction solar cells. *Adv. Funct. Mater.* **2006**, 16, 1669-1672.
20. Kippelen, B.; Brédas, J.-L., Organic photovoltaics. *Energy Environ. Sci.* **2009**, 2, 251-261.
21. Potscavage Jr, W. J.; Sharma, A.; Kippelen, B., Critical interfaces in organic solar cells and their influence on the open-circuit voltage. *Acc. Chem. Res.* **2009**, 42, 1758-1767.
22. El-Sayed, M. A., Some interesting properties of metals confined in time and nanometer space of different shapes. *Acc. Chem. Res.* **2001**, 34, 257-264.

23. Burda, C.; Chen, X.; Narayanan, R.; El-Sayed, M. A., Chemistry and properties of nanocrystals of different shapes. *Chem. Rev.* **2005**, 105, 1025-1102.

24. Kelly, K. L.; Coronado, E.; Zhao, L. L.; Schatz, G. C., The optical properties of metal nanoparticles: the influence of size, shape, and dielectric environment. *J.Phys. Chem.B* **2003**, 107, 668-677.

25. Brus, L., Noble metal nanocrystals: plasmon electron transfer photochemistry and single-molecule Raman spectroscopy. *Acc. Chem. Res.* **2008**, 41, 1742-1749.

26. Rycenga, M.; Cobley, C. M.; Zeng, J.; Li, W.; Moran, C. H.; Zhang, Q.; Qin, D.; Xia, Y., Controlling the synthesis and assembly of silver nanostructures for plasmonic applications. *Chem. Rev.* **2011**, 111, 3669-3712.

27. Xia, Y.; Xiong, Y.; Lim, B.; Skrabalak, S. E., Shape-Controlled Synthesis of Metal Nanocrystals: Simple Chemistry Meets Complex Physics? *Angew. Chem. Int. Ed.* **2009**, 48, 60-103.

28. Atwater, H. A.; Polman, A., Plasmonics for improved photovoltaic devices. *Nat. Mater.* **2010**, 9, 205-213.

29. Dunbar, R. B.; Hesse, H. C.; Lembke, D. S.; Schmidt-Mende, L., Light-trapping plasmonic nanovoid arrays. *Phys. Rev. B* **2012**, 85, 035301.

30. Wei, E.; Choy, W. C.; Liu, Y. G.; Chew, W. C., Near-field multiple scattering effects of plasmonic nanospheres embedded into thin-film organic solar cells. *Appl. Phys. Lett.* **2011**, 99, 113304.

31. Kim, S.-S.; Na, S.-I.; Jo, J.; Kim, D.-Y.; Nah, Y.-C., Plasmon enhanced performance of organic solar cells using electrodeposited Ag nanoparticles. *Appl. Phys. Lett.* **2008**, 93, 073307.

32. Morfa, A. J.; Rowlen, K. L.; Reilly III, T. H.; Romero, M. J.; van de Lagemaat, J., Plasmon-enhanced solar energy conversion in organic bulk heterojunction photovoltaics. *Appl. Phys. Lett.* **2008**, 92, 013504.

33. Lee, J. H.; Park, J. H.; Kim, J. S.; Lee, D. Y.; Cho, K., High efficiency polymer solar cells with wet deposited plasmonic gold nanodots. *Org. Electron.* **2009**, 10, 416-420.

34. Chen, F.-C.; Wu, J.-L.; Lee, C.-L.; Hong, Y.; Kuo, C.-H.; Huang, M. H., Plasmonic-enhanced polymer photovoltaic devices incorporating solution-processable metal nanoparticles. *Appl. Phys. Lett.* **2009**, 95, 013305.

35. Yoon, W.-J.; Jung, K.-Y.; Liu, J.; Duraisamy, T.; Revur, R.; Teixeira, F. L.; Sengupta, S.; Berger, P. R., Plasmon-enhanced optical absorption and photocurrent in organic bulk heterojunction photovoltaic devices using self-assembled layer of silver nanoparticles. *Sol. Energy Mater. Sol. Cells* **2010**, 94, 128-132.

36. Wu, J.-L.; Chen, F.-C.; Hsiao, Y.-S.; Chien, F.-C.; Chen, P.; Kuo, C.-H.; Huang, M. H.; Hsu, C.-S., Surface plasmonic effects of metallic nanoparticles on the performance of polymer bulk heterojunction solar cells. *Acs Nano* **2011**, 5, 959-967.

37. Pei, J.; Tao, J.; Zhou, Y.; Dong, Q.; Liu, Z.; Li, Z.; Chen, F.; Zhang, J.; Xu, W.; Tian, W., Efficiency enhancement of polymer solar cells by incorporating a self-assembled layer of silver nanodisks. *Sol. Energy Mater. Sol. Cells* **2011**, 95, 3281-3286.

38. Qiao, L.; Wang, D.; Zuo, L.; Ye, Y.; Qian, J.; Chen, H.; He, S., Localized surface plasmon resonance enhanced organic solar cell with gold nanospheres. *Appl. Energy* **2011**, 88, 848-852.

39. Oo, T. Z.; Mathews, N.; Xing, G.; Wu, B.; Xing, B.; Wong, L. H.; Sum, T. C.; Mhaisalkar, S. G., Ultrafine gold nanowire networks as plasmonic antennae in organic photovoltaics. *J. Phys. Chem. C* **2012**, 116, 6453-6458.

40. Lu, L.; Luo, Z.; Xu, T.; Yu, L., Cooperative plasmonic effect of Ag and Au nanoparticles on enhancing performance of polymer solar cells. *Nano Lett.* **2012**, 13, 59-64.

41. Liu, H.; Goh, W.-P.; Leung, M.-Y.; Li, Y.; Norsten, T. B., Effect of nanoparticle stabilizing ligands and ligand-capped gold nanoparticles in polymer solar cells. *Sol. Energy Mater. Sol. Cells* **2012**, 96, 302-306.

42. Wang, X.; Ho, J. W.; Yang, Q.; Tam, H. L.; Li, G. X.; Cheah, K. W.; Zhu, F., Performance enhancement in organic photovoltaic devices using plasma-polymerized fluorocarbon-modified Ag nanoparticles. *Org. Electron.* **2011**, 12, 1943-1947.

43. Yakimov, A.; Forrest, S. R., High photovoltage multiple-heterojunction organic solar cells

incorporating interfacial metallic nanoclusters. *Appl. Phys. Lett.* **2002**, 80, 1667-1669.

44. Atwater, H. A.; Polman, A., Plasmonics for improved photovoltaic devices. *Nat. Mater.* **2010**, 9, 205-213.

45. Yang, J.; You, J.; Chen, C.-C.; Hsu, W.-C.; Tan, H.-r.; Zhang, X. W.; Hong, Z.; Yang, Y., Plasmonic Polymer Tandem Solar Cell. *ACS Nano* **2011**, 5, 6210-6217.

46. Kalfagiannis, N.; Karagiannidis, P. G.; Pitsalidis, C.; Panagiotopoulos, N. T.; Gravalidis, C.; Kassavetis, S.; Patsalas, P.; Logothetidis, S., Plasmonic silver nanoparticles for improved organic solar cells. *Solar Energy Materials and Solar Cells* **2012**, 104, 165-174.

47. Spyropoulos, G. D.; Stylianakis, M. M.; Stratakis, E.; Kymakis, E., Organic bulk heterojunction photovoltaic devices with surfactant-free Au nanoparticles embedded in the active layer. *Appl. Phys. Lett.* **2012**, 100, 213904.

48. Wang, C. C. D.; Choy, W. C. H.; Duan, C.; Fung, D. D. S.; Sha, W. E. I.; Xie, F.-X.; Huang, F.; Cao, Y., Optical and electrical effects of gold nanoparticles in the active layer of polymer solar cells. *J.Mater. Chem.* **2012**, 22, 1206-1211.

49. Wang, D. H.; Kim, D. Y.; Choi, K. W.; Seo, J. H.; Im, S. H.; Park, J. H.; Park, O. O.; Heeger, A. J., Enhancement of Donor–Acceptor Polymer Bulk Heterojunction Solar Cell Power Conversion Efficiencies by Addition of Au Nanoparticles. *Angew. Chem. Int. Ed.* **2011**, 50, 5519-5523.

50. Wang, D. H.; Park, K. H.; Seo, J. H.; Seifter, J.; Jeon, J. H.; Kim, J. K.; Park, J. H.; Park, O. O.; Heeger, A. J., Enhanced Power Conversion Efficiency in PCDTBT/PC70BM Bulk Heterojunction Photovoltaic Devices with Embedded Silver Nanoparticle Clusters. *Adv. Energy Mater.* **2011**, 1, 766-770.

51. Naidu, B. V. K.; Park, J. S.; Kim, S. C.; Park, S.-M.; Lee, E.-J.; Yoon, K.-J.; Joon Lee, S.; Wook Lee, J.; Gal, Y.-S.; Jin, S.-H., Novel hybrid polymer photovoltaics made by generating silver nanoparticles in polymer:fullerene bulk-heterojunction structures. *Solar Energy Materials and Solar Cells* **2008**, 92, 397-401.

52. Sha, W. E. I.; Choy, W. C. H.; Liu, Y. G.; Chew, W. C., Near-field multiple scattering effects of plasmonic nanospheres embedded into thin-film organic solar cells. *Appl. Phys. Lett.* **2011**, 99, 113304.

53. Shen, H.; Bienstman, P.; Maes, B., Plasmonic absorption enhancement in organic solar cells with thin active layers. *J. Appl. Phys.* **2009**, 106, 073109.

54. Zhu, J.; Xue, M.; Hoekstra, R.; Xiu, F.; Zeng, B.; Wang, K. L., Light concentration and redistribution in polymer solar cells by plasmonic nanoparticles. *Nanoscale* **2012**, 4, 1978-1981.

55. Kim, C.-H.; Cha, S.-H.; Kim, S. C.; Song, M.; Lee, J.; Shin, W. S.; Moon, S.-J.; Bahng, J. H.; Kotov, N. A.; Jin, S.-H., Silver Nanowire Embedded in P3HT:PCBM for High-Efficiency Hybrid Photovoltaic Device Applications. *ACS Nano* **2011**, 5, 3319-3325.

56. Wang, D. H.; Kim, J. K.; Lim, G.-H.; Park, K. H.; Park, O. O.; Lim, B.; Park, J. H., Enhanced light harvesting in bulk heterojunction photovoltaic devices with shape-controlled Ag nanomaterials: Ag nanoparticles versus Ag nanoplates. *RSC Advances* **2012**, 2, 7268-7272.

57. Xie, F.-X.; Choy, W. C. H.; Wang, C. C. D.; Sha, W. E. I.; Fung, D. D. S., Improving the efficiency of polymer solar cells by incorporating gold nanoparticles into all polymer layers. *Appl. Phys. Lett.* **2011**, 99, 153304.

58. Topp, K.; Borchert, H.; Johnen, F.; Tunc, A. V.; Knipper, M.; von Hauff, E.; Parisi, J.; Al-Shamery, K., Impact of the Incorporation of Au Nanoparticles into Polymer/Fullerene Solar Cells†. *The J. Phys. Chem. A* **2009**, 114, 3981-3989.

59. Xue, M.; Li, L.; Villers, B. J. T. d.; Shen, H.; Zhu, J.; Yu, Z.; Stieg, A. Z.; Pei, Q.; Schwartz, B. J.; Wang, K. L., Charge-carrier dynamics in hybrid plasmonic organic solar cells with Ag nanoparticles. *Appl. Phys. Lett.* **2011**, 98, 253302.

60. Yang, L.; Li, X.; Tuo, X.; Van Nguyen, T. T.; Luo, X.; Hong, M., Alloy nanoparticle plasmon resonance for enhancing broadband antireflection of laser-textured silicon surfaces. *Opt. Express* **2011**, 19, A657-A663.

61. Kochergin, V.; Neely, L.; Jao, C.-Y.; Robinson, H. D., Aluminum plasmonic nanostructures for improved absorption in organic photovoltaic devices. *Appl. Phys. Lett.* **2011**, 98, 133305.

62. Kim, K.; Carroll, D. L., Roles of Au and Ag nanoparticles in efficiency enhancement of poly(3-octylthiophene)/C[sub 60] bulk heterojunction photovoltaic devices. *Appl. Phys. Lett.* **2005**, 87, 203113.

63. Paci, B.; Generosi, A.; Albertini, V. R.; Spyropoulos, G. D.; Stratakis, E.; Kymakis, E., Enhancement of photo/thermal stability of organic bulk heterojunction photovoltaic devices via gold nanoparticles doping of the active layer. *Nanoscale* **2012**, 4, 7452-7459.

64. Paci, B.; Spyropoulos, G. D.; Generosi, A.; Bailo, D.; Albertini, V. R.; Stratakis, E.; Kymakis, E., Enhanced Structural Stability and Performance Durability of Bulk Heterojunction Photovoltaic Devices Incorporating Metallic Nanoparticles. *Adv. Funct.Mater.* **2011**, 21, 3573-3582.

65. Kulkarni, A. P.; Noone, K. M.; Munechika, K.; Guyer, S. R.; Ginger, D. S., Plasmon-Enhanced Charge Carrier Generation in Organic Photovoltaic Films Using Silver Nanoprisms. *Nano Lett.* **2010**, 10, 1501-1505.

66. Vedraine, S.; Torchio, P.; Merlen, A.; Bagierek, J.; Flory, F.; Sangar, A.; Escoubas, L., Optical characterization of organic blend films integrating metallic nanoparticles. *Sol. Energy Mater. Sol. Cells* **2012**, 102, 31-35.

67. Brabec, C. J.; Shaheen, S. E.; Winder, C.; Sariciftci, N. S.; Denk, P., Effect of LiF/metal electrodes on the performance of plastic solar cells. *Appl. Phys. Lett.* **2002**, 80, 1288-1290.

68. Wienk, M. M.; Kroon, J. M.; Verhees, W. J.; Knol, J.; Hummelen, J. C.; van Hal, P. A.; Janssen, R. A., Efficient methano [70] fullerene/MDMO-PPV bulk heterojunction photovoltaic cells. *Angew. Chem.* **2003**, 115, 3493-3497.

69. Padinger, F.; Rittberger, R. S.; Sariciftci, N. S., Effects of postproduction treatment on plastic solar cells. *Adv. Funct. Mater.* **2003**, 13, 85-88.

70. Bao, Z.; Dodabalapur, A.; Lovinger, A. J., Soluble and processable regioregular poly (3-hexylthiophene) for thin film field-effect transistor applications with high mobility. *Appl. Phys. Lett.* **1996**, 69, 4108-4110.

71. Li, G.; Shrotriya, V.; Huang, J.; Yao, Y.; Moriarty, T.; Emery, K.; Yang, Y., High-efficiency solution processable polymer photovoltaic cells by self-organization of polymer blends. *Nat. Mater.* **2005**, 4, 864-868.

72. Ma, W.; Yang, C.; Gong, X.; Lee, K.; Heeger, A. J., Thermally stable, efficient polymer solar cells with nanoscale control of the interpenetrating network morphology. *Adv. Funct. Mater.* **2005**, 15, 1617-1622.

73. Mühlbacher, D.; Scharber, M.; Morana, M.; Zhu, Z.; Waller, D.; Gaudiana, R.; Brabec, C., High photovoltaic performance of a low-bandgap polymer. *Adv. Mater.* **2006**, 18, 2884-2889.

74. Peet, J.; Kim, J. Y.; Coates, N. E.; Ma, W. L.; Moses, D.; Heeger, A. J.; Bazan, G. C., Efficiency enhancement in low-bandgap polymer solar cells by processing with alkane dithiols. *Nat. Mater.* **2007**, 6, 497-500.

75. Blouin, N.; Michaud, A.; Leclerc, M., A low-bandgap poly (2, 7-carbazole) derivative for use in high-performance solar cells. *Adv. Mater.* **2007**, 19, 2295-2300.

76. Park, S. H.; Roy, A.; Beaupre, S.; Cho, S.; Coates, N.; Moon, J. S.; Moses, D.; Leclerc, M.; Lee, K.; Heeger, A. J., Bulk heterojunction solar cells with internal quantum efficiency approaching 100&percnt. *Nat. Photon.* **2009**, 3, 297-302.

77. Liang, Y.; Wu, Y.; Feng, D.; Tsai, S.-T.; Son, H.-J.; Li, G.; Yu, L., Development of new semiconducting polymers for high performance solar cells. *J. Am. Chem. Soc.* **2008**, 131, 56-57.

78. Liang, Y.; Feng, D.; Wu, Y.; Tsai, S.-T.; Li, G.; Ray, C.; Yu, L., Highly efficient solar cell polymers developed via fine-tuning of structural and electronic properties. *J. Am. Chem. Soc.* **2009**, 131, 7792-7799.

79. Chen, H.-Y.; Hou, J.; Zhang, S.; Liang, Y.; Yang, G.; Yang, Y.; Yu, L.; Wu, Y.; Li, G., Polymer solar cells with enhanced open-circuit voltage and efficiency. *Nat. Photon.* **2009**, 3, 649-653.

80. Price, S. C.; Stuart, A. C.; Yang, L.; Zhou, H.; You, W., Fluorine substituted conjugated polymer of medium band gap yields 7% efficiency in polymer− fullerene solar cells. *J. Am. Chem. Soc.* **2011**, 133, 4625-4631.

81. Zhou, H.; Yang, L.; Stuart, A. C.; Price, S. C.; Liu, S.; You, W., Development of fluorinated

benzothiadiazole as a structural unit for a polymer solar cell of 7% efficiency. *Angew. Chem.* **2011**, 123, 3051-3054.

82. Yang, J.; Zhu, R.; Hong, Z.; He, Y.; Kumar, A.; Li, Y.; Yang, Y., A Robust Inter-Connecting Layer for Achieving High Performance Tandem Polymer Solar Cells. *Adv. Mater.* **2011**, 23, 3465-3470.

83. Amb, C. M.; Chen, S.; Graham, K. R.; Subbiah, J.; Small, C. E.; So, F.; Reynolds, J. R., Dithienogermole as a fused electron donor in bulk heterojunction solar cells. *J. Am. Chem. Soc.* **2011**, 133, 10062-10065.

84. Cheng, Y.-J.; Yang, S.-H.; Hsu, C.-S., Synthesis of conjugated polymers for organic solar cell applications. *Chem. Rev.* **2009**, 109, 5868-5923.

85. Liang, Y.; Yu, L., Development of semiconducting polymers for solar energy harvesting. *Polymer Rev.* **2010**, 50, 454-473.

86. Scharber, M. C.; Mühlbacher, D.; Koppe, M.; Denk, P.; Waldauf, C.; Heeger, A. J.; Brabec, C. J., Design rules for donors in bulk-heterojunction solar cells—Towards 10% energy-conversion efficiency. *Adv. Mater.* **2006**, 18, 789-794.

87. Yun, J.-J.; Jung, H.-S.; Kim, S.-H.; Han, E.-M.; Vaithianathan, V.; Jenekhe, S. A., Chlorophyll-layer-inserted poly (3-hexyl-thiophene) solar cell having a high light-to-current conversion efficiency up to 1.48%. *Appl. Phys. Lett.* **2005**, 87, 123102.

88. McCullough, R. D.; Tristram-Nagle, S.; Williams, S. P.; Lowe, R. D.; Jayaraman, M., Self-orienting head-to-tail poly (3-alkylthiophenes): new insights on structure-property relationships in conducting polymers. *J. Am. Chem. Soc.* **1993**, 115, 4910-4911.

89. Yu, W.-L.; Meng, H.; Pei, J.; Huang, W., Tuning redox behavior and emissive wavelength of conjugated polymers by p-n diblock structures. *J. Am. Chem. Soc.* **1998**, 120, 11808-11809.

90. Zhou, Q.; Hou, Q.; Zheng, L.; Deng, X.; Yu, G.; Cao, Y., Fluorene-based low band-gap copolymers for high performance photovoltaic devices. *Appl. Phys. Lett.* **2004**, 84, 1653-1655.

91. Gadisa, A.; Mammo, W.; Andersson, L. M.; Admassie, S.; Zhang, F.; Andersson, M. R.; Inganäs, O., A new donor–acceptor–donor polyfluorene copolymer with balanced electron and hole mobility. *Adv. Funct. Mater.* **2007**, 17, 3836-3842.

92. Huo, L.; Hou, J.; Zhang, S.; Chen, H. Y.; Yang, Y., A Polybenzo [1, 2-b: 4, 5-b′] dithiophene Derivative with Deep HOMO Level and Its Application in High-Performance Polymer Solar Cells. *Angew. Chem. Int. Ed.* **2010**, 49, 1500-1503.

93. Vandewal, K.; Tvingstedt, K.; Gadisa, A.; Inganäs, O.; Manca, J. V., On the origin of the open-circuit voltage of polymer–fullerene solar cells. *Nat. Mater.* **2009**, 8, 904-909.

94. Liang, Y.; Yu, L., A new class of semiconducting polymers for bulk heterojunction solar cells with exceptionally high performance. *Acc. Chem. Res.* **2010**, 43, 1227-1236.

95. Havinga, E.; Ten Hoeve, W.; Wynberg, H., Alternate donor-acceptor small-band-gap semiconducting polymers; Polysquaraines and polycroconaines. *Synth. Met.* **1993**, 55, 299-306.

96. Zhang, Q. T.; Tour, J. M., Low optical bandgap polythiophenes by an alternating donor/acceptor repeat unit strategy. *J. Am. Chem. Soc.* **1997**, 119, 5065-5066.

97. Huang, F.; Chen, K.-S.; Yip, H.-L.; Hau, S. K.; Acton, O.; Zhang, Y.; Luo, J.; Jen, A. K.-Y., Development of New Conjugated Polymers with Donor− π-Bridge− Acceptor Side Chains for High Performance Solar Cells. *J. Am. Chem. Soc.* **2009**, 131, 13886-13887.

98. Hou, J.; Chen, H.-Y.; Zhang, S.; Li, G.; Yang, Y., Synthesis, characterization, and photovoltaic properties of a low band gap polymer based on silole-containing polythiophenes and 2, 1, 3-benzothiadiazole. *J. Am. Chem. Soc.* **2008**, 130, 16144-16145.

99. Chen, H. Y.; Hou, J.; Hayden, A. E.; Yang, H.; Houk, K.; Yang, Y., Silicon Atom Substitution Enhances Interchain Packing in a Thiophene-Based Polymer System. *Adv. Mater.* **2010**, 22, 371-375.

100. Zhang, Y.; Zou, J.; Yip, H.-L.; Chen, K.-S.; Zeigler, D. F.; Sun, Y.; Jen, A. K.-Y., Indacenodithiophene and quinoxaline-based conjugated polymers for highly efficient polymer solar cells. *Chem. Mater.* **2011**, 23, 2289-2291.

101. He, F.; Wang, W.; Chen, W.; Xu, T.; Darling, S. B.; Strzalka, J.; Liu, Y.; Yu, L.,

Tetrathienoanthracene-based copolymers for efficient solar cells. *J. Am. Chem. Soc.* **2011**, 133, 3284-3287.

102. Liang, Y.; Feng, D.; Wu, Y.; Tsai, S. T.; Li, G.; Ray, C.; Yu, L., Highly efficient solar cell polymers developed via fine-tuning of structural and electronic properties. *J. Am. Chem. Soc.* **2009**, 131, 7792-7799.

103. Zhou, H.; Yang, L.; Stuart, A. C.; Price, S. C.; Liu, S.; You, W., Development of Fluorinated Benzothiadiazole as a Structural Unit for a Polymer Solar Cell of 7 % Efficiency. *Angew. Chem. Int. Ed.* **2011**, 50, 2995-2998.

104. Chen, D.; Liu, F.; Wang, C.; Nakahara, A.; Russell, T. P., Bulk heterojunction photovoltaic active layers via bilayer interdiffusion. *Nano Lett.* **2011**, 11, 2071-2078.

105. Piliego, C.; Holcombe, T. W.; Douglas, J. D.; Woo, C. H.; Beaujuge, P. M.; Fréchet, J. M., Synthetic control of structural order in N-alkylthieno [3, 4-c] pyrrole-4, 6-dione-based polymers for efficient solar cells. *J. Am. Chem. Soc.* **2010**, 132, 7595-7597.

106. Chu, T.-Y.; Lu, J.; Beaupré, S.; Zhang, Y.; Pouliot, J.-R.; Wakim, S.; Zhou, J.; Leclerc, M.; Li, Z.; Ding, J.; Tao, Y., Bulk Heterojunction Solar Cells Using Thieno[3,4-c]pyrrole-4,6-dione and Dithieno[3,2-b:2′,3′-d]silole Copolymer with a Power Conversion Efficiency of 7.3%. *J. Am. Chem. Soc.* **2011**, 133, 4250-4253.

107. Shaheen, S. E.; Brabec, C. J.; Sariciftci, N. S.; Padinger, F.; Fromherz, T.; Hummelen, J. C., 2.5% efficient organic plastic solar cells. *Appl. Phys. Lett.* **2001**, 78, 841-843.

108. Zhang, F.; Jespersen, K. G.; Bjoerstroem, C.; Svensson, M.; Andersson, M. R.; Sundström, V.; Magnusson, K.; Moons, E.; Yartsev, A.; Inganäs, O., Influence of solvent mixing on the morphology and performance of solar cells based on polyfluorene copolymer/fullerene blends. *Adv. Funct. Mater.* **2006**, 16, 667-674.

109. Peet, J.; Kim, J.; Coates, N. E.; Ma, W. L.; Moses, D.; Heeger, A. J.; Bazan, G. C., Efficiency enhancement in low-bandgap polymer solar cells by processing with alkane dithiols. *Nat. Mater.* **2007**, 6, 497-500.

110. Hoppe, H.; Sariciftci, N. S., Morphology of polymer/fullerene bulk heterojunction solar cells. *J. Mater. Chem.* **2006**, 16, 45-61.

111. Hoth, C. N.; Schilinsky, P.; Choulis, S. A.; Brabec, C. J., Printing highly efficient organic solar cells. *Nano Lett.* **2008**, 8, 2806-2813.

112. Liu, J.; Shi, Y.; Yang, Y., Solvation-induced morphology effects on the performance of polymer-based photovoltaic devices. *Adv. Funct. Mater.* **2001**, 11, 420.

113. Hoppe, H.; Niggemann, M.; Winder, C.; Kraut, J.; Hiesgen, R.; Hinsch, A.; Meissner, D.; Sariciftci, N. S., Nanoscale morphology of conjugated polymer/fullerene-based bulk-heterojunction solar cells. *Adv. Funct. Mater.* **2004**, 14, 1005-1011.

114. Hoppe, H.; Glatzel, T.; Niggemann, M.; Schwinger, W.; Schaeffler, F.; Hinsch, A.; Lux-Steiner, M. C.; Sariciftci, N., Efficiency limiting morphological factors of MDMO-PPV: PCBM plastic solar cells. *Thin solid films* **2006**, 511, 587-592.

115. Yao, Y.; Shi, C.; Li, G.; Shrotriya, V.; Pei, Q.; Yang, Y., Effects of C 70 derivative in low band gap polymer photovoltaic devices: Spectral complementation and morphology optimization. *Appl. Phys. Lett.* **2006**, 89, 153507-153507-3.

116. Soci, C.; Hwang, I. W.; Moses, D.; Zhu, Z.; Waller, D.; Gaudiana, R.; Brabec, C. J.; Heeger, A. J., Photoconductivity of a low-bandgap conjugated polymer. *Adv. Funct. Mater.* **2007**, 17, 632-636.

117. Yao, Y.; Hou, J.; Xu, Z.; Li, G.; Yang, Y., Effects of Solvent Mixtures on the Nanoscale Phase Separation in Polymer Solar Cells. *Adv. Funct. Mater.* **2008**, 18, 1783-1789.

118. Moulé, A. J.; Meerholz, K., Controlling morphology in polymer–fullerene mixtures. *Adv. Mater.* **2008**, 20, 240-245.

119. Chen, F.-C.; Tseng, H.-C.; Ko, C.-J., Solvent mixtures for improving device efficiency of polymer photovoltaic devices. *Appl. Phys. Lett.* **2008**, 92, 103316-103316-3.

120. Alargova, R. G.; Deguchi, S.; Tsujii, K., Stable colloidal dispersions of fullerenes in polar organic solvents. *J. Am. Chem. Soc.* **2001**, 123, 10460-10467.

121. Lee, J. K.; Ma, W. L.; Brabec, C. J.; Yuen, J.; Moon, J. S.; Kim, J. Y.; Lee, K.; Bazan, G. C.; Heeger, A. J., Processing Additives for Improved Efficiency from Bulk Heterojunction Solar Cells. *J. Am. Chem. Soc.* **2008**, 130, 3619-3623.

122. Hwang, I.-W.; Cho, S.; Kim, J. Y.; Lee, K.; Coates, N. E.; Moses, D.; Heeger, A. J., Carrier generation and transport in bulk heterojunction films processed with 1, 8-octanedithiol as a processing additive. *J. Appl. Phys.* **2008**, 104, 033706.

123. Koppe, M.; Egelhaaf, H. J.; Dennler, G.; Scharber, M. C.; Brabec, C. J.; Schilinsky, P.; Hoth, C. N., Near IR sensitization of organic bulk heterojunction solar cells: towards optimization of the spectral response of organic solar cells. *Adv. Funct. Mater.* **2010**, 20, 338-346.

124. Cheng, P.-C., The contrast formation in optical microscopy. In *Handbook Of Biological Confocal Microscopy*, Springer: **2006**; pp 162-206.

125. Yang, L.; Zhou, H.; Price, S. C.; You, W., Parallel-like bulk heterojunction polymer solar cells. *J. Am. Chem. Soc.* **2012**, 134, 5432-5435.

126. Garcia-Belmonte, G.; Bisquert, J., Open-circuit voltage limit caused by recombination through tail states in bulk heterojunction polymer-fullerene solar cells. *Appl. Phys. Lett.* **2010**, 96, 113301.

127. Qi, B.; Wang, J., Open-circuit voltage in organic solar cells. *J. Mater. Chem.* **2012**, 22, 24315-24325.

128. Thompson, B. C.; Kim, Y.-G.; Reynolds, J. R., Spectral broadening in MEH-PPV: PCBM-based photovoltaic devices via blending with a narrow band gap cyanovinylene-dioxythiophene polymer. *Macromolecules* **2005**, 38, 5359-5362.

129. Suresh, P.; Balraju, P.; Sharma, G.; Mikroyannidis, J. A.; Stylianakis, M. M., Effect of the incorporation of a low-band-gap small molecule in a conjugated vinylene copolymer: PCBM blend for organic photovoltaic devices. *ACS Appl. Mater. Interfaces* **2009**, 1, 1370-1374.

130. Chen, C.-H.; Hsieh, C.-H.; Dubosc, M.; Cheng, Y.-J.; Hsu, C.-S., Synthesis and characterization of bridged bithiophene-based conjugated polymers for photovoltaic applications: acceptor strength and ternary blends. *Macromolecules* **2009**, 43, 697-708.

131. Adam, G.; Pivrikas, A.; Ramil, A. M.; Tadesse, S.; Yohannes, T.; Sariciftci, N. S.; Egbe, D. A., Mobility and photovoltaic performance studies on polymer blends: effects of side chains volume fraction. *J. Mater. Chem.* **2011**, 21, 2594-2600.

132. Mikroyannidis, J.; Tsagkournos, D.; Balraju, P.; Sharma, G., Synthesis and photovoltaic properties of an alternating phenylenevinylene copolymer with substituted-triphenylamine units along the backbone for bulk heterojunction and dye-sensitized solar cells. *J. Power Sources* **2011**, 196, 2364-2372.

133. Kim, Y.; Shin, M.; Kim, H.; Ha, Y.; Ha, C.-S., Influence of electron-donating polymer addition on the performance of polymer solar cells. *J.of Phys.D: Appl.Phys.* **2008**, 41, 225101.

134. Cheng, Y. J.; Hsieh, C. H.; Li, P. J.; Hsu, C. S., Morphological stabilization by in situ polymerization of fullerene derivatives leading to efficient, thermally stable organic photovoltaics. *Adv. Funct. Mater.* **2011**, 21, 1723-1732.

135. Huang, J.-H.; Velusamy, M.; Ho, K.-C.; Lin, J.-T.; Chu, C.-W., A ternary cascade structure enhances the efficiency of polymer solar cells. *J. Mater. Chem.* **2010**, 20, 2820-2825.

136. Peet, J.; Tamayo, A.; Dang, X.-D.; Seo, J.; Nguyen, T.-Q., Small molecule sensitizers for near-infrared absorption in polymer bulk heterojunction solar cells. *Appl. Phys. Lett.* **2008**, 93, 163306.

137. Khlyabich, P. P.; Burkhart, B.; Thompson, B. C., Efficient Ternary Blend Bulk Heterojunction Solar Cells with Tunable Open-Circuit Voltage. *J. Am. Chem. Soc.* **2011**, 133, 14534-14537.

138. Brabec, C. J.; Sariciftci, N. S.; Hummelen, J. C., Plastic solar cells. *Adv. Funct. Mater.* **2001**, 11, 15-26.

139. Burroughes, J.; Bradley, D. D. C.; Brown, A.; Marks, R.; Mackay, K.; Friend, R.; Burns, P.; Holmes, A., Light-emitting diodes based on conjugated polymers. *Nature* **1990**, 347, 539-541.

140. Dennler, G.; Scharber, M. C.; Brabec, C. J., Polymer Fullerene Bulk Heterojunction Solar Cells. *Adv. Mater.* **2009**, 21, 1323-1338.

141. Gustafsson, G.; Cao, Y.; Treacy, G.; Klavetter, F.; Colaneri, N.; Heeger, A., Flexible light-

emitting diodes made from soluble conducting polymers. *Nature* **1992**, 357, 477-479.

142. Liang, Y.; Xu, Z.; Xia, J.; Tsai, S. T.; Wu, Y.; Li, G.; Ray, C.; Yu, L., For the bright future--bulk heterojunction polymer solar cells with power conversion efficiency of 7.4%. *Adv. Mater.* **2010**, 22, E135-E138.

143. http://www.konarka.com.

144. Kim, H.; Gilmore, C.; Pique, A.; Horwitz, J.; Mattoussi, H.; Murata, H.; Kafafi, Z.; Chrisey, D., Electrical, optical, and structural properties of indium–tin–oxide thin films for organic light-emitting devices. *J. Appl. Phys.* **1999**, 86, 6451.

145. Chen, Z.; Cotterell, B.; Wang, W.; Guenther, E.; Chua, S. J., A mechanical assessment of flexible optoelectronic devices. *Thin Solid Films* **2001**, 394, 201-205.

146. Na, S. I.; Kim, S. S.; Jo, J.; Kim, D. Y., Efficient and flexible ITO-free organic solar cells using highly conductive polymer anodes. *Adv. Mater.* **2008**, 20, 4061-4067.

147. Du Pasquier, A.; Unalan, H. E.; Kanwal, A.; Miller, S.; Chhowalla, M., Conducting and transparent single-wall carbon nanotube electrodes for polymer-fullerene solar cells. *Appl. Phys. Lett.* **2005**, 87, 203511.

148. Kang, M.-G.; Xu, T.; Park, H. J.; Luo, X.; Guo, L. J., Efficiency Enhancement of Organic Solar Cells Using Transparent Plasmonic Ag Nanowire Electrodes. *Adv. Mater.* **2010**, 22, 4378-4383.

149. Lee, J. Y.; Connor, S. T.; Cui, Y.; Peumans, P., Solution-processed metal nanowire mesh transparent electrodes. *Nano Lett.* 2008, 8, 689-692.

150. Zou, J.; Yip, H. L.; Hau, S. K.; Alex, K. Y. J., Metal grid/conducting polymer hybrid transparent electrode for inverted polymer solar cells. *Appl. Phys. Lett.* **2010**, 96, 203301.

151. Levermore, P. A.; Chen, L.; Wang, X.; Das, R.; Bradley, D. D. C., Fabrication of Highly Conductive Poly (3, 4-ethylenedioxythiophene) Films by Vapor Phase Polymerization and Their Application in Efficient Organic Light-Emitting Diodes. *Adv. Mater.* **2007**, 19, 2379-2385.

152. Kylberg, W.; de Castro, F. A.; Chabrecek, P.; Sonderegger, U.; Chu, B. T. T.; Nüesch, F.; Hany, R., Flexible Mesh Electrodes: Woven Electrodes for Flexible Organic Photovoltaic Cells (Adv. Mater. 8/2011). *Adv. Mater.* **2011**, 23, 920-920.

153. Yim, Y.; Park, J.; Park, B., Solution-processed flexible Ito-free organic light-emitting diodes using patterned polymeric anodes. *IEEE/OSA J. Display Technol.* **2010**, 6, 252-256.

154. Lee, T.-W.; Chung, Y., Control of the Surface Composition of a Conducting-Polymer Complex Film to Tune the Work Function. *Adv. Funct. Mater.* **2008**, 18, 2246-2252.

155. Nardes, A. M.; Janssen, R. A. J.; Kemerink, M., A Morphological Model for the Solvent-Enhanced Conductivity of PEDOT:PSS Thin Films. *Adv. Funct. Mater.* **2008**, 18, 865-871.

156. Ouyang, J.; Chu, C. W.; Chen, F. C.; Xu, Q.; Yang, Y., High Conductivity Poly (3, 4 ethylenedioxythiophene): Poly (styrene sulfonate) Film and Its Application in Polymer Optoelectronic Devices. *Adv. Funct. Mater.* **2005**, 15, 203-208.

157. Schwertheim, S.; Grewe, O.; Hamm, I.; Mueller, T.; Pichner, R.; Fahrner, W. In *PEDOT: PSS layers as replacements for the transparent conductive coatings of organic solar cells*, IEEE: **2010**; pp 001639-001642.

158. Na, S. I.; Yu, B. K.; Kim, S. S.; Vak, D.; Kim, T. S.; Yeo, J. S.; Kim, D. Y., Fully spray-coated ITO-free organic solar cells for low-cost power generation. *Sol. Energy Mater. Sol. Cells* **2010**, 94, 1333-1337.

159. Heo, M.; Cho, H.; Jung, J.-W.; Jeong, J.-R.; Park, S.; Kim, J. Y., High-Performance Organic Optoelectronic Devices Enhanced by Surface Plasmon Resonance. *Adv. Mater.* **2011**, 23, 5689-5693.

160. Derkacs, D.; Lim, S.; Matheu, P.; Mar, W.; Yu, E., Improved performance of amorphous silicon solar cells via scattering from surface plasmon polaritons in nearby metallic nanoparticles. *Appl. Phys. Lett.* **2006**, 89, 093103.

161. Kim, S. S.; Na, S. I.; Jo, J.; Kim, D. Y.; Nah, Y. C., Plasmon enhanced performance of organic solar cells using electrodeposited Ag nanoparticles. *Appl. Phys. Lett.* **2008**, 93, 073307.

162. Feng, J.; Okamoto, T.; Kawata, S., Highly directional emission via coupled surface-plasmon tunneling from electroluminescence in organic light-emitting devices. *Appl. Phys. Lett.* **2005**, 87, 241109.

163. Fujiki, A.; Uemura, T.; Zettsu, N.; Akai-Kasaya, M.; Saito, A.; Kuwahara, Y., Enhanced fluorescence by surface plasmon coupling of Au nanoparticles in an organic electroluminescence diode. *Appl. Phys. Lett.* **2010**, 96, 043307.

164. Liu, C.; Kamaev, V.; Vardeny, Z., Efficiency enhancement of an organic light-emitting diode with a cathode forming two-dimensional periodic hole array. *Appl. Phys. Lett.* **2005**, 86, 143501.

165. Nien, S. Y.; Chiu, N. F.; Tsai, Y. C.; Lin, C. W.; Liu, K. C.; Lee, J. H. In *Extraction efficiency enhancement of an OLED using surface plasmon resonance*, IEEE: **2007**; pp 239-241.

166. Morfa, A. J.; Rowlen, K. L.; Reilly, T. H.; III; Romero, M. J.; Lagemaat, J. v. d., Plasmon-enhanced solar energy conversion in organic bulk heterojunction photovoltaics. *Appl. Phys. Lett.* **2008**, 92, 013504.

167. Yang, B.; Lu, N.; Qi, D.; Ma, R.; Wu, Q.; Hao, J.; Liu, X.; Mu, Y.; Reboud, V.; Kehagias, N., Tuning the Intensity of Metal-Enhanced Fluorescence by Engineering Silver Nanoparticle Arrays. *Small* **2010**, 6, 1038-1043.

168. Neogi, A.; Lee, C. W.; Everitt, H. O.; Kuroda, T.; Tackeuchi, A.; Yablonovitch, E., Enhancement of spontaneous recombination rate in a quantum well by resonant surface plasmon coupling. *Phys. Rev. B* **2002**, 66, 153305.

169. Collier, C.; Saykally, R.; Shiang, J.; Henrichs, S.; Heath, J., Reversible tuning of silver quantum dot monolayers through the metal-insulator transition. *Science* **1997**, 277, 1978.

170. Haruta, M., Size- and support-dependency in the catalysis of gold. *Catal. Today* **1997**, 36, 153-166.

171. Matsui, I., Nanoparticles for electronic device applications: A brief review. *J. Chem. Eng. Jpn.* **2005**, 38, 535-546.

172. West, P. R.; Ishii, S.; Naik, G. V.; Emani, N. K.; Shalaev, V. M.; Boltasseva, A., Searching for better plasmonic materials. *Laser Photon. Rev.* **2010**, 4, 795-808.

173. Reilly, T. H.; III; Lagemaat, J. v. d.; Tenent, R. C.; Morfa, A. J.; Rowlen, K. L., Surface-plasmon enhanced transparent electrodes in organic photovoltaics. *Appl. Phys. Lett.* **2008**, 92, 243304.

174. Hongsheng, Y.; Bo, Q.; Shengbo, M.; Zhijian, C.; Lixin, X.; Qihuang, G., Indium tin oxide-free polymer solar cells using a PEDOT : PSS/Ag/PEDOT : PSS multilayer as a transparent anode. *J. Phys. D: Appl. Phys.* **2012**, 45, 425102.

175. Lee, W.; Choi, H.; Hwang, S.; Kim, J. Y.; Woo, H. Y., Efficient Conventional- and Inverted-Type Photovoltaic Cells Using a Planar Alternating Polythiophene Copolymer. *Chem. Eur. J.* **2012**, 18, 2551-2558.

176. Jeon, S. H.; Xu, P.; Mack, N. H.; Chiang, L. Y.; Brown, L.; Wang, H. L., Understanding and controlled growth of silver nanoparticles using oxidized N-methyl-pyrrolidone as a reducing agent. *J. Phys. Chem. C* **2009**, 114, 36-40.

177. Ouyang, J.; Xu, Q.; Chu, C. W.; Yang, Y.; Li, G.; Shinar, J., On the mechanism of conductivity enhancement in poly (3, 4-ethylenedioxythiophene): poly (styrene sulfonate) film through solvent treatment. *Polymer* **2004**, 45, 8443-8450.

178. Amendola, V.; Bakr, O.; Stellacci, F., A Study of the Surface Plasmon Resonance of Silver Nanoparticles by the Discrete Dipole Approximation Method: Effect of Shape, Size, Structure, and Assembly. *Plasmonics* **2010**, 5, 85-97.

179. Smits, F., Measurement of sheet resistivities with the four-point probe. *Bell Syst. Tech. J* **1958**, 37, 711-18.

180. Ouyang, J.; Xu, Q.; Chu, C.-W.; Yang, Y.; Li, G.; Shinar, J., On the mechanism of conductivity enhancement in poly(3,4-ethylenedioxythiophene):poly(styrene sulfonate) film through solvent treatment. *Polymer* **2004**, 45, 8443-8450.

181. Kim, Y. H.; Sachse, C.; Machala, M. L.; May, C.; Müller-Meskamp, L.; Leo, K., Highly Conductive PEDOT:PSS Electrode with Optimized Solvent and Thermal Post-Treatment for ITO-Free Organic Solar Cells. *Adv. Funct. Mater.* **2011**, 21, 1076-1081.

182. Li, G.; Zhu, R.; Yang, Y., Polymer solar cells. *Nat. Photon.* **2012**, 6, 153-161.

183. Darling, S. B.; You, F., The case for organic photovoltaics. *Rsc Advances* **2013**, 3, 17633-17648.

184. Huo, L.; Zhang, S.; Guo, X.; Xu, F.; Li, Y.; Hou, J., Replacing alkoxy groups with alkylthienyl

groups: a feasible approach to improve the properties of photovoltaic polymers. *Angew. Chem.* **2011**, 123, 9871-9876.

185. Chu, T.-Y.; Lu, J.; Beaupré, S.; Zhang, Y.; Pouliot, J.-R.; Wakim, S.; Zhou, J.; Leclerc, M.; Li, Z.; Ding, J., Bulk heterojunction solar cells using thieno [3, 4-c] pyrrole-4, 6-dione and dithieno [3, 2-b: 2′, 3′-d] silole copolymer with a power conversion efficiency of 7.3%. *J. Am. Chem. Soc.* **2011**, 133, 4250-4253.

186. Dou, L.; You, J.; Yang, J.; Chen, C.-C.; He, Y.; Murase, S.; Moriarty, T.; Emery, K.; Li, G.; Yang, Y., Tandem polymer solar cells featuring a spectrally matched low-bandgap polymer. *Nat. Photon.* **2012**, 6, 180-185.

187. Kim, J. Y.; Lee, K.; Coates, N. E.; Moses, D.; Nguyen, T. Q.; Dante, M.; Heeger, A. J., Efficient tandem polymer solar cells fabricated by all-solution processing. *Science* **2007**, 317, 222.

188. Cabanetos, C. m.; El Labban, A.; Bartelt, J. A.; Douglas, J. D.; Mateker, W. R.; Fréchet, J. M.; McGehee, M. D.; Beaujuge, P. M., Linear side chains in benzo [1, 2-b: 4, 5-b′] dithiophene–thieno [3, 4-c] pyrrole-4, 6-dione polymers direct self-assembly and solar cell performance. *J. Am. Chem. Soc.* **2013**, 135, 4656-4659.

189. He, Z.; Zhong, C.; Su, S.; Xu, M.; Wu, H.; Cao, Y., Enhanced power-conversion efficiency in polymer solar cells using an inverted device structure. *Nat. Photon.* **2012**, 6, 591-595.

190. Son, H. J.; Lu, L.; Chen, W.; Xu, T.; Zheng, T.; Carsten, B.; Strzalka, J.; Darling, S. B.; Chen, L. X.; Yu, L., Synthesis and Photovoltaic Effect in Dithieno [2, 3-d: 2′, 3′-d′] Benzo [1, 2-b: 4, 5-b′] dithiophene-Based Conjugated Polymers. *Adv. Mater.* **2013**, 25, 838-843.

191. Chen, H.-C.; Chen, Y.-H.; Liu, C.-C.; Chien, Y.-C.; Chou, S.-W.; Chou, P.-T., Prominent Short-Circuit Currents of Fluorinated Quinoxaline-Based Copolymer Solar Cells with a Power Conversion Efficiency of 8.0%. *Chem. Mater.* **2012**, 24, 4766-4772.

192. Schroeder, B. C.; Huang, Z.; Ashraf, R. S.; Smith, J.; D'Angelo, P.; Watkins, S. E.; Anthopoulos, T. D.; Durrant, J. R.; McCulloch, I., Silaindacenodithiophene-Based Low Band Gap Polymers – The Effect of Fluorine Substitution on Device Performances and Film Morphologies. *Adv. Funct. Mater.* **2012**, 22, 1663-1670.

193. Zhang, Y.; Chien, S.-C.; Chen, K.-S.; Yip, H.-L.; Sun, Y.; Davies, J. A.; Chen, F.-C.; Jen, A. K. Y., Increased open circuit voltage in fluorinated benzothiadiazole-based alternating conjugated polymers. *Chem. Commun.* **2011**, 47, 11026-11028.

194. Li, Z.; Lu, J.; Tse, S.-C.; Zhou, J.; Du, X.; Tao, Y.; Ding, J., Synthesis and applications of difluorobenzothiadiazole based conjugated polymers for organic photovoltaics. *J. Mater. Chem.* **2011**, 21, 3226-3233.

195. Wang, Y.; Parkin, S. R.; Gierschner, J.; Watson, M. D., Highly fluorinated benzobisbenzothiophenes. *Org. Lett.* **2008**, 10, 3307-3310.

196. Babudri, F.; Farinola, G. M.; Naso, F.; Ragni, R., Fluorinated organic materials for electronic and optoelectronic applications: the role of the fluorine atom. *Chem. Commun.* **2007**, 0, 1003-1022.

197. Reichenbacher, K.; Suss, H. I.; Hulliger, J., Fluorine in crystal engineering-"the little atom that could". *Chem. Soc. Rev.* **2005**, 34, 22-30.

198. Guo, X.; Quinn, J.; Chen, Z.; Usta, H.; Zheng, Y.; Xia, Y.; Hennek, J. W.; Ortiz, R. P.; Marks, T. J.; Facchetti, A., Dialkoxybithiazole: A New Building Block for Head-to-Head Polymer Semiconductors. *J. Am. Chem. Soc.* **2013**, 135, 1986-1996.

199. Guo, X.; Kim, F. S.; Jenekhe, S. A.; Watson, M. D., Phthalimide-Based Polymers for High Performance Organic Thin-Film Transistors. *J. Am. Chem. Soc.* **2009**, 131, 7206-7207.

200. Beljonne, D.; Pourtois, G.; Silva, C.; Hennebicq, E.; Herz, L. M.; Friend, R. H.; Scholes, G. D.; Setayesh, S.; Müllen, K.; Brédas, J. L., Interchain vs. intrachain energy transfer in acceptor-capped conjugated polymers. *Proc. Natl. Acad. Sci.* **2002**, 99, 10982-10987.

201. Bredas, J. L.; Street, G. B.; Themans, B.; Andre, J. M., Organic polymers based on aromatic rings (polyparaphenylene, polypyrrole, polythiophene): Evolution of the electronic properties as a function of the torsion angle between adjacent rings. *J. Chem. Phys.* **1985**, 83, 1323-1329.

202. Street, R.; Northrup, J.; Salleo, A., Transport in polycrystalline polymer thin-film transistors. *Phys. Rev. B* **2005**, 71, 165202.

203. Biniek, L.; Chochos, C. L.; Leclerc, N.; Boyron, O.; Fall, S.; Lévèque, P.; Heiser, T., 3,6-Dialkylthieno[3,2-b]thiophene moiety as a soluble and electron donating unit preserving the coplanarity of photovoltaic low band gap copolymers. *J. Polym. Sci., Part A: Polym. Chem.* **2012**, 50, 1861-1868.

204. Jheng, J.-F.; Lai, Y.-Y.; Wu, J.-S.; Chao, Y.-H.; Wang, C.-L.; Hsu, C.-S., Influences of the Non-Covalent Interaction Strength on Reaching High Solid-State Order and Device Performance of a Low Bandgap Polymer with Axisymmetrical Structural Units. *Adv. Mater.* **2013**, 25, 2445-2451.

205. Carlé, J. E.; Andreasen, J. W.; Jørgensen, M.; Krebs, F. C., Low band gap polymers based on 1, 4-dialkoxybenzene, thiophene, bithiophene donors and the benzothiadiazole acceptor. *Sol. Energy Mater. Sol. Cells* **2010**, 94, 774-780.

206. Lee, W.; Kim, G.-H.; Ko, S.-J.; Yum, S.; Hwang, S.; Cho, S.; Shin, Y.-H.; Kim, J. Y.; Woo, H. Y., Semicrystalline D–A Copolymers with Different Chain Curvature for Applications in Polymer Optoelectronic Devices. *Macromolecules* **2014**, 47, 1604-1612.

207. Yum, S.; An, T. K.; Wang, X.; Lee, W.; Uddin, M. A.; Kim, Y. J.; Nguyen, T. L.; Xu, S.; Hwang, S.; Park, C. E., Benzotriazole-containing planar conjugated polymers with noncovalent conformational locks for thermally stable and efficient polymer field-effect transistors. *Chem. Mater.* **2014**, 26, 2147-2154.

208. Yum, S.; An, T. K.; Wang, X.; Uddin, M. A.; Nguyen, T. L.; Xu, S.; Ryu, H.; Kim, Y. J.; Hwang, S.; Park, C. E., Thienothiophene-benzotriazole-based semicrystalline linear copolymers for organic field effect transistors. *Pure Appl. Chem.* **2014**, 86, 1293-1302.

209. Jackson, N. E.; Savoie, B. M.; Kohlstedt, K. L.; Olvera de la Cruz, M.; Schatz, G. C.; Chen, L. X.; Ratner, M. A., Controlling conformations of conjugated polymers and small molecules: The role of nonbonding interactions. *J. Am. Chem. Soc.* **2013**, 135, 10475-10483.

210. Zhao, Y.; Truhlar, D. G., The M06 suite of density functionals for main group thermochemistry, thermochemical kinetics, noncovalent interactions, excited states, and transition elements: two new functionals and systematic testing of four M06-class functionals and 12 other functionals. *Theor. Chem. Acc.* **2008**, 120, 215-241.

211. Zhao, Y.; Truhlar, D. G., Density functionals with broad applicability in chemistry. *Acc. Chem. Res.* **2008**, 41, 157-167.

212. Doemer, M.; Tavernelli, I.; Rothlisberger, U., Intricacies of Describing Weak Interactions Involving Halogen Atoms within Density Functional Theory. *J. Chem. Theory Comput.* **2012**, 9, 955-964.

213. Bravaya, K. B.; Epifanovsky, E.; Krylov, A. I., Four Bases Score a Run: Ab Initio Calculations Quantify a Cooperative Effect of H-Bonding and π-Stacking on the Ionization Energy of Adenine in the AATT Tetramer. *J. Phys. Chem. Lett.* **2012**, 3, 2726-2732.

214. Walker, M.; Harvey, A. J.; Sen, A.; Dessent, C. E., Performance of M06, M06-2X, and M06-HF density functionals for conformationally flexible anionic clusters: M06 functionals perform better than B3LYP for a model system with dispersion and ionic hydrogen-bonding interactions. *J. Phys. Chem. A* **2013**, 117, 12590-12600.

215. Stuart, A. C.; Tumbleston, J. R.; Zhou, H.; Li, W.; Liu, S.; Ade, H.; You, W., Fluorine Substituents Reduce Charge Recombination and Drive Structure and Morphology Development in Polymer Solar Cells. *J. Am. Chem. Soc.* **2013**, 135, 1806-1815.

216. Bronstein, H.; Frost, J. M.; Hadipour, A.; Kim, Y.; Nielsen, C. B.; Ashraf, R. S.; Rand, B. P.; Watkins, S.; McCulloch, I., Effect of Fluorination on the Properties of a Donor–Acceptor Copolymer for Use in Photovoltaic Cells and Transistors. *Chem. Mater.* **2013**, 25, 277-285.

217. Kumar, P.; Bilen, C.; Feron, K.; Zhou, X.; Belcher, W. J.; Dastoor, P. C., Enhanced regeneration of degraded polymer solar cells by thermal annealing. *Appl. Phys. Lett.* **2014**, 104, 193905.

218. Griffini, G.; Douglas, J. D.; Piliego, C.; Holcombe, T. W.; Turri, S.; Fréchet, J. M.; Mynar, J. L., Long-Term Thermal Stability of High-Efficiency Polymer Solar Cells Based on Photocrosslinkable Donor-Acceptor Conjugated Polymers. *Adv. Mater.* **2011**, 23, 1660-1664.

219. Peet, J.; Cho, N. S.; Lee, S. K.; Bazan, G. C., Transition from Solution to the Solid State in Polymer Solar Cells Cast from Mixed Solvents. *Macromolecules* **2008**, 41, 8655-8659.

220. Liao, H.-C.; Ho, C.-C.; Chang, C.-Y.; Jao, M.-H.; Darling, S. B.; Su, W.-F., Additives for morphology control in high-efficiency organic solar cells. *Materials today* **2013**, 16, 326-336.

221. Chang, L.; Lademann, H. W.; Bonekamp, J. B.; Meerholz, K.; Moulé, A. J., Effect of trace solvent on the morphology of P3HT: PCBM bulk heterojunction solar cells. *Adv. Funct. Mater.* **2011**, 21, 1779-1787.

222. Seo, J. H.; Gutacker, A.; Sun, Y.; Wu, H.; Huang, F.; Cao, Y.; Scherf, U.; Heeger, A. J.; Bazan, G. C., Improved High-Efficiency Organic Solar Cells via Incorporation of a Conjugated Polyelectrolyte Interlayer. *J. Am. Chem. Soc.* **2011**, 133, 8416-8419.

223. Zhou, H.; Zhang, Y.; Seifter, J.; Collins, S. D.; Luo, C.; Bazan, G. C.; Nguyen, T.-Q.; Heeger, A. J., High-Efficiency Polymer Solar Cells Enhanced by Solvent Treatment. *Adv. Mater.* **2013**, 25, 1646-1652.

224. Yang, X.; Loos, J.; Veenstra, S. C.; Verhees, W. J. H.; Wienk, M. M.; Kroon, J. M.; Michels, M. A. J.; Janssen, R. A. J., Nanoscale Morphology of High-Performance Polymer Solar Cells. *Nano Lett.* **2005**, 5, 579-583.

225. Shen, Y.; Hosseini, A. R.; Wong, M. H.; Malliaras, G. G., How to make ohmic contacts to organic semiconductors. *ChemPhysChem* **2004**, 5, 16-25.

226. Blom, P.; De Jong, M.; Van Munster, M., Electric-field and temperature dependence of the hole mobility in poly (p-phenylene vinylene). *Phys. Rev. B* **1997**, 55, R656.

227. Ye, L.; Zhang, S.; Ma, W.; Fan, B.; Guo, X.; Huang, Y.; Ade, H.; Hou, J., From binary to ternary solvent: morphology fine-tuning of D/A blends in PDPP3T-based polymer solar cells. *Adv. Mater.* **2012**, 24, 6335-6341.

228. Chen, W.; Nikiforov, M. P.; Darling, S. B., Morphology characterization in organic and hybrid solar cells. *Energy Environ. Sci.* **2012**, 5, 8045-8074.

229. Guo, X.; Zhou, N.; Lou, S. J.; Smith, J.; Tice, D. B.; Hennek, J. W.; Ortiz, R. P.; Navarrete, J. T. L.; Li, S.; Strzalka, J., Polymer solar cells with enhanced fill factors. *Nat. Photon.* **2013**, 7, 825-833.

230. Lloyd, M. T.; Peters, C. H.; Garcia, A.; Kauvar, I. V.; Berry, J. J.; Reese, M. O.; McGehee, M. D.; Ginley, D. S.; Olson, D. C., Influence of the hole-transport layer on the initial behavior and lifetime of inverted organic photovoltaics. *Sol. Energy Mater. Sol. Cells* **2011**, 95, 1382-1388.

231. Peet, J.; Wen, L.; Byrne, P.; Rodman, S.; Forberich, K.; Shao, Y.; Drolet, N.; Gaudiana, R.; Dennler, G.; Waller, D., Bulk heterojunction solar cells with thick active layers and high fill factors enabled by a bithiophene-co-thiazolothiazole push-pull copolymer. *Appl. Phys. Lett.* **2011**, 98, 043301.

232. Li, W.; Hendriks, K. H.; Roelofs, W. S. C.; Kim, Y.; Wienk, M. M.; Janssen, R. A. J., Efficient Small Bandgap Polymer Solar Cells with High Fill Factors for 300 nm Thick Films. *Adv. Mater.* **2013**, 25, 3182-3186.

233. Kirchartz, T.; Agostinelli, T.; Campoy-Quiles, M.; Gong, W.; Nelson, J., Understanding the thickness-dependent performance of organic bulk heterojunction solar cells: the influence of mobility, lifetime, and space charge. *J. Phys. Chem. Lett.* **2012**, 3, 3470-3475.

234. Koster, L.; Shaheen, S. E.; Hummelen, J. C., Pathways to a new efficiency regime for organic solar cells. *Adv. Energy Mater.* **2012**, 2, 1246-1253.

235. Cowan, S. R.; Banerji, N.; Leong, W. L.; Heeger, A. J., Charge formation, recombination, and sweep-out dynamics in organic solar cells. *Adv. Funct. Mater.* **2012**, 22, 1116-1128.

236. Clarke, T. M.; Peet, J.; Nattestad, A.; Drolet, N.; Dennler, G.; Lungenschmied, C.; Leclerc, M.; Mozer, A. J., Charge carrier mobility, bimolecular recombination and trapping in polycarbazole copolymer: fullerene (PCDTBT: PCBM) bulk heterojunction solar cells. *Org. Electron.* **2012**, 13, 2639-2646.

237. Nguyen, T. L.; Choi, H.; Ko, S.-J.; Uddin, M. A.; Walker, B.; Yum, S.; Jeong, J.-E.; Yun, M. H.; Shin, T.; Hwang, S., Semi-crystalline photovoltaic polymers with efficiency exceeding 9% in a [similar] 300 nm thick conventional single-cell device. *Energy Environ. Sci.* **2014**, 7, 3040-3051.

238. Al-Kuhaili, M.; Durrani, S.; Khawaja, E., Effects of preparation conditions and thermocoloration on the optical properties of thin films of molybdenum oxide. *Thin solid films* **2002**, 408, 188-193.

239. Yeom, H. R.; Heo, J.; Kim, G.-H.; Ko, S.-J.; Song, S.; Jo, Y.; Kim, D. S.; Walker, B.; Kim, J. Y., Optimal top electrodes for inverted polymer solar cells. *Phys. Chem. Chem. Phys.* **2015**, 17, 2152-2159.

240. Burkhard, G. F.; Hoke, E. T.; McGehee, M. D., Accounting for interference, scattering, and electrode absorption to make accurate internal quantum efficiency measurements in organic and other thin solar cells. *Adv. Mater.* **2010**, 22, 3293-3297.

241. Dante, M.; Peet, J.; Nguyen, T.-Q., Nanoscale charge transport and internal structure of bulk heterojunction conjugated polymer/fullerene solar cells by scanning probe microscopy. *J. Phys. Chem. C* **2008**, 112, 7241-7249.

242. Moon, J. S.; Lee, J. K.; Cho, S.; Byun, J.; Heeger, A. J., "Columnlike" structure of the cross-sectional morphology of bulk heterojunction materials. *Nano Lett.* **2008**, 9, 230-234.

243. Seifter, J.; Sun, Y.; Heeger, A. J., Transient Photocurrent Response of Small-Molecule Bulk Heterojunction Solar Cells. *Adv. Mater.* **2014**, 26, 2486-2493.

244. Cowan, S. R.; Street, R.; Cho, S.; Heeger, A., Transient photoconductivity in polymer bulk heterojunction solar cells: Competition between sweep-out and recombination. *Phys. Rev. B* **2011**, 83, 035205.

245. MacKenzie, R. C.; Shuttle, C. G.; Chabinyc, M. L.; Nelson, J., Extracting microscopic device parameters from transient photocurrent measurements of P3HT: PCBM solar cells. *Advanced Energy Materials* **2012**, 2, 662-669.

246. Punke, M.; Valouch, S.; Kettlitz, S.; Christ, N.; Gärtner, C.; Gerken, M.; Lemmer, U., Dynamic characterization of organic bulk heterojunction photodetectors. *Appl. Phys. Lett.* **2007**, 91, 071118.

247. Zhang, Y.; Zhou, H.; Seifter, J.; Ying, L.; Mikhailovsky, A.; Heeger, A. J.; Bazan, G. C.; Nguyen, T. Q., Molecular doping enhances photoconductivity in polymer bulk heterojunction solar cells. *Adv. Mater.* **2013**, 25, 7038-7044.

248. Sariciftci, N.; Smilowitz, L.; Heeger, A. J.; Wudl, F., Photoinduced electron transfer from a conducting polymer to buckminsterfullerene. *Science* **1992**, 258, 1474-1476.

249. Yu, G.; Gao, J.; Hummelen, J. C.; Wudl, F.; Heeger, A. J., Polymer photovoltaic cells: enhanced efficiencies via a network of internal donor-acceptor heterojunctions. *Science-AAAS-Weekly Paper Edition* **1995**, 270, 1789-1790.

250. Chen, Y.; Zhang, S.; Wu, Y.; Hou, J., Molecular Design and Morphology Control Towards Efficient Polymer Solar Cells Processed using Non-aromatic and Non-chlorinated Solvents. *Adv. Mater.* **2014**, 26, 2744-2749.

251. Choi, H.; Park, J. S.; Jeong, E.; Kim, G.-H.; Lee, B. R.; Kim, S. O.; Song, M. H.; Woo, H. Y.; Kim, J. Y., Combination of Titanium Oxide and a Conjugated Polyelectrolyte for High-Performance Inverted-Type Organic Optoelectronic Devices. *Adv. Mater.* **2011**, 23, 2759-2763.

252. Choi, H.; Ko, S.-J.; Choi, Y.; Joo, P.; Kim, T.; Lee, B. R.; Jung, J.-W.; Choi, H. J.; Cha, M.; Jeong, J.-R., Versatile surface plasmon resonance of carbon-dot-supported silver nanoparticles in polymer optoelectronic devices. *Nat. Photon.* **2013**, 7, 732-738.

253. Kang, H.; Kee, S.; Yu, K.; Lee, J.; Kim, G.; Kim, J.; Kim, J. R.; Kong, J.; Lee, K., Simplified Tandem Polymer Solar Cells with an Ideal Self-Organized Recombination Layer. *Adv. Mater.* **2014**.

254. Zhang, Y.; Deng, D.; Lu, K.; Zhang, J.; Xia, B.; Zhao, Y.; Fang, J.; Wei, Z., Synergistic Effect of Polymer and Small Molecules for High-Performance Ternary Organic Solar Cells. *Adv. Mater.* **2014**.

255. Liu, Y.; Zhao, J.; Li, Z.; Mu, C.; Ma, W.; Hu, H.; Jiang, K.; Lin, H.; Ade, H.; Yan, H., Aggregation and morphology control enables multiple cases of high-efficiency polymer solar cells. *Nat. Commun.* **2014**, 5.

256. Choi, H.; Lee, J.-P.; Ko, S.-J.; Jung, J.-W.; Park, H.; Yoo, S.; Park, O.; Jeong, J.-R.; Park, S.; Kim, J. Y., Multipositional Silica-Coated Silver Nanoparticles for High-Performance Polymer

Solar Cells. *Nano Lett.* **2013**, 13, 2204-2208.

257. Li, W.; Hendriks, K. H.; Furlan, A.; Roelofs, W. C.; Wienk, M. M.; Janssen, R. A., Universal correlation between fibril width and quantum efficiency in diketopyrrolopyrrole-based polymer solar cells. *J. Am. Chem. Soc.* **2013**, 135, 18942-18948.

258. Liu, F.; Gu, Y.; Wang, C.; Zhao, W.; Chen, D.; Briseno, A. L.; Russell, T. P., Efficient Polymer Solar Cells Based on a Low Bandgap Semi-crystalline DPP Polymer-PCBM Blends. *Adv. Mater.* **2012**, 24, 3947-3951.

259. Bronstein, H.; Collado-Fregoso, E.; Hadipour, A.; Soon, Y. W.; Huang, Z.; Dimitrov, S. D.; Ashraf, R. S.; Rand, B. P.; Watkins, S. E.; Tuladhar, P. S., Thieno [3, 2-b] thiophene-diketopyrrolopyrrole Containing Polymers for Inverted Solar Cells Devices with High Short Circuit Currents. *Adv. Funct. Mater.* **2013**, 23, 5647-5654.

260. Zhou, P.; Zhang, Z.-G.; Li, Y.; Chen, X.; Qin, J., Thiophene-Fused Benzothiadiazole: A Strong Electron-Acceptor Unit to Build D−A Copolymer for Highly Efficient Polymer Solar Cells. *Chem. Mater.* **2014**, 26, 3495-3501.

261. Jung, J. W.; Liu, F.; Russell, T. P.; Jo, W. H., Semi-crystalline random conjugated copolymers with panchromatic absorption for highly efficient polymer solar cells. *Energy Environ. Sci.* **2013**, 6, 3301-3307.

262. Wang, D. H.; Kyaw, A. K. K.; Pouliot, J. R.; Leclerc, M.; Heeger, A. J., Enhanced Power Conversion Efficiency of Low Band-Gap Polymer Solar Cells by Insertion of Optimized Binary Processing Additives. *Adv. Energy Mater.* **2014**, 4.

263. Lu, L.; Xu, T.; Chen, W.; Landry, E. S.; Yu, L., Ternary blend polymer solar cells with enhanced power conversion efficiency. *Nat. Photon.* **2014**, 8, 716-722.

264. Zhou, H.; Chen, Q.; Li, G.; Luo, S.; Song, T.-b.; Duan, H.-S.; Hong, Z.; You, J.; Liu, Y.; Yang, Y., Interface engineering of highly efficient perovskite solar cells. *Science* 2014, 345, 542-546.

265. Jeon, N. J.; Noh, J. H.; Kim, Y. C.; Yang, W. S.; Ryu, S.; Seok, S. I., Solvent engineering for high-performance inorganic–organic hybrid perovskite solar cells. *Nat. Mater.* **2014**.

266. Seo, J.; Park, S.; Kim, Y. C.; Jeon, N. J.; Noh, J. H.; Yoon, S. C.; Seok, S. I., Benefits of very thin PCBM and LiF layers for solution-processed p–i–n perovskite solar cells. *Energy Environ. Sci.* **2014**, 7, 2642-2646.

267. Schilinsky, P.; Waldauf, C.; Brabec, C. J., Recombination and loss analysis in polythiophene based bulk heterojunction photodetectors. *Appl. Phys. Lett.* **2002**, 81, 3885-3887.

268. Li, Z.; Lin, J. D.; Phan, H.; Sharenko, A.; Proctor, C. M.; Zalar, P.; Chen, Z.; Facchetti, A.; Nguyen, T. Q., Competitive Absorption and Inefficient Exciton Harvesting: Lessons Learned from Bulk Heterojunction Organic Photovoltaics Utilizing the Polymer Acceptor P (NDI2OD-T2). *Adv. Funct. Mater.* **2014**, 24, 6989-6998.

269. Guo, X.; Zhou, N.; Lou, S. J.; Hennek, J. W.; Ponce Ortiz, R.; Butler, M. R.; Boudreault, P.-L. T.; Strzalka, J.; Morin, P.-O.; Leclerc, M., Bithiopheneimide–dithienosilole/dithienogermole copolymers for efficient solar cells: information from structure–property–device performance correlations and comparison to thieno [3, 4-c] pyrrole-4, 6-dione analogues. *J. Am. Chem. Soc.* **2012**, 134, 18427-18439.

270. Szarko, J. M.; Guo, J.; Liang, Y.; Lee, B.; Rolczynski, B. S.; Strzalka, J.; Xu, T.; Loser, S.; Marks, T. J.; Yu, L., When function follows form: effects of donor copolymer side chains on film morphology and BHJ solar cell performance. *Adv. Mater.* **2010**, 22, 5468-5472.

271. Hou, J.; Chen, H.-Y.; Zhang, S.; Li, G.; Yang, Y., Synthesis, Characterization, and Photovoltaic Properties of a Low Band Gap Polymer Based on Silole-Containing Polythiophenes and 2,1,3-Benzothiadiazole. *J. Am. Chem. Soc.* **2008**, 130, 16144-16145.

272. Huang, F.; Chen, K.-S.; Yip, H.-L.; Hau, S. K.; Acton, O.; Zhang, Y.; Luo, J.; Jen, A. K. Y., Development of New Conjugated Polymers with Donor−π-Bridge−Acceptor Side Chains for High Performance Solar Cells. *J. Am. Chem. Soc.* **2009**, 131, 13886-13887.

273. Zhang, M.; Gu, Y.; Guo, X.; Liu, F.; Zhang, S.; Huo, L.; Russell, T. P.; Hou, J., Efficient Polymer Solar Cells Based on Benzothiadiazole and Alkylphenyl Substituted Benzodithiophene with a Power Conversion Efficiency over 8%. *Adv. Mater.* **2013**, 25, 4944-4949.

274. Yang, L.; Tumbleston, J. R.; Zhou, H.; Ade, H.; You, W., Disentangling the impact of side chains and fluorine substituents of conjugated donor polymers on the performance of photovoltaic blends. *Energy Environ. Sci.* **2013**, 6, 316-326.

275. He, Z.; Zhong, C.; Su, S.; Xu, M.; Wu, H.; Cao, Y., Enhanced power-conversion efficiency in polymer solar cells using an inverted device structure. *Nat. Photon.* **2012**, 6, 591-595.

276. Lai, Y.-Y.; Shih, P.-I.; Li, Y.-P.; Tsai, C.-E.; Wu, J.-S.; Cheng, Y.-J.; Hsu, C.-S., Interface Engineering to Enhance the Efficiency of Conventional Polymer Solar Cells by Alcohol-/Water-Soluble C60 Materials Doped with Alkali Carbonates. *ACS Appl. Mater. Interfaces* **2013**, 5, 5122-5128.

277. Lee, W.; Seo, J. H.; Woo, H. Y., Conjugated polyelectrolytes: A new class of semiconducting material for organic electronic devices. *Polymer* **2013**, 54, 5104-5121.

278. Kim, J. Y.; Lee, K.; Coates, N. E.; Moses, D.; Nguyen, T.-Q.; Dante, M.; Heeger, A. J., Efficient Tandem Polymer Solar Cells Fabricated by All-Solution Processing. *Science* **2007**, 317, 222-225.

279. Ameri, T.; Li, N.; Brabec, C. J., Highly efficient organic tandem solar cells: a follow up review. *Energy Environ. Sci.* **2013**, 6, 2390-2413.

280. Li, W.; Furlan, A.; Hendriks, K. H.; Wienk, M. M.; Janssen, R. A. J., Efficient Tandem and Triple-Junction Polymer Solar Cells. *J. Am. Chem. Soc.* **2013**, 135, 5529-5532.

281. You, J.; Chen, C.-C.; Hong, Z.; Yoshimura, K.; Ohya, K.; Xu, R.; Ye, S.; Gao, J.; Li, G.; Yang, Y., 10.2% Power Conversion Efficiency Polymer Tandem Solar Cells Consisting of Two Identical Sub-Cells. *Adv. Mater.* **2013**, 25, 3973-3978.

282. Choi, H.; Ko, S.-J.; Choi, Y.; Joo, P.; Kim, T.; Lee, B. R.; Jung, J.-W.; Choi, H. J.; Cha, M.; Jeong, J.-R.; Hwang, I.-W.; Song, M. H.; Kim, B.-S.; Kim, J. Y., Versatile surface plasmon resonance of carbon-dot-supported silver nanoparticles in polymer optoelectronic devices. *Nat. Photon.* **2013**, 7, 732-738.

283. Guo, X.; Zhou, N.; Lou, S. J.; Smith, J.; Tice, D. B.; Hennek, J. W.; Ortiz, R. P.; Navarrete, J. T. L.; Li, S.; Strzalka, J.; Chen, L. X.; Chang, R. P. H.; Facchetti, A.; Marks, T. J., Polymer solar cells with enhanced fill factors. *Nat. Photon.* **2013**, 7, 825-833.

284. Kang, H.; Kim, K.-H.; Kang, T. E.; Cho, C.-H.; Park, S.; Yoon, S. C.; Kim, B. J., Effect of Fullerene Tris-adducts on the Photovoltaic Performance of P3HT:Fullerene Ternary Blends. *ACS Appl. Mater. Interfaces* **2013**, 5, 4401-4408.

285. Khlyabich, P. P.; Burkhart, B.; Thompson, B. C., Compositional Dependence of the Open-Circuit Voltage in Ternary Blend Bulk Heterojunction Solar Cells Based on Two Donor Polymers. *J. Am. Chem. Soc.* **2012**, 134, 9074-9077.

286. Street, R. A.; Davies, D.; Khlyabich, P. P.; Burkhart, B.; Thompson, B. C., Origin of the Tunable Open-Circuit Voltage in Ternary Blend Bulk Heterojunction Organic Solar Cells. *J. Am. Chem. Soc.* **2013**, 135, 986-989.

Chapter 9. Acknowledgements

Since beginning of my research in UNIST, I have received help from many people, and I have successfully finished my Master & Ph. D course.

First of all, I gratefully thank my advisor, Prof. Jin Young Kim to give me encouragement and compliment during my Master & Ph. D course. Whenever I faced a variety of research problems that cannot be solved by myself, many professors including Prof. Alan J. Heeger (UCSB), Han Young Woo (PNU), Dongwook Chang (PKNU), Sujin Park (UNIST), Myoung Hoon Song (UNIST), Changduk Yang (UNIST), Byeong-Su Kim (UNIST) and Tae-Hyuk Kwon (UNIST) gave me good directions and meaningful advices. I would like to thank all professors for their help.

Also, I would like to thank all NGEL members for their help for my research. In addition, I would like to express my thanks to Wonho Lee (KAIST), Taehee Kim (UNIST), Bo Ram Lee (UNIST), Jungmin Lim(CWRU) and Prof. Woo's Group (PNU).

Last, I thank my father, mother, sister, and my brother in law, Sven for encouraging me to continuosly do my research well. If it had not been for help from everyone, I could not have made great achievement and finished my Master & Ph. D program in five and half years. I would like to thank everyone once more.

감사의 글

시간이 흘러 어느새 논문을 마치고 '감사의 글'이란 것을 적게 될지 몰랐습니다. 지금까지 모든 저의 대학원 생활이 주마등처럼 떠오릅니다. UNIST에 처음 관심을 가지고 학교를 알아본 후 현재 저의 지도교수님 이신 김진영교수님께 찾아가 학부전공이 전혀 달랐던 저였지만 에너지분야 특히 유기태양전지 분야를 해보고 싶다고 말씀을 드린 후, 김진영교수님께서 "새로운 것에 도전해 보는 것도 나쁘지 않다. 하지만 열정은 반드시 있어야 한다. 한번 열심히 해봐~"라는 조언과 함께 흔쾌히 "OK" 사인을 해주셔서 2010년부터 지금까지 '대학원생'이라는 연구자의 길을 걸어왔습니다.

실험실 생활을 전혀 해보지 않았던 저에게 UNIST에서의 첫 대학원 생활은 그리 쉽지가 않았습니다. 학부에서 해왔던 전공도 아니었기에, 남들보다 더 열심히 해야 했고, 지치고 힘들고 다사다난한 날들을 보냈습니다. 그래도 시간이 지날수록 실험에 더욱 재미를 느끼고 연구에 대한 열정도 커져가는 제 자신을 발견할 수 있었습니다. 지금 생각해 보면 김진영 교수님과 NGEL 멤버들의 원동력 없이는 불가했을 것 같습니다. 모자란 저에게 항상 "대학원 생활은 버텨내는 것이야~" 라고 말씀해주신 교수님의 말씀이 항상 저 자신에 대한 버팀목으로 남아있습니다. 다시 한번 감사의 말을 전해드리고 싶습니다. 5년 반 동안의 석박 통합과정을 빠른 시일에 그리고 잘 마무리 할 수 있었던 것은 김진영 교수님의 뛰어난 지도력과 따뜻한 격려는 물론 NGEL멤버등 많은 분들의 도움이 있었기 때문이었습니다. 더불어 유니스트의 우수한 실험 기반과 활발한 콜라보레이션의 조화는 저를 더욱 빛나게 만들어 준 것 같습니다.

또한 연구적으로 적절한 충고와 지도를 해주신 우한영 교수님, 장동욱 교수님, 박수진 진 교수님, 송명훈 교수님, 양창덕 교수님님께 정말 감사드립니다. 그리고 박사 학위 심사를 하면서 많은 조언과 지도를 해주신 권태혁 교수님께도 감사의 말씀을 전합니다.

박사과정 동안 동고동락했던 유니스트 모든 연구실 분들께 감사의 인사를 전합니다. 항상 내일을 자기일처럼 도와 줬던 연구 선배 Bright Walker 박사님, 정말 나를 친동생처럼 대해줬던 따뜻한 성범이형, 이제는 토론토대학교에서 연구를 시작한 양산짱 기환이형, 나의 Motivation 이었고 친구이고 인생 동반자인 이제 교수가 된 Prof. Choi, 따뜻한 맘을 가진 우리 실험실 큰 언니 명희, 항상 나를 잘이해해줬고 이제곧 미국갈 태효, 재기를 꿈꾸는 제기차는 착한 재기, 아주 위엄 있어진 NGEL의 실세 학가시 학범, 애키우느라 연구하느라 열심히인 혜림이, 연구열정이 어마어마한 세영이, 항상 나를 응원해준 애플의 정우, 일 많아도 항상 해내는 성실의 대명사 송이 와 택호, 나의 어깨를 책임졌던 강택이, QD팀을 혼자 이끌며 고군분투하는 영진이, 매사에 열심히인 수연이, 나이는 한참 어리지만 친구같은놈 재원이 그리고 막내 혜연이. 모두들 너무 감사해요. 앞으로도 NGEL의 멤버로써 김진영 교수님과 함께 더욱더 좋은 연구와 미래를 개척해주세요. 그리고 또, 항상 나를 응원해준 동생이고 친구인 태희, 도움도 많이줬고 곧 좋은대

로 포닥갈 보람이, 지금 미국서 고생하는 정만이, 카이스트에서 열심히 박사중인 원호, 형민이형, 승민이형, 시혁, 은용이형, 필재 등등 같이 보낸 시간들 너무 소중하게 생각합니다. 또 학부 해자회 친구들 정신적으로 나에게 많은 도움을 줘서 고맙습니다. 모두 대박나서 원하는 것 이룰수 있길 바랄께요. 미국 UCSB에서 교환학생 동안 내외적으로 많이 도와준 멋있는 병규형과 예쁜 고은이에게도 감사의 말씀을 전합니다.

항상, 저를 믿어주시고 응원해 주신 우리 아버지, 어머니, 누나, 스벤, 주일이형 등 많은분들께 정말 감사했습니다. 지금까지 받았던 이 감사함들에 조금이나마 보답할 수 있도록 더욱더 노력하겠습니다.

마지막으로 지면으로 통해서 일일이 언급을 하지 못했지만 그 동안 저를 아끼고 사랑해주신 모든 분들께 다시 한번 진심으로 감사 드립니다.

고서진 올림